TECHNICAL UNIVERSITY OF VIENNA

DIPLOMA THESIS

Collagen Fibril Orientation and Modulus Mapping of Osteonal Cortical Human Bone

Author:

Amraish N., BSC

Supervisors:

Univ.Prof. Dipl.Ing. Dr.sc.nat.

Thurner P.J

Senior Scientist

Andriotis O. PhD

Carried out for the purpose of obtaining the degree of Dipl.-Ing submitted at TU Wien, Faculty of Mechanical and Industrial Engineering in the

Bioengineering Research Group Institute of Lightweight Design and Structural Biomechanics

Declaration of Authorship

I, Amraish N., BSC, declare that this thesis titled, *Collagen Fibril Orientation and Modulus Mapping of Osteonal Cortical Human Bone*:

The elastic modulus maps and their evaluation and analysis, and the work presented in it are my own. I confirm that:

- This work was done wholly or mainly while in candidature for a research degree at this University.
- Where any part of this thesis has previously been submitted for a degree or any other qualification at this University or any other institution, this has been clearly stated.
- Where I have consulted the published work of others, this is always clearly attributed.
- Where I have quoted from the work of others, the source is always given. Except for such quotations, this thesis is entirely my own work.
- I have acknowledged all main sources of help.
- Where the thesis is based on work done by myself jointly with others, I have made clear exactly what was done by others and what I have contributed myself.

Signed:

_____

Date:

_____

TECHNICAL UNIVERSITY OF VIENNA

Abstract

Faculty of Mechanical Engineering Institute of Lightweight Design and Structural Biomechanics

Dipl. Ing

Collagen Fibril Orientation and Modulus Mapping of Osteonal Cortical Human Bone

by Amraish N., BSC

Bone mechanical properties at the tissue level are affected due to changes of bone components and structure at the nanoscale. Studying bone structure and material properties at various length scales is therefore important to attain a better understanding of the origin of bone mechanical properties and discern the origin changes with age and disease as well as their influence and impact on bone fracture. Cantilever-based nanoindentation Atomic Force Microscopy offers a possibility to interrogate bone mechanical properties at the nanoscale. It has previously been suggested that the heterogeneity of bone at the lamellar level may be a critical factor influencing bone fracture toughness. Within this thesis this suggestion was further investigated. Thirty bone samples from the human femur with existing fracture toughness measurements were obtained from a collaborator and were investigated using Atomic Force Microscopy in cantilever-based nanoindentation mode and Second Harmonic Generation Microscopy to interrogate collagen fibril orientation. The heterogeneity in indentation modulus between osteonal lamellae showed a potential statistically non-significant trend due to age. Similarly, collagen fibril orientation distributions did not change significantly with age. However, the Atomic Force Microscope imaging of osteonal lamellae revealed a distinctive lamellar structure (height topography) even when sampled were immersed in Phosphate-Buffered Saline for more than 24h in contrast to a previous study. Most importantly high fracture initiation toughness and high resistance to crack propagation correlate significantly with high degree of nanoelasticity heterogeneity between osteonal lamellae and interlamellar areas. However, fracture toughness parameters do not correlate at a significant level with the collagen fibril orientation distributions. This shows that indeed the modulation of stiffness at the lamellar level is influencing fracture toughness, but it does not seem to depend on age.

Acknowledgements

Even though words fail to express sincere appreciation to all persons supported and assisted me, I would like to thank my husband and life partner (Michael Kramer) and my parents (Aida and Sade), who always supported and encouraged me to pursue my dreams, especially my father, who would have been happy to see these images of bone, but time didn't help us!

I deeply thank Prof. Philip Thurner, who gave me this opportunity to conduct this research with the biomechanical research group at the TU Wien. I deeply and sincerely thank Dr. Orestis Andriotis, who without his patience, continuous support and help, I would not have achieved or reached this level of knowledge. As well thanks to Dr. Ruth Byrne, who assisted us with SHG.

Table of Contents

Declaration of Authorship ii

Abstract iii

Acknowledgements iv

List of Tables vii

List of Figures viii

List of Abbreviations xi

Introduction 1
- **1.1 Background and motivation** 1
- **1.2 Problem definition** 4
- **1.3 Thesis goal** 4
- **1.4 Structure of the thesis** 5

Bone Structure and Mechanics 6
- **2.1 Bone Structure and Material** 6
- **2.2 Bone Cells** 8
- **2.3 Aging and Osteoporosis** 9
- **2.4 Bone Mechanics** 10
  - **2.4.1 Tensile and Compression Tests** 12
  - **2.4.2 Bending Tests** 16
  - **2.4.3 Torsional Tests** 17
  - **2.4.4 Fatigue Tests** 18
  - **2.4.5 Fracture Mechanics Tests** 18
  - **2.4.6 Indentation Tests** 20

Atomic Force Microscopy 24
- **3.1 Overview of the Atomic Force Microscope** 24
- **3.2 Measurement Principles** 24
  - 3.2.1 AFM Cantilever and Tip 26
  - 3.2.2 Determination of Cantilever Spring Constant 27
  - 3.2.3 Detection Method (Optical Lever Sensitivity) 30
- **3.3 Measurement Modes** 32
  - 3.3.1 Contact mode 33
  - 3.3.2 Non-contact mode 35
  - 3.3.3 Intermittent mode 35
- **3.4 AFM cantilever-based nanoindentation** 35
  - 3.4.1 Mechanical Characterization using QI™ mode 36

Second Harmonic Generation Microscopy 40
- **4.1 Working Principle** 40
- **4.2 Collagen Fibers as non- centrosymmetric structure** 42

Materials and Methods 46
- **5.1 Experiments Overview and Sample Description** 46
- **5.2 Sample Preparation** 47
- **5.3 Experimental Techniques** 50
  - 5.3.1 Bone Samples Imaging with SHG 50
  - 5.3.2 AFM Nanoindentation Experiments 51
- **5.4 Data Processing** 52
  - 5.4.1 SHG Image Processing 52
  - 5.4.2 QI Data Processing 57

Results and Discussion 62

6.1 Collagen Fibril Orientation 62
6.1 Indentation modulus 68
6.1 Correlation between the Collagen Fibrils Orientation and Indentation Modulus 73
6.1 Fracture Toughness Data 77
6.1 Measured Height 81
6.2 Limitations and challenges 83
6.3 Conclusion 84

References 85

Appendix 94
Annex i: Optical Microscope Images 94
Annex ii: SHG Microscope Images 109
Annex iii: Sample Preparation Protocol 134
Annex iv: Measurement on Bone Surface via AFM 136
Annex v: Bone Specimens List 140
Annex vi: Statistical Summary of the Indentation Modulus 141
Annex vii: Statistical Summary of Collagen Fibrils Orientation 142

List of Tables

Table 2. 1: Data from Wet Specimens at room temperature (Femur/Tibia) 15
Table 2. 2: Data from human femur specimens at room temperature 17

Table 3. 1: Fitting equations for different tip shapes 37

Table 6. 1: Linear fitting equation for lamellae and interlamellar areas 67
Table 6. 2: Linear fitting equations for collagen fibril orientation angle correlating with age 68
Table 6. 3: Linear fitting equations for Median Lamellae and Interlamellar areas correlating with age 70
Table 6. 4: Linear fitting equation for median ratio between the lamellae and interlamellar areas correlating with age 71
Table 6. 5: Linear fitting equations for collagen fibril orientation angle correlating with the smoothed indentation modulus 76
Table 6. 6: Linear fitting equations fracture toughness parameters and collagen fibril orientation angle and the indentation modulus 81

List of Figures

Figure 1. 1: Bone structure at different length scales. 3

Figure 2. 1: Collagen structure. (Wegst *et al.* 2015)..... 7
Figure 2. 2: Histological cut showing details of lamellar bone concentrically organized and woven bone mixed with cartilage and calcified cartilage tissues. (Matos et al. 2008)..... 8
Figure 2. 3: Stress-Strain curve of a tensile test for Bone. Show the different definitions discussed above..... 13
Figure 2. 4 :Left: Loading and un-loading indentation curve. Right: schematic representation of the indenter on a specimen. 21

Figure 3. 1: The setup of an atomic force microscope. The AFM cantilever deflects due to the interaction forces, attractive or repulsive, with the surface topography. A laser is reflected off the back side of the cantilever and onto a photodiode. The vertical deflection is measured by change in voltage between the left (A+C) and right (B+D) half of the photodiode. 25
Figure 3. 2: (I) illustrates different tip shapes, if the tip is very sharp (a), it has a higher depth of field (high aspect ratio), resulting in better distinguishing of sharp edges. *i.e.* tip (c) is a low aspect ratio while imaging a step won't be sharply distinguished. (II) Results of scanning a step with different types of tips (Morris *et al.*) 26
Figure 3. 3: Cantilever chip and cantilever tip. (adapted from: AFM Manual)..... 27
Figure 3. 4: when the cantilever and the sample comes in contact, the deformation is zero. Only when the cantilever moves with the Z-piezo pushing into the sample, this Z-displacement of the cantilever equals to the sum of cantilever deflection and the sample deformation ($Z=Dc+\delta$). 28
Figure 3. 5: Deflection-Displacement Curve for AFM tip indentation on Mica 31
Figure 3. 6: AFM Contact, Intermittent and Non-contact mode. (source: JPK.com)..... 32
Figure 3. 7: The potential curve shows the interatomic distance vs. the force experienced on the tip. (Adapted from JPK.com)..... 33
Figure 3. 9: PID Controller. (source: Morris, 2009)..... 34
Figure 3. 10: Schematic representation of tip scanning over a region of interest, x is the fast scanning direction and y is the slow scanning direction..... 36
Figure 3. 11: Schematic representation of cantilever deflection and tip-sample distance..... 37

Figure 4. 1: Schematic representation of SHG. (source: Wiki). 40
Figure 4. 2: Collagen fibril orientations within lamellae in osteons (source: teambone.com). 42
Figure 4. 3: SHG image of specimen a (25 years old – F) in slide N1-A, scale bar 300 μm .. 43
Figure 4. 4: Autofluorescence channel from multiphoton imaging of specimen A in slide N1, scale bar 300 μm 44
Figure 4. 5: Overlapped SHG and autofluorescence images, scale bar 300 μm..... 45

Figure 5. 1: schematic overview of the experimental techniques used. scale bar 300 μm for full sample images and 5 μm for AFM images 47
Figure 5. 2: Glass-slide N1 is mounted with 5 samples (*i.e.* A =25 indicates the number of the sample and the age of the donor), a small glass piece is glued at the level of the specimens for cantilever sensitivity measure. 48
Figure 5. 3: Prepared glass slide with specimens N1 48

Figure 5. 4: Optical microscope image of sample N1A, M, 25 years old..... 49
Figure 5. 5: Optical microscope image of sample, N3E, F, 101 years old 50
Figure 5. 6: AFM instrument..... 51
Figure 5. 7: AFM cantilever during indentation of a bone sample as viewed with the video microscope 52
Figure 5. 8: Images of SHG channel 0 (left) and autofluoresence channel 1 (right), from sample N3E (101 years) for each sample 25-30 images were obtained, scale bar 100 μm 53
Figure 5. 9: Optical microscope image of sample N3E (101 years), scale bar 300 μm..... 53
Figure 5. 10: Stitched SHG image of N3E (101 years) using MosaicJ, scale bar 300 μm 54
Figure 5. 11: Stitched autofluorescence image of N3E (101 years) using MosaicJ, scale bar 300 μm 54
Figure 5. 12: SHG and bone autofluerescnec overlay of sample N3E, produced with MosaicJ, scale bar 300 μm..... 55
Figure 5. 13: Cropped osteon of S2E (left), QI07 is then cropped with dimensions 25 μm x 25 μm, scale bar 5μm (right) 56
Figure 5. 14: Intensity profiles (from right to left) along the diagonal of S2E-QI07 both as SHG intensity and as orientation angle. 57
Figure 5. 15: Indentation modulus map (left). Setpoint height, (right). Scale bar 5 μm..... 58
Figure 5. 16: Indentation modulus map plotted using Matlab..... 58
Figure 5. 17: selected lamellae for mean and median calculation, S2E_QI07 59
Figure 5. 18: One manually selected lamella 59
Figure 5. 19: A resized & smoothed QI (medfilt2d function) 60
Figure 5. 20: Structural and mechanical results of the measurement methods, SHG and smoothed AFM. Scale bar 5 μm..... 61

Figure 6. 1: SHG images converted into collagen orientation angle (left) and corresponding histograms (right) for samples S2E 87 years old, female (top) and N3A 47 years old, female (bottom)..... 63
Figure 6. 2: N3A sample represented as collagen fibril degree values..... 63
Figure 6. 3: S2E sample represented as collagen fibril degree values..... 64
Figure 6. 4: Histogram of collagen fibril degrees observed in S2E sample 65
Figure 6. 5: Collagen fibril degree of orientation vs age 65
Figure 6. 6: Collagen fibril degree of orientation vs age for lamellae (red) and interlamellar areas (blue)..... 66
Figure 6. 7: Median of the collagen fibril orientation angle vs age (all samples) 67
Figure 6. 8: Median ratio between lamella and interlamellar areas vs age (all samples) 68
Figure 6. 9: Median of the indentation modulus (GPa) of lamellae and interlamellar areas vs age..... 69
Figure 6. 10: Median ratio between lamella and interlamellar areas vs age (all samples) 71
Figure 6. 11: Median of the indentation modulus (GPa) vs age (all osteons) 72
Figure 6. 12: Median of the indentation modulus (GPa) vs osteons of sample S2D (80 years old). Lamella (Red), Interlamellar area (Blue) 73
Figure 6. 13: Overlapped QI and SHG (A) S2EQI06 and (B) S2EQI07, (C) S2EQI04 and (D) S2EQI05, scale bar 5 μm 74
Figure 6. 14: S2EQI07-Modulus, in red selected intensity profile line (right to left), dimensions 25 μm x 25 μm..... 75
Figure 6. 15: S2EQI07 intensity profiles along with the SHG intensity 75
Figure 6. 16: S2EQI07 Collagen fibril orientation angle vs smoothed indentation modulus.. 76

Figure 6. 17: The crack initiation toughness as a function of the ratio of median collagen fibrils angle 77
Figure 6. 18: The crack growth toughness as a function of the ratio of median collagen fibrils angle 78
Figure 6. 19: The overall resistance to crack propagation as a function of the ratio of median collagen fibrils angle 78
Figure 6. 20: The crack initiation toughness as a function of the ratio of median between Lamellae and Interlamellar areas 79
Figure 6. 21: The crack growth as a function of the ratio of median between Lamellae and Interlamellar areas 79
Figure 6. 22: The overall resistance to crack propagation as a function of the ratio of median between Lamellae and Interlamellar areas 80
Figure 6. 23: S2EQI07 (Left), S2EQI08 (Right) measured height, scale bar 5 μm 82
Figure 6. 24: S2EQI04 (Left), S2DQI03 (Right) measured height, scale bar 5 μm 82
Figure 6. 25: S2BQI06 (Left), S2AQI03 (Right) measured height, scale bar 5 μm 83

List of Abbreviations

AFM	Atomic Force Microscopy
BMD	Bone Mineral Density
DEXA	Dual Energy X-ray Absorptiometry
ECM	Extra Cellular Matrix
HBSS	Hank's Balanced Salt Solution
IDI	Indentation Depth Increase
NCP	Non-Collagenous Proteins
PBS	Phosphate-Buffered Saline
PMMA	Polymethylmethacrylat
SEM	Scanning Electron Microscopy
SHG	Second Harmonic Generation
STM	Scanning Tunnelling Microscopy
WHO	World Health Organization

Chapter 1
Introduction

1.1 Background and motivation

Mechanical properties of bone alter with age and disease. Bone is a dynamic tissue that remodels due to external mechanical stimuli. Briefly, during remodeling process osteoclasts, dissolve bone matrix and osteoblasts deposit newly formed bone matrix. Osteons are the product and the fundamental element of bone remodeling. Osteons are composed of collagen fibers; the orientation of which may be an influencing factor of fracture toughness in bone (Thurner, 2014). Due to age, an imbalance in bone cell activities leads to considerable loss of bone mass, affecting its micro-architecture, and resulting in deterioration in toughness and a higher fracture risk (Zioupos, 1998; Boskey, 2010, Ager, 2006; Thurner, 2014; Granke, 2015). Osteoporosis is a condition during which bone composition structure and material properties are altered, leading to increase in fracture risk (Osterhoff, 2016, Dickenson, 1981; Schneider, 2008). Currently, the most common method to detect osteoporosis is the assessment of bone mineral density (BMD), in other words the quantity of bone. For a whole population, osteoporosis has an obvious effect on bone mass. However, this method does not succeed in

predicting bone fragility in more than third of the cases, and it is ineffective for individual diagnosis (Cowin, 2001, Osterhoff, 2016, Ager, 2006). Unfortunately, only at post-fracture, osteoporosis is discovered, and early diagnosis is difficult to achieve. Beyond changes in bone composition, *i.e.* bone quantity, changes in material properties have been shown in osteoporosis by (Dickenson, 1981; Boskey, 2006). However, the actual influence of osteoporosis on bone material properties is still not clearly well-defined. Jenkins *et al.* shows that the fracture toughness compromises due to age but not due to disease such as osteoporosis and osteoarthritis. (Jenkins, 2017). This suggests that assessment of the quality of bone at the lower length scale levels of the tissue hierarchy could provide valuable insight and help understand the underlying cause or effects of increased fractures in osteoporotic bones.

Hip fracture is the most severe site of fracture that causes immobility and while 90% of the patients that had a hip fracture are older than 65 years old (Carpintero, 2014). Especially among elderly, this in turn results in decreased quality of life, pain and leads to a higher risk of mortality. In addition, considering the aging societies, osteoporosis indirectly imposes a high burden on the health care sector. In the year 2000 about 9 million osteoporotic fractures have occurred worldwide, including 1.6 million hip fractures, 1.7 million forearm fractures, and 1.4 million clinical (symptomatic) vertebral fractures (Dimai, 2012). Furthermore, the combined annual costs of all osteoporotic fractures have been estimated to be $20 billion in the United States and €30 billion in the European Union (Cummings, 2002). In North America and Western Europe, health and social care costs in the 12 months following hip fracture to be $43,669 per patient (Williamson, 2017). In Austria, an estimated total of 119,911 patients with incident osteoporosis-related fractures were treated in 2008. This had a total cost of €685.6 million (Dimai, 2012). These costs on the health sector can be minimized if bone fracture could be predicted, and successively a counter measure can be implemented to reduce fracture risks, particularly among the elderlies.

Prediction of fractures can be achieved via a better understanding of bone mechanical properties and compositional structure. Therefore, a quantification of bone tissue properties is necessary to set a predictive model for bone fracture. This can be achieved by studying bone hierarchical structure and material at various length scale levels of the tissue hierarchy in young and old individuals.

Unlike engineering materials, bone is a structure with a hierarchical architecture that spans from the nanoscale to the micro-, macro- and tissue level. Bone can be considered as a nanocomposite

of nanocrystals, collagen type I, non-collagenous protein (NCP) and water (Cowin, 2001; Currey 2002). These components assemble into distinct structural units throughout different length scale levels of the tissue hierarchy.

The principle components of bone are collagen fibrils, mineral crystals, non-collagenous protein and water. Figure 1.1 shows the hierarchical structure of bone at different length scales. At the nanoscale, collagen molecules self-assemble into mineralized collagen fibrils, where calcium phosphate mineral platelets surround, and are arranged periodically among collagen molecules. At the sub microscale, these collagen fibrils are arranged into plates, of 2 to 5 µm thick, to form lamellae. The area between adjacent lamellae is known as interlamellar areas. At the microscale, lamellae wrap into concentric layers and form the fundamental building block of cortical bone, the osteons. The center of the osteons is known as Haversian canal where blood vessels and nerves pass through. Osteons are highly remodelled during life time. However, interstitial bone, which is the bone between the osteons is not remodelled. Finally, at the tissue level bone can be divided into cortical or compact and trabecular or spongy bone. (Cowin, 2001; Currey 2002; Rho, 1998).

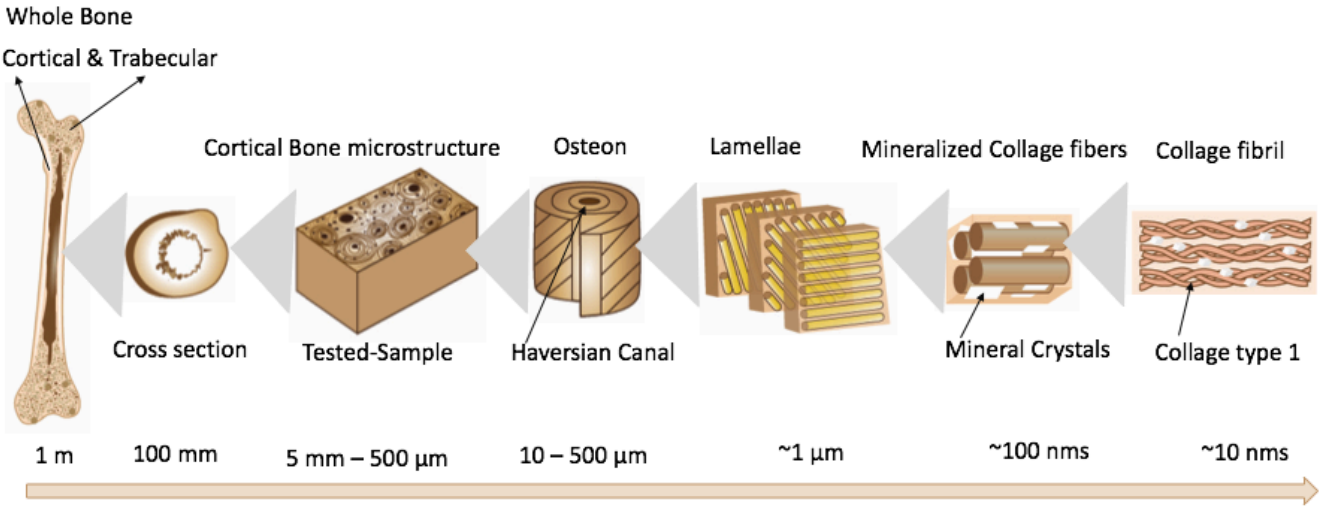

Figure 1. 1: Bone structure at different length scales.

As in most load-bearing biological tissues that possess a hierarchical architecture, tissue hierarchy in bone brings complexity when identifying the mechanical properties at the tissue level. The structure-mechanical properties at the lowest length scale level define the mechanical behaviour at the next length scale and so on. This heterogeneity of bone structure, results in non-uniform inelastic deformation and increased energy dissipation, which improves bone

toughening (Tai, 2004). To interrogate experimentally the bone mechanical properties at the microscale and nanoscale, different techniques have been developed and different type of tests have been conducted (Ascenzi, 1967, 1968; Hayes, 1976; Boskey, 2006; Cowin, 2001; Rho, 1998; Schrof, 2014; Hengsberger 2001; Ho Ba Tho 2012). Atomic Force Microscopy (AFM) is one technique where bone can be topographically scanned and mechanically investigated with high resolution at the nanoscale. Katsamenis (2012) showed via AFM cantilever-based nanoindentation that bone lamellae and interlamellar areas differ in their composition, mechanical behaviour, and collagen orientation. The latter is investigated in this thesis via Second Harmonic Generation (SHG) images.

1.2 Problem definition

Due to bone hierarchical structure, changes of this structure at the micro- and nanoscales directly affect the overall properties at the macroscale. The mechanical properties of bone at the nanoscale and the changes accompanied with it are partially investigated. This thesis focuses on indentation modulus mapping of osteons, and how collagen fibril orientations change between in- and out of plane along the long axis of osteons and due to age.

1.3 Thesis goal

The aim of this master thesis is divided into three parts:

a) To investigate the heterogeneity in indentation modulus of compact bone samples between lamellae and interlamellar areas, and how they change due to age.
b) To examine the changes in collagen fibrils orientation and how this relates to the measured mechanical properties.
c) To correlate the indentation modulus and the collagen fibrils orientation data with fracture toughness parameters, which were obtained from fracture experiments conducted on these bone samples by a collaborator (Nyman Lab – Granke *et al.* 2015).

The AFM cantilever-based nanoindentation technique was employed to investigate the mechanical properties of bone at the nanoscale. Briefly, a sharp tip indents the bone surface while the sample is fully hydrated in aqueous solution. The second part was achieved by imaging the same samples using SHG.

1.4 Structure of the thesis

This thesis consists of six chapters. In chapter two, bone structure at different length scale is explained. In addition to bone mechanics along with different measurement and evaluation methods are detailed. In chapter three, the first approach for achieving the aims of this research is detailed. Namely, the AFM measurement principle and cantilever-based nanoindentation mode. After that, the second approach is explained in chapter four, namely, the SHG measurement principle. In chapter five, the materials and methods used are presented, including the procedure of data analysis from the AFM and SHG measurements using Matlab, Fiji (ImageJ) and the JPKSPM Data Processing software. Finally, in chapter six, the results are presented and discussed.

Chapter 2
Bone Structure and Mechanics

The skeletal system provides structural support and protection to organs, while it is composed of long, short and irregular bones. The complex composition and structure of bone allows it to sustain physiological loads. In addition, bone is a self-healing tissue, if bone tissue is damaged, for instance due to a fracture, it can repair the damaged bone tissue to maintain performance. As well, bone is a highly-remodelled tissue. It adapts to loads under which it is placed according to Wolff's law (Wolff, 1892). However, bone properties deteriorate due to age and disease, making it an interesting tissue for scientific research. In this chapter, the structural properties of bone are presented as well as its mechanical properties that have been studied in the past through different experimental techniques.

2.1 Bone Structure and Material

Bone can be thought of as a nanocomposite of organic, mostly collagen fibrils and NCP, and inorganic mineral crystals (calcium phosphate). By weight, dry bone is made of about 62% inorganic and 38% organic matter, whereas by volume, there is more organic (68%) than inorganic (32%) matter (Cong, 1964; Cowin, 2001; Keaveny, 2004). In physiological conditions, bone is a highly-hydrated nanocomposite of collagen and inorganic matrix that share 33% by volume, water constitutes around 25 % and NCPs around 7% (Cowin, 2001; Rho 1998; Currey 2002).

The most abundant structural protein in bone is collagen. Collagen in bone is mainly constituted of fibril-forming collagen molecules, as shown in figure 2.1. A collagen molecule is composed of three tightly-packed polypeptide chains of amino acids arranged in a helical configuration. Collagen type I, is composed of two α_1-type 1 and one α_2-type 1 chains. Collagen molecules

self-assemble into larger cylindrical-like structures *i.e*. the collagen fibrils, with a characteristic 67 nm periodicity, also known as D-band (An, 2000; Cowin, 2001, Thurner 2009).

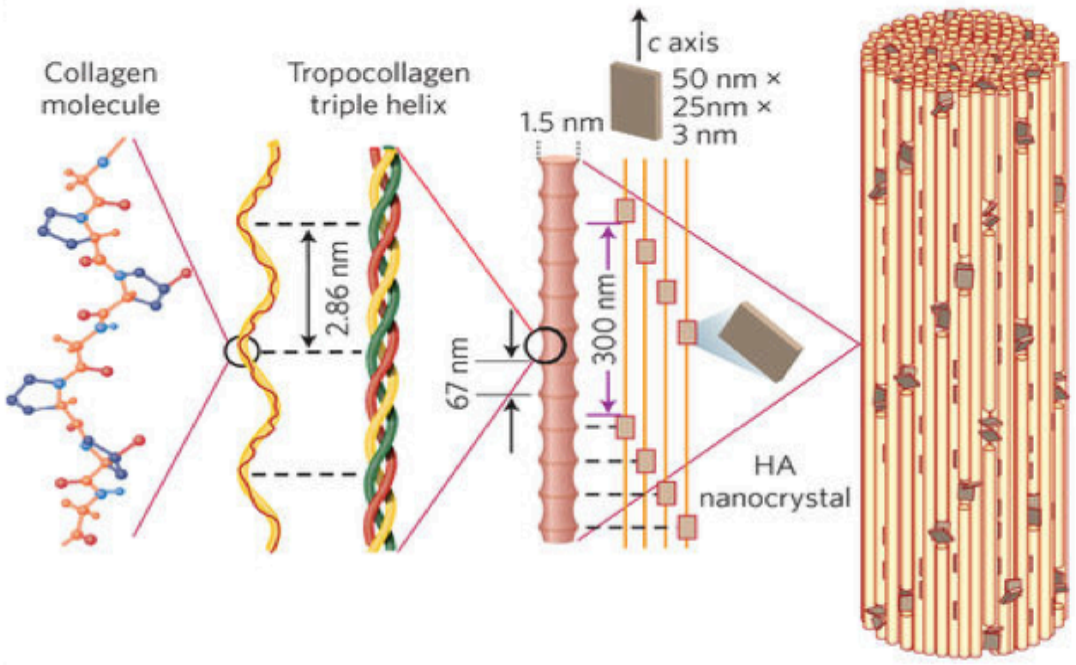

Figure 2. 1: Collagen structure. (Wegst *et al.* 2015)

NCPs makes about 10% of the organic component of bone, and include non-collagenous protein, proteoglycans, phospholipids, glycoproteins, and phosphoproteins. These components vary in their distribution and amounts depending on bone type and location (An, 2000; Cowin, 2001). NCPs could be thought of as mechanically relevant components because they are located on fracture surfaces, *i.e.* in between mineralized fibrils (Katsamenis, 2012), they provide specific attachment to collagen fibrils and hydroxyapatite crystals, as well as nucleation sites for mineralization and cell attachment sites (Thurner, 2009). Cement lines and lamellar boundaries are also rich in NCPs.

The non-organic component of bone is mainly minerals, calcium phosphate hydroxyapatite. Mineral crystals come in different sizes and shapes, such as needles and filaments. Mineralization of collagen fibrils occurs internally as well as externally (Thurner, 2009; Nudelman, 2010).

Cortical bone is dense and found in diaphysis long bones. Trabecular bone is spongy and is found in the epiphyses of long bone. The structure and location of trabecular bone helps to transfer loads and in this way stress concentration is minimized (An, 2000; Cowin, 2001; Currey 2002). Bone strength properties vary depending on bone type and anatomical location.

For instance, cortical bone is stiffer than trabecular bone, but more brittle (Osterhoff, 2016). Lamellar structure is characteristic of cortical and trabecular bone, in which fibrils are orderly oriented. However, woven bone is another type of bone, where fibrils are shorter than that of the lamellar bone and are arranged randomly, as shown in figure 2.2.

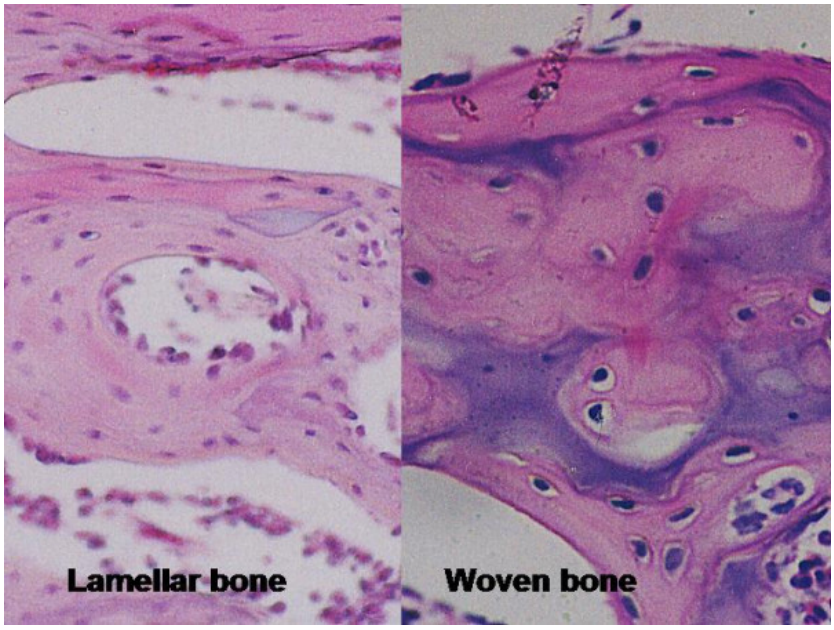

Figure 2. 2: Histological cut showing details of lamellar bone concentrically organized and woven bone mixed with cartilage and calcified cartilage tissues. (Matos *et al.* 2008)

It has been shown that woven bone is deposited in a shorter timescale during fracture repair compared to lamellar bone (An, 2000; Currey, 2002). As any biological tissues, bone matrix is deposited via specific type of bone cells, known as osteocytes. Bone does not only have cells that generate extracellular matrix (ECM), but also has cells that resorb bone matrix, making it one of the highly-remodelled tissues in the body.

2.2 Bone Cells

Bone cells are divided into four main types, osteoblast, osteocytes, bone lining cells, and osteoclasts. Osteoblasts are responsible of forming new bone, they synthesise and secrete un-mineralized bone matrix (osteoid). once these cells are trapped in the mineralized matrix they became osteocytes, the primary cell of mature bone. Osteoclasts, bone-resorbing cells, are large and multinucleated cells, they solubilize both the mineral and organic components of the matrix by secreting hydrogen ions (H^+) and lysosomal enzymes. Bone lining cells are osteoblasts that are not in the process of forming bone, they are flattened, elongated cells covering all quiescent bone surfaces (Cowin, 2001; Currey, 2002). In adult bone, 90% to 95% of all bone cells are

osteocytes, which as well, the longest-lived bone cell. However, with age osteocytes die in association with pathological conditions (osteoporosis and osteoarthritis) resulting in reduced remodelling and therefore increased fragility (Bonewald, 2011).

The continuous process of bone synthesis and destruction is called bone remodelling. Both osteoclasts and osteoblasts are very active during bone remodelling and adaptation, which goes through three phases, a) activation, b) resorption, and c) formation. In activation, osteocytes sense damaged matrix, and therefore, activate osteoblasts and osteoclasts. Osteoclasts resorb bone debris and damaged bone, forming cavities referred to as Howship's lacunae in trabecular bone, and as resorption cavities, in cortical bone. Finally, formation occurs in two stages: osteoblasts deposit un-mineralized bone matrix followed by extracellular mineralization. The whole process of bone formation lasts approximately 200 days (Cowin, 2001, Bonewald, 2011). This ability of bone to remodel and adapt explains how dynamic bone tissue is. Bone remodelling is not only active in fracture healing cases, but also a continuous process throughout the life of bone. These changes in bone density, architecture and structure impact bone properties at different ages, with consequences leading to bone fractures due to loss of bone density and strength.

2.3 Aging and Osteoporosis

With aging and due to hormonal changes, such as lower levels of estrogen in women after menopause, the metabolic activities of osteoclasts are much higher than that of the osteoblasts. This creates a gap between bone resorption and formation. The decrease in the functional capacity of osteoblasts leads to bone mass reduction and fragility, making it susceptible to fracture, increasing fracture risk, decreasing fracture toughness and crack initiation toughness (Ager, 2006, Zimmermann, 2015). This state of bone mass loss, increase pores, and decrease in bone strength is known as osteoporosis (Cowin, 2001; Seeman, 2008; Ammann, 2003). Studies show that estrogen deficiency not only induces a focal imbalance at remodeling sites, but also increases the remodeling rate of bone, thus accelerating bone loss (Parfitt, 1980).

The world health organization (WHO) defines osteoporosis based on bone mineral density (BMD), a T-score compares BMD to average values of young healthy adult and a score below 2.5 is considered osteoporotic (WHO, 1994). However, this definition does not consider many parameters that influence bone strength, such as body size, mass, microstructure, and health

record of patients, and so it does not capture many persons with low bone quality and higher fracture risks.

Dual energy X-ray absorptiometry (DEXA) is based on projectional images, and assesses the BMD of the examined bone. One of the main advantages of DEXA is its non-invasive application. However, this assessment is not necessarily a good insight on bone quality and strength. DEXA is not optimal for assessing the risk on an individual patient basis because it suffers from low specificity, which results in late diagnosis of many osteoporotic cases. Kanis reported that for the same BMD, older individuals may have 10 times increased fracture risk compared to younger individuals (Kanis, 2002). In addition, DEXA results can not differentiate between cortical and trabecular bone, and it is insensitive to structural changes within trabecular bone (Marshall, 1996; Cowin, 2001; Ammann, 2003; Siris, 2004; Nyman, 2007). Thus, osteoporosis is considered as a silent disease without symptoms.

As the cortical bone supports the body load, it is important to investigate its role in the fracture resistance and strength of whole bones. Which is not only a matter of bone mineralization and matrix, but also of structural organization at different length scales. This creates the necessity to study in detail smaller building blocks of bone, such as the osteons.

Age and age-related factors, among others, accelerate bone loss and increase fracture risk, such as vitamin D deficiency, which is characterized with higher amount of un-mineralized bone matrix, leading to osteoporosis and fracture (Cowin, 2001; Zimmermann, 2015). Additional causes of higher fracture risk are genetics, environmental, endogenous hormones, chronic diseases, and physical characteristics.

As mentioned above, different factors, including age, play a role and influence bone structure and therefore its mechanical properties. Testing techniques and methods are widely spread, which were adapted from mechanical testing of metallic or non-metallic materials. Due to the specialty of biological tissue, dimensions, hydration, and composite; testing techniques are adapted for each type of tissue.

2.4 Bone Mechanics

What determines and affects bone tissue properties? Compositional components, such as degree of mineralization and density. Or, are the microstructure features responsible of these properties? The ideal answer might be more complex than assigning the changes in bone tissue

properties to one parameter. Mechanical properties of bone are a matter of both, *i.e.* its compositional components and hierarchical structure. However, these properties compromise due to aging and disease, *i.e.* bone fracture risk increases due to reduced fracture toughness (Nalla, 2006). Therefore, it is important to investigate how aging affects, at the nano scale, the mechanical properties of bone.

At different length scales, different measurement techniques are applied. The varieties of testing techniques provide a wide range of tested parameters. Thus, it is important to consider, among others, the testing protocols, bone type and size, loading direction, hydration and pH under which the bone is being tested. The variations in mechanical properties, between cortical and trabecular bone, emerge due to their density difference. Trabecular bone is extremely heterogeneous, it shows a wide variability in strength and stiffness, and its elastic modulus can vary 100-fold depending on the anatomical position (Keaveny, 1993).

In describing bone mechanics or material properties, different parameters are measured and indicated. Here are some definitions related to these parameters. (1) The *Elastic Modulus*, (GPa), used to describe bone stiffness, is the slope of the linear-elastic part of the stress-strain curve, which is for a uniaxial tension test, is simply the ratio of normal stress in the loading direction to the normal strain in the same direction. (2) *Strain,* (dimensionless), is the proportional changes in length, $\Delta L/L$. (3) *Poisson's ratio*, ν (dimensionless), is the negative of the ratio of the lateral strain to the axial strain measured in axial loading. The Poisson's ratio shows that the elongation produced by an axial load is accompanied by a contraction in each of the transverse directions. For bone the Poisson's ratio has been estimated to be 0.3 (Reilly, 1974). (4) *Stress,* σ (N/m^2 or Pa) is the load applied over a defined area. (5) *Yield strength*, σ_y (MPa), is defined as the point where deformations are no longer elastic, and stresses begin to cause permanent damage to the bone structure. Classically, as shown in figure 2.3, the yield strength is measured at the intersection of a line parallel to the elastic region of the stress-strain curve but at a positive offset of 0.2% strain (Turner, 1989). (6) The *ultimate (tensile) strength,* $\sigma_{u,}$ is the maximum stress that bone can sustain. (7) *Strain rate* is the rate at which the bone is loaded during testing. (8) *Elastic Energy,* (J or N.m), is the area under the elastic part of stress-strain curve, and it describes the energy stored elastically without any damage to the material, and which is released again on unloading. (9) *Post-yield Energy* is the area under the plastic part of the stress-strain curve, when the energy distortion due to load applied is greater than the elastic energy, the material fails. In other words, it describes the energy needed to cause damage

in the sample. (10) *Hardness*, H (MPa), is a measure of the resistance of a material to penetration by an indenter with an external force applied to it. (11) *Toughness or critical strain energy release,* G_c (KJ/m^2), and the *fracture toughness or critical stress intensity factor*, K_c ($MPa{\cdot}m^{0.5}$), measure the resistance of the material to crack propagation, it describes the material ability to absorb energy up to fracture, which is the total area under the stress-strain curve up to fracture. (12) *Fatigue Failure* is the number of cycles necessary to cause a specimen to lose 30% of its elastic modulus. (13) *Crack Initiation Toughness*, K_{init} ($MPa{\cdot}m^{0.5}$), is the ability to withstand crack initiation. (14) *Crack Growth Toughness,* K_{grow} ($MPa{\cdot}m^{0.5}/mm^{0.5}$), is the ability to resist crack propagation. (15) *Elasticity* is the ability of a material to return to its original shape when an applied stress is removed. (Ashby 1999; An, 2000; Cowin, 2001; Currey, 2002).

Some of the conventional methods for bone mechanical testing, mainly but not exclusively, are tensile, compression, bending, torsion, fracture mechanic, fatigue, and indentation tests. Here some of them and values related to the elastic modulus will be described. In general, the elastic modulus values of trabecular bone from different sites vary from 6.9 to 23.5 GPa, whereas cortical bone values vary from 7.4 to 31.6 GPa (Thurner, 2009).

2.4.1 Tensile and Compression Tests

The idea of tensile and compression tests is simple, it measures the changes in length due to the application of tensile loading for tensile tests, and as, the intensity of a force acting on a plane (stress) for compression tests. It is known that stresses and strains change according to orientation due to the orthotropy of the material. In fact, in a simple tensile test, the material experiences tension in the loading direction and compression on other faces and shear in various directions on all faces.

Tensile and compression tests result in a stress-strain curve from which the following parameters are obtained; elastic modulus, ultimate strength, yield point, post yield energy and work to failure (area under load-displacement curve). In many biological materials, the stresses depend on the orientation of the considered plane as well as the loading rate. The latter is known as the viscoelastic behaviour. Bone is considered to be viscoelastic. Hence, the stress developed within bone is dependent on the rate at which the bone is strained (Hayes, 1976; An, 2000; Cowin, 2001).

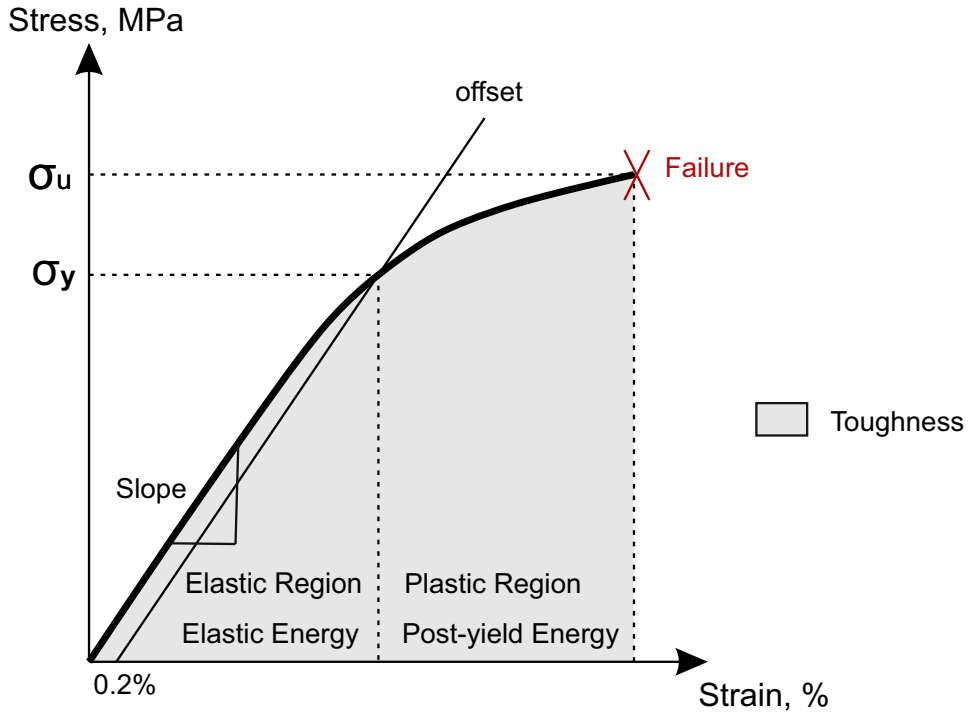

Figure 2. 3: Stress-Strain curve of a tensile test for Bone. Show the different definitions discussed above.

At the beginning, the load varies linearly and proportionally with the deformation, this linear elastic behaviour gives the elastic modulus, which is the slope of the linear portion of the curve, and is described in terms of stress and strain as;

$$\sigma = E * \varepsilon$$

where σ is the stress (MPa), E is the elastic modulus (MPa), and ε is the strain. This equation holds true for loading in one direction and for very small strains (Cowin, 2001; Currey, 2002).

At the yield point, bone starts to plastically deform. However, one should keep in mind that load and deformation depends on the size and shape of the tested sample (An, 2000; Currey, 2002). Still, this curve tells us that the stress-strain relation is proportional (linear), for very small strains < 0.2%.

The area under the stress-strain curve is the work done per unit volume, or the energy absorption or modulus of toughness. Under the linear part, the elastic-energy is the amount of energy that dissipates in bone without breaking it, after the yield point, the area under the curve is the post-yield energy. For young child, bone is ductile and has a greater area under the curve, work to

failure, and thus it undergoes large deformation before breaking. In osteoporotic bone, the elastic modulus tends to be lower, consequently, the area under the curve, and the work to failure is reduced, resulting in increased fracture risk (An, 2000; Cowin, 2001).

Because bone is a three-dimensional structure, stress and strains need to be described as tensors in all the three directions, for small strain approximation, the same equation holds but in tensor sense;

$$\sigma = \mathbb{C} * \varepsilon \qquad (1)$$

whereas σ is the stress tensor, ε is the strain tensor, and $\mathbb{C}$ is the elasticity or stiffness tensor. The inverse of the equation can be written as

$$\varepsilon = \mathbb{S} * \sigma \qquad (2)$$

whereas $\mathbb{S}$ is the Compliance tensor.

The stiffness tensor, for anisotropic material, has 81 independent components, due to hyperelasticity as well as stress and strain tensor symmetries, the components reduce to 21. Moreover, due to orthotropic symmetries, there are only nine distinct orthotropic elastic constants. These nine constants are the three elastic moduli (E_1, E_2, E_3) in the three perpendicular planes, the three shear moduli (G_{12}, G_{13}, G_{23}), and the six Poisson's ratios (ν_{23}, ν_{32}, ν_{13}, ν_{31}, ν_{12}, ν_{21}) only three of which are independent. In transverse isotropic, the number of independent components are reduced to five, two elastic moduli (E_1, E_2) and three Poisson's ratios (ν_1, ν_{12}, ν_{21}) (Holzapfel, 2000; Cowin 2001). Bone is assumed to be orthotropic or transverse isotropic. However, due to bone morphology and shape, the principal material directions are not necessarily aligned with the loading directions.

Tests that simulate the *in vivo* loading conditions of bone are compressive tests. However, compressive tests have end effects imposed on the specimen during loading, and some additional factors that contribute to measurement errors *i.e.* friction between the specimen and the platens. Tensile tests do not have these end effects, and therefore are favourable as mechanical tests (An, 2000; Cowin, 2001).

For hydrated cortical bone, long bone tensile test in the longitudinal direction shows elastic modulus in the 10-20 GPa range, while in the transverse direction it is around 9.6 GPa. For dry

tibial specimen elastic modulus is 18.6 GPa for cortical and 10.4 GPa for trabecular (Cowin, 2001; Currey, 2002).

Bone is stronger in compression, than in tension, than in shear. The ultimate strength, σ_u, in wet conditions, is shown to be around 200 MPa, 120 MPa and 60 MPa for the three loading conditions respectively (Kundson, 2007; Hayes, 1986; Currey, 2002). Tension and compression tests were applied by Ascenzi and Bonucci at the osteonal level in hydrated environment. For single osteon, it has been shown that in the longitudinal direction, bone is stronger in tension than in compression. The elastic modulus showed 11.7 GPa and 6.3 GPa for tension and compression respectively, which are lower than those at the continuum level. As well in the transverse direction, the elastic modulus for compression is 9.3 GPa. Moreover, the tensile strength is 120 MPa and the compressive strength is 110 MPa (Ascenzi, 1967).

The table below summarizes the elastic modulus, ultimate strength and strain for tension and compression tests on femur/tibia wet specimens.

Table 2. 1: Data from Wet Specimens at room temperature (Femur/Tibia)[1]

Age (years)							
	20-30	30-40	40-50	50-60	60-70	70-80	80-90
Elastic Modulus (GPa)							
Tension	17.0/18.9	17.6/27.	17.7/28.	16.6/23.	17.1/19.1	16.3/19.9	15.6/29.2
Compression	18.1/-	18.6/35.	18.7/30.	18.2/24.	15.9/25.1	18.0/26.7	15.4/25.9
Ultimate Strength (MPa)							
Tension	140/161	136/154	139/170	131/164	129/147	129/145	120/156
Compression	209/-	209/213	200/204	192/192	179/183	190/183	180/197
Ultimate Strain (%)							
Tension	3.4/4.0	3.2/3.9	3.0/2.9	2.8/3.1	2.5/2.7	2.5/2.7	2.4/2.3
Compression	-	-	-	-	-	-	-

[1] *Source:* Burstein, A.H., *et al*., J. Bone Joint Surg. 1976; 58A, 82.

From the above table, one can notice that tibial specimens have greater ultimate strength, stiffness and ultimate strain than femoral specimens. In addition, consistent decreases with age for all mechanical properties (Burstein, 1976).

Mirzaali *et al.* found that for macro-mechanical tests of femur bone, under environmental conditions, the E-modulus is 18.6±1.88 GPa in tension and 18.97±1.84 GPa in compression and did not depend on donor age as expected (Mirzaali, 2016).

2.4.2 Bending Tests

In vivo, bone is subjected to bending forces during a boot-top fracture. Hence, bending tests are relevant because they reveal information on bone strength. In bending tests, one side of the sample is loaded in compression and the other in tension until failure. From this test, stiffness and strength are calculated. The maximum stress σ in a beam at a particular cross-section is given by;

$$\sigma = \frac{Mc}{I} \qquad (3)$$

Whereas M is the bending moment at that section, I is the second moment of area, and c is the half the depth of the section. This formula is valid only for specimens with symmetric cross sections, and as long as the sample remains linearly elastic up to the point of failure. However, this does not apply to bone but still one can measure the bending strength (An, 2000; Currey, 2002). As mentioned above, bone is stronger in compression than in tension. Consequently, in bending tests, failure usually occur on the side experiencing tension.

Two types of bending tests, three-point and four-point loading. Three-point bending test creates high shear stresses near the midsection of the bone. On the other side, four-point bending test produces pure bending between the two upper loading points and eliminate the shear stresses (Cowin, 2001).

Three-point bending test, for the tibia, shows an average elastic modulus of around 5.44 GPa for cortical bone and 4.59 GPa for trabecular bone. Furthermore, four-point bending test, for the tibia, shows an average elastic modulus of around 6.75 GPa for cortical bone and 5.72 GPa for trabecular bone (Choi, 1990; 1993).

Funk *et al.* examined human femur in dynamic three-point bending test. The table below summarizes the elastic modulus, ultimate strength and ultimate strain, for 8 femur specimens tested from the right and left legs.

Table 2. 2: Data from human femur specimens at room temperature [2]

	Age (years)							
	40	51	55	59	66	67	69	70
E-Modulus (GPa)								
Left	11.7	12.5	14.2	11.8	12.5	7.1	12.2	11.5
Right	16.1	15.9	13.0	11.5	--	14.9	12.1	14.0
Ultimate Strength (MPa)								
Left	89	123	107	105	126	53	73	67
Right	156	104	127	64	--	97	90	119
Ultimate Strain (%)								
Left	3.82	2.68	2.41	2.46	2.96	1.57	1.78	2.76
Right	3.17	2.02	2.64	1.85	--	1.63	2.01	2.34

2.4.3 Torsional Tests

Torsional tests measure the mechanical properties of bone in shear. In this test, a cylinder of long bone is twisted by applying load. For a circular specimen, shear stress varies from zero at the centre of the specimen to a maximum at the surface, the shear Modulus (G) is calculated from this equation;

$$G = \frac{T*L}{\theta*J} \qquad (4)$$

whereas T is applied torque, L is the length of the specimen test region, θ is rotational displacement, and J is the polar moment of inertia of the specimen. The Shear stress, τ, is given by;

[2] *Source:* Funk, J.R., *et al.* Association for the adv. of Automotive Medicine. 2004; 48:215-233.

$$\tau = \frac{T*r}{J} \qquad (5)$$

r is the radius of the specimen (An, 2000; Cowin, 2001).

Complications and errors associated to specimen mounting are a major disadvantage of this type of test. However, it as a comparative advantage over bending tests, specially for specimens with grafts, because torsion tests allow the load to be applied at the ends of the bone and not directly on the graft.

2.4.4 Fatigue Tests

Fatigue is the degradation of strength and elastic modulus of bone due to repetitive loading with loads within the pre-yield region of the stress-strain curve. As many load cycles are applied on bone specimen, bone forms small cracks, which later grow and combine until bone fails. For fatigue testing, loads applied can be tensile, compressive, bending, or torsional. The result of this test is an S-N diagram, which depicts the peak applied stress as a function of the number of fatigue cycles before failure (Cowin, 2001).

As mentioned above, fatigue failure is the number of cycles necessary to cause a specimen to lose 30% of its elastic modulus. For cortical bone, fatigue failure can be as many as 37 million low-stress (24 MPa) loading cycles, which can be achieved in 43 days fatigue testing at 10 cycles/s. This type of test is considered time- and labour- consuming than other tests (Schaffler *et al.,* 1990). Choi and Goldstein demonstrated that trabecular bone has significantly lower fatigue resistance than cortical bone due to differences in their microstructure (Choi, 1993).

2.4.5 Fracture Mechanics Tests

Bone fracture mechanics aim to explain the fracture process of bone fracture and the dynamics of crack propagation. The two main parameters from this test are a) the critical stress intensity factor (Toughness), K_c, and b) the critical strain energy release rate, G_c. The most commonly used specimens are notched bones tested in three-point bending configuration. A very sharp crack can be made in a bone beam, and the minimum value of K_c can be empirically determined.

The stress intensity factor is given by;

$$K = \sigma . f \sqrt{\pi a} \qquad (6)$$

which implies that the fracture stress must be reached over some critical distance (a_c) for the critical stress intensity factor K_c to be reached and for the crack to propagate (Stampfl and Koch, 2011).

Having a notched beam with a crack of a certain depth, *a*, the elastic energy is given by;

$$U_{el} = -\frac{\sigma^2}{2E}\frac{\pi a^2 t}{2} \qquad (7)$$

Where *t* is the thickness of the specimen and $\frac{\pi a^2 t}{2}$ is the volume of the half circle. For the crack to advance, additional energy is needed and is expressed as the derivative of the elastic energy;

$$\delta U_{el} = -\frac{\sigma^2}{2E}\,\pi a t.\delta a \qquad (8)$$

The energy required to create the new surface as the crack advances is;

$$\delta U_s = Gt.\delta a \qquad (9)$$

The crack will grow unsteadily if $\delta U_s \leq -\delta U_{el}$, in other words, if the energy available for crack propagation is greater than or equal to the energy needed to make new surface, where for this case, the critical stress intensity factor is given by;

$$K_c = \sqrt{(2E.G)} = \sigma_c.f\sqrt{\pi a_c} \qquad (10)$$

f is a geometrical factor, and when K_c is reached, the specimen breaks (Stampfl and Koch, 2011).

Another method to assess fracture toughness is via *J*-integral, which quantifies the total energy spent before bone fractures. This describes both the energies absorbed in the elastic-plastic deformations. This method is considered a better technique in estimating bone toughness, by Yan *et al.,* who conducted experiments on bovine specimens. They found out that the energy spent in the plastic deformation was 3.6-4.1 times the energy spent in the elastic deformation. The toughness measured using the critical stress intensity factor K_c is much lower than this measured using the *J*-integral (Yan, 2007).

Zioupos *et al.* tested the effect of age on the mechanical properties of human femoral bone. These authors found a steady and significant decrease of the elastic modulus (*E*), strength (σ_u), and fracture toughness (K_c and *J*-integral) with age. For example, the elastic properties of the

material deteriorated, E dropped by 2.3% per decade. This reduced the (elastically calculated) critical stress intensity factor (K_c), required to initiate a macrocrack, from 6.4 MPa·1m$^{1/2}$ by 4.1% or the nonlinear energy associated with the onset of fracture, J-integral from 1.2 KJ m^{-2} by 3% (Zioupos; 1998).

2.4.6 Indentation Tests

Historically, indentation tests were used for minerals to determine the hardness of a material. Then conventional nanoindentation was developed to meet the needs of testing thin films, which were not able to be tested with the classical hardness tests. Lately, with the development of the AFM, indentation tests have been adapted for biological tissues at a lower scale than conventional nanoindentation.

The length scale of the measurement determines which method and indenter, size and shape, are used. AFM cantilever-based nanoindentation uses borosilicate spheres tips for micro-indentation, or silicon nitride tips for nanoindentation. Conventional nanoindentation uses diamond tips, and reference point indentation uses steel tips.

AFM cantilever-based nanoindentation uses a sharp tip and an AFM cantilever to indent the sample. While the tip penetrates the surface of the sample, the cantilever deflects. This information is used to record the true load-indentation data. Various methods exist to estimate the elastic modulus of the sample from the load-indentation data. The Oliver-Pharr method takes into account adhesion forces between the tip and the sample and the analysis of the unloading part, *i.e.* the elastic response, of the load-indentation curve. Hertz model is another method to analyse the elastic modulus; it assumes a linear elastic behaviour of the sample.

Conventional nanoindentation uses a diamond indenter that penetrates the surface of the sample. By observing the residual imprint of the indent under an optical microscope or an AFM, the contact area is measured. Indenters come in different sizes and shapes. The main disadvantage of this technique is that applied forces are limited up to few micro-newton and indentation depth of 100 nm.

Reference point indentation can be applied on bone *in vivo* and does not require sample preparation. This test uses a reference probe to establish a localized reference point, which is then used as a reference to calculate the Indentation Distance Increase (IDI) from the last loading cycles. Figure 2.4 shows the first and last cycle of probe indentation. IDI is a description

of bone fragility which is the difference between the max of the last and first cycle depth, the greater the indentation the more fragile the bone is. The main disadvantage of this technique is that measurement, on biological tissues *in vivo*, is only possible at the tibia which is not a fracture site.

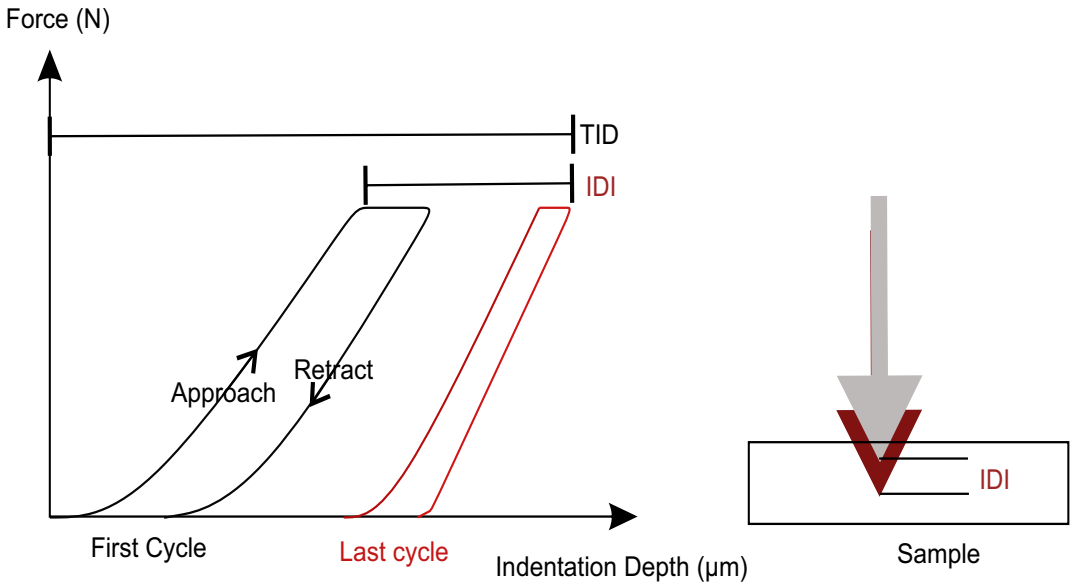

Figure 2. 4 :Left: Loading and un-loading indentation curve. Right: schematic representation of the indenter on a specimen.

For conventional indentation test, using Berkovich-tip on four specimens from the femoral bone under dry conditions, Hengsberger *et al.* showed that the E-modulus ranged from 18±1.7 GPa in compact bone to 22.5±3.1 GPa in trabecular bone, surprisingly here that the elastic modulus of trabecular bone is higher than that of compact bone. For the same study, hardness showed values between 0.6±0.11 GPa for compact bone and 1.1±0.17 GPa for trabecular bone (Hengsberger, 2001).

At the osteonal level, using AFM, Katsamenis *et al.* showed that the elasticity inhomogeneity between lamellae and interlamellar areas largely contributes to the fracture toughness and the damage resistance of bone. The loss of elasticity inhomogeneity in the osteonal level correlates with decreased damage resistance (higher damage susceptibility) at the micro scale and lower toughness at the tissue level (Katsamenis, 2015).

As an example of conventional nanoindentation using a diamond tip, Rho *et al*. examined nine

specimens from the femoral bone under dry conditions, they found a clear and consistent difference between the stiffness of the bone in the osteons and in the surrounding interstitial bone. The interstitial bone was on average 2.3 GPa stiffer than the osteonal bone specimens. In addition, the elastic modulus ranged between 21.5 and 25.4 GPa in interstitial sites, and 18.6 and 23.6 GPa in osteonal bone (Rho, 2002). Additionally, Rho *et al.* showed a decrease in elastic modulus and hardness within an osteon when going from the centre outwards (Rho, 1999).

Rho *et al.* showed that bone samples tested under dry conditions are stiffer than that tested under wet conditions. Using a Berkovich indenter on dry tibial specimens, they reported that the elastic modulus was 22.5 GPa and 25.8 GPa for osteons and interstitial bone respectively. In wet conditions, the elastic modulus was 18.6 GPa and 20.3 GPa for osteons and interstitial bone respectively. They also showed that cortical bone is stiffer than trabecular bone, for bone specimens from the vertebrae, the elastic modulus was 22.3 GPa and 13.4 GPa for cortical and trabecular bone respectively (Rho, 1997).

As well, Turner *et al.* showed that cortical bone is stiffer than trabecular bone. Using Berkovich indenter, the elastic modulus was 20.02 GPa and 18.14 GPa for dry cortical and trabecular bone respectively (Turner, 1999). Zysset *et al.* showed that that the elastic modulus ranged from 6.9 to 15.9 for hydrated trabecular bone (Zysset, 1998). As well, they showed that the average elastic modulus was 19.1 GPa and 21.2 GPa in osteonal and interstitial lamellae respectively. (Zysset, 1999). In the femoral neck, the average elastic modulus was 15.8 GPa, 17.5 and 11.4 in osteonal, interstitial and trabecular lamellae (Zysset, 1999).

Mirzaali *et al*. indented wet bone specimens using Berkovich-diamond tip. They found that the elastic modulus is independent from age, reporting that age has negligible effect on the tissue micro-indentation. However, the same test found significant differences of approximately 10% between interstitial (20.07 ± 1.19 GPa) and osteonal bone (18.09 ± 1.73 GPa) (Mirzaali, 2016).

To make an informed conclusion on bone mechanical properties, it is important to always keep in mind the length scale at which bone is tested, the conditions under which the experiment was conducted, and the donors' sex, age and health record.

To date bone mechanics have been investigated with different techniques. As the sample size decreases, the more difficult the measurement becomes. At the submicro- to nanoscales, Scanning Electron Microscopy (SEM) was classically used, which however, does not offer the

possibility to have mechanical characterization of bone. AFM cantilever-based nanoindentation technique is by far the only technique that offer quantified mechanical characterization of different biological tissues at the nanoscale, including bone. In the next chapter, the working principle and mode of operation of AFM cantilever-based nanoindentation are discussed.

Chapter 3
Atomic Force Microscopy

3.1 Overview of the Atomic Force Microscope

AFM could be conceptually perceived as a new type of microscopes. AFM measures the nanoscale topography by 'sensing' rather than "looking" at the surface. This is accomplished by bringing a very sharp tip (nanometre range) close to the surface. Then interatomic forces between the tip and the sample are causing the cantilever to bend while scanning the surface. In practise, these forces are kept constant by adjusting the vertical height of the tip through a feedback loop. Eventually the height changes correspond to topographical changes of the surface and are used to record a high-resolution image of the surface. AFM emerged after the invention of scanning tunnelling microscope (STM) by Binning and Rohrer in 1982 (Binning, 1982). Not only the high-resolution images produced by AFM makes it a favourable over other conventional techniques, but also its applicability of imaging and measuring under various conditions (hydrated, pH, temperature etc.) which opened a myriad of applications for biological tissues (Reifenberger, 2012).

3.2 Measurement Principles

The main parts of the AFM are the AFM head, cantilever and tip, laser source and photodetector, and piezo crystals. AFM images the topography of a specimen surface by scanning the cantilever over the surface. While scanning, the AFM cantilever bends and deflects in response to interaction forces between the tip and the surface. A laser beam reflecting off the

back of the cantilever, as shown in figure 3.1, is detecting the cantilever bending and deflection on a photodetector.

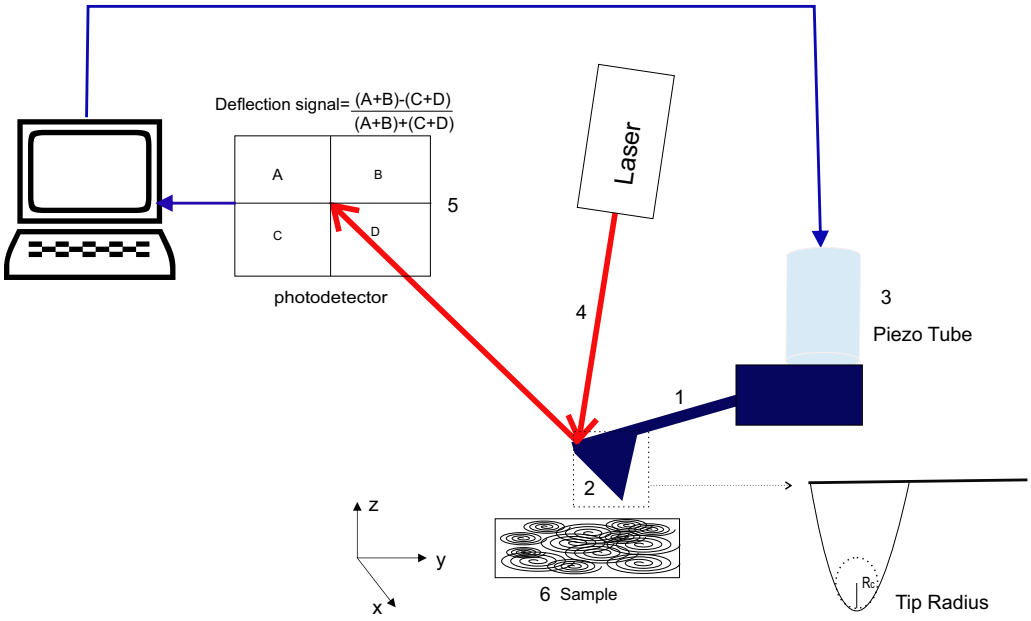

Figure 3. 1: The setup of an atomic force microscope. The AFM cantilever deflects due to the interaction forces, attractive or repulsive, with the surface topography. A laser is reflected off the back side of the cantilever and onto a photodiode. The vertical deflection is measured by change in voltage between the left (A+C) and right (B+D) half of the photodiode.

The AFM head and the cantilever moves in three directions, horizontal movement in the x and y plane, and vertical movement in the z direction. The movement of the Head and the cantilever is controlled by a piezo crystal transducers. A Z-Piezo controls the movement in the vertical direction, it drives the cantilever in a vertical axis towards and away from the surface with subnanometer precision.

The Z-Piezo allows the AFM to generate an accurate topographic map of the surface through a feedback loop to control the height of the tip above the surface to maintain constant forces

between the tip and the surface (Reifenberger, 2012; Morris, 2009). This setup allows for a three-dimensional information of the surface topography of the specimen.

The AFM cantilevers are usually attached on a chip, this chip is mounted on the AFM head at the beginning of the experiment. Therefore, AFM setup must be calibrated every time a chip is mounted. (NanoWizard® AFM Handbook, 2015).

3.2.1 AFM Cantilever and Tip

With regards to material, the AFM cantilever is made of silicon, silicon nitride (Si_3N_4), silicon oxide, high density carbon, or quartz like. The top side of the cantilever can be coated or not. In non-coated cantilevers, the reflectance of the laser is weak and sometimes can not be detected if measurements are performed in fluid. In contrast, coated cantilevers, which are usually coated with aluminium to increase the reflectance of the laser, which is favourable on one hand, but on the other hand, these types of cantilevers get corroded once immersed in salt solutions, such as Hank's Balanced Salt Solution (HBSS). To avoid this issue, some cantilevers are coated with gold.

The tip shape can take different forms, among others, 4-sided pyramidal, 3-sided pyramidal, spherical, spike, and conical. Depending on the imaging purpose and the sample topography the relevant tip shape is chosen, however, one should keep in mind that the tip geometry and the surface topography convolve, especially when the tip is in contact with the surface. Nevertheless, this envelop effect result in imaging the tip, which helps in identifying the exact tip geometry (Morris, 2009).

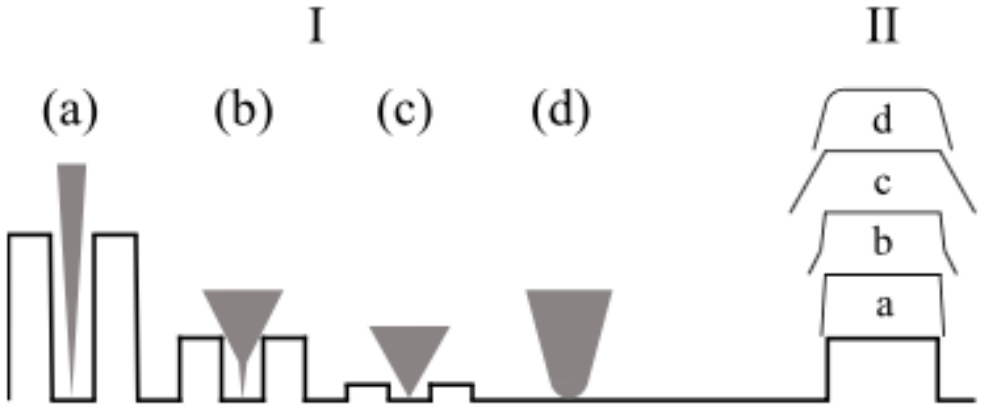

Figure 3. 2: (I) illustrates different tip shapes, if the tip is very sharp (a), it has a higher depth of field (high aspect ratio), resulting in better distinguishing of sharp edges. i.*e.* tip (c) is a low aspect ratio while

imaging a step won't be sharply distinguished. (II) Results of scanning a step with different types of tips (Morris *et al.)*

The AFM cantilever is regarded as a spring with spring constant. AFM cantilever come with different spring constants that range from 0.004 N/m up to 40 N/m. The cantilever is chosen depending on the scanning mode for imaging and in case of mechanical assessment is chosen such that the spring constant of the cantilever matches the stiffness of the samples. Here, we used cantilevers with nominal stiffness values of 40 N/m.

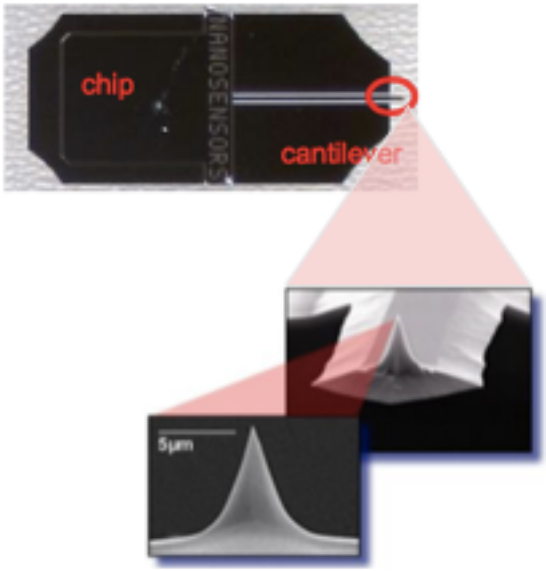

Figure 3.3: Cantilever chip and cantilever tip. (adapted from: AFM Manual)

As a spring, the AFM cantilever can be considered as a load cell. Depending on the stiffness of the cantilever, the load sensor has different sensitivity. A soft cantilever is generally used to generate forces in the range of several pN to 10s of nN, whereas a stiffer cantilever can be used to generate larger forces 100 nN up to several µN. The spring constant of the cantilever must be determined since the quoted value provided by the manufacturer is only a nominal value based on the dimensions and the material of the cantilevers.

3.2.2 Determination of Cantilever Spring Constant

Mechanical assessment via AFM require the highest possible sensitivity, which is achieved by matching the spring constant of the cantilever with the stiffness of the sample. Figure 3.4 depicts an illustration of a cantilever and the sample in series. The resulted Z-displacement is the sum of the deformation of the cantilever (D_c) and the deformation of the sample (δ). If the sample

is much stiffer than cantilever (K_c), then measurements would not be possible, because the tip will not indent the surface of the sample.

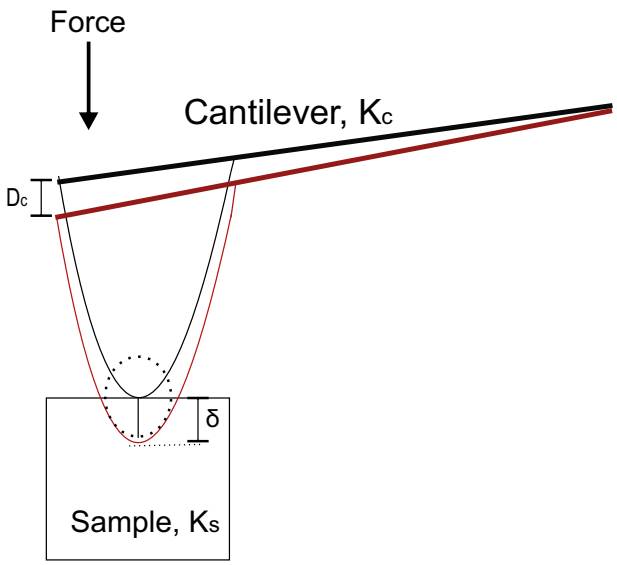

Figure 3. 4: when the cantilever and the sample comes in contact, the deformation is zero. Only when the cantilever moves with the Z-piezo pushing into the sample, this Z-displacement of the cantilever equals to the sum of cantilever deflection and the sample deformation ($Z=D_c + \delta$).

This series connection has three parameters:

- δ: actual indentation into the sample (unknown)
- D_c: deflection of the cantilever (known)
- Z: total displacement (known)

The Z-displacement is equal to the sum of the indentation (displacement of the sample) and the deflection of the cantilever *i.e.* $Z = \delta + D_c$. For the ideal case that the cantilever stiffness K_c and the sample stiffness K_s are equal, the indentation equals the cantilever deflection *i.e.* $\delta = D_c$. For this case, the Z-displacement can be calculated as $Z = \delta + D_c = 2D_c$. Consequently, the DZ-slope is 0.5 (Wenger, 2007), this is the highest sensitivity in term of cantilever selection ($K_s = K_c$), where the information of indentation is half coming from the cantilever deflection D and half from the extension of the Z-piezo. However, this ideal case can be hardly achieved, therefore the accepted range for the DZ-slope was set to 0.5 ± 0.3 (Wenger, 2007).

The cantilever spring constant can be determined through two methods a) Sader method, and b) Thermal noise method.

The first method to determine the spring constant was proposed by Sader *et al*. This method requires the width, the length, the experimentally measured resonant frequency (f_0) and the quality factor of the cantilever (Q) as well as the density and viscosity of the medium at which the determination of the spring constant is conducted. Properties of air: density $\rho_{air} = 1.18\ kgm^{-3}$ at 25 °C and viscosity $\eta_{air} = 1.86\times10^{-5}\ kgm^{-1}s^{-1}$. In addition to the ($\Gamma_i$) imaginary component of the hydrodynamic function, which is a function of the Reynolds number, Re. (Ohler, 2007).

According to Sader's method, the following equation provide the spring constant of the cantilever:

$$K = 7.5246\rho w^2 L Q f_0^2 \Gamma_i(Re) \qquad (11)$$

$$Re = \frac{2\pi\rho f_0 w^2}{4\eta} \qquad (12)$$

The second method, the thermal noise method considers the cantilever as a simple harmonic oscillator. Here, the cantilever is vibrating with amplitude in the picometer range driven only by its own thermal energy at room temperature. The equipartition theorem describes the relationship between the thermal energy and the spring constant of the cantilever, thermal energy equals potential energy at the spring, in other words, measuring the thermal vibrations gives the spring constant.

$$K = 0.971\frac{K_B T}{z_c^2} \qquad (13)$$

where, K_B is Boltzmann constant (1.38×10^{-23} J/K), T is the temperature, and (z_c^2) is the mean square deflection of the cantilever (Ohler, 2007; Reifenberger, 2012). The deflection of the cantilever is found by performing a power spectral density analysis of the cantilever oscillations and integrating the area under the peak of the fundamental mode. The peak is usually found at 270 KHz for the aluminium-coated (backside only) NSC cantilevers. Since the oscillation energy of a cantilever is split into different bending modes the formula should be corrected by a factor (0.971) for the fundamental resonance bending mode (Ohler, 2007).

3.2.3 Detection Method (Optical Lever Sensitivity)

The most commonly used detection method in AFMs is the optical lever technique. The deflection is measured by a laser beam that reflects off the back of the cantilever on a four-quadrant photodiode, see Figure 3.1, which is a semiconductor converting the intensity of light falling on it into electrical voltage signal. The photodiode is usually split into four sections, enabling recording of both vertical and lateral movements of the cantilever. (Reifenberger, 2012; Andriotis, 2013).

Each quadrant generates a voltage proportional to the portion of the laser spot hitting it. The difference in voltage between the upper and lower quadrants correspond to the vertical deflection signal generated from the vertical movement. The higher the displacement of the cantilever the higher the signal will be, even a small change in the deflection of the cantilever is measurable. The angular displacement of the cantilever results due to frictional forces originated by the lateral motion of the tip with respect to the sample. The lateral displacement measures the difference in voltage between the right and left quadrants of the photodiode.

The cantilever vertical deflection is initially measured in Volts. If the tip is away from the sample, the photodetector voltage has a constant value that corresponds to a zero interaction force with the surface. This offset value must be subtracted from the deflection data when the tip is in actual contact with the surface to calculate the true interaction force. Moreover, the photodetector signal, in Volts, must be converted to cantilever deflection in nm.

The cantilever deflection in nm is calculated by multiplying the sensitivity (dZ/dV) with the cantilever deflection in volts, as in figure 3.5 and the equation:

$$Caltilever\ defl.(nm) = sensitivity\ \left(\frac{nm}{V}\right) x\ measured\ Cantilever\ defl.(V) \qquad (14)$$

The cantilever calibration is a mandatory step before each experiment. To determine the sensitivity, an indentation curve is performed on a stiff substrate (mica or glass) where the approach and retraction curves must be the same because indentation will be zero, resulting in a Z-displacement equals the cantilever deflection.

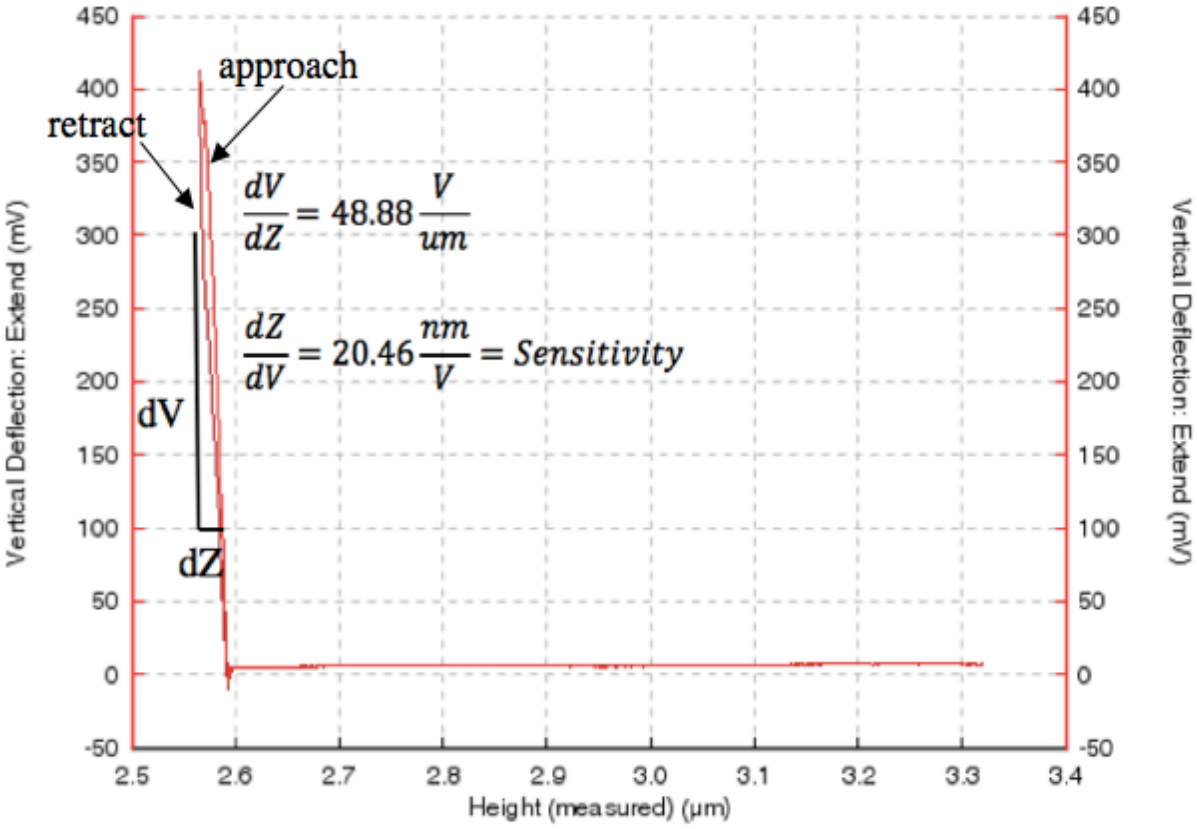

Figure 3. 5: Deflection-Displacement Curve for AFM tip indentation on Mica

By linear fitting the upper linear portion of this unloading deflection (Volts) vs. Z-displacement (µm) curve, the calculation of the inverse slope (µm/Volts) is the sensitivity calibration value.

$$Sensitivity = \frac{dZ}{dV}, (\mu m.V^{-1})$$

Once the sensitivity calibration value is applied the DZ-slope, *i.e.* the ratio of deflection (nm) vs. Z-displacement (nm) of the unloading indentation curve measured on a stiff substrate, *i.e.* glass, should be equal to 1. If this is not the case, sensitivity calibration should be repeated. For precise measurements, the accepted glass reference DZ-slopes of 1 ± 0.1. For measuring in liquid, the sensitivity of the cantilever needs to be checked again, the spring constant K_c depends only on the material properties of the cantilever and its geometrical dimensions and is independent of the surrounding environment.

However, using a sharp and small tip makes it highly sensible to surface roughness, to avoid any distortion resulted from surface roughness, bone samples were milled using the ultramiller (Leica Sp2600) to have a clean and flat surface. This process is described in more detail in annex iii.

As mentioned previously, for each application the suitable cantilever must be chosen and calibrated accordingly. AFM has a wide range of applications in biological tissues, such as imaging of the surface topography of collagen fibrils or mechanical characterization of tissues using nanoindentation mode.

3.3 Measurement Modes

AFM has three main different imaging modes, contact, tapping, and non-contact mode. These measuring modes have different separation distance between the tip and the sample.

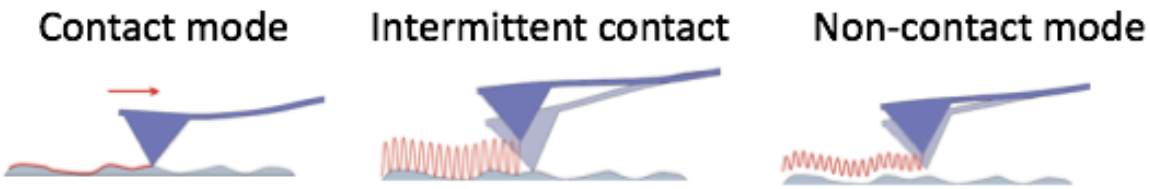

Figure 3. 6: AFM Contact, Intermittent and Non-contact mode. (source: JPK.com)

Imaging mode is selected depending on the purpose of the experiment. For this thesis, contact mode was applied to investigate the indentation modulus of bone. Before discussing imaging modes in more detail, the forces generated between the tip and the sample at different separation distance will be discussed.

AFM uses a highly precise cantilever, which measures the attractive and repulsive forces between the cantilever tip and the sample. The Lennard-Jones potential curve (Figure 3.7) depicts these forces. Long range van der Waals attractive forces dominate between the tip and the surface when the cantilever is away from the surface. And short range electrostatic repulsive force applies when the tip is close enough to the surface.

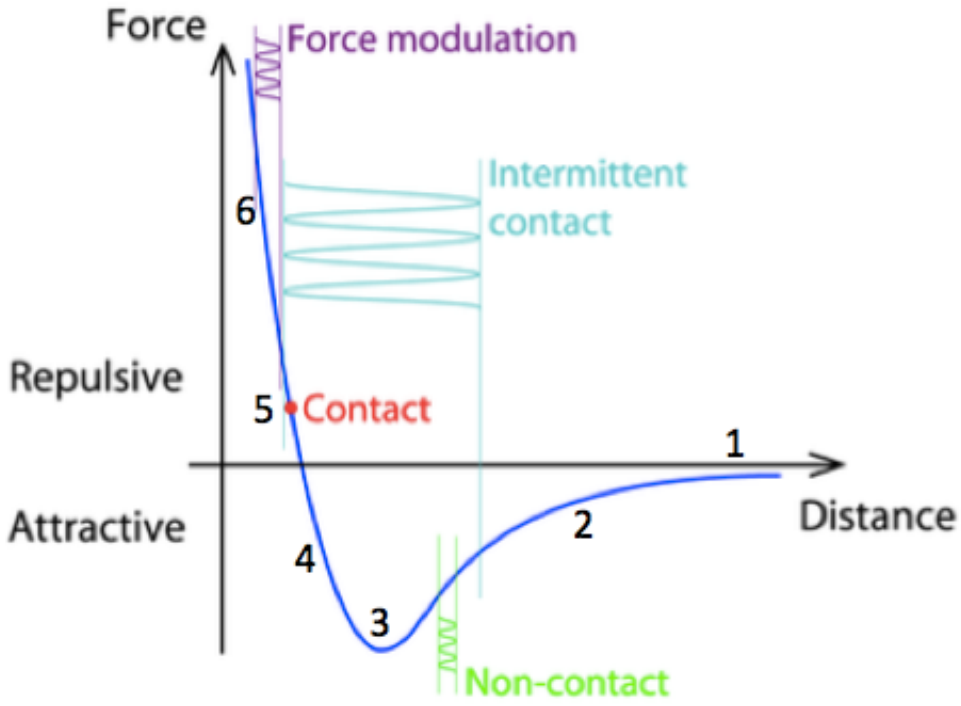

Figure 3. 7: The potential curve shows the interatomic distance vs. the force experienced on the tip. (Adapted from JPK.com)

While approaching the surface, the Z-piezo brings the cantilever to the surface. At (1) the tip and sample are far away. So, no interaction forces between the surface and the tip, and hence, no deflection of the cantilever. At (2) if the distance between the tip and the sample is less than 100 nm, here the tip starts to bend due to the attraction forces with the surface. At (3) increased attraction forces resulting in increased deflection of the cantilever, and at this point the tip jumps to contact with the surface. At (4) the Z-stepper progressively pushes the cantilever towards the surface and the deflection reduces, with attractive overall forces. At (5) the net deflection on the cantilever is zero due to equal attractive and repulsive forces on the cantilever tip, the tip-sample separation (δ) is zero too. At (6) the cantilever enters the net repulsive regime. The moment the deflection equals to the setpoint, the approach stops at the defined Z-height. After approaching, the scanning can be performed in one of the three measuring modes. These modes are discussed here briefly.

3.3.1 Contact mode

In contact mode, the cantilever tip scans across the specimen while the tip touches the surface and a repulsive interaction between the AFM tip and the specimen is generated. Two approaches are followed to apply this mode, a) Constant height where the cantilever is kept at

constant height, and the deflection force is measured. Here, the Z-piezo extends and retracts, according to the topographical changes of the surface and force changes, to maintain a constant height above the surface. This changing of the force could lead to damaging of the sample or the tip, which makes this approach not preferable. And, b) Constant force where the cantilever deflection is maintained at the setpoint (identified by the user), and the feedback loop uses Proportional-Integral-Differential (PID) controller to adjust the height the height of the Z-piezo at the setpoint.

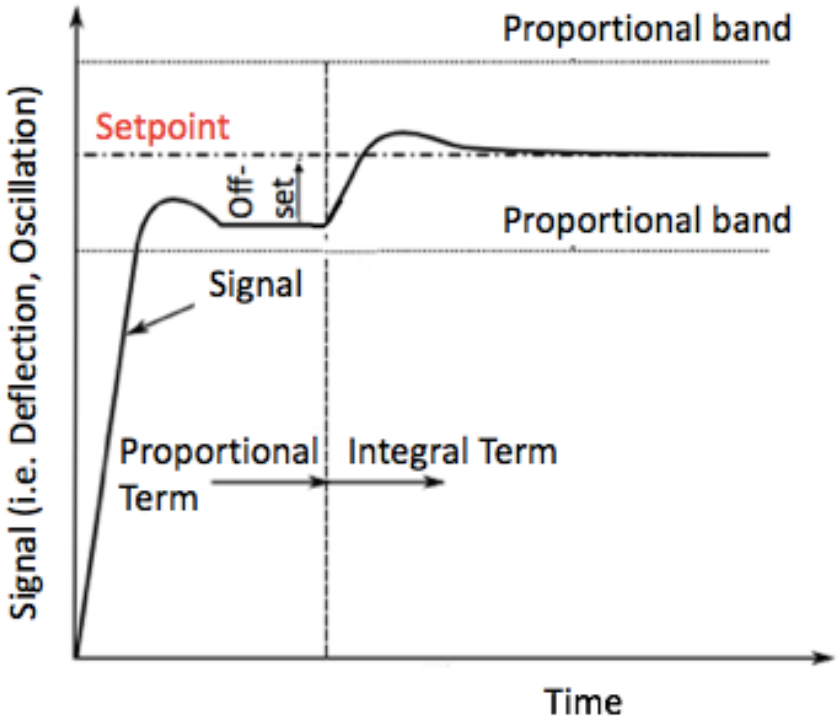

Figure 3. 8: PID Controller. (source: Morris, 2009)

The error is calculated as the difference between the setpoint and the measured signal, see figure 3.9. The proportional term basically amplifies the error between the signal and the setpoint by defining a proportional band that represents how much the controller reacts to an error signal. Due to the offset, reaching the exact setpoint is not possible. While the integral term tries to eliminate the offset, by integrating the error over time. Finally, the derivative term estimates the future trend of the error and reacts proportionally to the changing rate of the signal. The controller applies correction to the height of the Z-piezo based on the three terms and attempts to minimize the error over time.

3.3.2 Non-contact mode

As the name indicates, here the tip does not touch the surface. Instead, the cantilever oscillates some nanometres above the surface while it scans. A precise high speed feedback loop is used to keep the tip from crashing into the surface. As the tip approaches the surface, the interactions between the tip and the surface cause the oscillation amplitude of the cantilever to decrease, and then, the feedback loop corrects for this deviation and constructs an image of the surface topography. For this mode, softer cantilevers being used with stiffnesses of 0.5 N/m – 5 N/m.

3.3.3 Intermittent mode

In intermittent (contact) mode (tapping mode), the cantilever oscillates near its resonance frequency while the tip touches the surface for very short period. Using the feedback loop to control the oscillation amplitude (setpoint), an image of the surface topography is constructed. During scanning across the sample, the oscillation amplitude of the cantilever changes due to topographical changes. The change in amplitude is fed back to a control system which always tries to maintain the oscillation amplitude at the setpoint. Due to the limited contact time between the tip and the sample surface, the tip contamination is reduced. However, due to oscillation and touching of the surface, thin layers of absorbed water can cause adhesion forces which in turn leads to artefacts in obtained images. Nevertheless, this issue can be solved by using a stiffer cantilever which is able to penetrate these thin layers of absorbed water, or by increasing the setpoint amplitude (Morris, 2009; Reifenberger, 2012).

3.4 AFM cantilever-based nanoindentation

As explained in the contact mode, the AFM tip touches the surface and produces a topographical image. If force is applied on the surface through the tip, indentation of the surface of the sample is possible. For each indentation point, a highly accurate force-distance measurement in x and y directions is recorded. This combination between force measurement and topographic imaging is known as force volume mapping.

In QI^{TM} mode, the tip starts scanning a defined area row by row. After finishing the first row, the tip returns to the beginning of the row and scans the second row and so on, figure 3.10. The lateral forces are zero because the cantilever is completely retracted from the surface after each pixel, this results in a high image resolution.

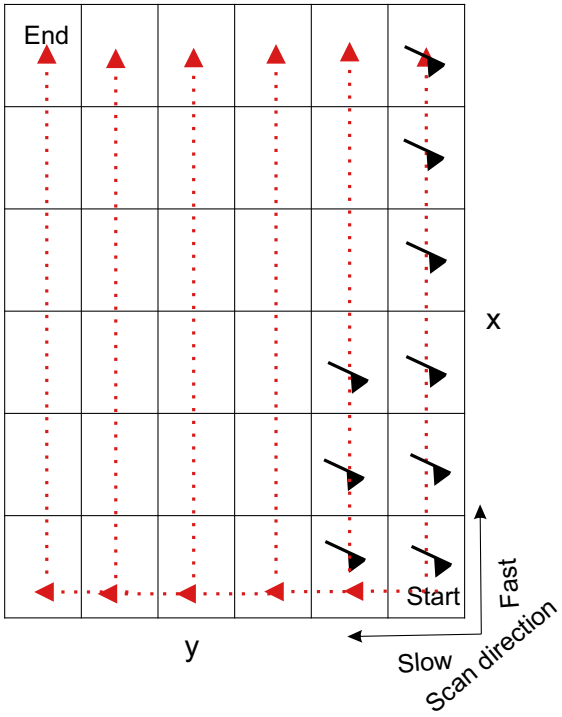

Figure 3. 9: Schematic representation of tip scanning over a region of interest, x is the fast scanning direction and y is the slow scanning direction.

3.4.1 Mechanical Characterization using QI™ mode

Using QI™ mode, the scanning region of the surface of the bone was set to 25 µm x 25 µm with 256 x 256 pixel resolution. Initially, the deflection measured from the photodetector is in Volts, thus, some steps are necessary to transfer the deflection into force (nN). As mentioned in section 3.2.3, first, sensitivity (µm/Volts) value transforms the initial curve into deflection (nm) vs. z-displacement (µm). Second, the curve is transformed into Force (nN) vs z-displacement (µm) by applying Hooke's law, which describes the force exerted by a spring as a function of its deformation (D_c, µm) multiplied by its spring constant (K_c, N/m),

$$F = -K_c * D_c \qquad (15)$$

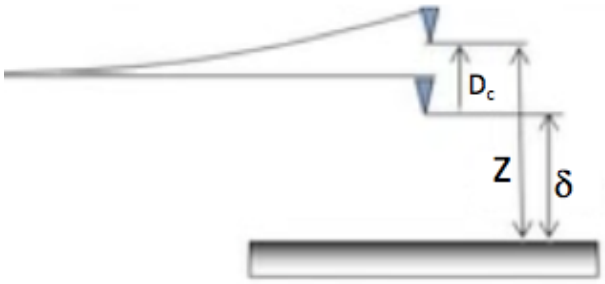

Figure 3. 10: Schematic representation of cantilever deflection and tip-sample distance

Third, Force (nN) vs z-Indentation (μm) is obtained via correction of the cantilever height. The true tip position relative to the surface should be corrected by subtracting the cantilever deflection from the z-displacement (measured height), $\delta = \mathrm{Z} - D_c$.

The load-indentation curve is the basis for obtaining mechanical information about the sample, such as indentation modulus. Two approaches are available to analyse the load-indentation curve, a) The Oliver-Pharr method, and, b) The Hertz Fit Models.

In general, calculation of the indentation modulus requires the knowledge of the contact area between the sample and the tip. This can be done by imaging the tip of the cantilever using the TGT1 grating, but following this approach had some complications because the cantilevers got crashed while imaged with the TGT1 grating. Hence, Hertz fit model calculates the indentation depth from the tip geometry, and assumes it to be less than the radius of the tip if the tip is parabolic. Different tip shapes are available (Parabolic, Spherical, Conical and Four-sided pyramid), and consequently, different equations apply to measure the indentation modulus depending on the tip geometry.

Table 3. 1: Fitting equations for different tip shapes

Tip geometry	**Fitting equation**	**Contact circle/ Comments**
Spherical	$F = \frac{E}{1-v^2}[\frac{a^2+R^2}{2}\ln\left(\frac{R+a}{R-a}\right) - aR]$	$\delta = \frac{a}{2}\ln\left(\frac{R+a}{R-a}\right)$
Parabolic	$F = \frac{4\sqrt{R_c}}{3}\left(\frac{E}{1-v^2}\right)\delta^{\frac{3}{2}}$	$a = \sqrt{(R_c\delta)}$

Conical	$F = \frac{E}{1-v^2}\frac{2\tan\alpha}{\pi}\delta^2$	$a = \frac{2\,tan\alpha}{\pi}\delta$ α, semi-opening angle of the cone
Four-sided pyramid	$F = \frac{E}{1-v^2}\frac{2\tan\alpha}{\sqrt{2}}\delta^2$	$a = \frac{tan\alpha}{\sqrt{2}}\delta$ α, face angle for Si_3N_4

For this thesis, a parabolic tip was used, the indentation modulus can be calculated according to the Hertz equation for parabolic tips. Whereas F is the force produced by the cantilever, obtained from the experiment (nN), δ is the maximum indentation depth, obtained from the experiment $\delta = Z - D_c$, v is the Poisson's ratio, for bone between 0.2-0.4 and assumed 0.3 (Reilly, 1974), R_c is the effective radius of contact (10 nm), and E is indentation modulus, fitting parameter.

The other way to calculate the indentation modulus, accurately more than the Hertz Fit model, is the Oliver-Pharr method. This method assumes an elastic-plastic deformation instead. The constitutive behaviour of the sample is elastic with time-independent plasticity without damage, the indented surface is a semi-finite half-space, and that the sample is an isotropic solid (Thurner, 2009). Here too, for bone samples not all assumptions are met. The Hertz Fit model is available as JPK Data Processing Software, and for investigate the indentation modulus changes between lamella and interlamellar areas, the Hertz Fit model suffice.

Measuring with the AFM allows us to have a high-resolution map of the indentation modulus of the measured region. Nevertheless, scanning small bone samples, even 3 mm x 3 mm in dimension, offers a significant amount of scanning regions because the max scanning dimensions using the available JPK Instrument is 30 µm x 30 µm. Thus, if the measurements are done randomly, the process can become time consuming, considering that each QI™ takes about 12 minutes for 128 x 128 pixels.

These AFM cantilever based nanoindentation experiments were conducted in fluid. The features of the bone surface, and the alternation of lamellas and interlamellar areas can not be

distinguished on the AFM camera. However, to be able to target a specific osteon that has the alternation of lamellas and interlamellar areas, the SHG images were necessary to have an optical overview of the collagen fibril orientation and to quantify this orientation. In the next chapter, the working principle of the SHG is discussed.

Chapter 4

Second Harmonic Generation Microscopy

4.1 Working Principle

The basic idea behind SHG is that in a medium of non-linear material two near-infrared incident photons with the same frequency (ω) are combined to generate new photons with twice the energy, twice the frequency (2ω) and half the wavelength. SHG does not give a signal with all types of material, the main condition for SHG signal to be generated is that the material must be non-centrosymetric. Luckily, most biological materials, including collagen fibers, lack the centre of inversion, this property allows for a label-free imaging of collagen. Aligned collagen fibers within bone nonlinearly scatter photons producing SHG signal, the signal intensity increases with aligned collagen, making it possible to distinguish whether the collagen fibers are in- or out of the plane of measurement (Campagnola, 2003, 2012).

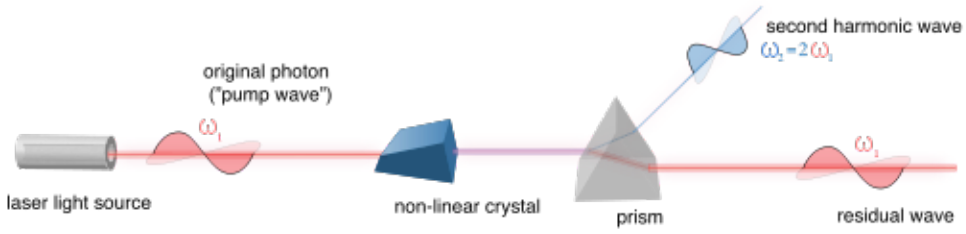

Figure 4. 1: Schematic representation of SHG. (source: Wiki).

Three types of SHG signal occurring, depending on the type of polarization the photons have. In SHG, the combined photons have extraordinary polarization which happens when a photon passes through a material with double refractive indices (a birefringence material). In this type of materials, rays split either parallel or perpendicular to the optical axis, the former is known as extraordinary polarization and the latter as ordinary polarization.

Type 0 SHG occur when two photons having extraordinary polarization combine to form a single photon with double the frequency and energy and maintain the extraordinary polarization. The opposite occurs in type I SHG where two photons with ordinary polarization combine to form a single photon with double the frequency and energy and extraordinary polarization. In type II SHG, two photons having orthogonal polarizations will combine to form one photon with double the frequency and extraordinary polarization (Kajzar, 2002).

At higher power intensity, the polarization is no longer linear to the electric field, thus polarization can be expressed as power series on the electric field (Campagnola, 2003). The nonlinear polarization for a material is defined by:

$$P = \chi^1 E + \chi^2 E^2 + \chi^3 E^3 + \cdots \qquad (16)$$

where P is the induced polarization, E is the electric field, χ is the nonlinear susceptibility (χ^1: 1st order process, absorption and reflection. χ^2: 2nd order process, SHG. χ^3: 3rd order process, Third Harmonic Generation (THG)).

The second nonlinear susceptibility is a bulk property and is the quantity measured in an experiment, it is related to the molecular hyperpolarizability, β, and the density of molecules, N_s, by:

$$\chi^2 = N_s < \beta > \qquad (17)$$

the brackets denote an orientational average, which shows the need for an environment lacking a centre of symmetry (Campagnola, 2003). β is defined in terms of the permanent dipole moment, $d^{(2)} = \beta EE$. Thus, harmonophores must have a permanent dipole moment, and, further, for efficient SHG, these must be aligned within the focal volume of the microscope so that χ^2 is non-zero. Collagen type I meet this criterion.

Consequently, the SHG signal is a function of the second nonlinear susceptibility, and it will scale with the laser pulse energy (ρ) and width (τ) as follow,

$$SHG_{sig} \propto \rho^2 \tau (\chi^2)^2 \qquad (18)$$

from these equations, the aligned collagen within the plane is proportional to the square root of SHG intensity (Campagnola, 2003).

4.2 Collagen Fibers as non- centrosymmetric structure

Bone is mostly consisting of collagen type I, one fibril contains many assemblies of parallel, crosslinked, triple helical collagen molecules, each also called tropocollagen. These fibrils, in the range of 10 nm – 300 nm, assemble into collagen fibers in the range of 0.3-3 μm thick (Naik, 2014). Collagen is a non-centrosymmetric structure, and thus it can absorb two low energy incident photos and re-emit them as a single photon with twice the energy and half the wavelength (Strupler, 2007). High SHG signals correspond to fibrils tilted by a small degree with respect to the observation plane. If the collagen fibers line up transversely (in plane) to the direction of the light, the image will have the maximum brightness. In contrast, organized fibrils at almost right degree (in the direction of the light) to the observation plane produce dark regions in the SHG image. In bone samples, collagen fibers are usually oriented between longitudinal and transverse directions (Deniset-Besseau, 2010; Bakbak, 2011; Genthial, 2017). In polarized light microscopy, osteons appearing entirely bright or dark were assumed to have mostly transversely or longitudinally oriented fibers, respectively (Bromage, 2003).

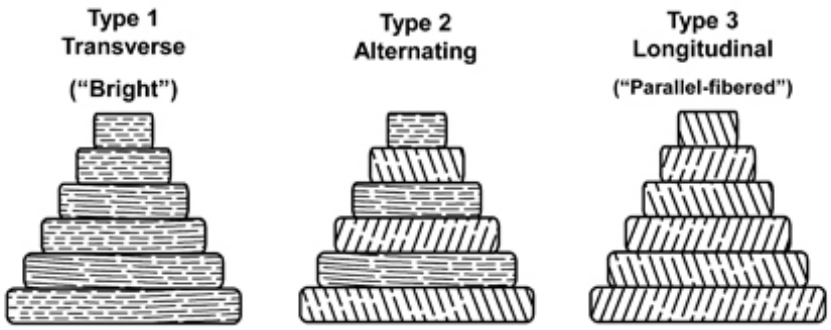

Figure 4. 2: Collagen fibril orientations within lamellae in osteons (Source: teambone.com).

As explained in the introduction, osteons are formed by layers of collagen fibers called lamellas, that wrap into concentric layers forming a Haversian canal, each lamella is composed of several sublayers with unidirectional aligned fibrils and the fibril orientation varies depending on the position within the lamella (Schrof, 2014). The orientations of these collagen fibers are generally categorized in three groups: dominantly transverse, dominantly longitudinal, and a combination of transverse and longitudinal orientations, figure 4.2 (Bakbak, 2011). Due to age collagen fibers change orientations, which then, influences the mechanical properties of bone (Leng, 2013), *i.e.* reports show that collagen fibers have greater tensional strength if oriented along the longer axis of the bone – longitudinal orientation –compared with the bones having densely transverse collagen fibre orientation (Bakbak, 2011). In addition, Leng *et al.* showed

that the indentation modulus and ultimate strength of demineralized bone samples decreased with aging in both the longitudinal and transverse orientations.

Therefore, for this research, SHG images of bone samples elucidate collagen fibrils orientation, and thus, a better visualization of the bone sample, which allows us to target specific osteons for the AFM tests. Furthermore, SHG images of tested osteons are combined with the corresponding AFM indentation modulus maps. Not only SHG signal is collected in SHG microscopy, but also autofluorescence. Both signals can be collected in separate channels. In figure 4.3, SHG image, of specimen A (25 years old) in slide N1, shows osteons with collage fibers lies in (bright) and out of plane (dark). In AFM test, we aimed to see how the indentation modulus changes between these two distinctive fibril orientations.

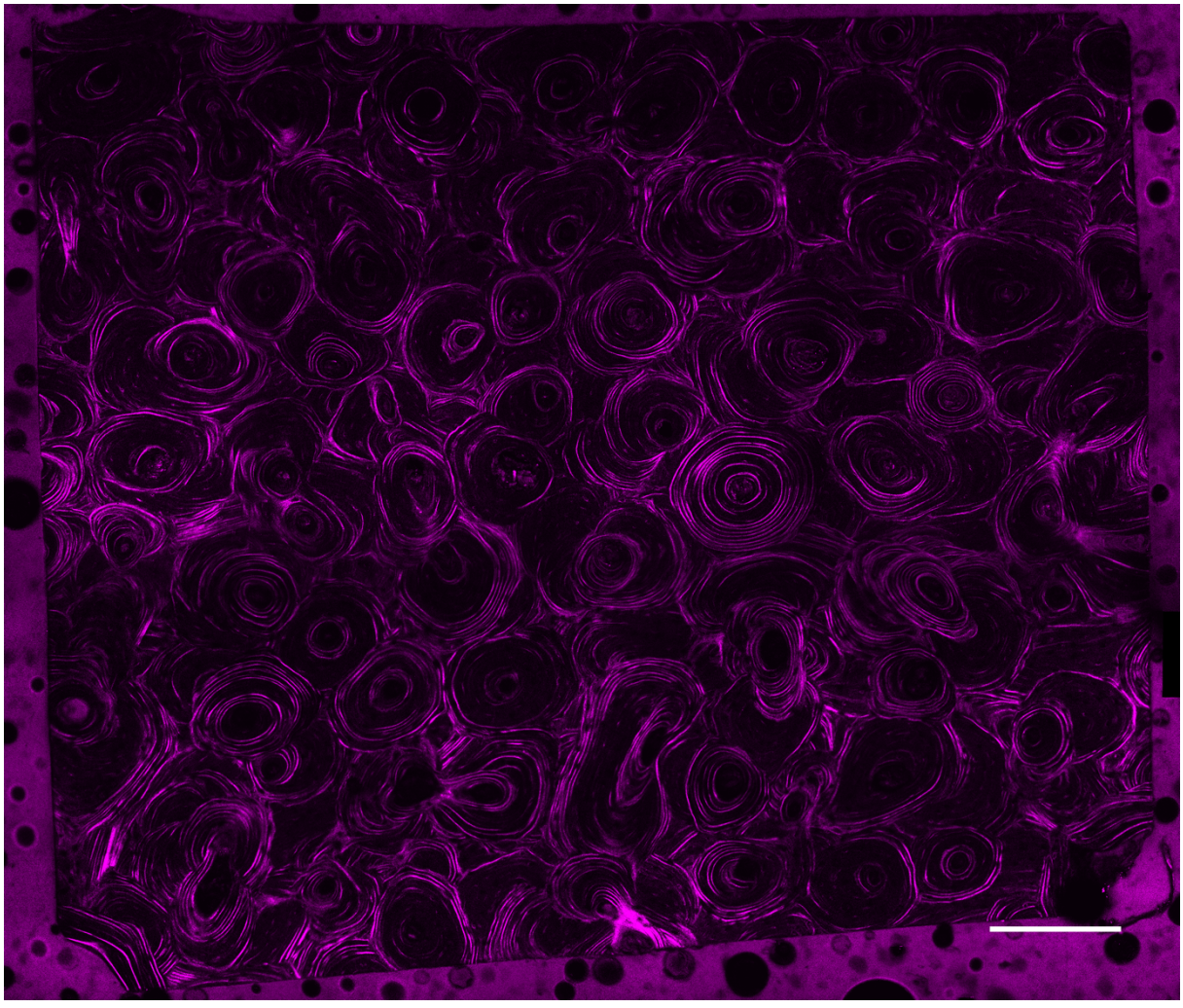

Figure 4. 3: SHG image of specimen a (25 years old – F) in slide N1-A, scale bar 300 µm

Figure 4.4 shows autofluorescence image of specimen A (25 years old) in slide N1. Collagen shows autofluorescence when irradiated by ultraviolet light, even though being the main

organic component of bone, not all osteons autofloresce with the same extent. This is because oldest bone components fluoresce most and the newest least (Prentice, 1967).

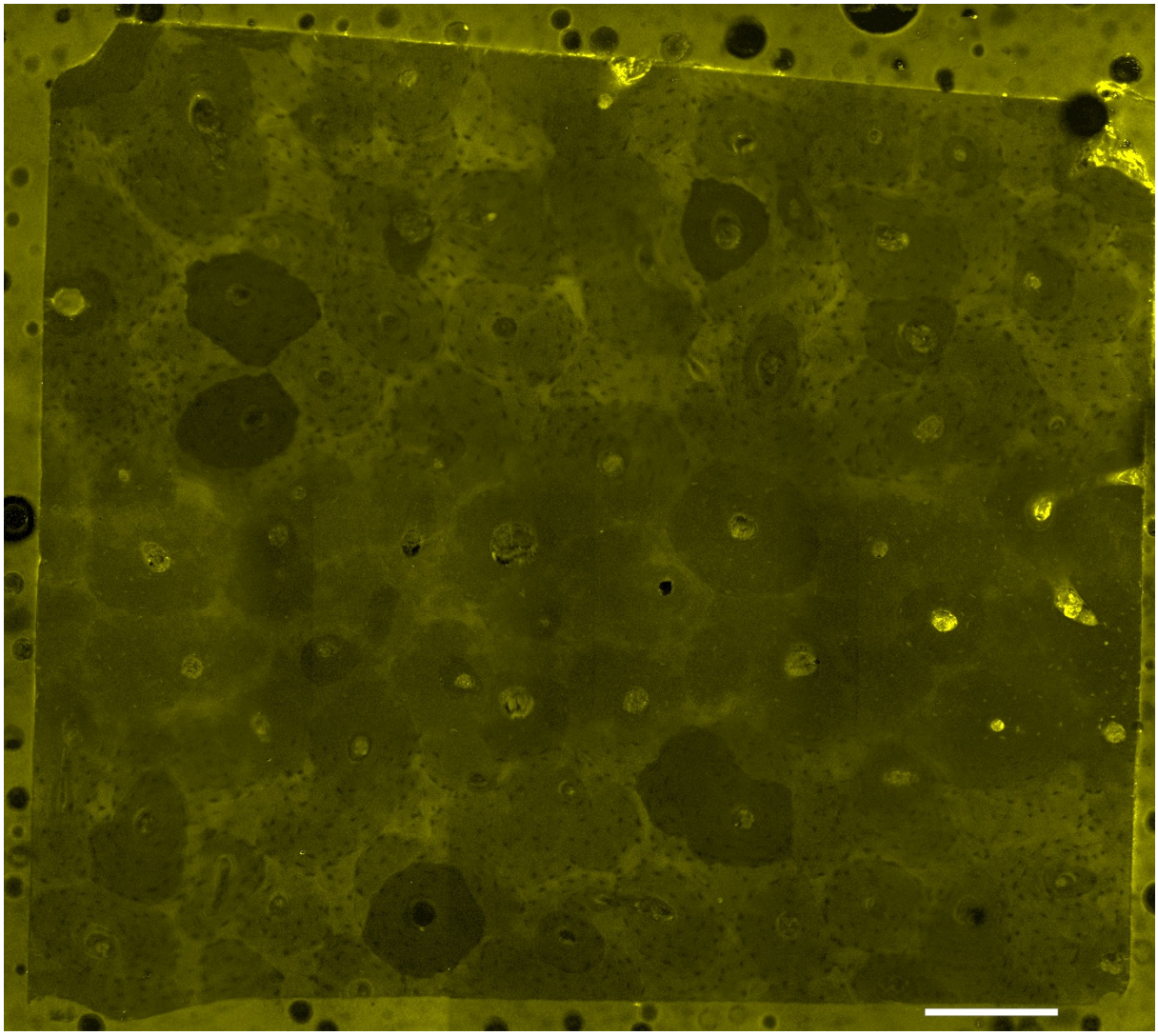

Figure 4. 4: Autofluorescence channel from multiphoton imaging of specimen A in slide N1, scale bar 300 μm

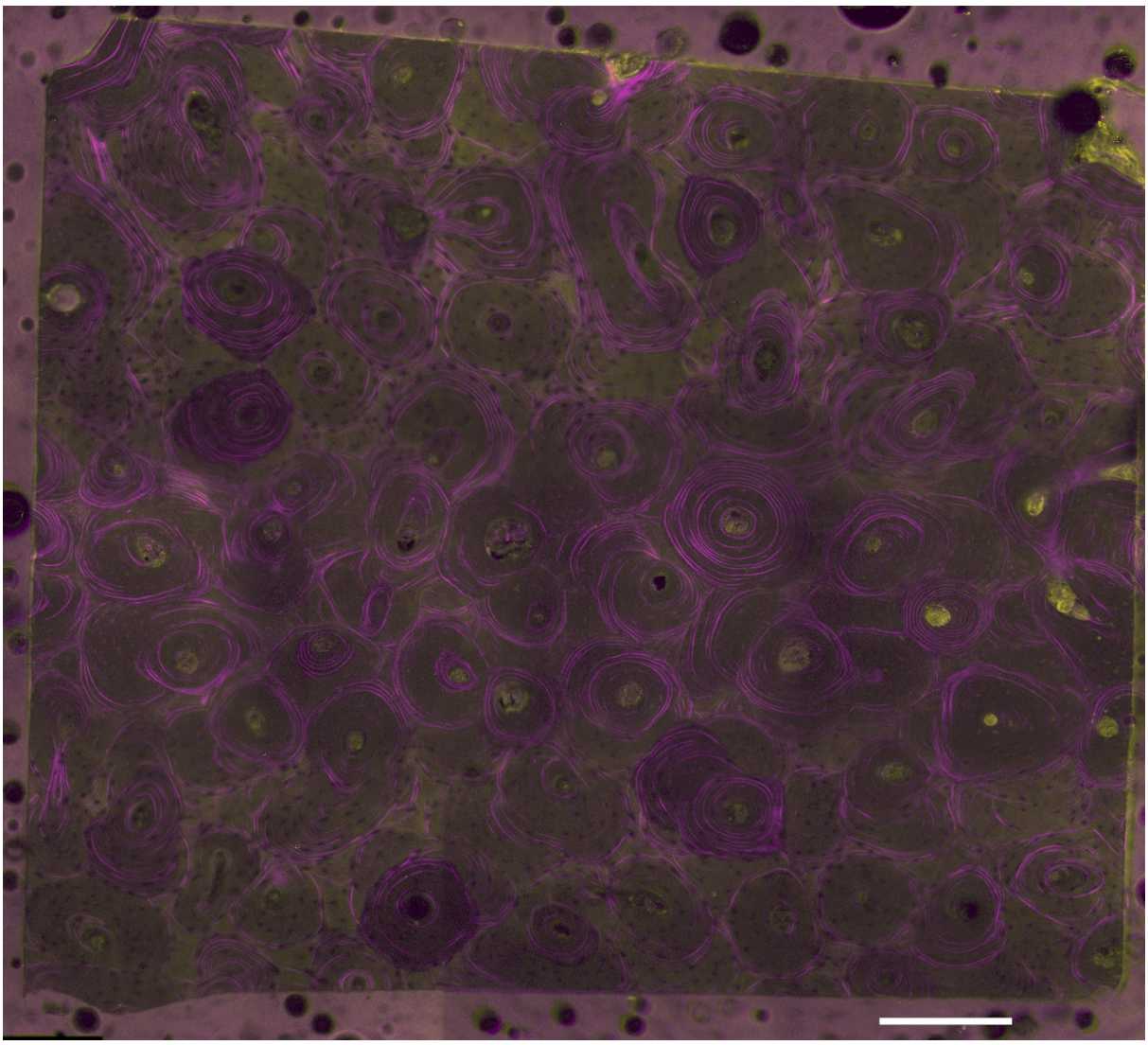

Figure 4. 5: Overlapped SHG and autofluorescence images, scale bar 300 μm

SHG images helped getting better insight on the orientation of collagen fibers and thus targeting selected osteons for AFM measurements. The next chapter explains the sample preparation and the measurement protocols.

Chapter 5

Materials and Methods

5.1 Experiments Overview and Sample Description

Thirty bone specimens from cadaver femurs, aged between 25 and 101 years old, were obtained from bone beams that were used for fracture test by Granke *et al*. Bone beams were cut into slices and fixed to six glass slides, with five specimens mounted on each slide as shown in Figure 5.1. Full details on all specimens including ID, age and sex, and the distribution on the slides N1, N2, N3, S1, S2, and S3 are provided in Annex v.

An overview of the experimental strategy is shown in Figure 5.1: the scheme is divided into sample preparation and experimental techniques. In sample preparation, samples were prepared, glued on glass slides and then milled using a micromiller. The conducted experiments have two main pillars, SHG and AFM cantilever-based nanoindentation. First, microscopy images using the optical microscope gave an overview of the bone surface, making it possible to differentiate osteons from interstitial bone. Second, SHG provides information on the orientation of the collagen fibrils of the lamellae and interlamellar areas as explained in chapter four. Third, AFM cantilever-based nanoindentation was used for the actual indentation on the bone surface; height topography and indentation modulus maps were obtained of each sample., Both the sample preparation and the experimental protocols are explained in detail below.

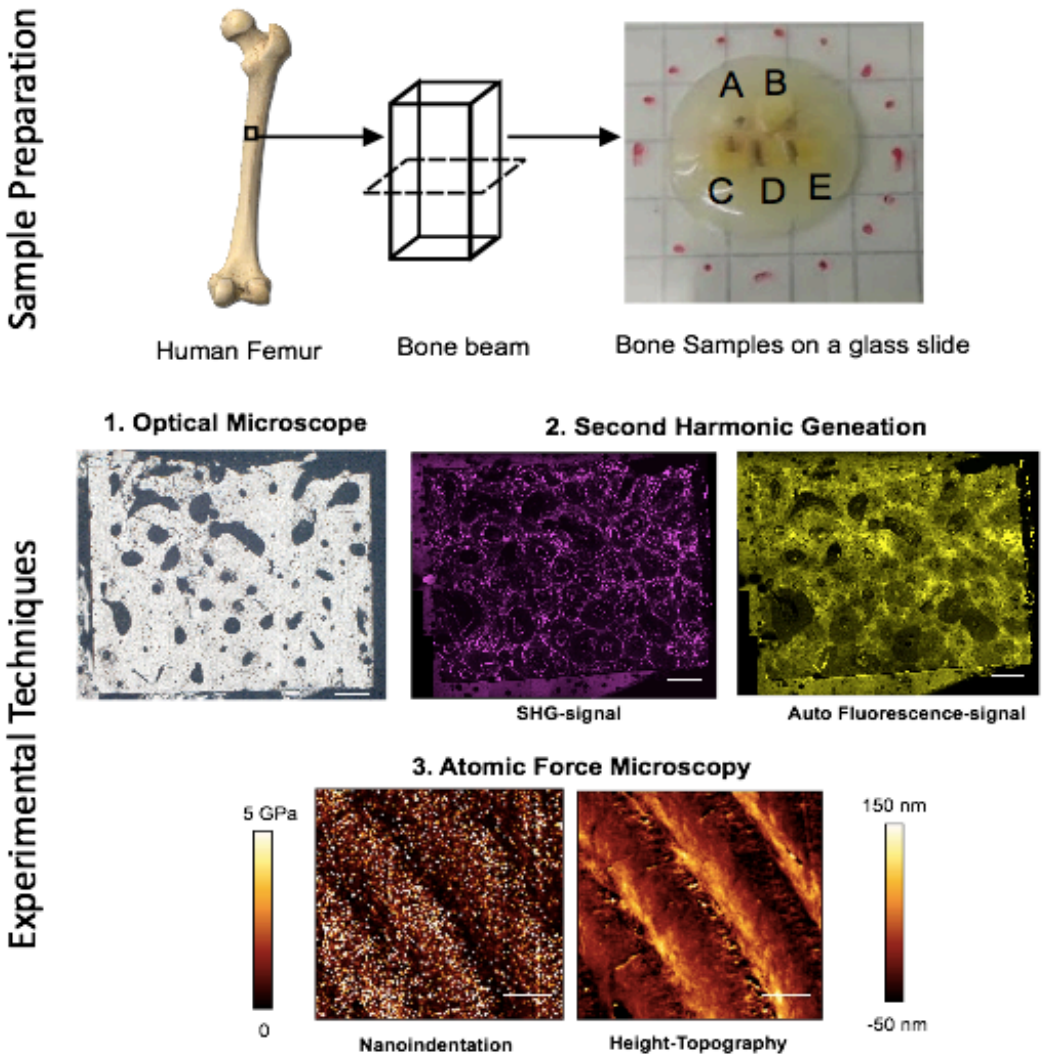

Figure 5. 1: schematic overview of the experimental techniques used. scale bar 300 µm for full sample images and 5 µm for AFM images

5.2 Sample Preparation

Bone beams and slides with mounted samples were stored in a freezer at -80°, before each measurement or use of the samples. They were defrosted for 15 minutes, and they were always stored in the freezer after each measurement, each sample experienced four to five freeze-thaw cycles. The very first step for sample preparation was to identify the samples' anatomical axes (longitudinal and transverse). For this, samples were investigated using the inverse optical microscope (Zeiss Axio). Circular cross-sections of osteons were identified to be located on the transverse plane of the bone beams. Accordingly, the samples were cut, using the IsoMet® Low Speed Saw (Buehler, Illinois, United States), transversely to the osteons.

Figure 5.2 shows one glass slide mounted with five specimens asymmetrically to be able to differentiate where each specimen was located afterwards.

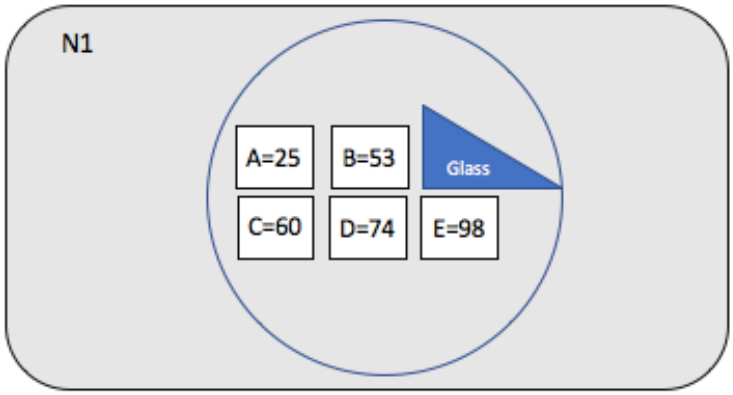

Figure 5. 2: Glass-slide N1 is mounted with 5 samples *(i.e.* A =25 indicates the number of the sample and the age of the donor), a small glass piece is glued at the level of the specimens for cantilever sensitivity measure.

Bone samples were glued on Polysine microscopic glass slides (25 x 75 x 1.0 mm), (Thermo Scientific Polysine®), these glass slides can withstand -80°, other types of glass slides would break after repeated freezing and de-freezing.

Gluing was done by mixing two epoxy components (UHU® Plus Endfest, mixed 1:1) in a weighing tray (Rotilabo®, PS, Item no. 1878.2, Carl Roth GmbH+Co. KG) with a stirring spatula (Item no. 4893.2, Carl Roth GmbH+Co. KG). Using the spatula, a little amount of the epoxy was placed on the glass slide, then specimens A to E were placed carefully in the epoxy using stainless steel tweezers (DU-MONT SWISSMADE, Item no. PK78.1, Carl Roth GmbH+Co. KG). The glass slide was left on a flat surface for 90 minutes to allow the epoxy to solidify as shown in Figure 5.3.

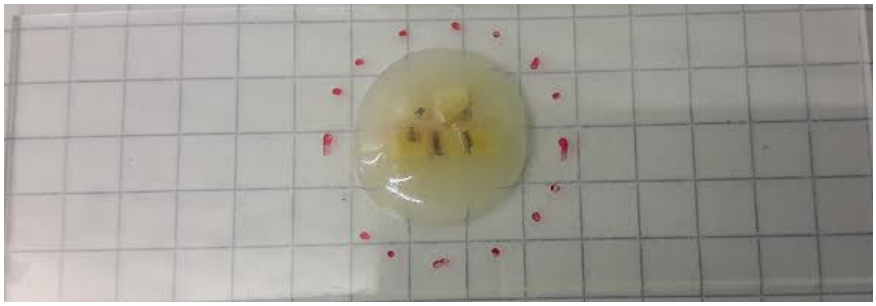

Figure 5. 3: Prepared glass slide with specimens N1

Polishing the surface, to reach a flat surface with equal height over all the specimens surfaces, is a necessary step for efficient measurent with AFM. A micromiller (Leica Sp2600, Germany) was used for this purpose, after the milling process the specimens appeared shiny and bone microstructure was clearly visible with a light microscope (c.f. Figure 5.4 & 5.5).

As AFM nanoindentation experiments are conducted in hydrated condition, two further preparation steps are needed a) a tiny glass piece was glued next to the bone samples to measure the cantilever deflection sensitivity in fluid. And, b) a fluid cell (25 mm outer diameter, 21.5 mm inner diameter, 6.5 mm height) was glued on the glass slide using two component dental silicon (picodent twinsil®, 1:1), mixed in a weighing tray with a stirring spatula. The edges of the cylindrical fluid cell (made of PMMA) were gently dipped into the silicon mixture to be slightly coated, and then placed on the glass slide. Care must be taken here; the dimensions of the AFM glass-block need to be taken into account, such that, the AFM cantilever can indeed approach the surface of all bone samples and is not blocked by the edges of the fluid cell.

Finally, microscopy images of the 30 bone samples were captured and saved using a 2.5x objective on an optical microscope (Zeiss Axio).

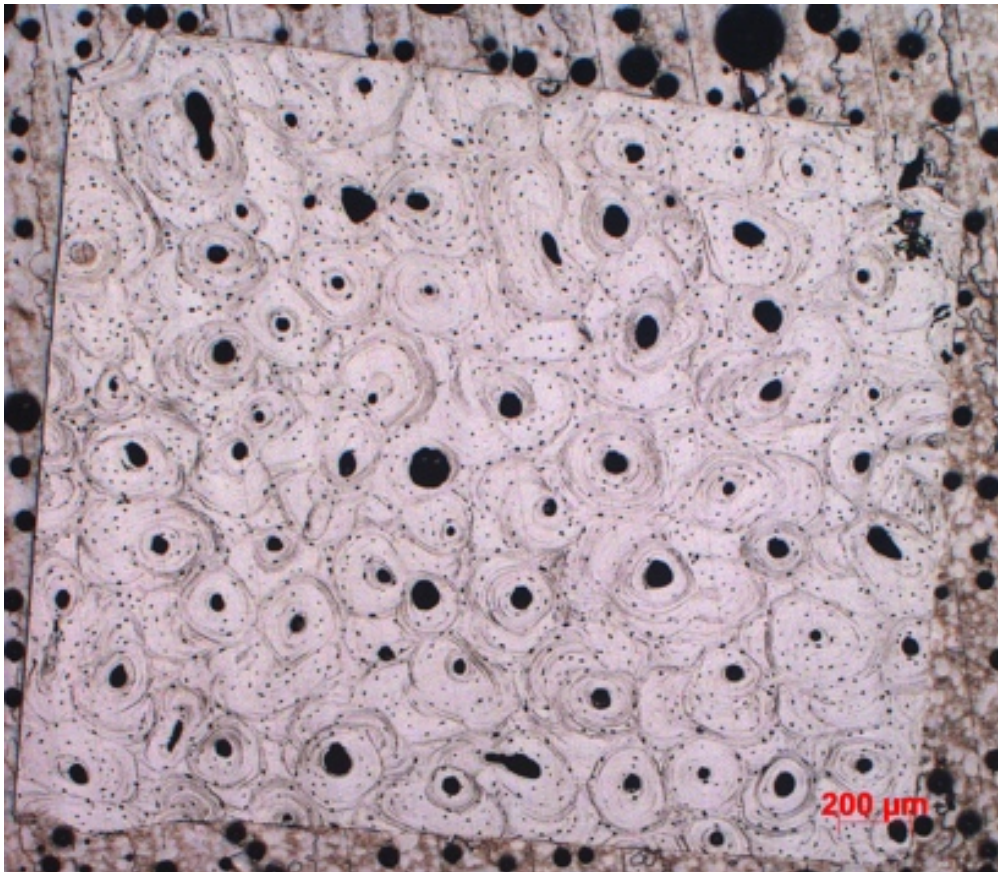

Figure 5. 4: Optical microscope image of sample N1A, M, 25 years old

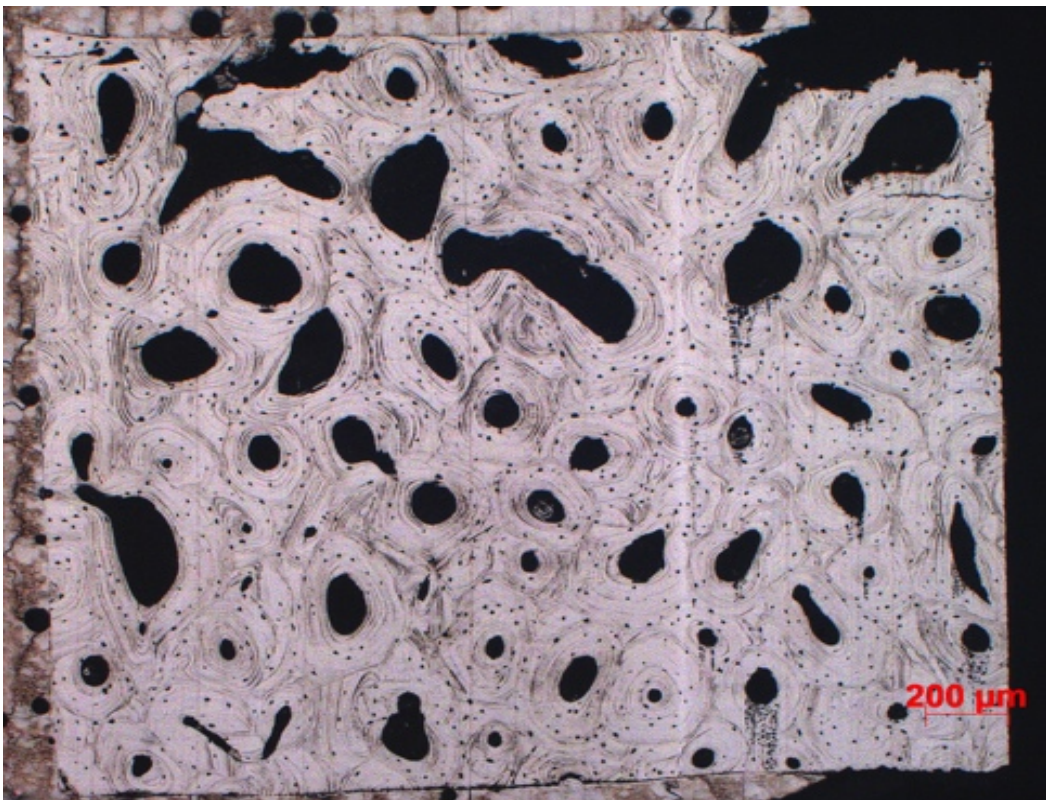

Figure 5. 5: Optical microscope image of sample, N3E, F, 101 years old

5.3 Experimental Techniques

Indentation modulus maps of parts of individual osteons were obtained via AFM cantilever-based nanoindentation. As shown in the microscopy images in Figure 5.3 and 5.4, the surface of the bone samples contains many osteons as well as interstitial bone and Haversian canals. The aim is to obtain indentation modulus maps of lamellae and interlamellar areas within osteons. These maps have the dimension of 25 µm x 25 µm. The AFM in cantilever-based nanoindentation mode uses a top view video microscope with x2.5 magnification. Especially when measuring in fluid, this setup makes it challenging to see the features of the sample surface. To correlate nanoindentation with structural properties of the samples SHG was used to obtain the orientation of the collagen fibril of the lamellae and interlamellar areas. This also made it easier to target osteons with similar fibril orientation in all donors for the AFM measurements and to avoid confounding effects.

5.3.1 Bone Samples Imaging with SHG

SHG images allow for collagen fibril orientation to be recognized. All samples were scanned using an SHG microscope (LEICA SP5, Germany) equipped with a multiphoton-laser (MaiTai,

SpectraPhysics). The imaging was done in hydrated conditions in PBS (pH 7.4) at 400~nm wavelength and laser power of 1.8W. The multiphoton microscope generates two images: the SHG image (collagen polarization or electrical susceptibility) and collagen autofluorescence. The obtained images from SHG have dimensions of 775.76 µm x 775.76 µm. To reconstruct a full image of the sample (sized 3 mm x 3 mm) 25-30 images were taken. Subsequently, these image sections were stitched together using the MosaicJ plugin of Fiji (ImageJ).

5.3.2 AFM Nanoindentation Experiments

AFM cantilever-based nanoindentation experiments were conducted on bone samples in fluid (immersed in PBS). Before each experiment, the AFM was calibrated and the spring constant of the cantilever was determined. These experiments were conducted using a Nanowizard® AFM (JPK Instruments, Berlin, Germany) as shown in Figure 5.6.

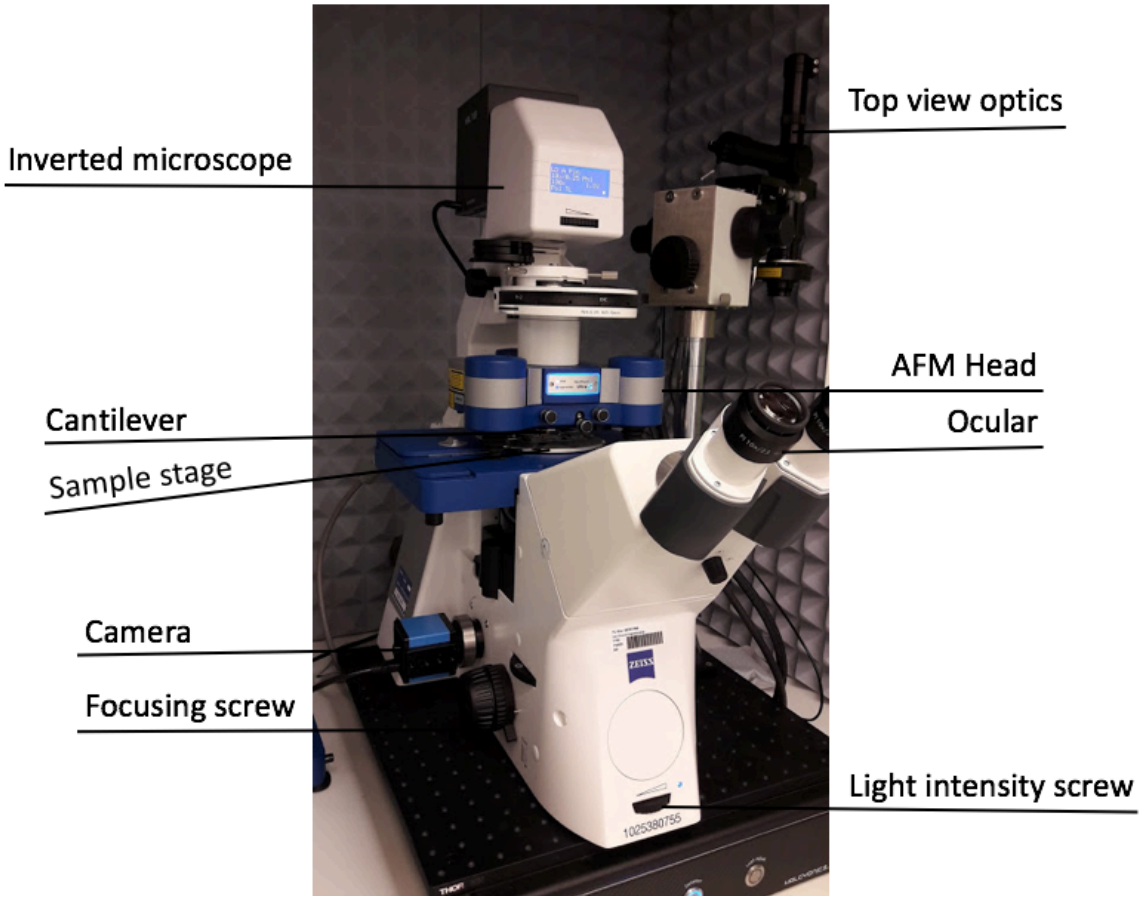

Figure 5. 6: AFM instrument

Bone specimens were indented in PBS and at 28° inside using the AFM-setup shown in Figure 5.6. Aluminum-coated, silicon AFM tips of 270 kHz resonance frequency and 20 N/m nominal

spring constant (NSC80-100; MikroMasch, Wetzlar, Germany) were used, actual spring constants were in the range of 13 - 30 N/m. The indentation area for each measurement was 25 μm x 25 μm with 128x128 indentation curves, consisting of 256 data points each. Figure 5.7 shows the AFM cantilever during a measurement on a bone sample, as mentioned earlier, the features of the sample surface (lamella and interlamellar areas) are not identifiable under ambient conditions with a x2.5 optical objective.

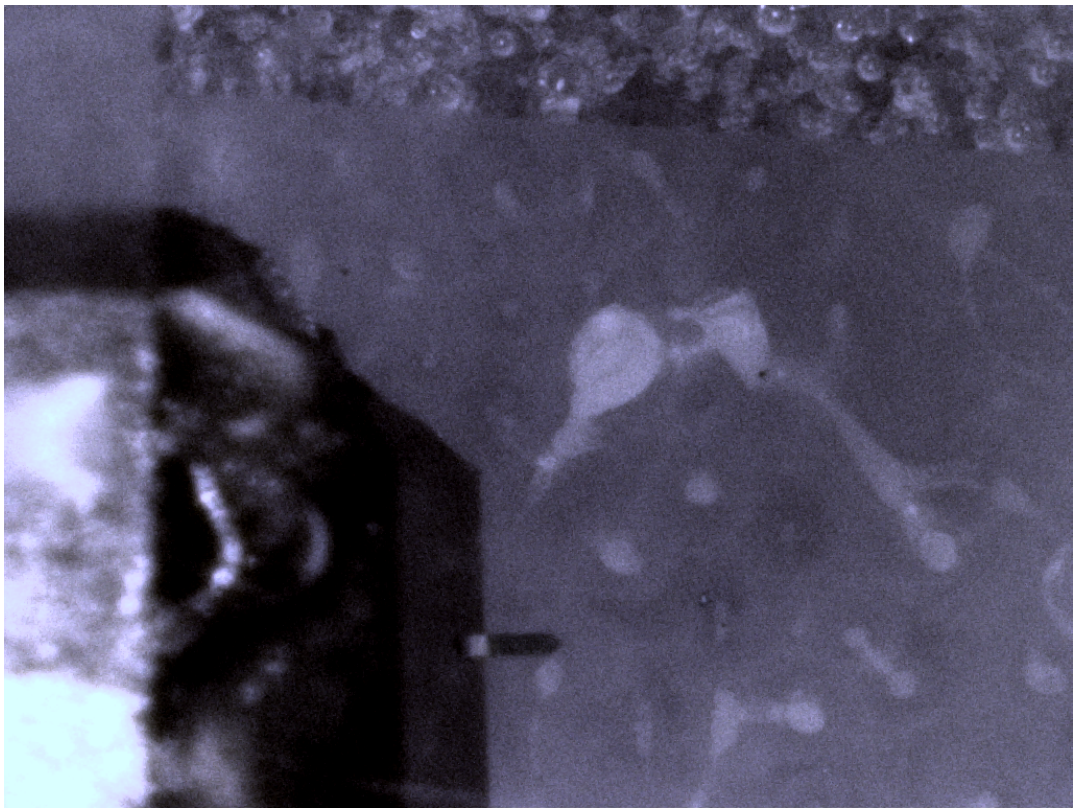

Figure 5. 7: AFM cantilever during indentation of a bone sample as viewed with the video microscope

5.4 Data Processing

Data analysis was applied through different phases to see whether the indentation modulus and collagen orientation correlate with age and with the fracture toughness data from Granke *et al.*, which was obtained from experiments conducted on bone beams from the same donors. Data analysis was done using JPK Data Processing Software, Matlab (R2015b), and Fiji (ImageJ).

5.4.1 SHG Image Processing

Images obtained from SHG needed some pre-processing to have them in a form that can be further processed. **First,** SHG images from one sample, as shown in Figure 5.8, were stitched

to form a full image of the sample using the MosaicJ plugin of Fiji (ImageJ) (Preibisch, 2009) as shown in Figure 5.10 for the SHG and Figure 5.11 for the collagen autofluorescence, and compared to an image obtained on an upright confocal microscope (Figure 5.9). Figure 5.12 shows an overlapped image of both the collagen polarization and the autofluorescence images.

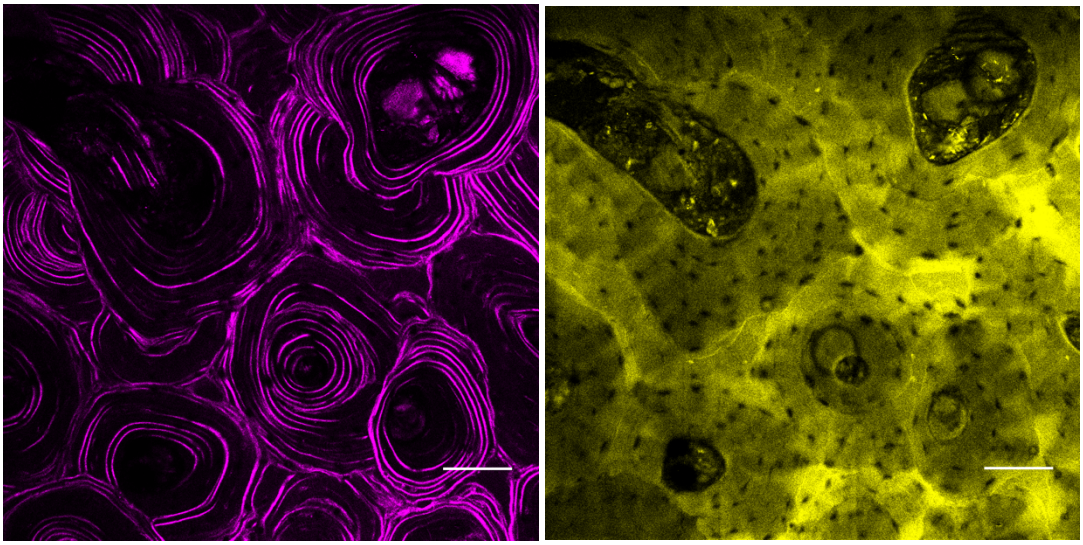

Figure 5. 8: Images of SHG channel 0 (left) and autofluoresence channel 1 (right), from sample N3E (101 years) for each sample 25-30 images were obtained, scale bar 100 µm

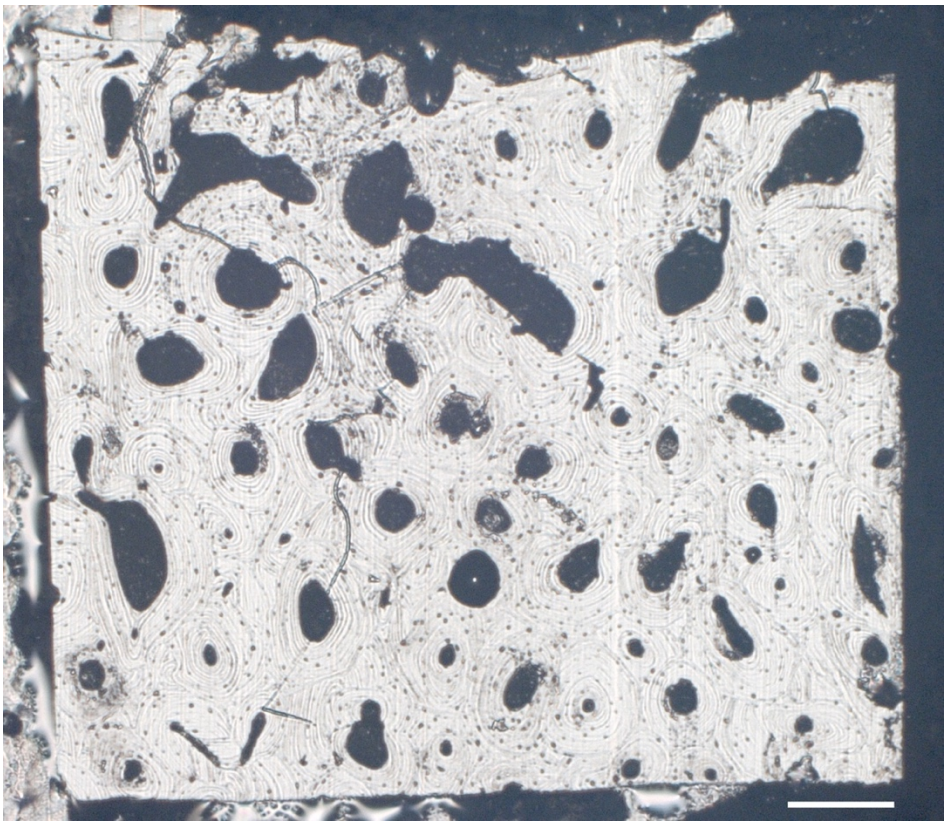

Figure 5. 9: Optical microscope image of sample N3E (101 years), scale bar 300 µm

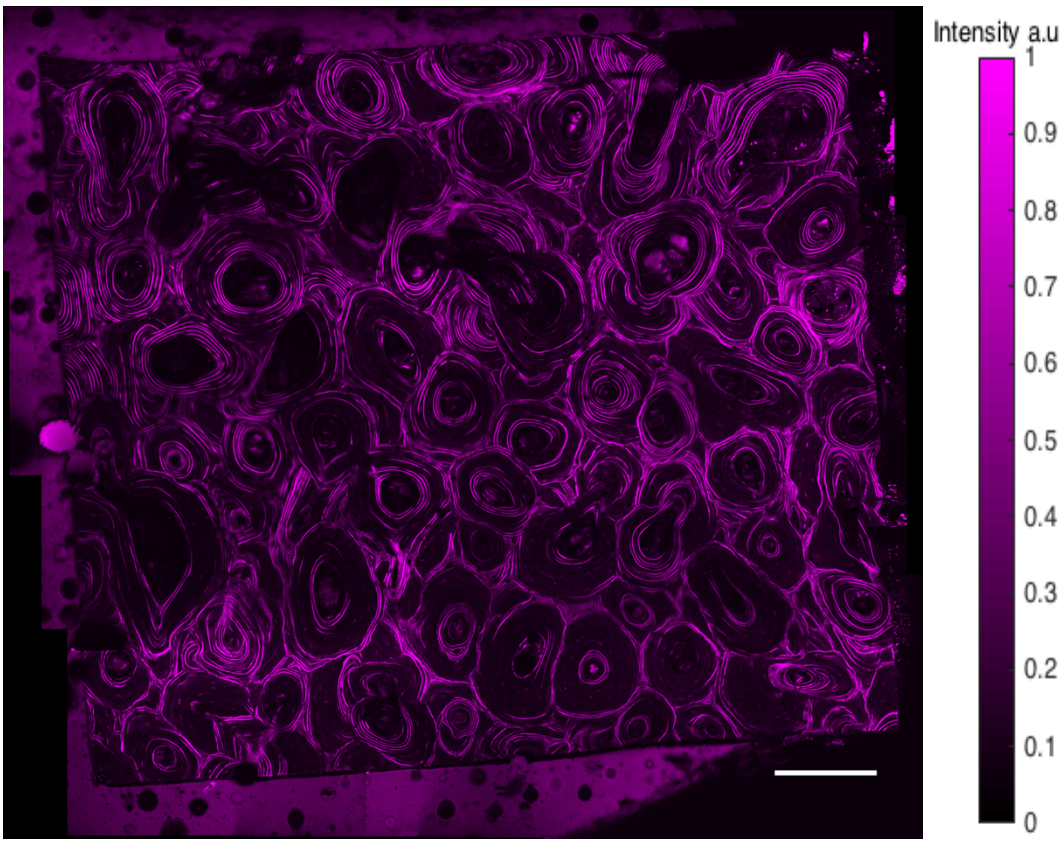

Figure 5. 10: Stitched SHG image of N3E (101 years) using MosaicJ, scale bar 300 µm

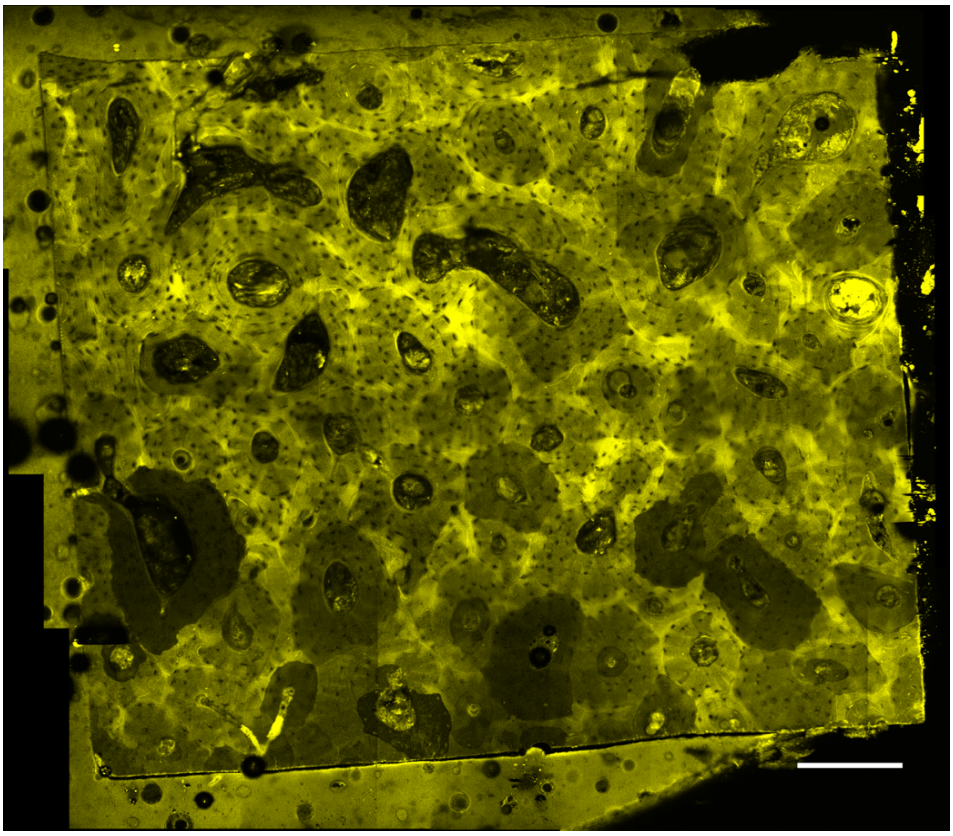

Figure 5. 11: Stitched autofluorescence image of N3E (101 years) using MosaicJ, scale bar 300 µm

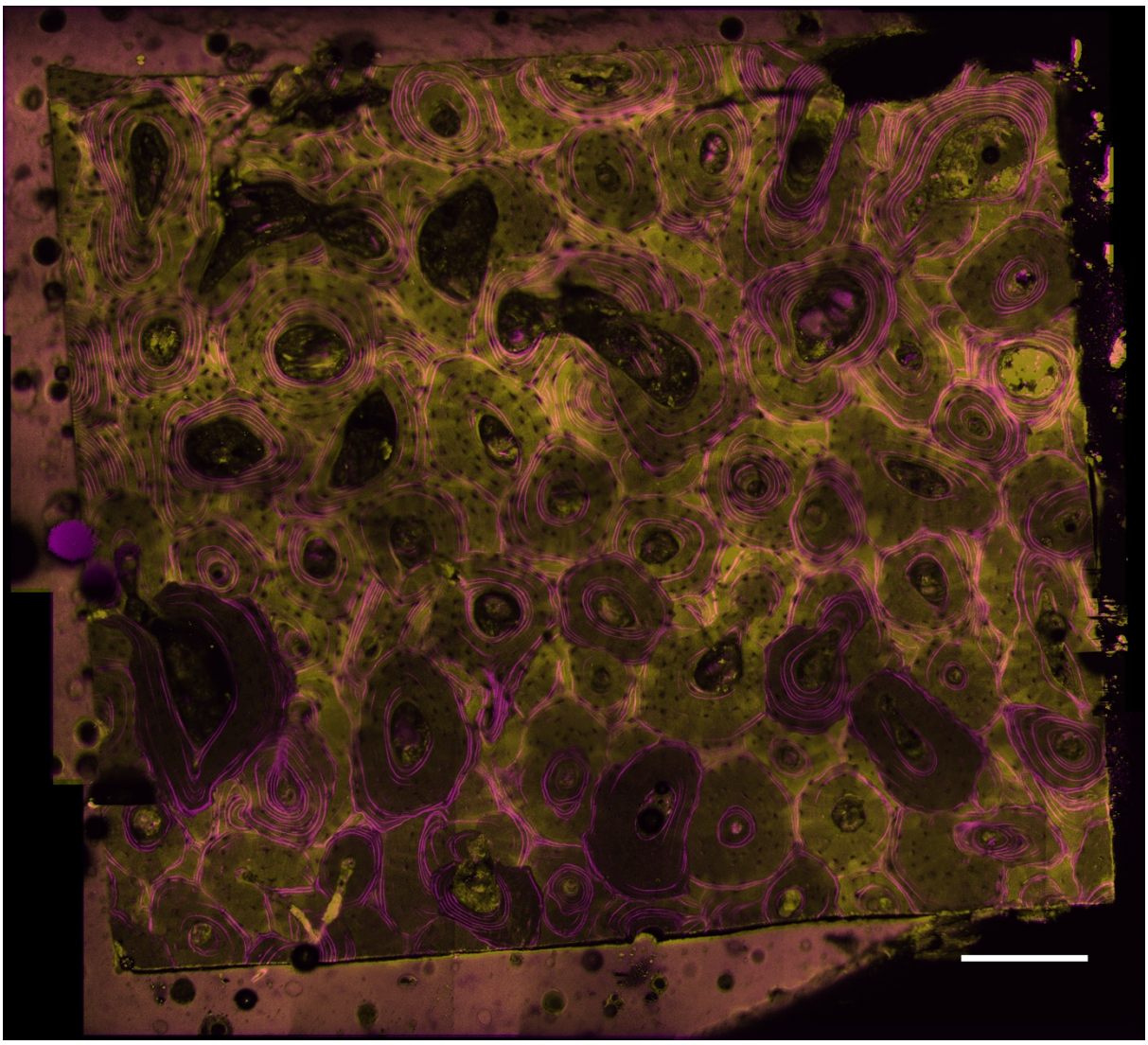

Figure 5. 12: SHG and bone autofluerescnec overlay of sample N3E, produced with MosaicJ, scale bar 300 μm

Second, due to different microscopes used, the images obtained can be flipped, mirrored or rotated images of the actual sample on stage. Thus, it was necessary to save all images obtained from AFM, SHG and optical microscope into their actual orientation. SHG images were imported into Fiji, then flipped horizontally and saved in the correct orientation such that they appeared as on the actual bone sample on the respective slide.

Third, Using Matlab, the orientation of collagen fibrils within the lamellae and interlamellar areas was determined to obtain the local in- and out of plane orientation. At first all the pores and surrounding epoxy were masked; the result is a matrix where only collagen orientation information was kept. Using a custom algorithm, the orientation was calculated, assuming the SHG intensity to be proportional to the square of the cosine of the collagen fibril angle with respect to the longitudinal or out of plane axis (Schürmann, 2010).

$$SHG_{int} \propto B * (\cos\theta)^2 \qquad (19)$$

B is a scale factor includes instrument constants as, *i.e.* laser power. We assume only the proportional relation between the SHG intensity and the angle of orientation. Thus, to calculate the collagen fibril angle, the equation is solved via arccos function:

$$\theta \propto \cos^{-1}(\sqrt{SHG_{int}}) \qquad (20)$$

Fourth, for each obtained QI™ map, the corresponding region in the SHG image was cropped as shown in Figure 5.13. This cropped SHG image has 33 x 33 pixels, which therefore, was interpolated using Matlab to 128x128 pixels to be then manually registered with the QI™.

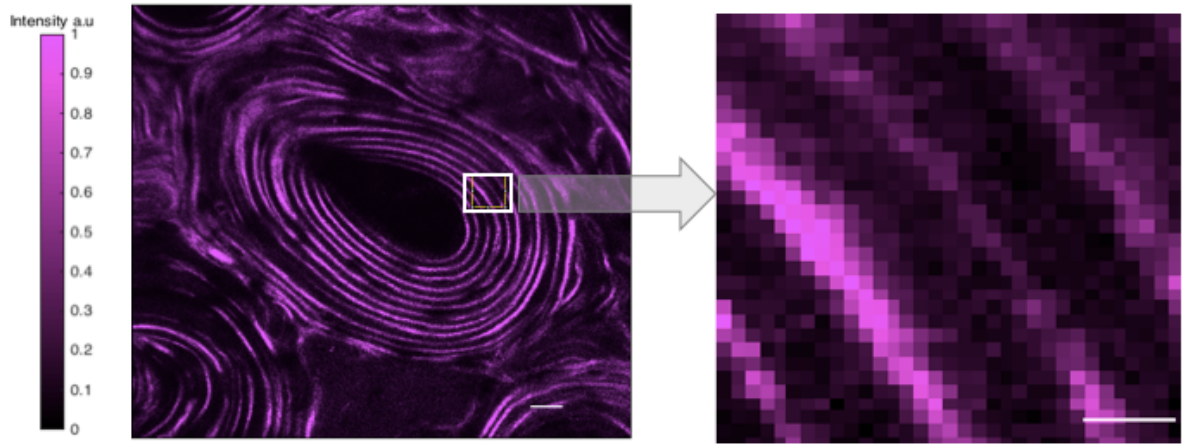

Figure 5. 13: Cropped osteon of S2E (left), QI07 is then cropped with dimensions 25 µm x 25 µm, scale bar 5µm (right)

Fifth, mean orientation angle values were calculated for lamellae and interlamellar areas of cropped SHG. Moreover, the intensity profiles of the cropped SHGs were plotted through interactively selecting lines of interests, *i.e.* across the lamellas and interlamellar areas. For SHG intensity profile Fiji (ImageJ) was used.

Figure 5.14 depicts an intensity profile along lamellae and interlamellar areas of one SHG image. The intensity values of this SHG image were then converted into orientation angle (in degrees) as explained above. After plotting the intensity profile of the orientation angles, we observe that a high intensity value corresponds to an in-plane orientation of the collagen fibril.

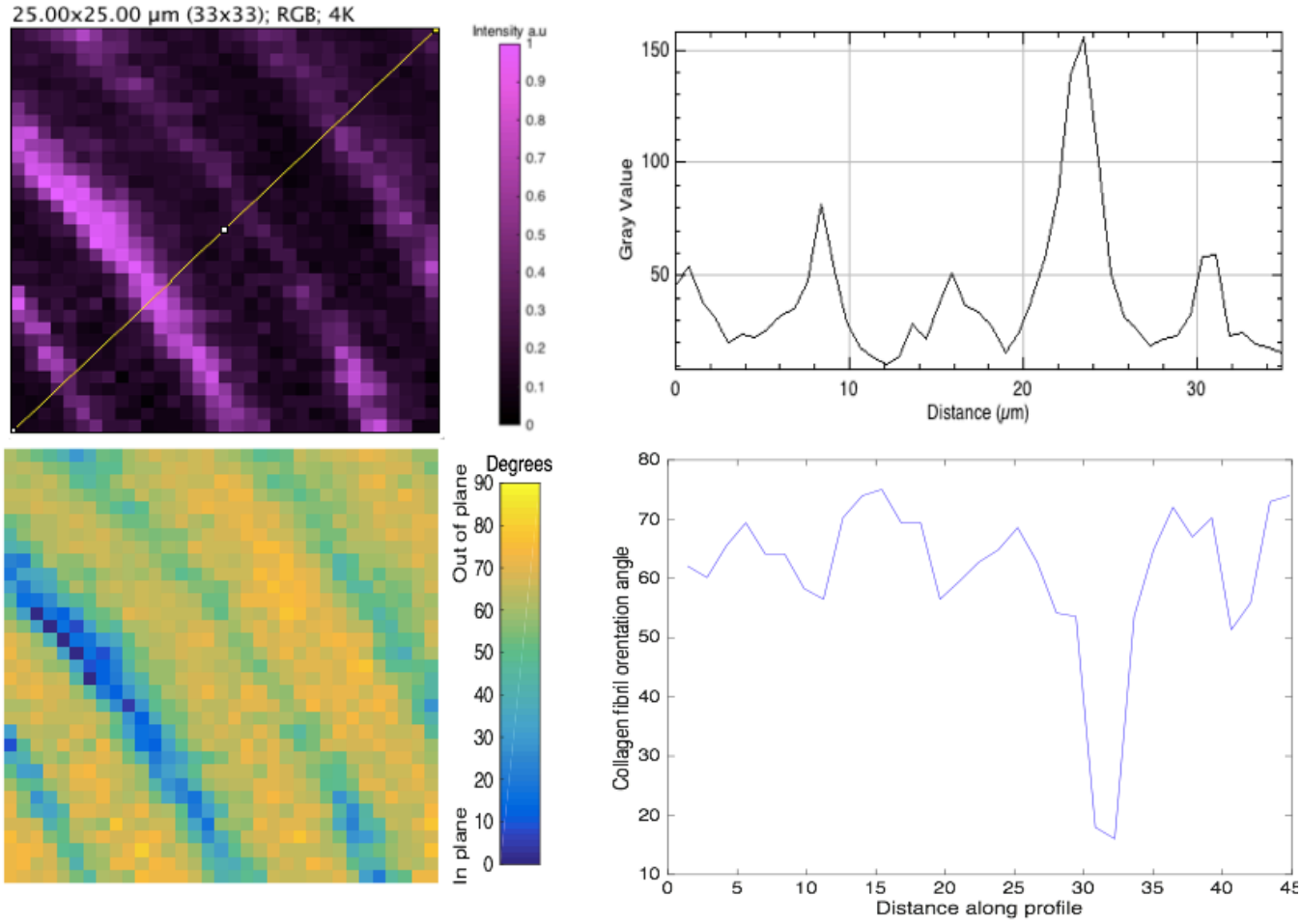

Figure 5. 14: Intensity profiles (from right to left) along the diagonal of S2E-QI07 both as SHG intensity and as orientation angle.

5.4.2 QI Data Processing

QI™ images were processed using JPKSPM Data Processing software (1999-2016, JPK Instruments AG, Berlin, Germany) applying Hertz Fit, as described in section (3.4.1). Hertz fit uses the vertical deflection maps to create indentation modulus maps, which are then analyzed using Matlab. In Figure 5.15 the indentation modulus map and the height topography channels of one QI™ image are shown

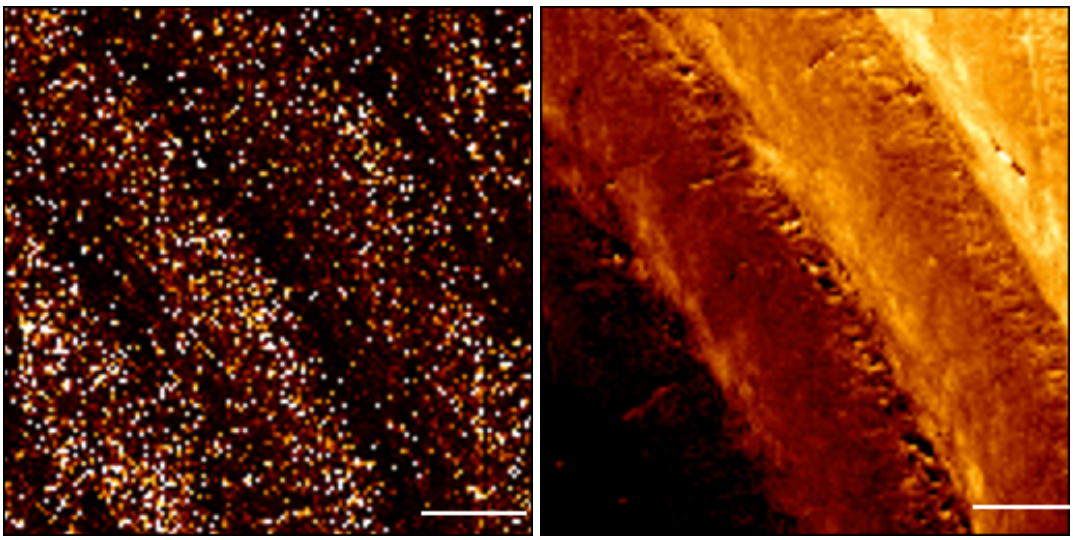

Figure 5. 15: Indentation modulus map (left). Setpoint height, (right). Scale bar 5 µm

First, while scanning the bone surface, the resulted scan image is rotated by 90 degrees with respect to the actual orientation. Hence, QI™ maps were imported into Matlab and read as a matrix of indentation modulus values. This indentation modulus map is then rotated 90-degree counter-clock wise, to have the correct orientation of the map as it was applied on the bone sample.

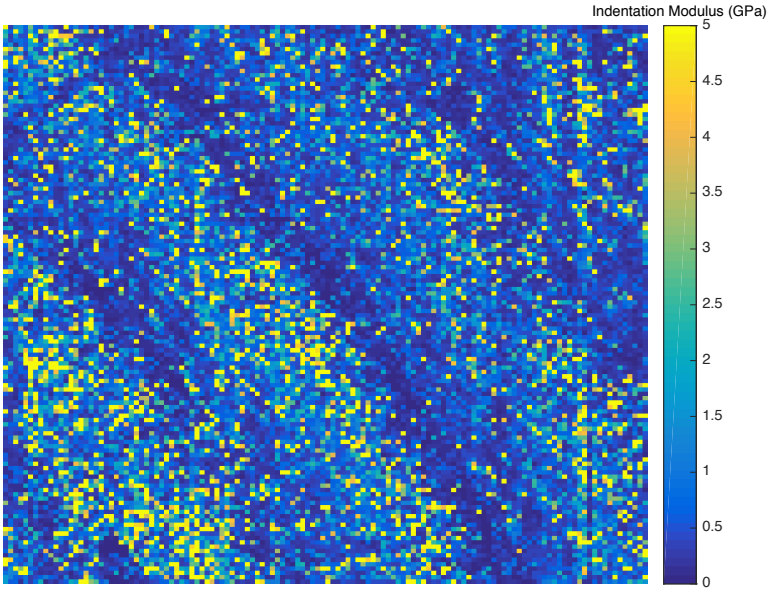

Figure 5. 16: Indentation modulus map plotted using Matlab

Second, the indentation Modulus maps were imported and plotted into Matlab (figure 5.16) for further analysis of indentation modulus, *i.e.* the average and mean of the indentation modulus between the lamella and interlamellar areas.

Using a custom Matlab script, lamellae and interlamellar areas were identified manually, then their mean, median and standard deviation were calculated. The script allows the user to manually select the lamellae (Figure 5.18), and accordingly unselected areas of the original matrix are considered as the interlamellar areas. However, due to noise, some interlamellar areas also contain some high values for the indentation modulus. The image below shows the selected lamellae within a sample map, numbered one to five.

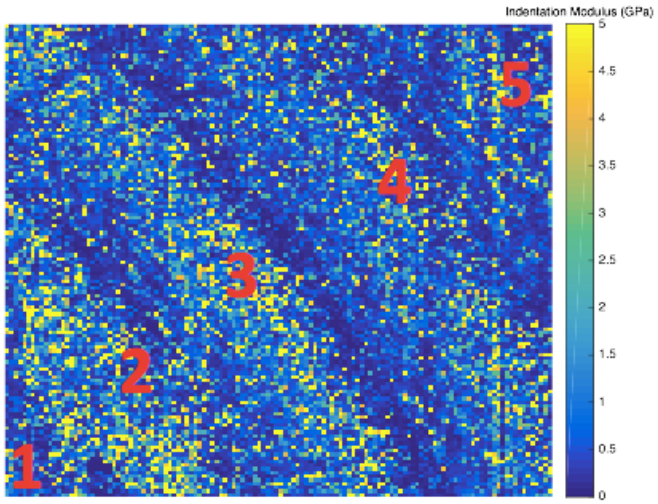

Figure 5. 17: selected lamellae for mean and median calculation, S2E_QI07

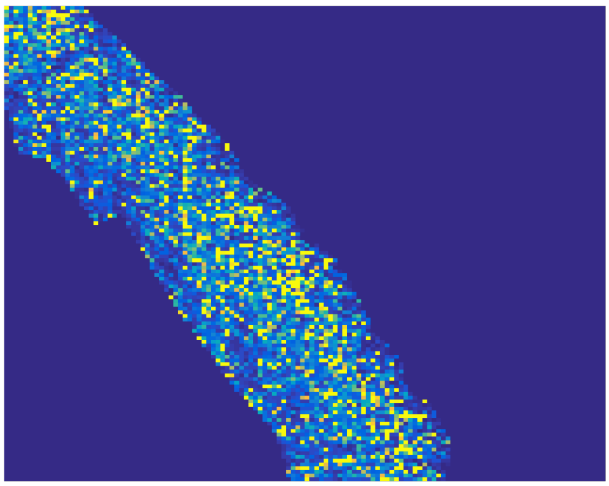

Figure 5. 18: One manually selected lamella

Lamellar and interlamellar values were extracted in two column matrices, then analysed further using Statistical Package for the Social Sciences (SPSS).

Third, QI images were resized to 33 x 33 pixels to match that of the SHG. Medfilt2d was applied to smooth the values and to be able to plot it against the SHG values of the corresponding pixels. Figure 5.19 shows a smoothed and resized QI.

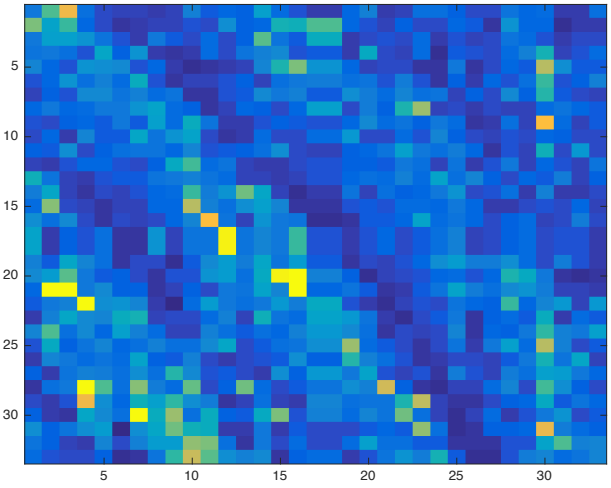

Figure 5. 19: A resized & smoothed QI (medfilt2d function)

In this chapter, the AFM and SHG data processing steps were explained, figure 5.20 shows an overview of some results obtained from the AFM and their corresponding SHG images.

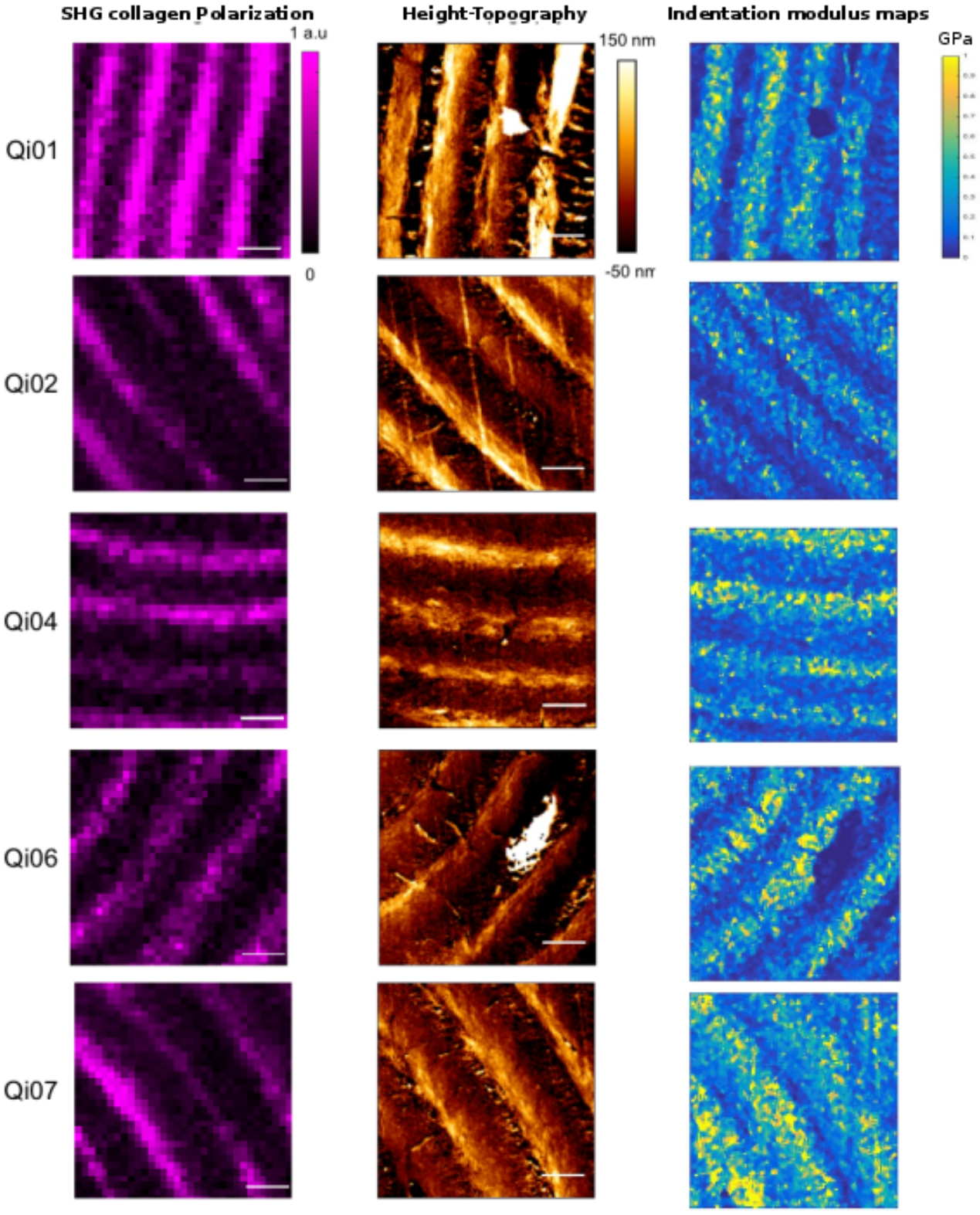

Figure 5. 20: Structural and mechanical results of the measurement methods, SHG and smoothed AFM. Scale bar 5 μm

Chapter 6
Results and Discussion

Bone mechanical properties at the sub-micrometer scale are identified with the properties of its smallest building block, the lamellae. Collagen fibrils in lamellae change their orientation among a range of degrees between in- and out of plane. The effect of this difference in collagen fibril orientation on the stiffness has been investigated as well as how this orientation influences the fracture toughness, if any. Along with investigating the correlation between the stiffness and fracture toughness (using the data of Granke *et al.* Granke (2015)). In addition, the height topography, in the AFM images, between lamellae and interlamellar areas was distinguishable in fluid in this study, which is in contrast to an earlier report. This section explains in detail these main findings.

6.1 Collagen Fibril Orientation

Collagen fibril orientation was analysed as mentioned in section (5.4.1), hence, intensity values were transformed into degrees between 0 and 90. The figure below shows processed SHG images of samples N3A and S2E in collagen fibril orientation in degrees. In Figure 6.1, lower intensity means the orientation tends to be in plane.

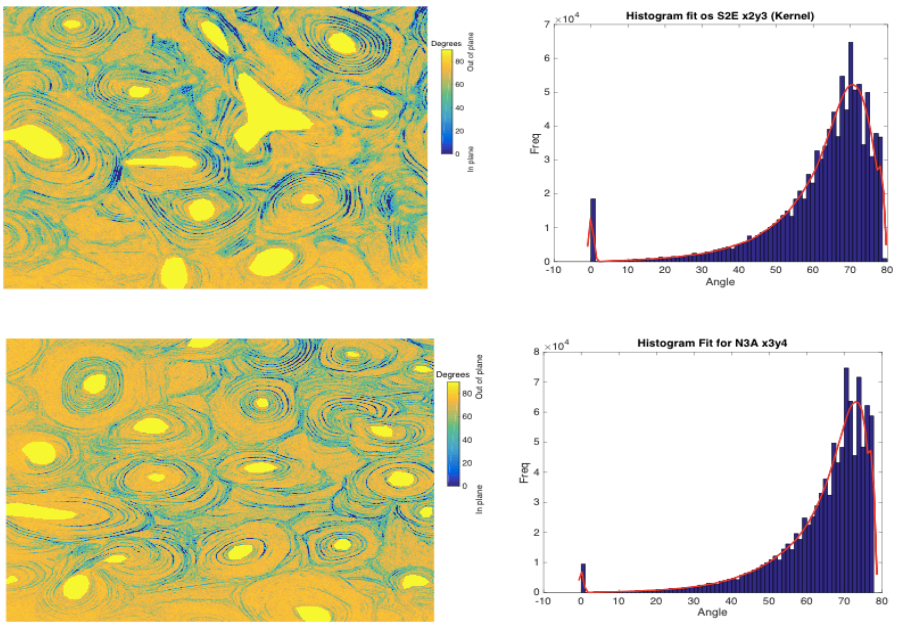

Figure 6. 1: SHG images converted into collagen orientation angle (left) and corresponding histograms (right) for samples S2E 87 years old, female (top) and N3A 47 years old, female (bottom).

Full SHG images converted into collagen orientation for samples S2E and N3A are shown in Figure 6.2 and 6.3.

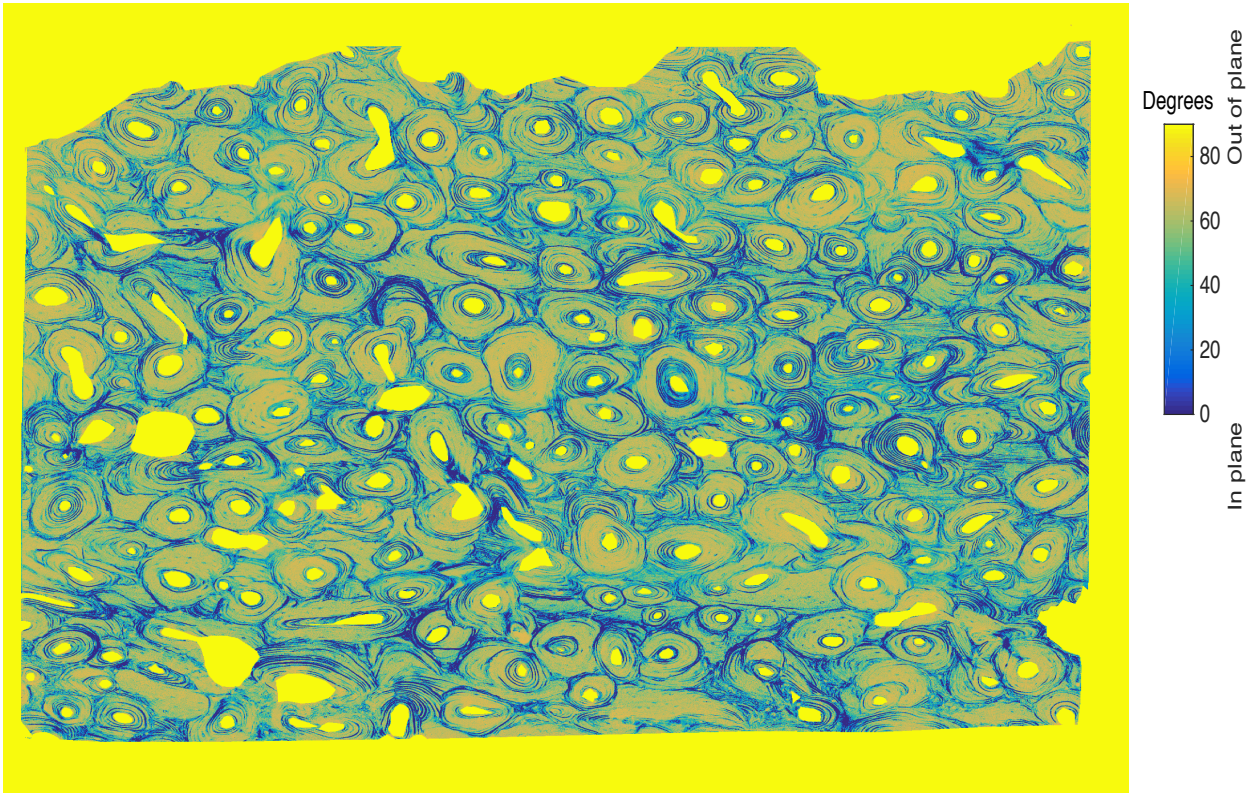

Figure 6. 2: N3A sample represented as collagen fibril degree values

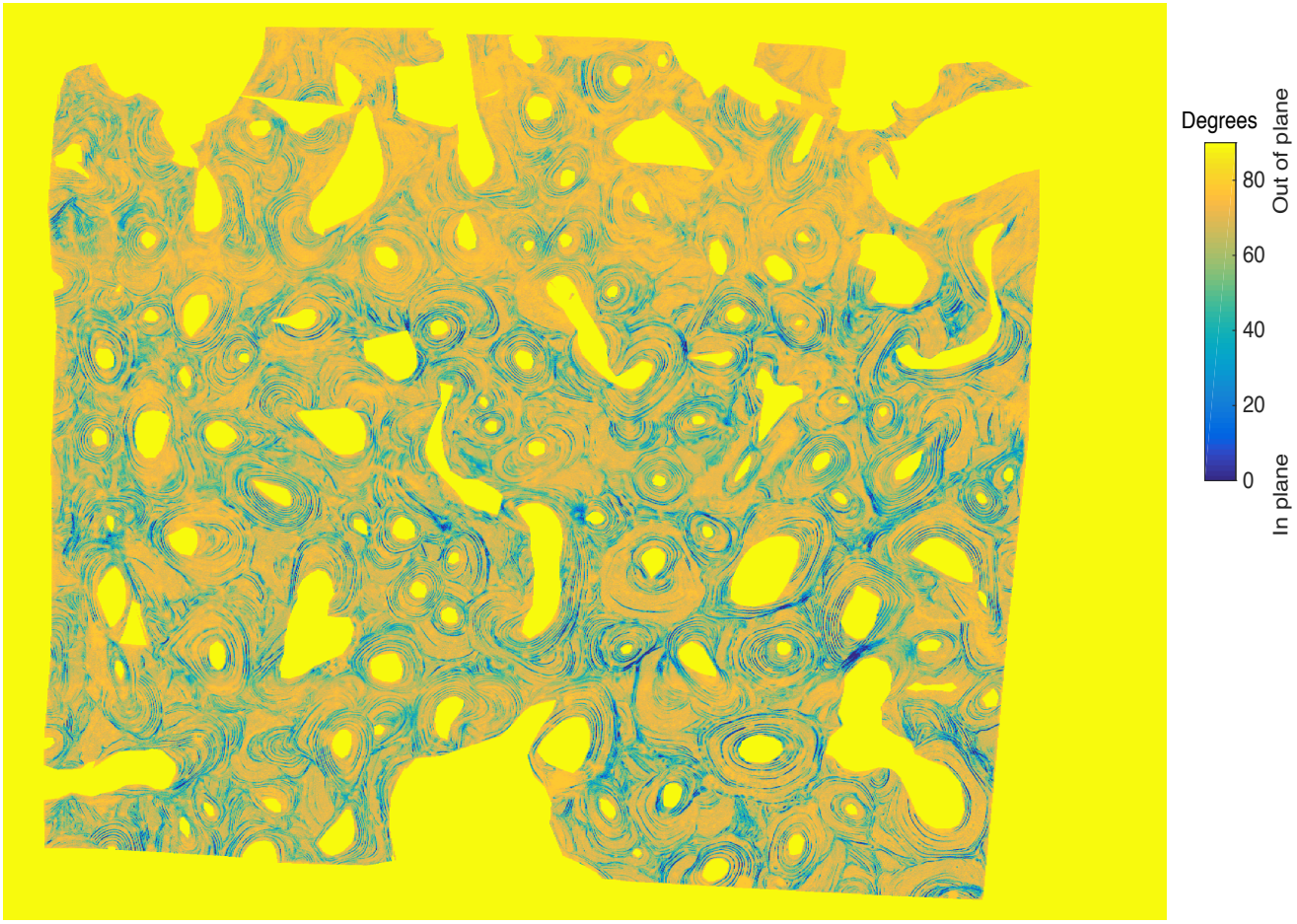

Figure 6. 3: S2E sample represented as collagen fibril degree values

The histograms of the local collagen fibril orientation show a tendency towards a mostly out of plane orientation (fitted using Kernel density distribution). However, the distribution has some spikes (Figure 6.4), which are likely a result of intensity adjustment during the stitching of the single SHG images to form a full sample image.

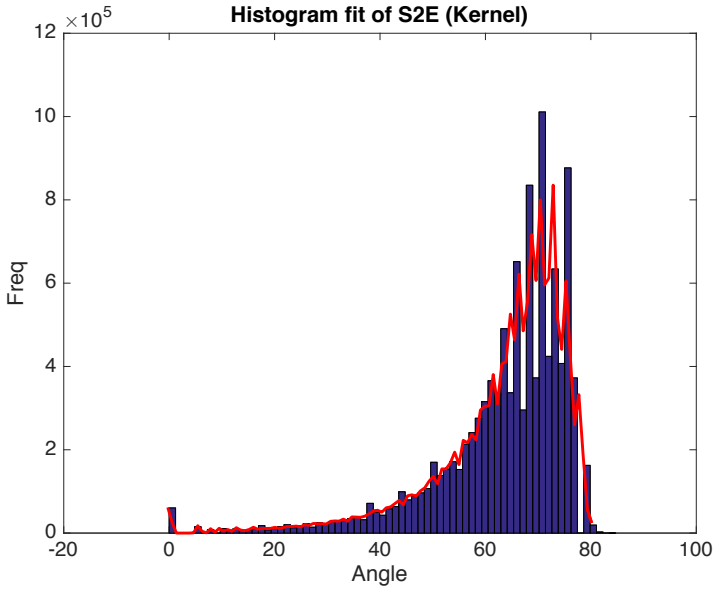

Figure 6. 4: Histogram of collagen fibril degrees observed in S2E sample

For all the 20 SHG images obtained, collagen fibril orientation, their mean and standard deviation were calculated, figure 6.5 depicts the mean and error bar of the orientation for each age.

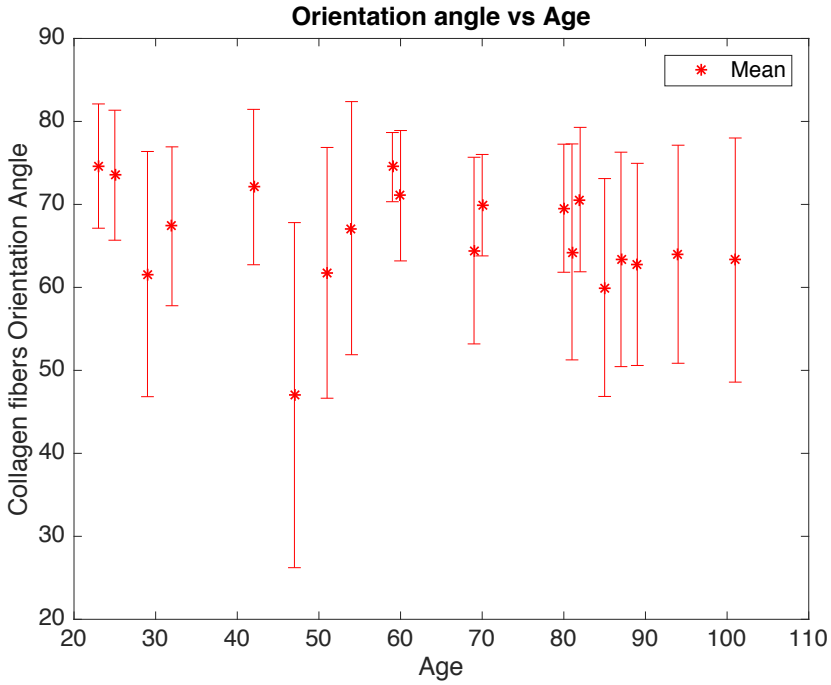

Figure 6. 5: Collagen fibril degree of orientation vs age

For these samples, no clear tendency of mean collagen fibril orientations as a function of age is observed for a whole sample data. Other studies, *i.e.* Goldman *et al.*, examined collagen fibril

orientation via circularly polarized light microscopy, orientation patterns were not identified, they suggested that other factors, including diseases and metabolic activity, may influence collagen fibril orientation patters (Goldman, 2003).

However, at the level of lamellae and interlamellar areas, the mean (figure 6.6) and median (figure 6.7) of collagen fibril orientation angle was calculated for each cropped SHG image (25 µm x 25 µm). Figure 6.6 shows a potential decline of average angle with respect to age, however, no correlation can be determined.

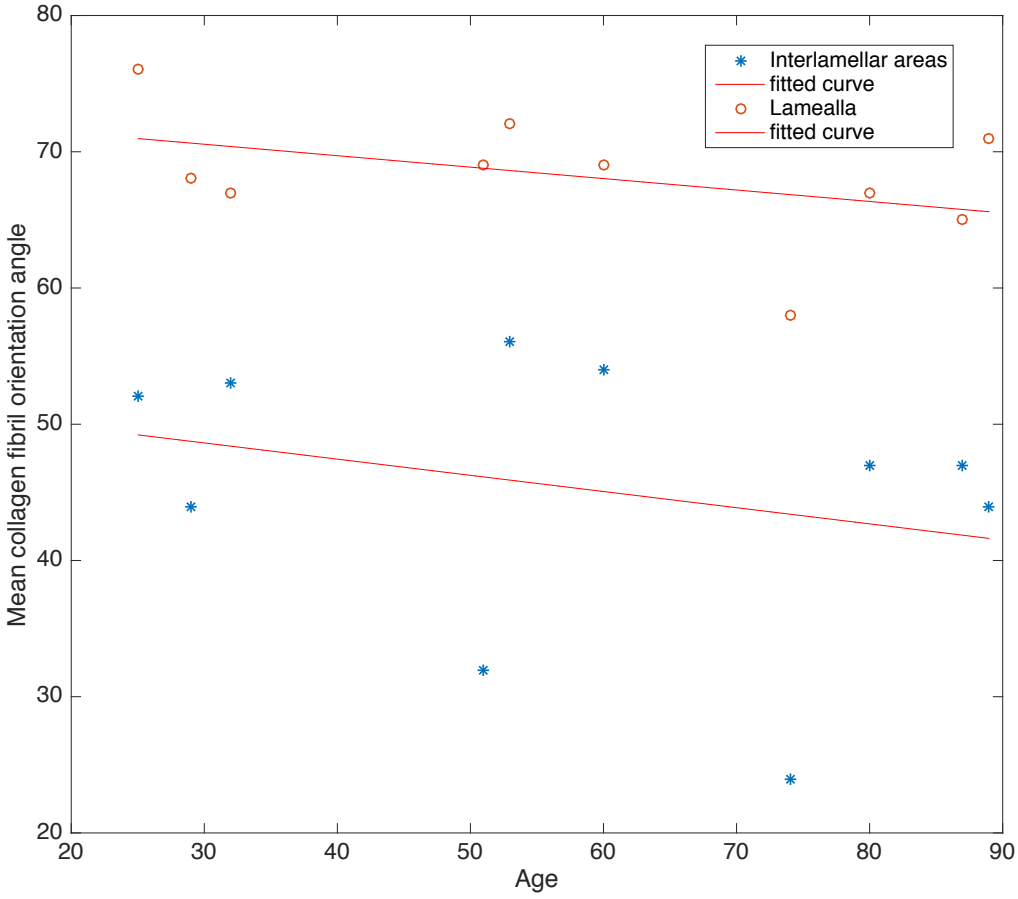

Figure 6. 6: Collagen fibril degree of orientation vs age for lamellae (red) and interlamellar areas (blue)

This decline in the mean collagen fibrils orientation does not show a statistical significant p-value for both lamellae and interlamellar areas. This suggests that the mean collagen fibril orientation is independent of age.

Table 6. 1: Linear fitting equation for lamellae and interlamellar areas

	Linear fit equation	P1	P2	p-value	R^2
Interlamellar Areas	y = p1*x + p2	-0.1188	52.19	0.431	7.9%
Lamellae		-0.084	73.07	0.218	18.3%

Figure 6.7 shows the median of the angle vs age for both lamellae and interlamellar areas. It is true that all the lamellae have higher median than the interlamellar areas, meaning they are more out of plane, but this does not show statistically relevant information. Thus, the relative difference was examined by dividing the orientation angle of the lamellae by the interlamellar areas.

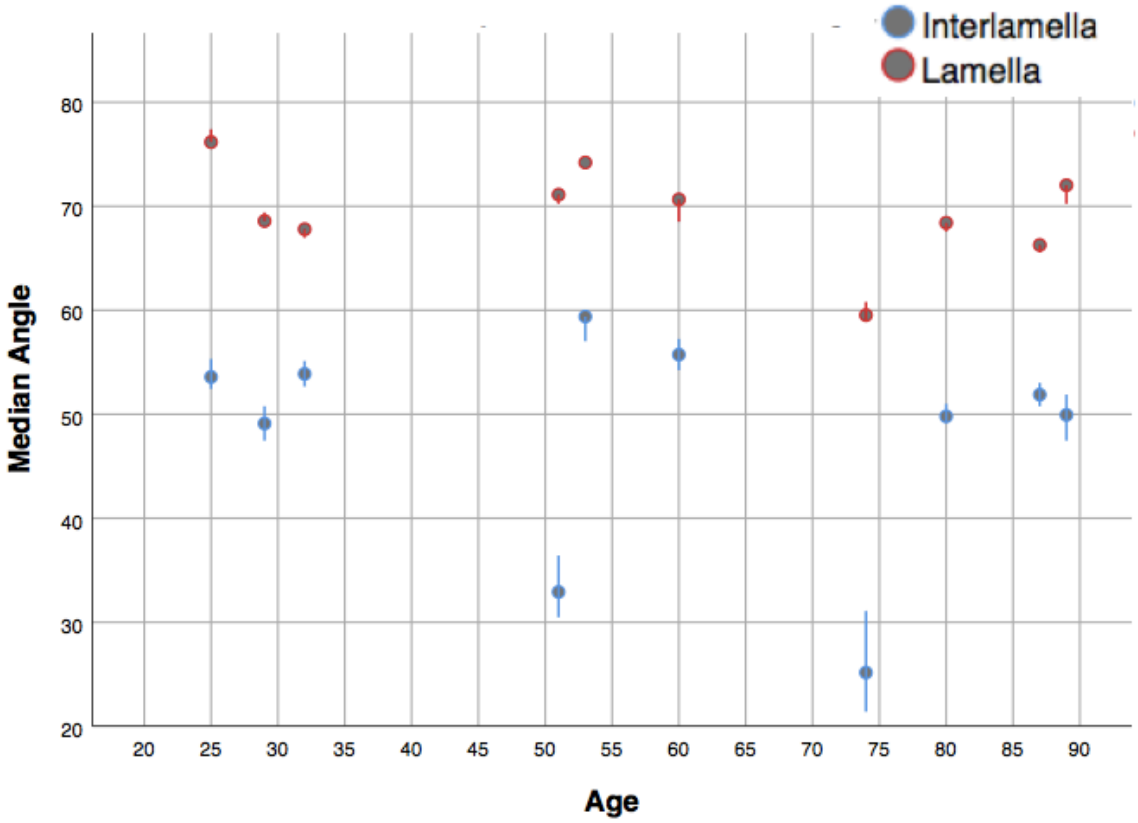

Figure 6. 7: Median of the collagen fibril orientation angle vs age (all samples)

The relative difference of the orientation angle measured for the lamellae and interlamellar areas is shown in figure 6.8. The linear fitting equation shows a non-significant correlation of this relative difference with age, table 6.2.

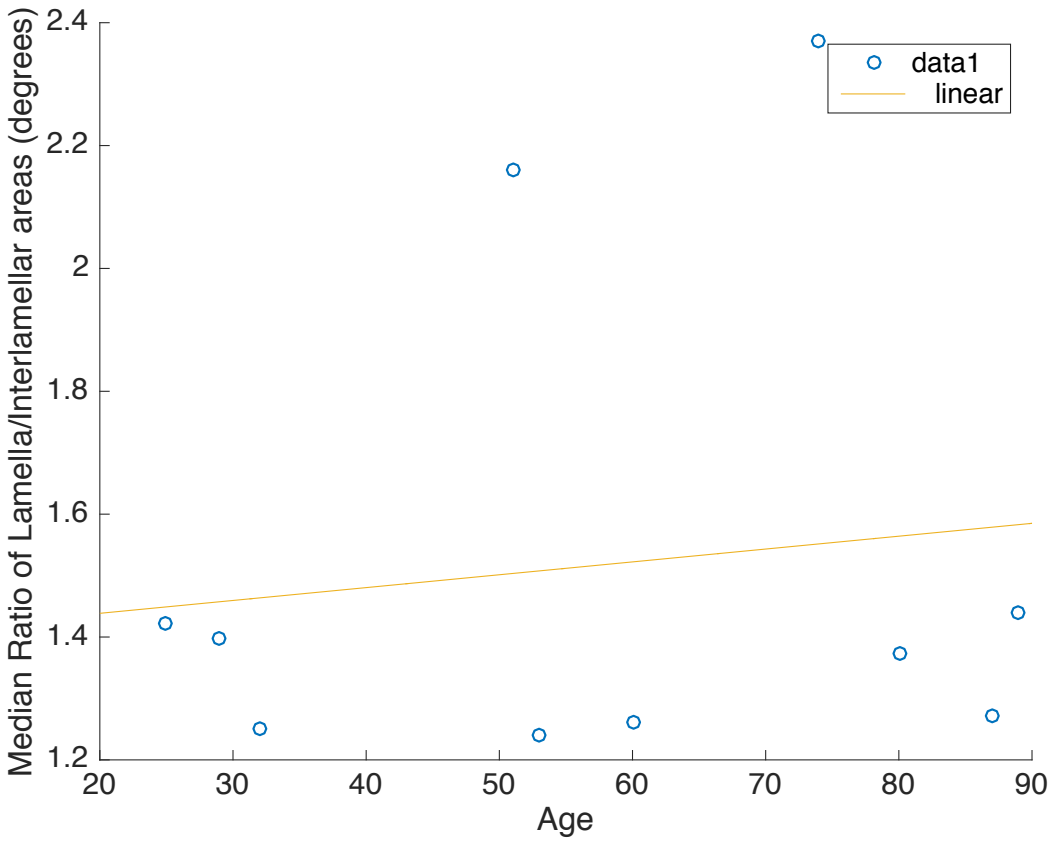

Figure 6. 8: Median ratio between lamella and interlamellar areas vs age (all samples)

Table 6. 2: Linear fitting equations for collagen fibril orientation angle correlating with age

	Linear fit equation	**P1**	**P2**	**p-value**	**R^2**
Median ratio vs age	y = p1*x + p2	0.0020	1.3967	0.731	1.56%

6.1 Indentation modulus

In QI plots, a difference between lamellae and interlamellar areas was found. However, some spots in the interlamellar areas had high values, even greater than the maximum value within the lamella. The indentation modulus maps were quantitatively analysed; the median of the indentation modulus of lamellae and interlamellar areas is depicted in figure 6.9. The median of the indentation modulus was plotted with 95% confidence interval.

Due to noise and other factors, the range of the indentation modulus obtained from these experiments is in the range between 0.5 - 60 GPa. Some even higher values were found and

removed as we considered them as outliers. The indentation modulus results are not comparable to other values from the literature that had a finer range between 18 – 24 GPa for cortical bone (Hengsberger, 2001; Rho, 2002; Zysset, 1998; Turner, 1999). It is worth mentioning that the Hertz model applied yielded significantly lower indentation modulus compared to the Oliver-Pharr method in other studies too (Andriotis, 2015).

At this scale level of measurement, the cantilever tip does not leave an imprint visible with optical microscopy on the bone surface and thus, cannot be compared to conventional nanoindetation or microindentation techniques. Nevertheless, difference in indentation modulus was observed between lamella and interlamellar areas. This heterogeneity between both areas is visible in both collagen fibril orientation angle and in indentation modulus maps. As lamellae are stiffer than interlamellar areas, in the former, the collagen fibrils are oriented out of plane, and in the latter, the collagen fibrils are oriented in plane.

The following figures show how the indentation modulus (GPa) behaves as a function of age.

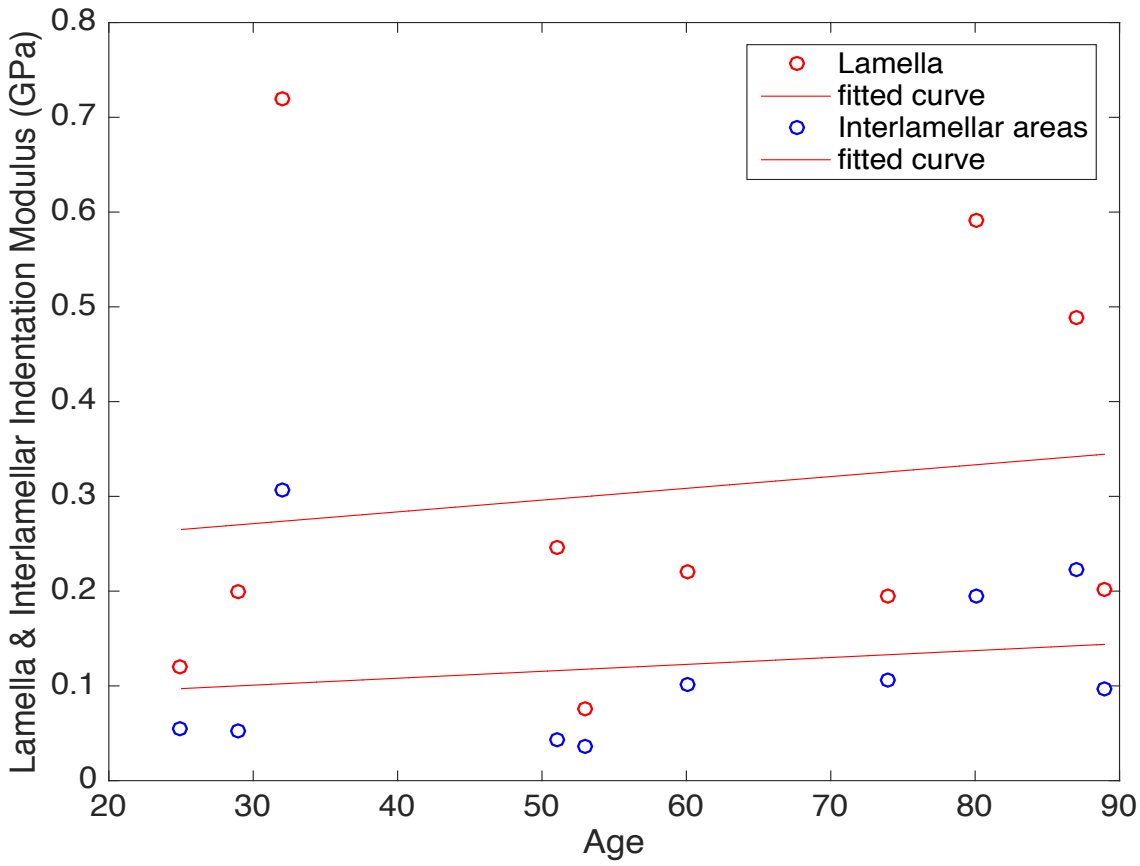

Figure 6. 9: Median of the indentation modulus (GPa) of lamellae and interlamellar areas vs age

Figure 6.9 shows the median of the indentation modulus (GPa) vs age for both lamellae and interlamellar areas. The median shows higher values for lamellae compared to interlamellar areas for all the sample measured. Correlation with age could not be defined (p-value > 0.05).

Table 6. 3: Linear fitting equations for Median Lamellae and Interlamellar areas correlating with age

	Linear fit equation	**P1**	**P2**	**p-value**	**R^2**
Median of lamella vs age	y = p1*x + p2	0.001242	0.234	0.702	1.93%
Median of interlamellar area vs age		0.00073	0.07886	0.591	3.77

Hengsberger *et al.* reported that samples from an elderly donor showed a significantly lower indentation modulus than the ones from a younger donor (Hensberger, 2002). As well, Leng *et al.* showed that the elastic modulus of demineralized bone specimens decreased with aging (Leng, 2013).

As a next step, the heterogeneity of the indentation modulus between lamellae and interlamellar areas was investigated against age, figure 6.10. Using a linear fitting equation, the older the samples are, the ratio declines.

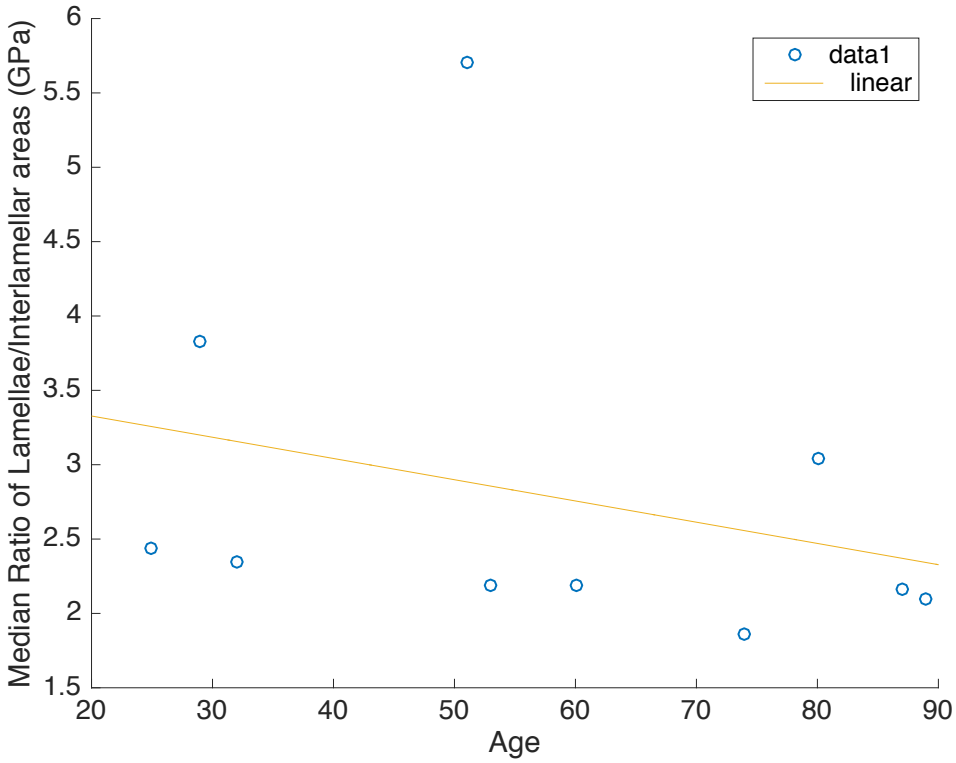

Figure 6. 10: Median ratio between lamella and interlamellar areas vs age (all samples)

Here too, the negative correlation does not show a statistical significant p-value.

Table 6. 4: Linear fitting equation for median ratio between the lamellae and interlamellar areas correlating with age

	Linear fit equation	**P1**	**P2**	**p-value**	**R^2**
Indentation median ratio vs age	y = p1*x + p2	-0.01255	3.4885	0.477	6.48%

For each sample, many osteons were tested, figure 6.11 shows the relative difference of the indentation modulus between the lamellae and the interlamellar areas for all osteons of all ages, no significant correlation was indicated (p-value=0.517).

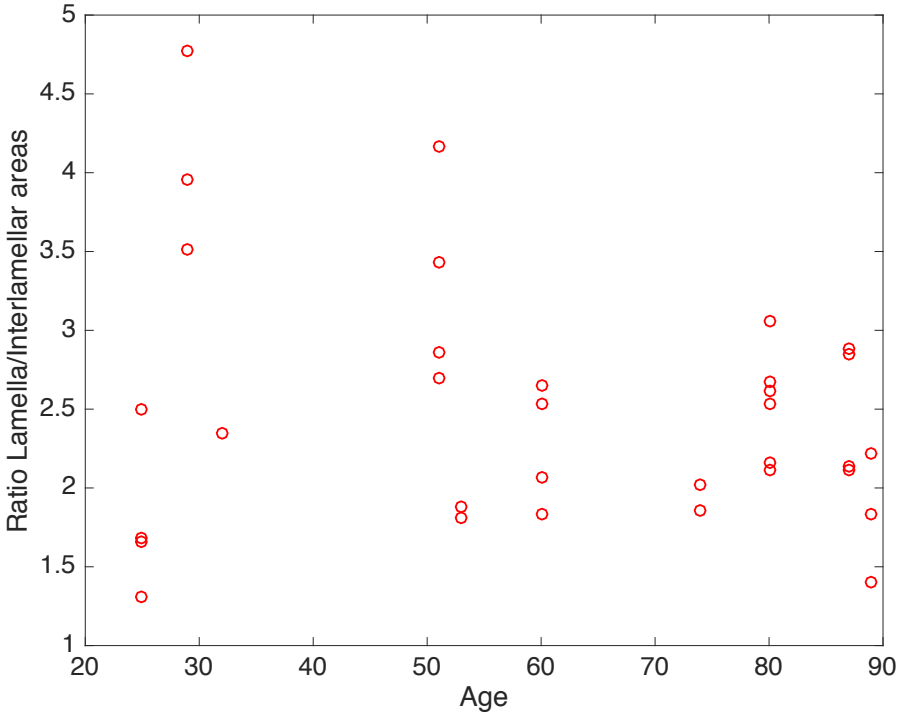

Figure 6. 11: Median of the indentation modulus (GPa) vs age (all osteons)

For one sample (80 years old), the figure below shows the relative difference between lamellae and interlamellar areas for all the osteons measured. As shown in Figure 6.12. there is considerable variation in elastic modulus between different osteons in the same donor. This may be related to osteon mineralization level and hence osteon age. Older osteons are thought to be more highly mineralized, which should result in a higher elastic modulus. Therefore, it was important to calculate the ratio between lamellar elastic modulus and interlamellar elastic modulus separately for each osteon.

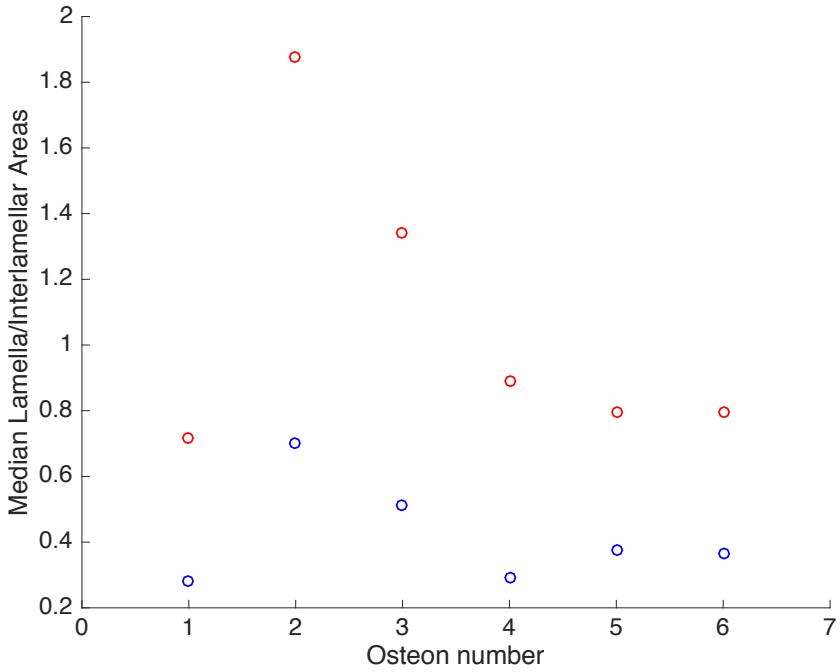

Figure 6. 12: Median of the indentation modulus (GPa) vs osteons of sample S2D (80 years old). Lamella (Red), Interlamellar area (Blue)

6.1 Correlation between the Collagen Fibrils Orientation and Indentation Modulus

SHG images were manually registered with their corresponding QI^{TM} maps using MosaicJ, as shown in Figure 6.13.

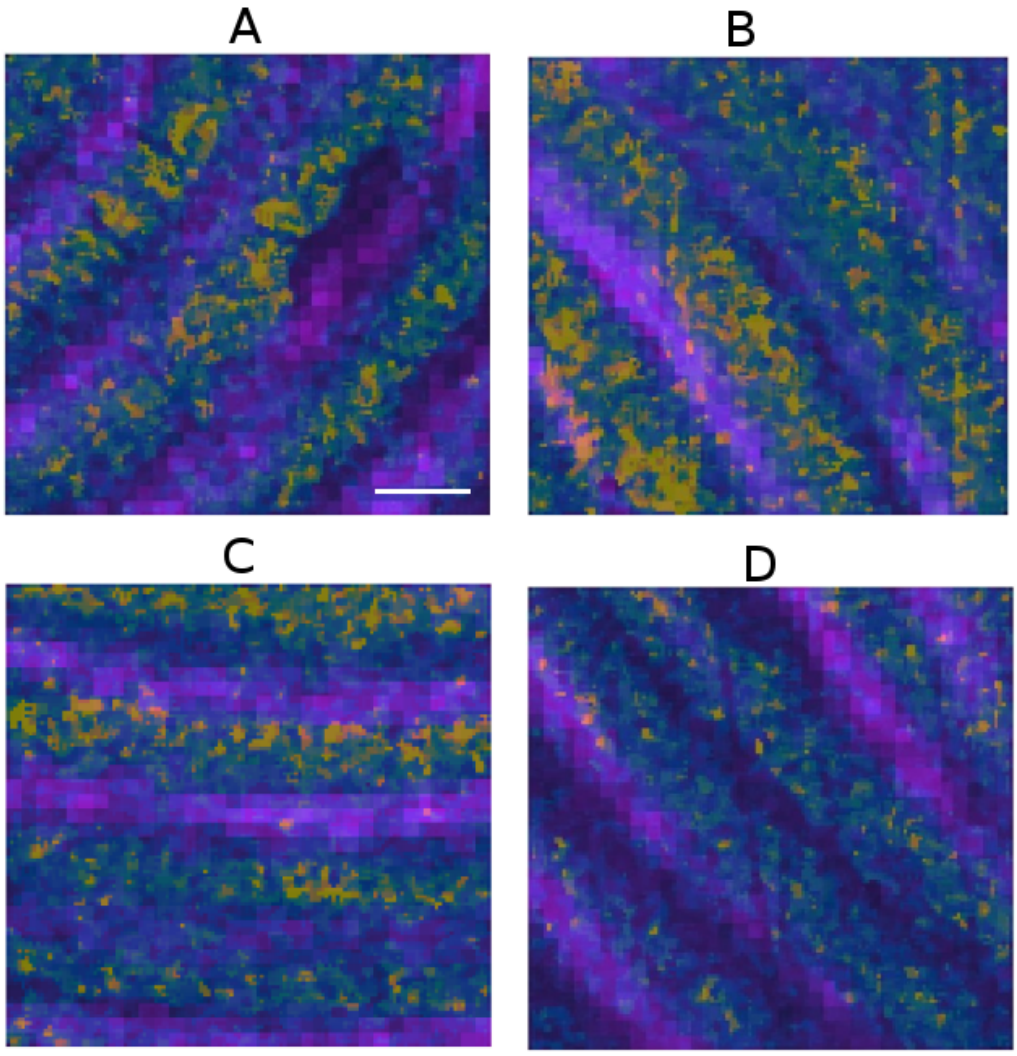

Figure 6. 13: Overlapped QI and SHG (A) S2EQI06 and (B) S2EQI07, (C) S2EQI04 and (D) S2EQI05, scale bar 5 µm

From the overlapped SHG and QI images and their intensity profiles, it can be qualitatively seen that the regions with higher indentation modulus are also the regions with lower SHG intensity. This means that the higher indentation modulus is associated with collagen fibrils oriented along the long or out of plane axis of the bone (longitudinal orientation).

Further, intensity profiles of indentation modulus maps, across the lamella and interlamellar areas, were plotted and overlaid with SHG intensity profiles, figure 6.12. Due to noise in the indentation modulus maps, smoothing (medfilt2) was applied to get a comparable overlap between SHG and the QI intensities.

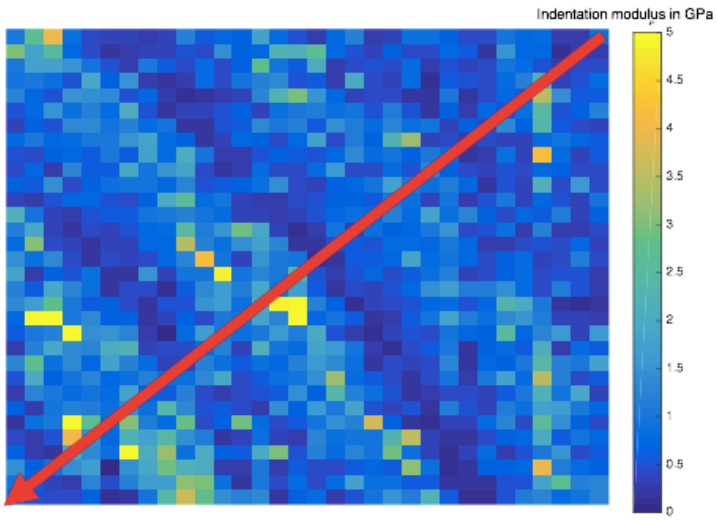

Figure 6. 14: S2EQI07-Modulus, in red selected intensity profile line (right to left), dimensions 25 µm x 25 µm

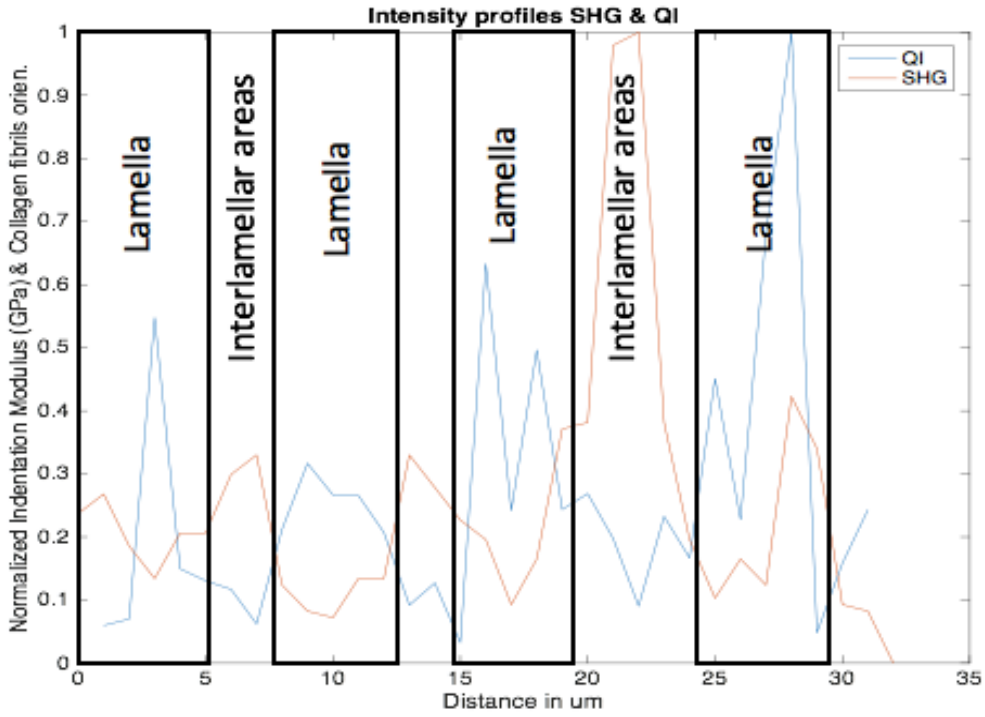

Figure 6. 15: S2EQI07 intensity profiles along with the SHG intensity

As expected and corresponding to the overlapped SHG images and QIs, the higher the indentation modulus is, the lower is the SHG intensity. These results are demonstrated quantitatively via average mean comparison between lamellae and interlamellar areas for indentation modulus and collagen fibril orientation angle.

Figure 6.16 depicts a scatter plot between the collagen fibrils orientation and indentation modulus. Applying a linear fit, the correlation is positive, meaning that that stiffer the collagen fibril is, the more it tends to be oriented out of plane. This correlation coefficient was plotted

using Matlab by resizing the filtered QI image from 128 x 128 pixels into 33 x 33 pixels, to match the size of the cropped SHG image.

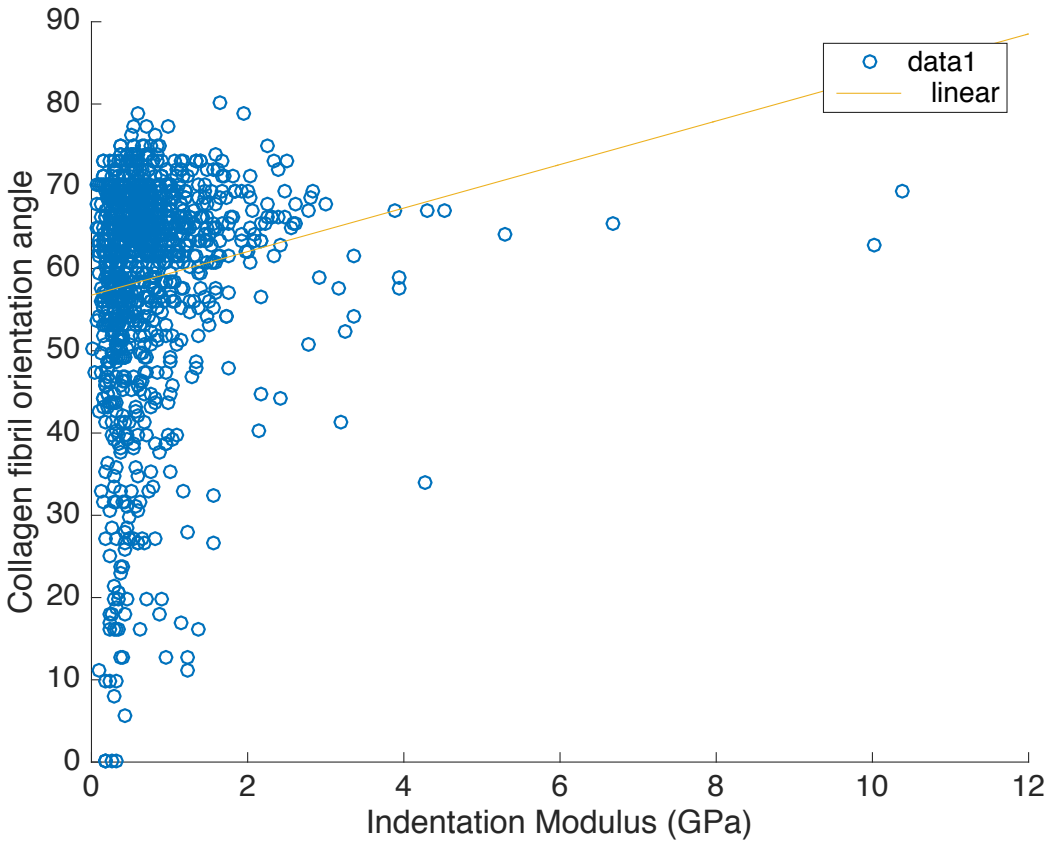

Figure 6. 16: S2EQI07 Collagen fibril orientation angle vs smoothed indentation modulus

The positive correlation between the indentation modulus and the collagen fibrils orientation is statistically significant (p-value<0.05). This is in contrast to a study by Spiesz *et al.* found no significant correlation between the indentation modulus among lamellar bone, using conventional nanoindentation, and the mean collagen fibrils orientation that was obtained from a quantitative polarized light microscopy (Spiesz, 2013).

Table 6. 5: Linear fitting equations for collagen fibril orientation angle correlating with the smoothed indentation modulus

	Linear fit equation	**P1**	**P2**	**p-value**	**R^2**
Smoothed QI vs SHG (Figure 6.16)	y = p1*x + p2	2.6469	56.761	9.06e-07	20.2%

6.1 Fracture Toughness Data

As mentioned earlier, bone sample used for the experiments reported in this thesis were obtained from bone beams that had underwent fracture toughness tests by a collaborator (Nyman Lab – Granke *et al.* 2015). These tests show a decrease in all fracture toughness properties with age. Crack initiation toughness (K_{init}) with p-value<0.0001, crack growth toughness (K_{grow}) with p-value<0.0044, and overall resistance to crack propagation (J-int) with p-value<0.0026 (Granke, 2015).

The fracture toughness properties were compared to indentation modulus obtained from the AFM, and to the collagen fibril orientation angle obtained from SHG. The relative difference of the collagen fibril orientation angle, measured for the lamellae and interlamellar areas, correlates positively with the crack initiation toughness (p-vale=0.398) and the overall resistance to crack propagation (p-vale=0.296), and negatively with the crack growth toughness (p-value=0.877). however, these values do not indicate a significant level of correlation.

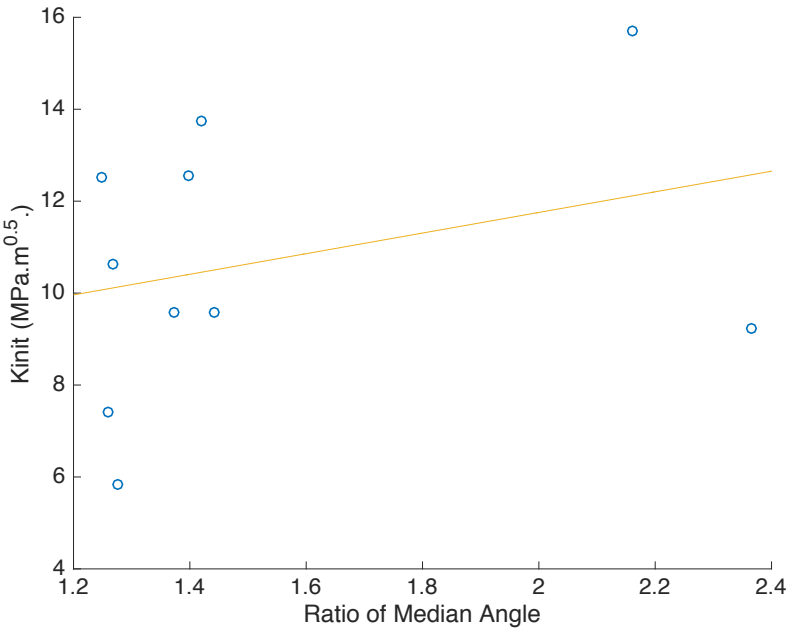

Figure 6. 17: The crack initiation toughness as a function of the ratio of median collagen fibrils angle

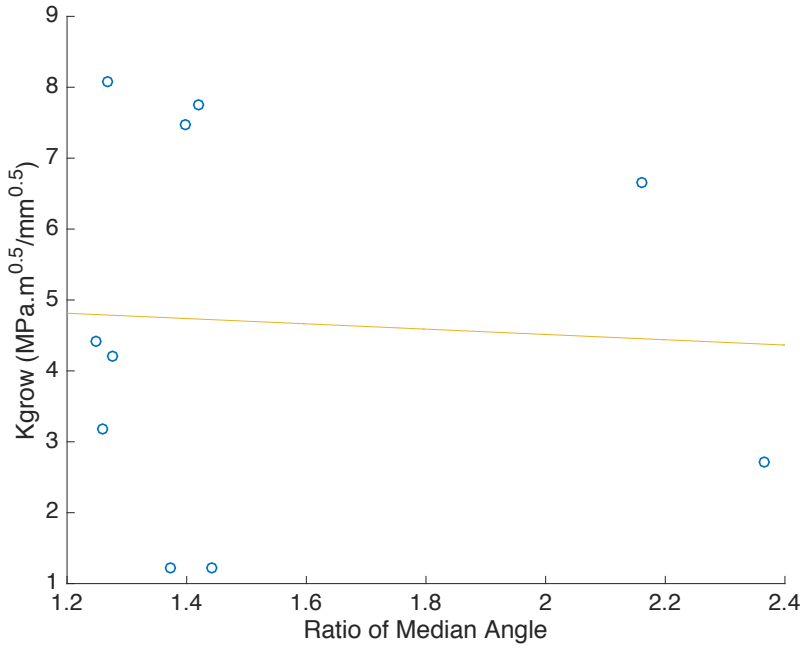

Figure 6. 18: The crack growth toughness as a function of the ratio of median collagen fibrils angle

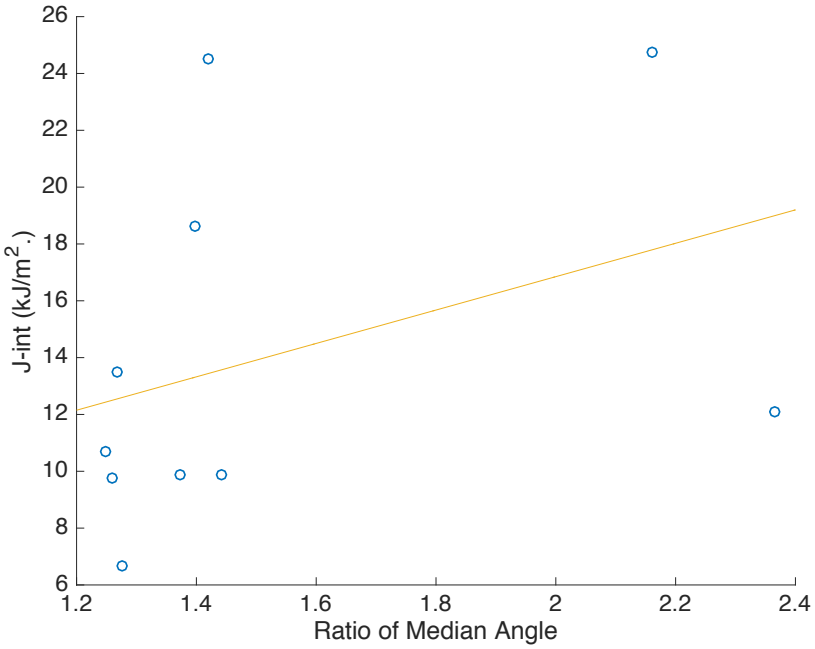

Figure 6. 19: The overall resistance to crack propagation as a function of the ratio of median collagen fibrils angle

The relative difference of the indentation modulus measured for the lamellae and interlamellar areas shows a positive correlation with all fracture toughness parameters. With the crack initiation toughness (p-vale=0.0537), the crack growth toughness (p-value=0.358), and the overall resistance to crack propagation (p-vale=0.0585).

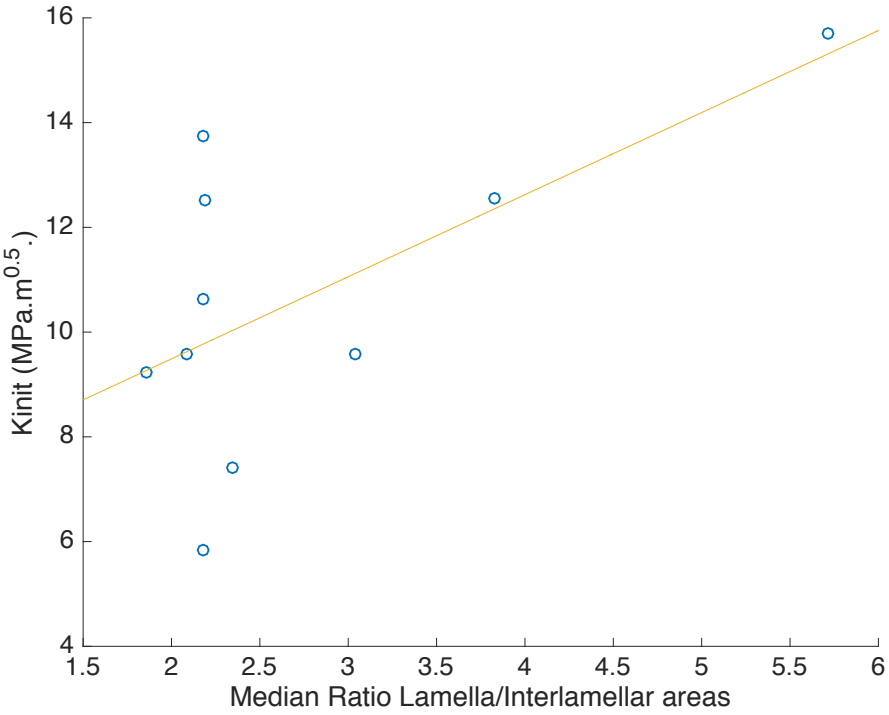

Figure 6. 20: The crack initiation toughness as a function of the ratio of median between Lamellae and Interlamellar areas

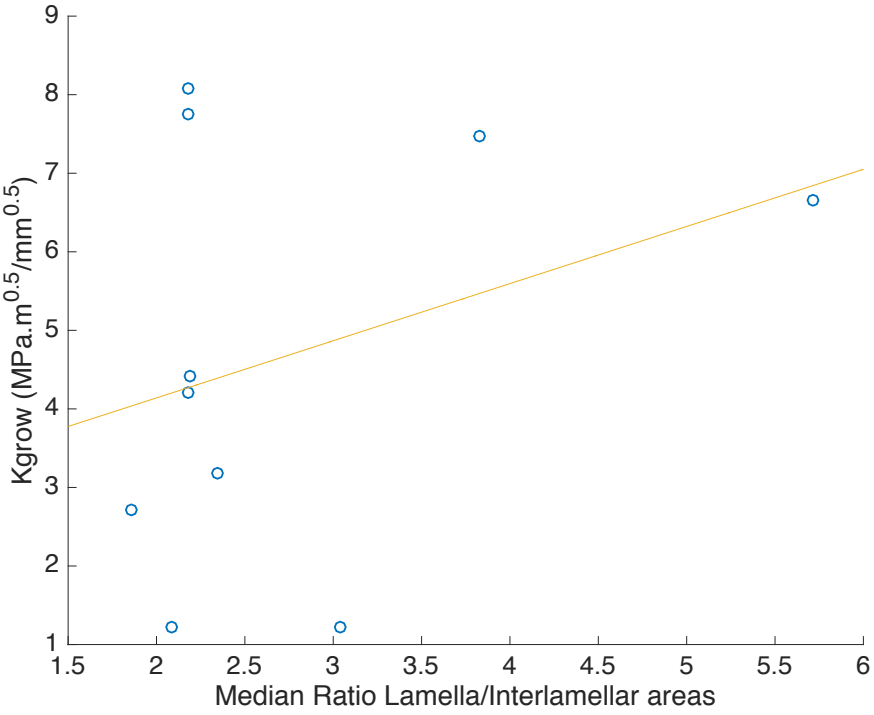

Figure 6. 21: The crack growth as a function of the ratio of median between Lamellae and Interlamellar areas

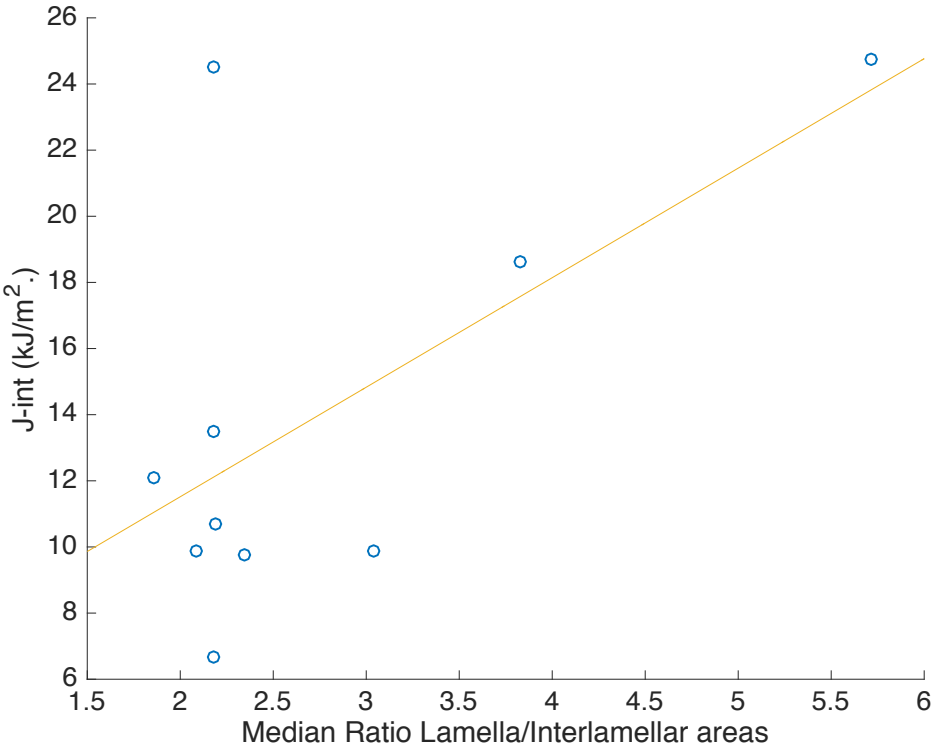

Figure 6. 22: The overall resistance to crack propagation as a function of the ratio of median between Lamellae and Interlamellar areas

Peterlik *et al*. showed that the J-integral increases significantly for mean collagen angle greater then 50° (Peterlik, 2006). Meaning that high fracture toughness, high crack growth toughness and high resistance to crack propagation correlate with high degree of nano-elasticity inhomogeneity between osteonal lamellae and interlamellar areas. This correlation is statistically significant for the crack initiation toughness and overall resistance to crack propagation, which corresponds to a study conducted by Katsamenis *et al.* on human cortical bone where the authors reported that the fracture toughness and crack growth resistance of bone are significantly correlated to mechanical inhomogeneity between lamellae and interlamellar areas at the osteonal-level (Katsamenis, 2015).

Table 6. 6: Linear fitting equations fracture toughness parameters and collagen fibril orientation angle and the indentation modulus

	Linear fit equation	P1	P2	p-value	R2
Crack initiation toughness & relative difference in Collagen fibrils orientation	y = p1*x + p2	2.2428	7.2693	0.398	9.08%
Crack growth & relative difference in Collagen fibrils orientation		-0.374	5.2619	0.877	0.319%
Overall resistance to crack propagation & relative difference in Collagen fibrils orientation		5.8752	5.0988	0.296	13.5%
Crack initiation toughness & relative difference in indentation modulus		1.5673	6.3551	0.0537	39%
Crack growth & relative difference in indentation modulus		0.7275	2.6849	0.358	10.6%
Overall resistance to crack propagation & relative difference in indentation modulus		3.3121	4.8939	0.0585	37.8%

6.1 Measured Height

AFM imaging of osteonal lamellae revels information of the surface topography. All the experiments were conducted while samples were submerged in PBS. It was possible to distinguish between lamellae and interlamellar areas in recorded topography maps. Figures 6.21 and 6.22 shown below show the height of selected osteonal lamellae. Raised height corresponds to the interlamellar areas and reduced height to the lamellae; likewise, elevated heights correspond to low indentation modulus and vice versa. This finding seems to be in contrast to a report by Faingold *et al*. who mentioned that AFM imaging of osteonal lamellae revealed a disappearance of the distinctive lamellar structure under wet conditions using PBS for at least 12 hours. However, a possible interpretation of the results presented here and the results of earlier studies (Katsamenis *et al.* and Faingold *et al.)* is that interlamellar areas swell more compared to lamellae. This can be explained by the fact that collagen fibrils, which make up the majority of the organic matrix of bone also swell more in the transverse direction (Interlamellar areas) compared to the longitudinal direction (lamellae). Thus, depending on the

height difference between Interlamellar areas and lamellae in dry state, hydration can either lead to a reduction, a complete cancellation or reversal of this height difference.

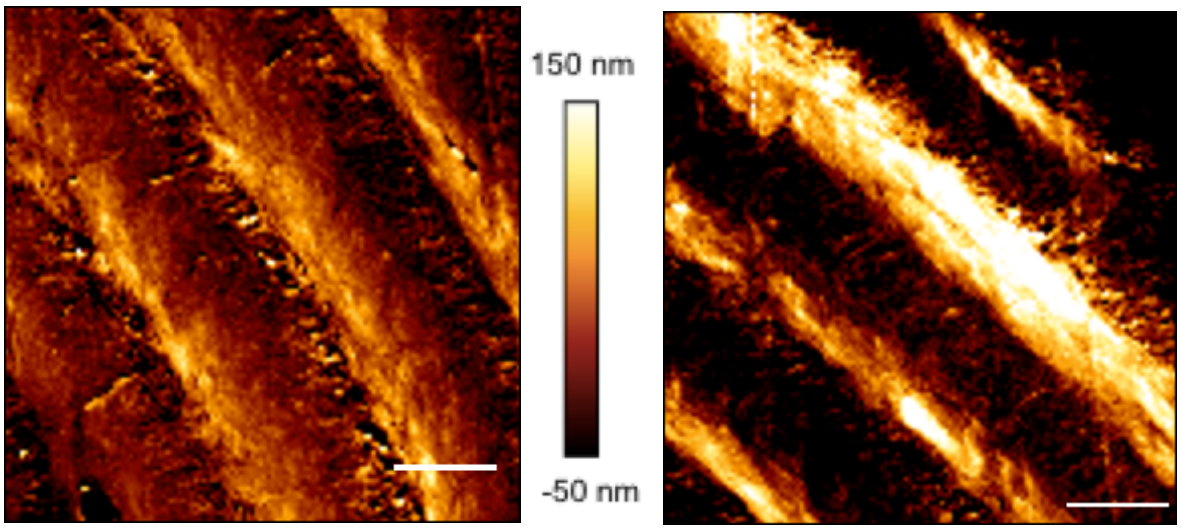

Figure 6. 23: S2EQI07 (Left), S2EQI08 (Right) measured height, scale bar 5 µm

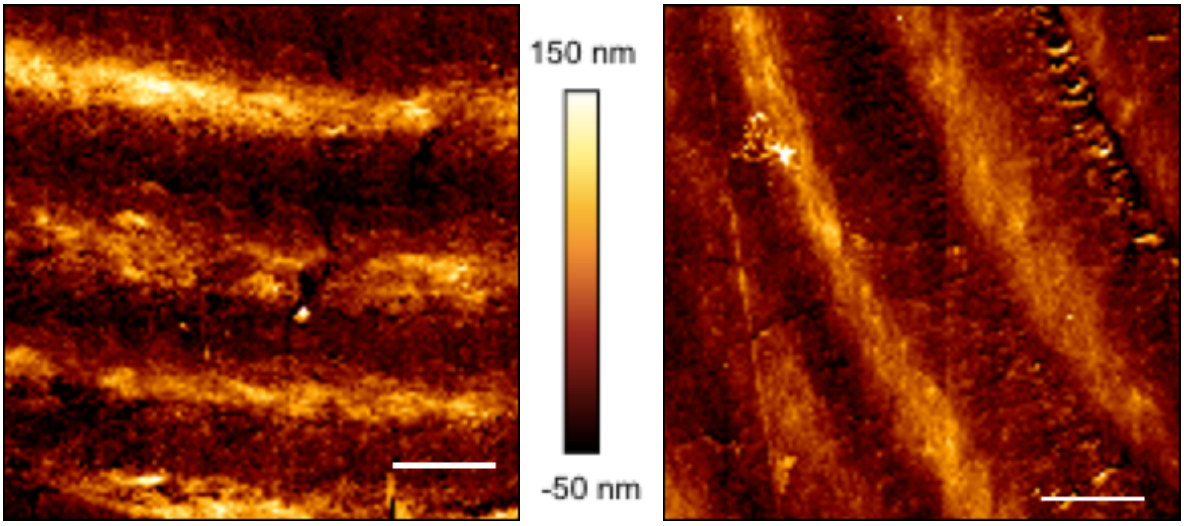

Figure 6. 24: S2EQI04 (Left), S2DQI03 (Right) measured height, scale bar 5 µm

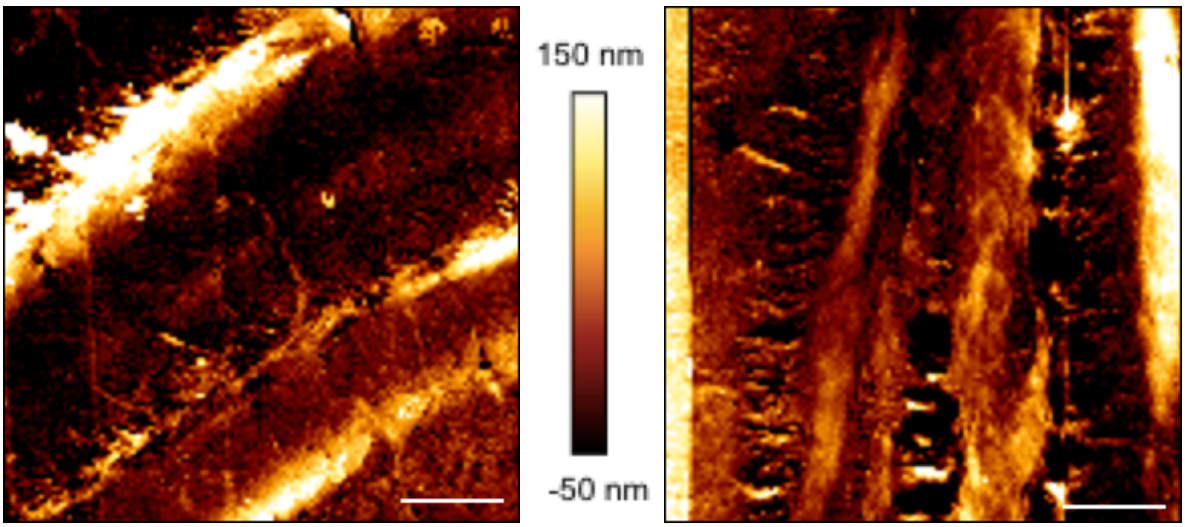

Figure 6. 25: S2BQI06 (Left), S2AQI03 (Right) measured height, scale bar 5 μm

6.2 Limitations and challenges

Certain limitations were faced while conducting these experiments. One of the most important issues that influences measurement in both AFM and SHG is achieving a 100% flat surface of the bone samples. If the surface is not flat, imaging with SHG will be at a different depth from the surface, and that impacts the intensity of the signal. Also, when measuring with the SHG, laser power should be constant, otherwise, over exposure of the signal might occur. In addition, stitching of SHG images might result in intensity adjustment at the edges of the stitched images, which in turn influences the final intensity value at these edges, which is then reflected into spikes as we saw in figure 6.4.

Furthermore, regarding the AFM, samples were tested using different cantilevers, this might have influenced the results to some extent, thus, it is advisable to conduct experiments under the same conditions and parameters, which would ensure a lesser user influence. On the other hand, ratios between lamellae and interlamellar elastic moduli were always computed for each osteon, making the use of different cantilevers likely a smaller issue.

Repeating the experiments while taking into account the above-mentioned issues might result in statistically significant results. In addition, including investigating of the collagen fibrils orientation via polarized light microscopy and comparing it with the results obtained from the SHG.

6.3 Conclusion

The aim of this master thesis was divided into three parts. First, to investigate the relative differences in indentation modulus of compact bone samples between lamellae and interlamellar areas, and how they change with age. Second, to examine the change of collagen fibril orientation angle with age too. Finally, to relate these findings to the fracture toughness results obtained from fracture experiments conducted on these samples. The following conclusions can be drawn from the results of this thesis:

1. Differences in indentation modulus are observed among lamellae and interlamellar areas of the specimens when tested with AFM cantilever based nanoindentation in PBS, samples were immersed in PBS for more than 24 hours and during measurement time.
2. The rise in inhomogeneity between osteonal lamellae and interlamellar areas with age is not statistically significant.
3. AFM imaging of osteonal lamellae revealed a distinctive lamellar structure (height topography).
4. We find a clear correlation from AFM nanoindentation that lamellar bone is stiffer in the longitudinal compared to a transverse orientation of mineralized collagen fibrils.
5. No statistically significance for the reduction in the inhomogeneity in collagen fibrils orientation with age.
6. High fracture initiation toughness and high resistance to crack propagation correlate with high degree of nanoelasticity inhomogeneity between osteonal lamellae and interlamellar areas.

References

AFM Handbook Version 4.3 – 07/2015.

AFM, Technical Note: A practical guide to AFM force spectroscopy and data analysis.

Ager J.W., Balooch G., Ritchie R.O. (2006). Fracture, aging, and disease in bone. Materials Research Society 2006, 21(8): 1878–1892.

Ammann P., Rizzoli R. (2003). Bone strength and its determinants. Osteoporos. Int. 2003, 14:13-18.

An Y.H., Draughn R.A. (2000). Mechanical testing of bone and the bone-implant interface. CRC Press.

Andriotis O.G. (2013). Nanostructure and mechanics of collagen fibrils from osteogenesis imperfecta mice and chronic asthma assessed with atomic force microscopy. University of Southampton, Faculty of Engineering and the Environment, PhD Thesis, p. 33-45.

Andriotis O.G., Manuyakom W., Zekonyte J., Kastamenis O.L., Howarth PH., Davis DE., Thurner PJ. (2015). Nanomechanical assessment of human and murine collagen fibrils via atomic force microscopy cantilever-based nanoindentation. J Mech Behav Biomed Mater. 39:9-26.

Ascenzi A., Bonucci E. (1967). The tensile properties of single osteons. Anatomical record 1967, 158:375-86.

Ascenzi A., Bonucci E. (1968). The compressive properties of single osteons. Anatomical record 1968, 161:377-88.

Ashby M.F. (1999). Materials selection in mechanical design. Oxford, UK, Butterworth Heinemann. 22-28.

Bakbak S., Kaycan R, Akkus O. (2011). Effect of collagen fiber orientation on mechanical prosperities of cortical bone. Journal of Biomechanics 2001, 44:11

Binnig G. and Rohrer H. (1982) Scanning tunnelling microscopy. *Helv. Phys. Acta.*, 1982, 55:726–735.

Bonewald, L. (2011). The amazing osteocyte. Journal of Bone and Mineral Research, 26: 229-238, ISSN 1523-4681.

Bromage T.G., Goldman H.M., McFarlin S.C., Warshaw J., Boyde A., Riggs C.M. (2003). Circularly polarized light standards for investigations of collagen fiber orientation in bone. Anat Rec, 274B, 157-68.

Boskey A.L., Coleman R. (2010). Aging and Bone. J Dent Res 89, 12:13333-1348.

Boskey A.L. (2006). Assessment of bone mineral and matrix using backscatter electron imaging and FTIR imaging. Current Osteoporosis Reports. 2006; 4:71-75.

Burstein A.H., Reilly D.T., Martens M. (1976). Aging of bone tissue: mechanical properties. J. Bone Joint Surg. 1976, 58(1):82-6.

Campagnola P.J., Loew L.M. (2003). Second-harmonic imaging microscopy for visualizing biomolecular arrays in cells, tissues and organisms. Nat Biotechnol 21:1356-1360.

Carpintero P., Caeiro J.R., Carpintero R., Morales A., Silva S., Mesa M. (2014). Complications of hip fractures: A review. *World Journal of Orthopedics*. 2014, 5(4):402-411.

Chen X., Nadiarynkh O., Plotnikov S., Campagnola P. (2012). Second harmonic generation microscopy for quantitative analysis of collagen fibrillary structure. Nature Protocols 7, 654-669.

Choi K., Kuhn J.L., Ciarelli M.J., Goldstein S.A. (1990). The elastic moduli of human subchondral, trabecular, and cortical bone tissue and the size-dependency of cortical bone modulus. J. Biomech. 1990, 23(11):1103-13.

Choi K., Goldstein S.A. (1993). A comparison of the fatigue behaviour of human trabecular and cortical bone tissue. J. Biomech., 1993, 25(12):1317-81.

Cowin S.C. (2001). Bone Mechanics Handbook. CRC Press.

Cummings S.R., Melton L.J., (2002). III Epidemiology and outcomes of osteoporotic fractures. Lancet., 359:1761–1767.

Currey J.D. (2002). Bones: Structure and Mechanics. Princeton University Press.

Deniset-Besseau A., Peixoto D.S., MosserP., Schanne-Klein G.M.-C. (2010). Nonlinear optical imaging of lyotropic cholesteric liquid crystals. *Opt. Express* 18, 1113–1121.

Dickenson R.P., Hutton W.C., Stott J.R.R. (1981). The mechanical properties of bone in osteoporosis. British Editorial Society of Bone and Joint Surgery, 63-B, No. 2.

Dimai H.P., Redlich K., Peretz M., Borgström F., Siebert U., Mahlich J. (2012). Economic burden of osteoporotic fractures in Austria. Health Econ Rev. 2:12.

Faingold A., Cohen S.R., Shahar R., Weiner S., Rapoport L., Wagner H.D. (2014). The effect of hydration on mechanical anisotropy, topography and fibril organization of the osteonal lamellae. Journal of Biomechanics. 2014, 47(2):367–372.

Florea C., Dreucean M., Laasanen M., Halvari A. (2011). Determination of Young's Modulus using AFM Nanoindentation. Applications on Bone Structures. 3rd International Conference on E-Health and Bioengineering – EHB, Iasi, Romania.

Funk J.R., Kerrigan J.R., Crandall J.R. (2004). Dynamic Bending Tolerance and Elastic-Plastic Material Properties of Human Femur. Association for the advancement of Automotive Medicine. 2004; 48:215-233.

Granke M., Makowski A.J., Uppuganti S., Does M.D., Nyman J.S. (2015). Identifying Novel Clinical Surrogates to Assess Human Bone Fracture Toughness. JBMR. 30(7):1290-1300.

Genthial R., Beaurepaire E., Schanne-Klein G.M.-C, Peyrin F., Farlay D., Olivier O., Bala Y., Boivin G., Vial J.C., Débarre D., Gourrier A. (2017). Label-free imaging of bone multiscale porosity and interfaces using third-harmonic generation microscopy. Nature. 2017, 7, 3419.

Goldman H.M, Bromage T.G., Thomas C.D., Celement J.G. (2003). Preferred collagen fiber orientation in the human mid-shaft femur. Anat Rec A Discov Mol Cell Evol Viol. 272(1):434-445.

Gong J. K., Arnold J. S., and Cohn S. H. (1964), Composition of trabecular and cortical bone, Anat. Rec. 1964, 149:325–332.

Hayes W.C., Wright T.M. (1976). Tensile testing of bone over a wide range of strain rates: effect of strain rate, microstructure and density. Medical and Biological Engineering 1976, 671-680.

Hengsberger S., Kulik A., Zysset Ph. (2001). A combined atomic force microscopy and nanoindentation technique to investigate the elastic properties of bone structural units. European Cells and Materials. 2001; 1:12-17.

Hengsberger S., Boivin G., Zysset Ph. (2002). Morphological and mechanical properties of bone structural units: a two-case study. JSME International Journal Series C Mechanical Systems, Machine Elements and Manufacturing. 2002; 45:936–943.

Ho Ba Tho M.C., Mazeran P.E., El Kirat K., Bensamoun S.F. (2012). Multiscale Characterization of Human Cortical Bone. Tech Science Press 2012, 87:6:557-577.

Holzapfel G.A., (2000). Nonlinear Solid Mechanics. A continuum Approach for Engineering. John Wiley & Sons, 2000.

Jenknis T., Katsamenis O.L., Andriotis O., Coutts L.V., Dunlop D.G., Oreffo R.O.C., Cooper C., Harvey N.C., Thurner P.J., the OStEO Group. (2017). The inferomedial femoral neck is compromised by age but not disease: Fracture toughness and the multifactorial mechanisms comprising reference point microindentation. J Mech Behav Biomed Mater. 75:399-412.

Kajzar F., Reinisch R. (2002). Beam shaping and control with nonlinear optics. NATO Advanced Science Institute Series, Springer.

Kanis J.A. (2002). Diagnosis of osteoporosis and assessment of fracture risk. *Lancet* 359:1929-1936.

Keaveny T.M., Morgean E.F., Yeh O.C. (2004). Bone Mechanics. McGraw-Hill. Chapter 8.

Keaveny T.M., Hayes W.C. (1993). A 20-year perspective on the mechanical properties of trabecular bone. Journal Biomechanical Engineering. 1993;115(4B):5, 34-42.

Katsamenis O.L. (2012). Bone matrix material properties on the micro- and nanoscale. University of Southampton, PhD Thesis.

Katsamenis O.L., Jenkins T., Thurner P.J. (2015). Toughness and damage susceptibility in human cortical bone is proportional to mechanical inhomogeneity at the osteonal- level. Bone 2015, 76:158–168.

Katsamenis O.L., Chong M.H., Andriotis O.G., Thurner P.J. (2012). Load-Bearing in Cortical Bone Microstructure: Selective Stiffening and Heterogeneous Strain Distribution at the Lamellar Level. JMBBM 2012, 17:152–165.

Thurner P.J., Katsamenis O.L. (2014). The Role of Nanoscale Toughening Mechanisms in Osteoporosis. Curr Osteoporos Rep. 12(3):351-356.

Knudson D. (2007). Fundamentals of Biomechanics. Springer. pp 73.

Lefèvre E., Guivier-Curien C., Pithioux M., Charrier A. (2013). Determination of mechanical properties of cortical bone using AFM under dry and immersed conditions. Computer Methods in Biomechanics and Biomedical Engineering 2013, 16(1).

Leng H., Reyes M.J., Dong N.X., Wang X. (2013). Effect of Age on mechanical properties of the collagen phase in different orientations of human cortical bone. Bone 2013, 55(2):288-291.

Marshall D., Johnell O., Wedel H. (1996). Meta-analysis of how well measures of bone mineral density predict occurrence of osteoporotic fractures. BMJ 1996, 312:1254–1259.

Mirzaali M.J., Schwiedrzik J.J., Thaiwichai S., Best J.P., Michler J., Zysset P.K., Wolfram U. (2016). Mechanical properties of cortical bone and their relationships with age, gender, composition and microindentation properties in the elderly. Bone 2016, 93:196–211.

Morris V.J., Kirby A.R., Gunning A.P. (2009). Atomic Force Microscopy for Biologists. 2009. ISBN: 9781908978219.

Naik N., Caves J., Chaikof E., Allen M.G. (2014). Generation of spatially aligned collagen fiber networks through microstransfer molding. Adv. Healthc. Mater., 3:367-374.

Nalla R.K., Kruzic J.J., Kinney J.H., Balooch M., Ager III J.W., Ritchie R.O. (2006). Role of microstructure in the aging-related deterioration of the toughness of human cortical bone. Mater Sci. Eng. C 2006, 26:1251–1260.

Nudelman F., Pieterse K., George A., Bomans PH., Friedrich H., Brylka LJ., Hilbers PA., De With G., Sommerdijk NA. (2010). The role of collagen in bone apatite formation in the presence of hydroxyapatite nucleation inhibitors. Natural Material 2010, 9(12):1004-9.

Nyman J.S., Roy A., Tyler J.H., Acuna R.L., Gayle H.J., Wand X. (2007). Age-related factors affecting the post-yield energy dissipation of human cortical bone. J. Prthop Res. 2007, 25(5):646-655.

Ohler B. (2007). Practical Advice on the Determination of Cantilever Spring Constants. Veeco Instruments Inc.

Osterhoff G., Morgan E.F., Shefelbine S.J., Karim L., McNamara L.M., Augat P. (2016). Bone mechanical properties and changes with osteoporosis. Injury, Int. J. Care Injured 47S2, 2016, 11-20.

Parfitt A.M. (1980). Morphologic basis of bone mineral measurements: Transient and steady state effects of treatment in osteoporosis. Mineral and Electrolyte Metabolism1980, 4(6):273-287.

Preibisch S., Saalfeld S., Tomancak P. (2009). Globally optimal stitching of tiled 3D microscopic image acquisitions, Bioinformatics, 25(11):1463-1465.

Prentice A.I.D. (1967). Autofluorescence of bone tissues. J. clin. Path. 1967, 20:717.

Reilly D.T., Burstein A.H., Frankel V.H. (1974). The elastic modulus for bone. J. Biomechanics. 1974, 7:271–275.

Reifenberger R.G., Baró A.M. (2012). Atomic force microscopy in liquid: biological applications. Wiley-VCH Verlag GmbH.

Rho J.Y., Kuhn-Spearing L., Zioupos P. (1998). Mechanical properties and the hierarchical structure of bone, Medical Engineering and Physics 1998, 20:92-102.

Rho J.Y., Tsui T.Y., Pharr G.M. (1997). Elastic properties of human cortical and trabecular lamellar bone measured by nanoindentation, Biomaterials 1997, 18: 1325-1330.

Rho J.Y., Zioupos P., Currey J.D., Pharr G.M. (2002). Microstructural Elasticity and Regional Heterogeneity in Human Femoral Bone of Various Ages Examined by Nano-Indentation. Journal of Biomechanics 2002, 35:189-198.

Rho J.Y., Zioupos P., Currey J.D., Pharr G.M. (1999). Variations in the individual thick lamellar properties within osteons by nanoindentation. Bone 1999, 25:295-300.

Sader J.E., Chon J.W.M., Mulvaney P. (1999). Calibration of rectangular atomic force microscope cantilevers. *Rev. Sci. Instrum.*, 70(10):3967 – 3969.

Schaffler M.B., Radin E.L., Burr D.B. (1990). Long-term fatigue behaviour of compact bone at low strain magnitude and rate. Bone 1990, 11:321-326.

Schneider D.L. (2008). Management of osteoporosis in geriatric populations. Current Osteoporosis Reports. 2008; 6:100-107.

Schrof S., Varga P., Galvis L., Raum K., Masic A. (2014). 3D Raman mapping of the collagen fibril orientation in human osteonal lamellae. Journal of Structural Biology, 187(3), 266-275.

Schürmann S., Wegner F., Fink R., Friedrich O., Vogel M. (2010). Second Harmonic Generation Microscopy Probes Different States of Motor Protein Interaction in Myofibrils. Biophysics J. 99(6): 1842-1851.

Seeman E. (2008). Bone Quality: The Material and Structural Basis of Bone Strength. Journal of Bone and Mineral Metabolism 2008, 26(1):1-8.

Spiesz E.M., Reisinger A.G., Kaminsky W., Roschger P., Pahr D.H, Zysset P.K. (2013). Computational and experimental methodology for site-matched investigations of the influence of mineral mass fraction and collagen orientation on the axial indentation modulus of lamellar bone. Journal Mechanical Behaviour Biomed Mater. 2013; 195-205.

Siris E.S., *et al.* (2004). Bone mineral density thresholds for pharmacological intervention to prevent fractures. Arch. Intern. Med. 164 (10):1108–1112.

Stampfl J., Koch T. (2011). Bruchmechanik. TU Wien, SS 308.120.

Strupler M., Pena A.-M, Hernest M., Tharaux P.-L., Martin J.-L., Beaurepaire E., Schanne-Klein M.-C. (2007). Second harmonic imaging and scoring of collagen in fibrotic tissues. Opt. Express, 15:4054-4065.

Tai K., Dao M., Suresh S., Palazoglu A., Ortiz C. (2004). Nanoscale heterogeneity promotes energy dissipation in bone.

Thévenaz P., Unser M. (2007). User-Friendly Semiautomated Assembly of Accurate Image Mosaics in Microscopy. Microscopy Research and Technique 2007, 70(2): 135-146.

Thurner P.J. (2009). Atomic Force Microscopy and indentation force measurements of bone. Wiley Interdisciplinary Reviews: Nanomedicine and Nanobiotechnology 2009, 1(6):624–649.

Turner C.H. (1989). Yield behaviour of cancellous bone. J. Biomech. Eng. 111:1-5.

Turner C.H., Takano Y., Tsui T.Y., Pharr G.M. (1999). The elastic properties of trabecular and cortical bone tissues are similar: results from two microscopic measurement techniques. J. Biomech., 1999, 32:437.

Vaz M.F., Canhao H., Fonseca J.E. Bone: A Composite Natural Material. ICEMS and Mechanical Engineering Department, Instituto Superior Técnico, Technical University of Lisbon, Rheumatology Research Unit, Instituto de Medicina Molecular, Faculty of Medicine, University of Lisbon and Rheumatology Department, Santa Maria Hospital, Lisbon, Portugal.

Vinckier A., Semenza G. (1998). Measuring elasticity of biological materials by atomic force microscopy. Federation of European Biochemical Societies 1998, 430:12-16.

Williamson S., Landeiro F., McConnell T., Fulford-Smith L., Javaid M.K., Judge A., Leal J. (2017). Costs of fragility hip fractures globally: a systematic review and meta-regression analysis. Osteoporos Int, 28:2791-2800.

Wegst U., Bai H., Saiz E., Tomsia A.P., Ritchie R.O. (2015). Bioinspired structural materials. Nature materials 2015, 14:23-36.

WHO. (1994). Assessment of fracture risk and its application to screening for postmenopausal osteoporosis. Report of a WHO Study Group. Geneva, World Health Organization, 1994 (WHO Technical Report Series, No. 843).

Wenger M., Bozec L., Horton M., Mesquida P. (2007). Mechanical properties of collagen fibrils. Biophysical Journal 93:1255-1263

Wolff J. (1892). Das Gesetz der Transformation der Knochen. Berlin: Springer-Verlag.

Yan J., Mecholsky J.J., Clifton K.B. (2007). How tough is bone? Application of elastic-plastic fracture mechanics to bone. Bone 2007, 40:479-484.

Zimmermann, A.E., Busse B., Richie O.R. (2015). The fracture mechanics of human bone: influence of disease and treatment. Bonekey Rep. 4:743.

Zioupos P., Currey J.D. (1998). Changes in the stiffness, strength, and toughness of human cortical bone with age. Bone 1998, 22(1):57-66.

Zysset P.K., Guo X.E., Hoffler C.H., Moore K.E., Goldstein S.A. (1998). Mechanical properties of human trabecular bone lammellae quantified by nanoindentation. Technol. Health Care 1998, 6:429.

Zysset P.K., Guo X.E., Hoffler C.H., Moore K.E., Goldstein S.A. (1999). Elastic Modulus and hardness of cortical and trabecular bone lamellae measured by nanoindentation in the human femur, J. Biomech., 1999, 32:1005.

Appendix

Annex i: Optical Microscope Images

N1A: 25 M (0170910354R)

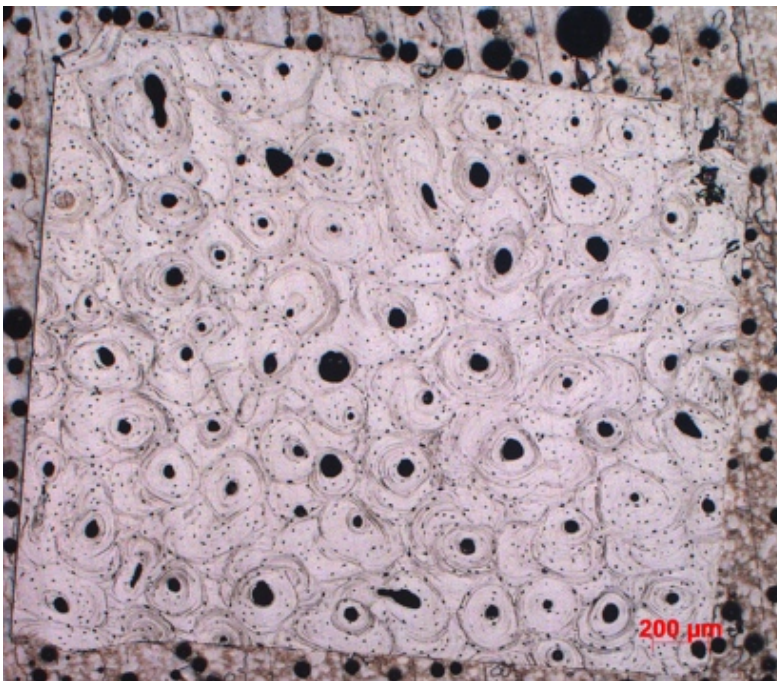

N1B: 53 F (2383854L)

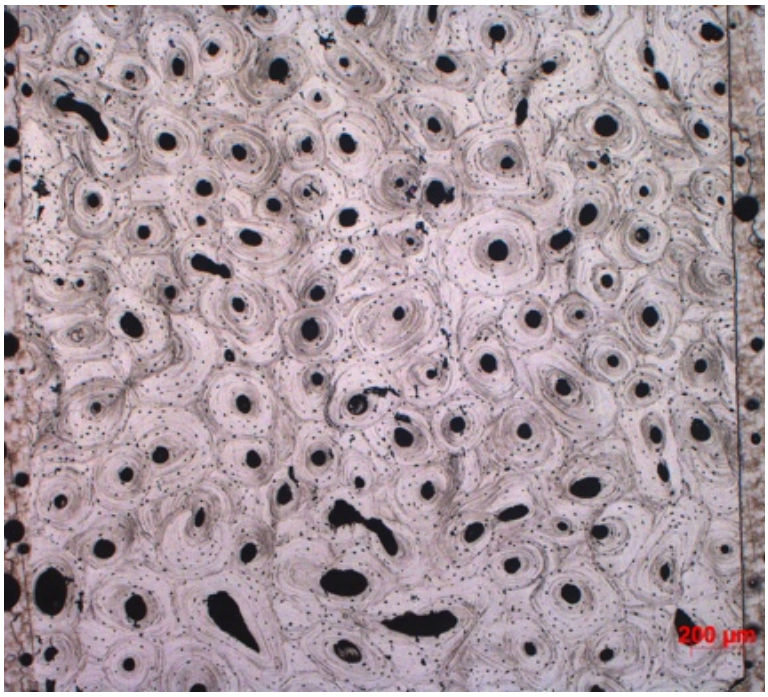

N1C: 60 F (0781204098L)

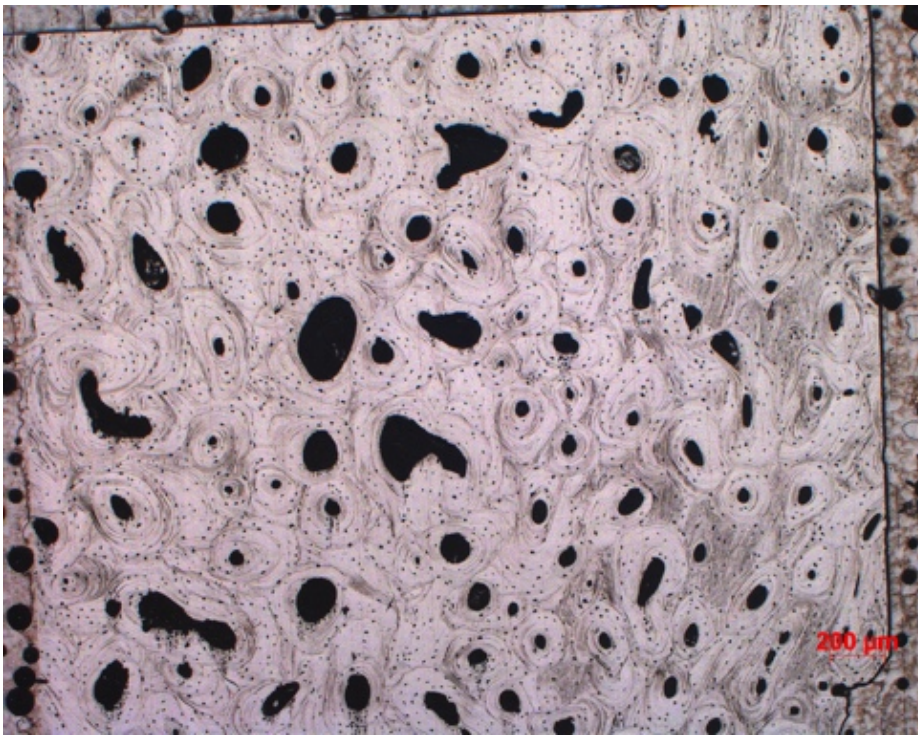

N1D: 74 M (6200L)

N1E: 89 F (6557L)

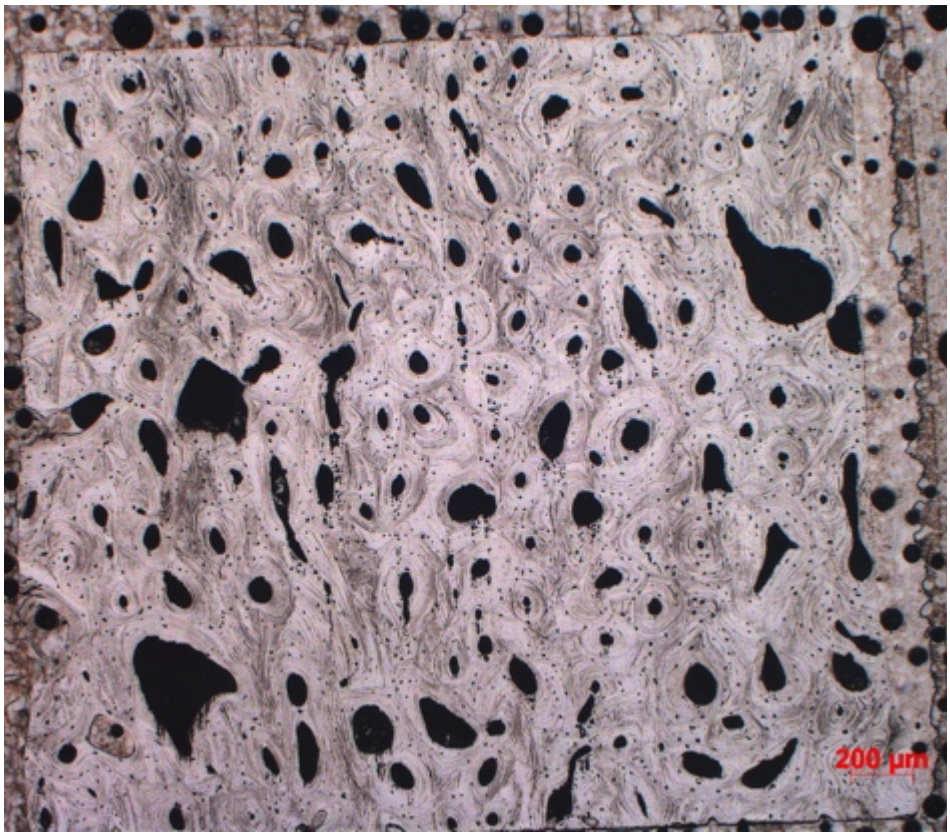

N2A: 32 F (290903379L)

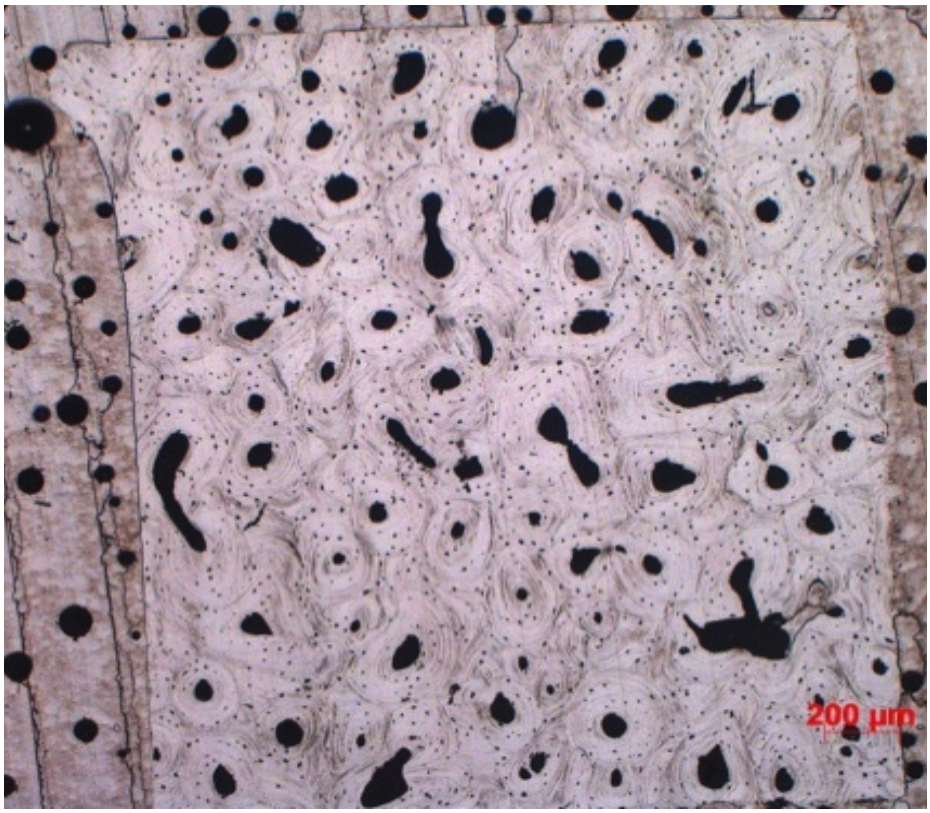

N2B: 54 F (0031205143L)

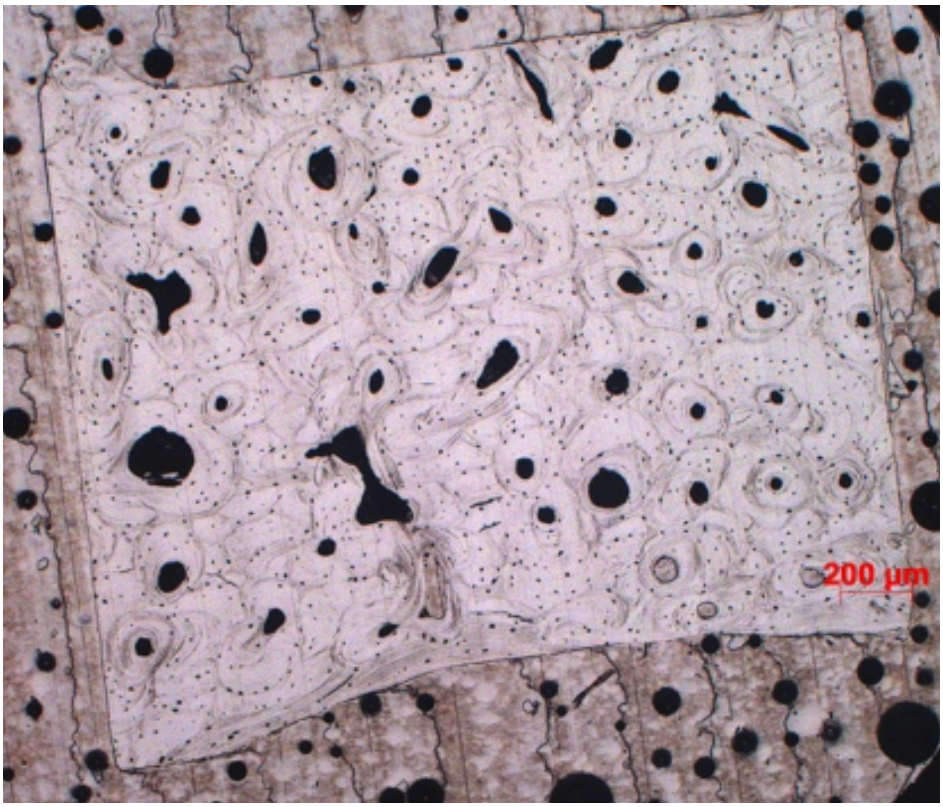

N2C: 63 F (0941207926L)

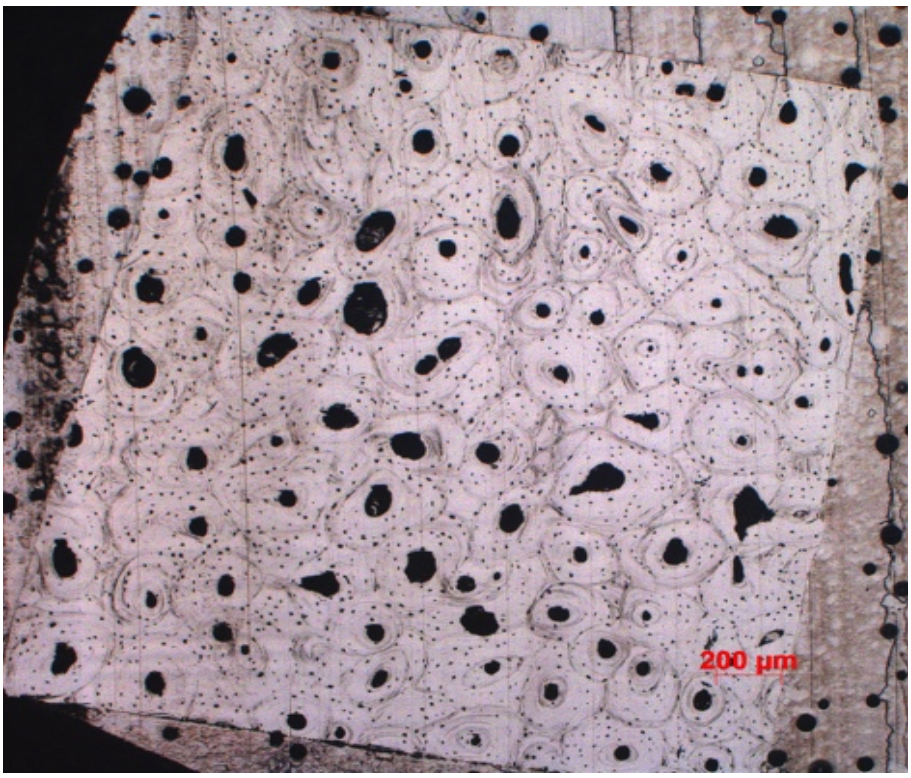

N2D: 81 F (6562R)

N2E: 94 F (6456L)

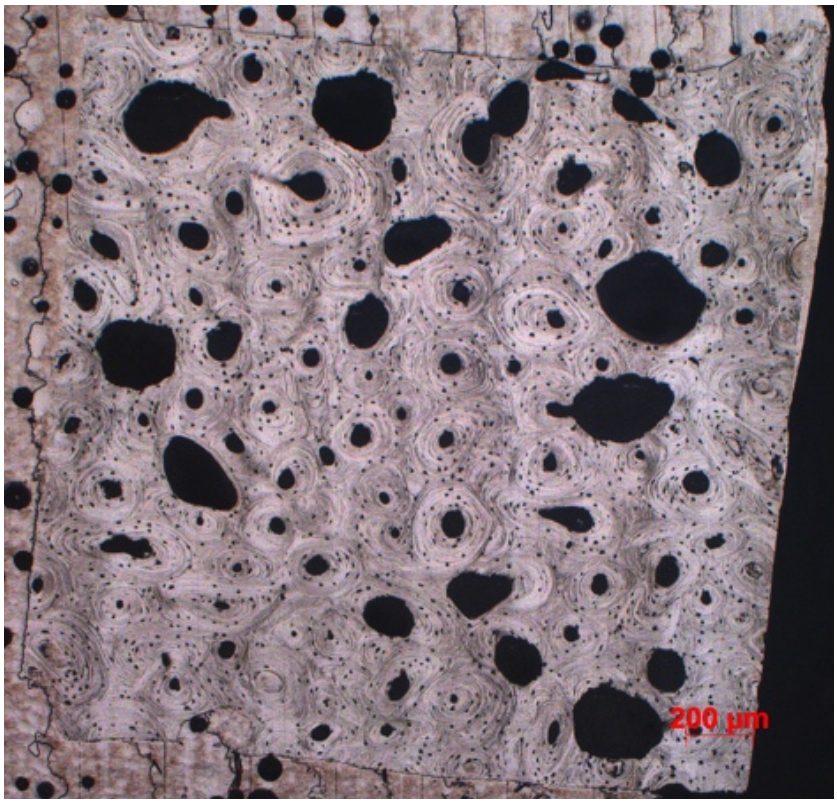

N3**A: 47 F (0231204243R)**

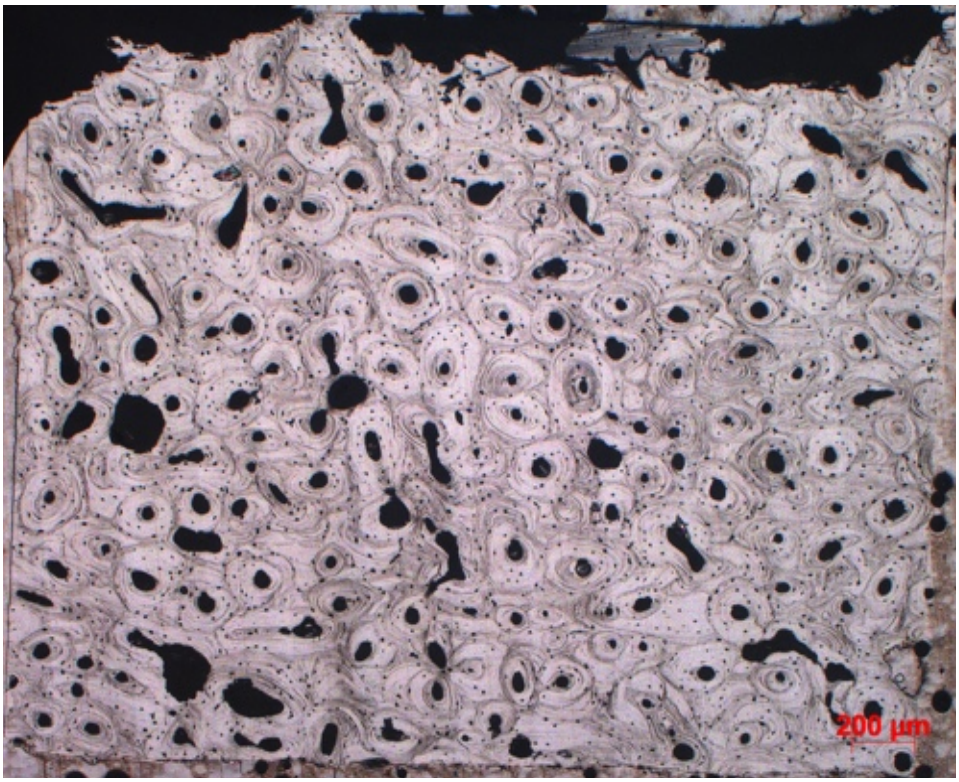

N3B: 58 F (0271205510R)

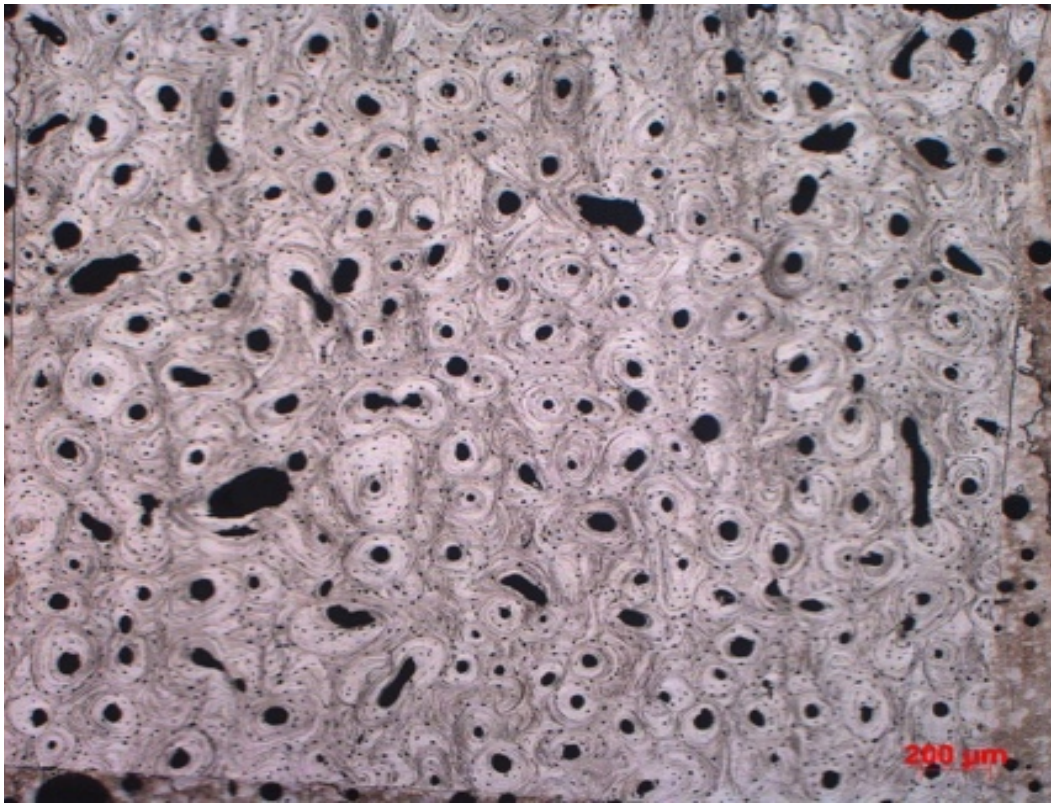

N3C: 69 F (6129R)

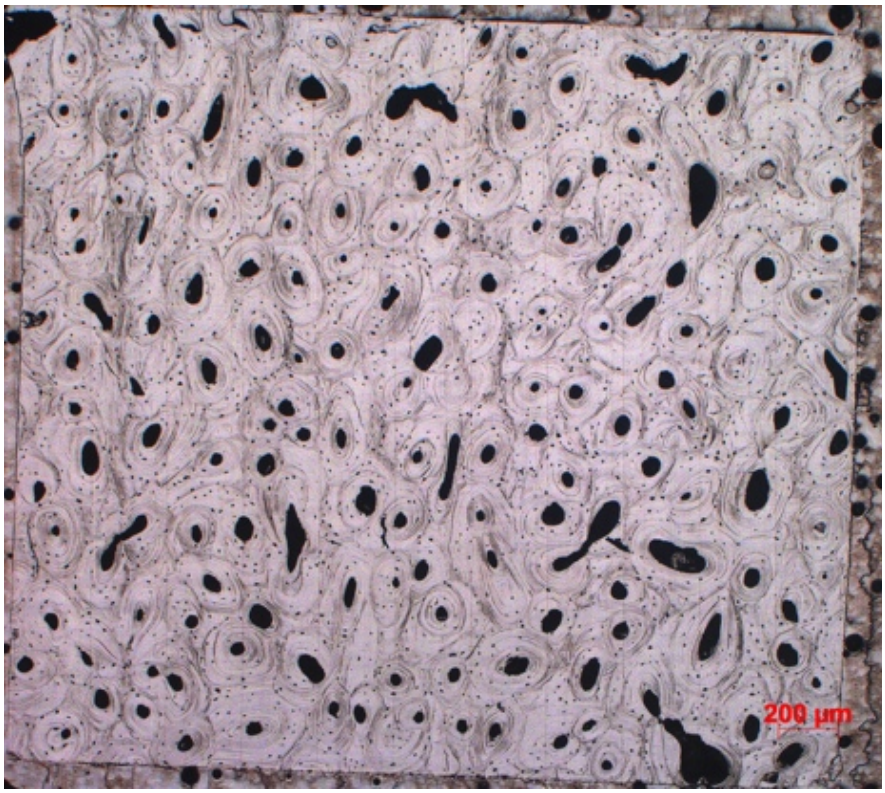

N3D:85 F (6568L)

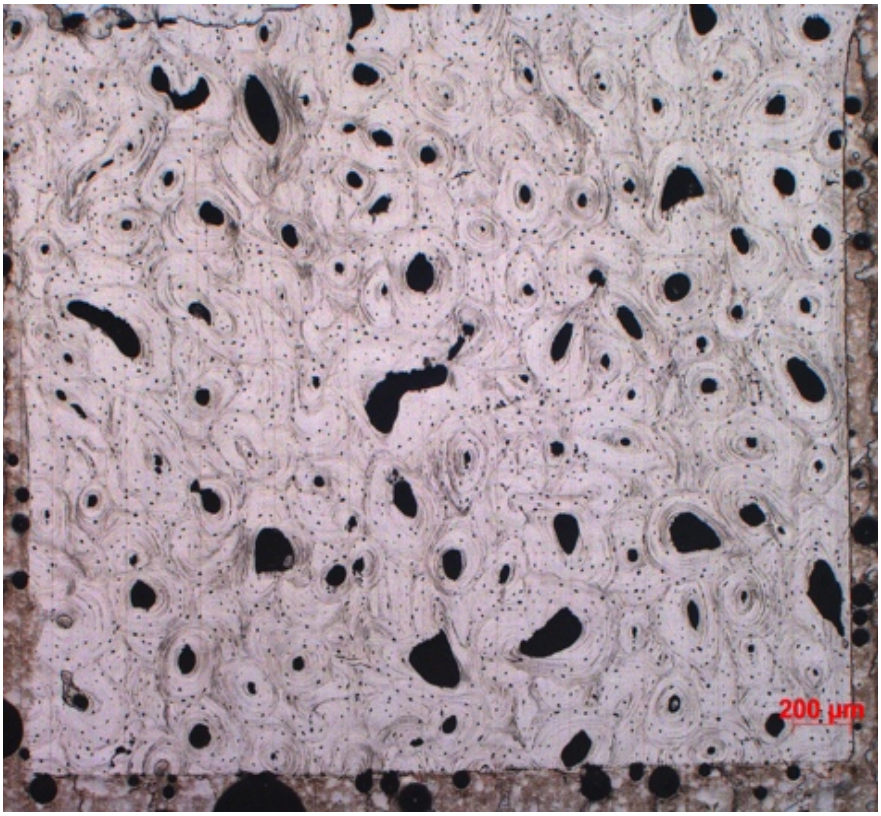

N3E:101 F (6434R)

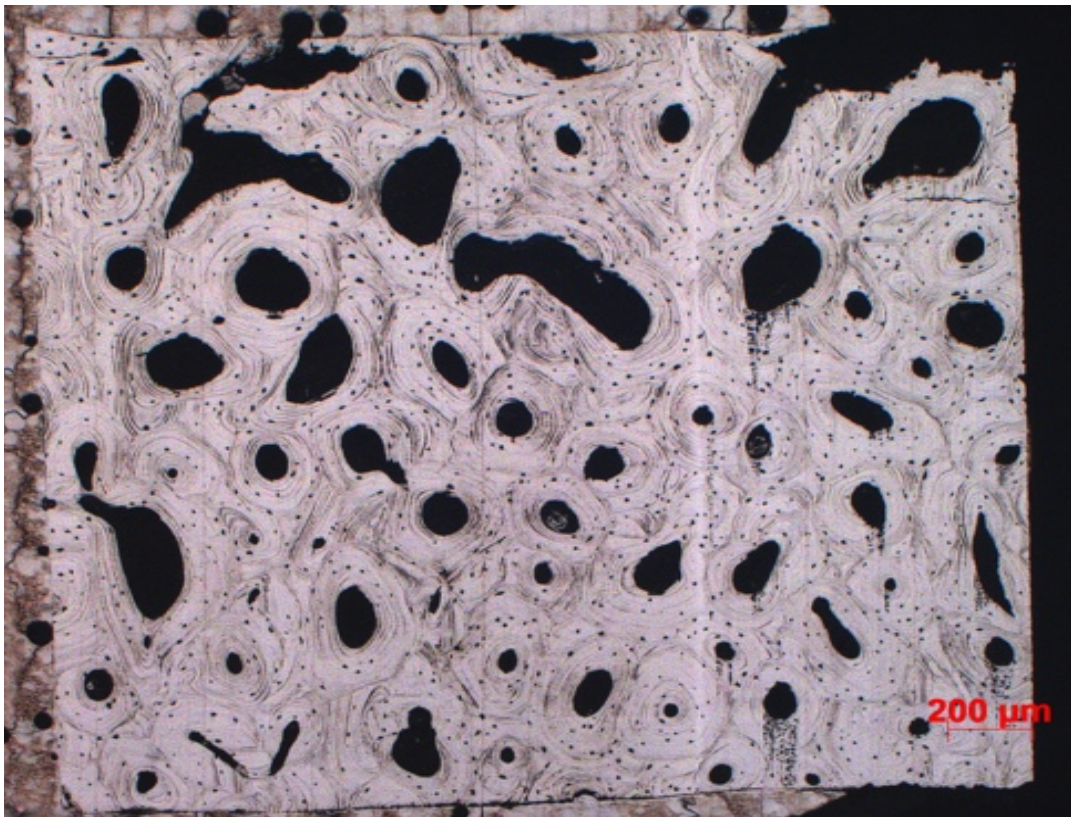

S1A

S1B:

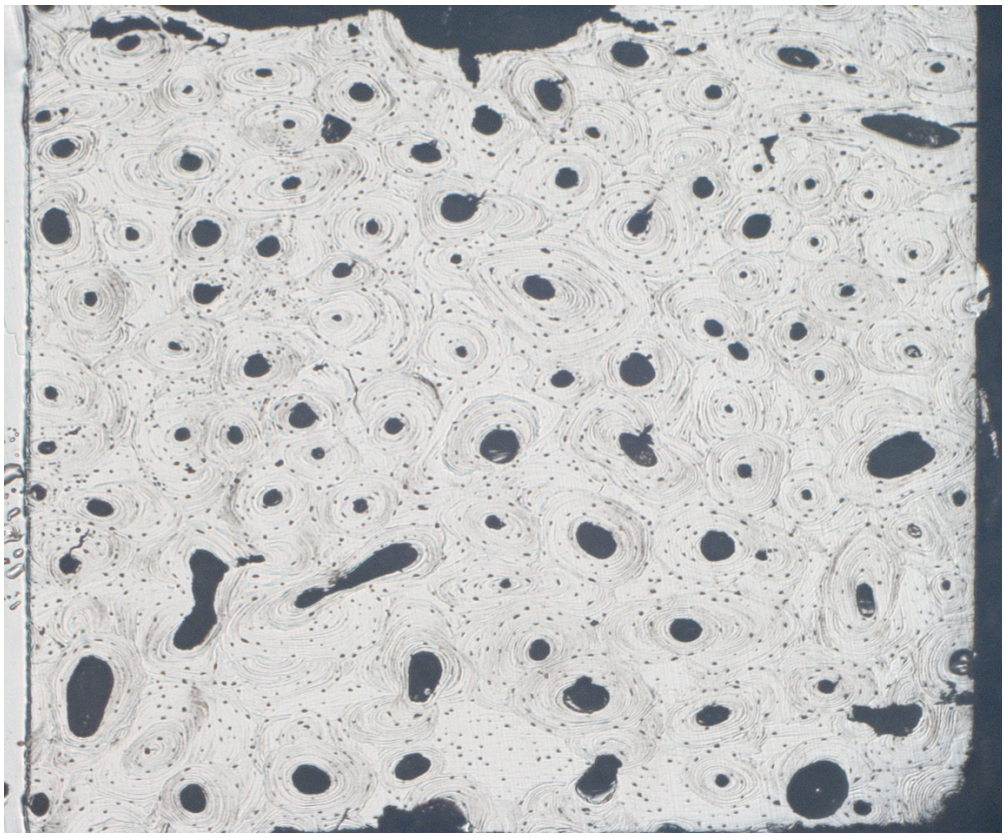

S1C:

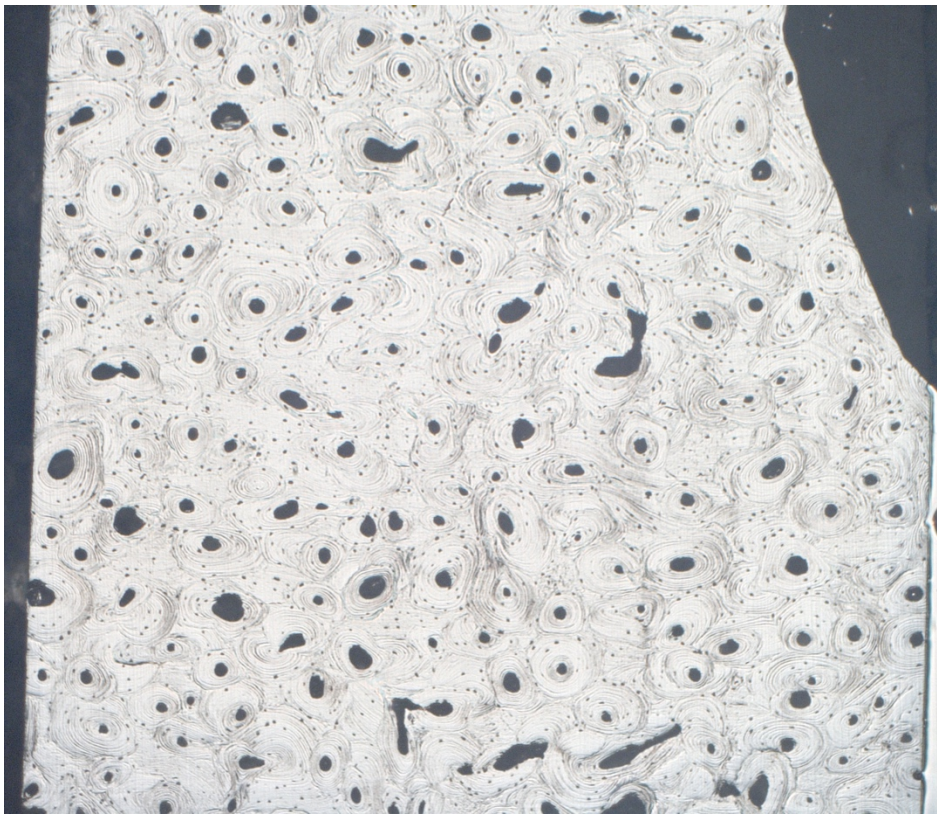

S1D:

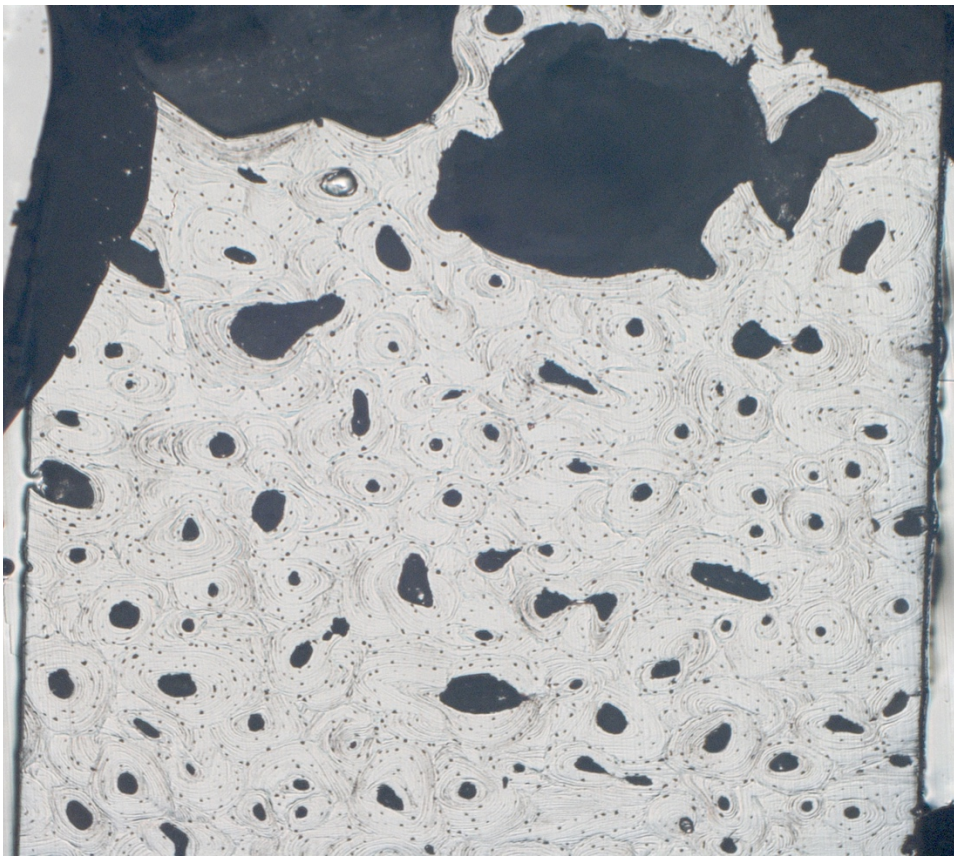

S1E:

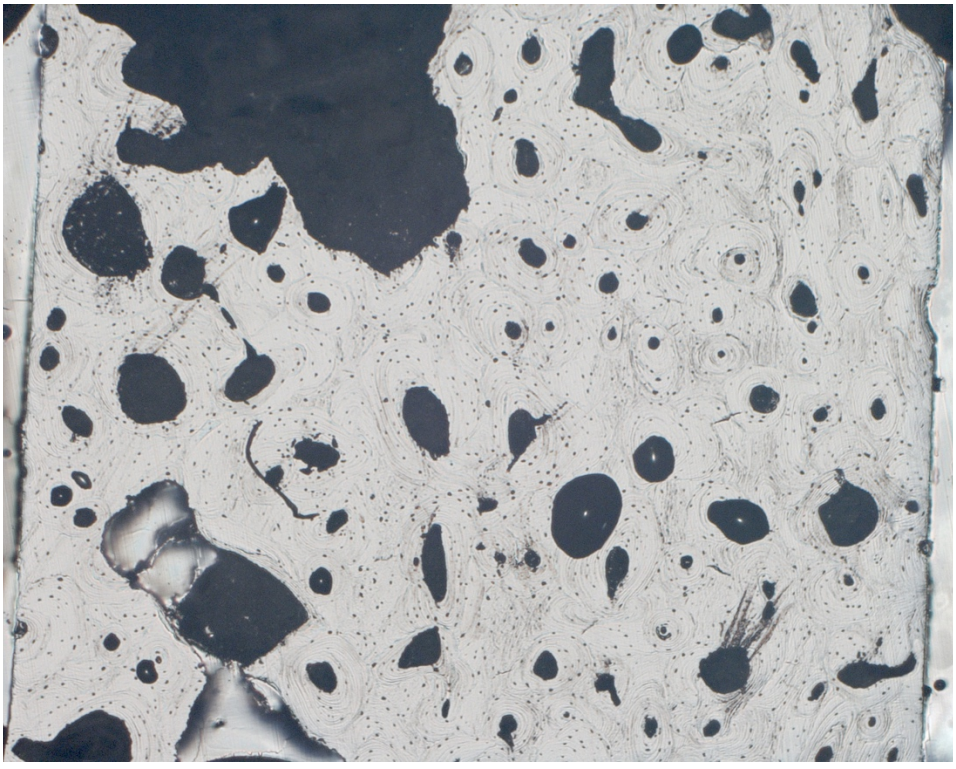

S2A:

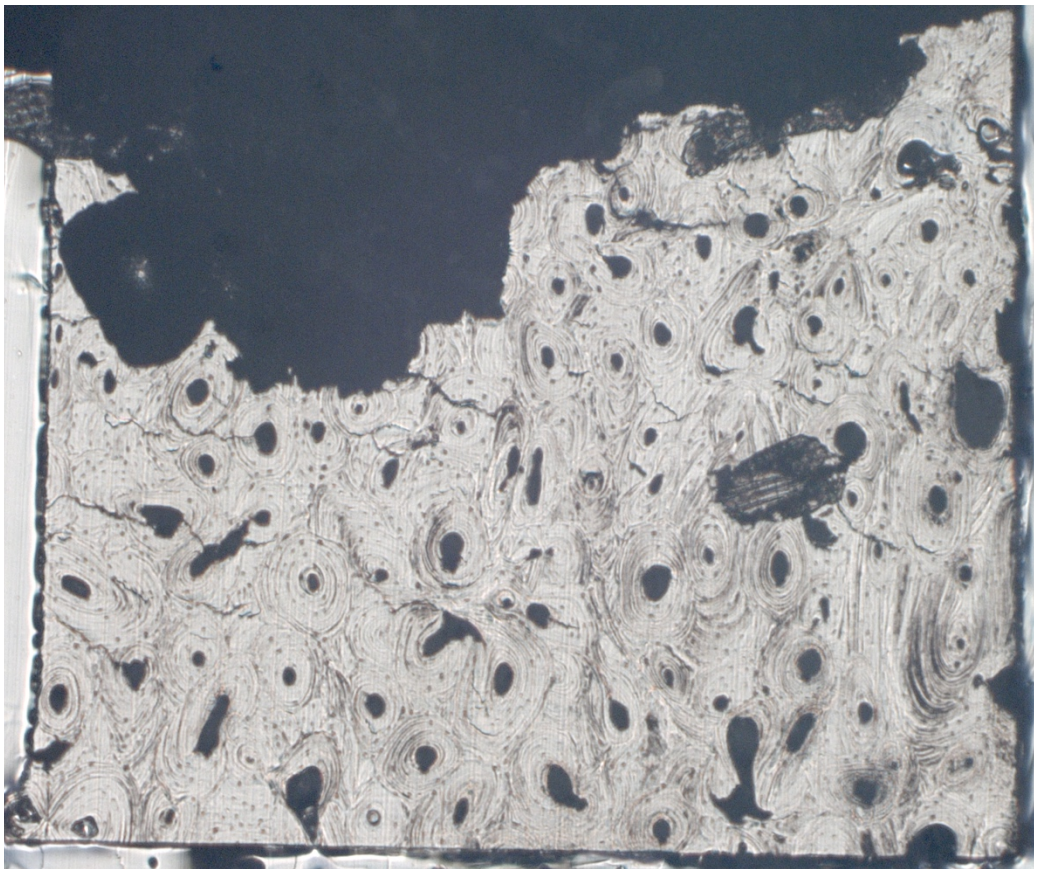

S2B:

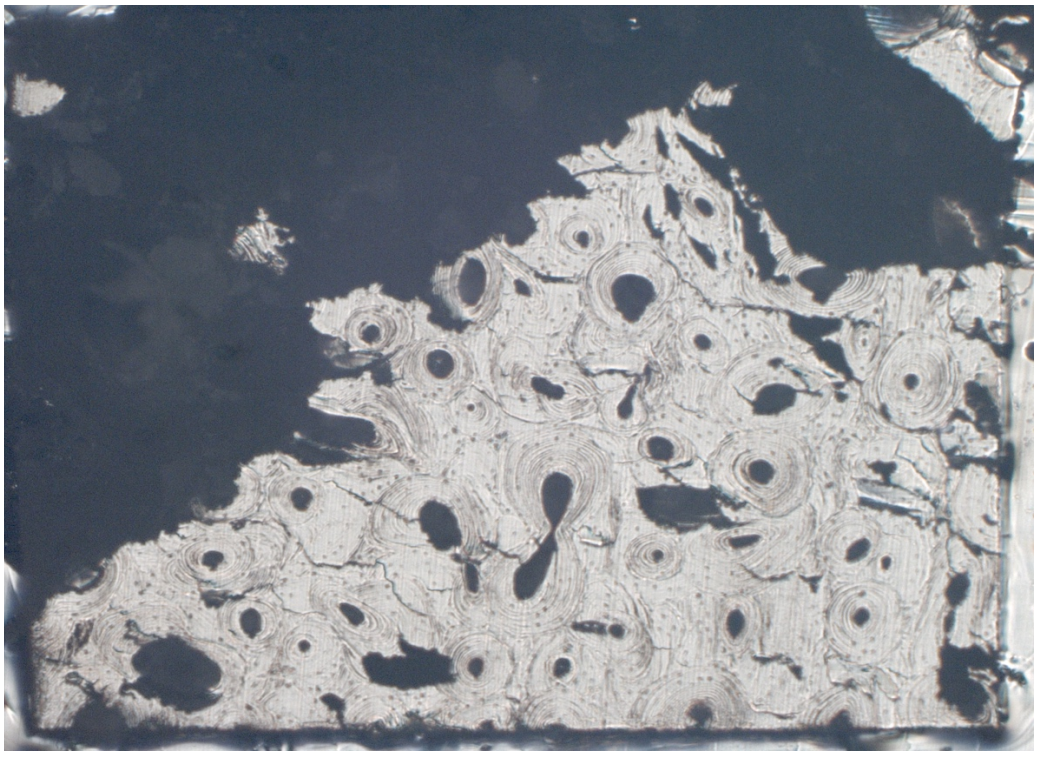

S2C:

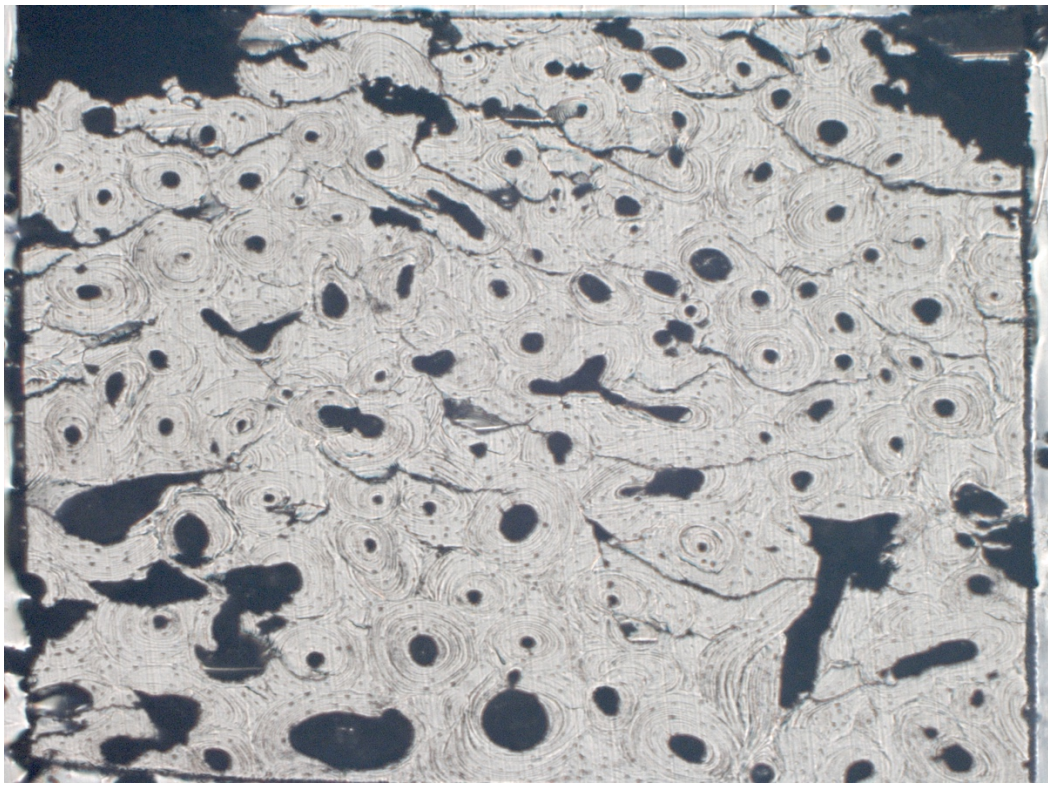

S2D:

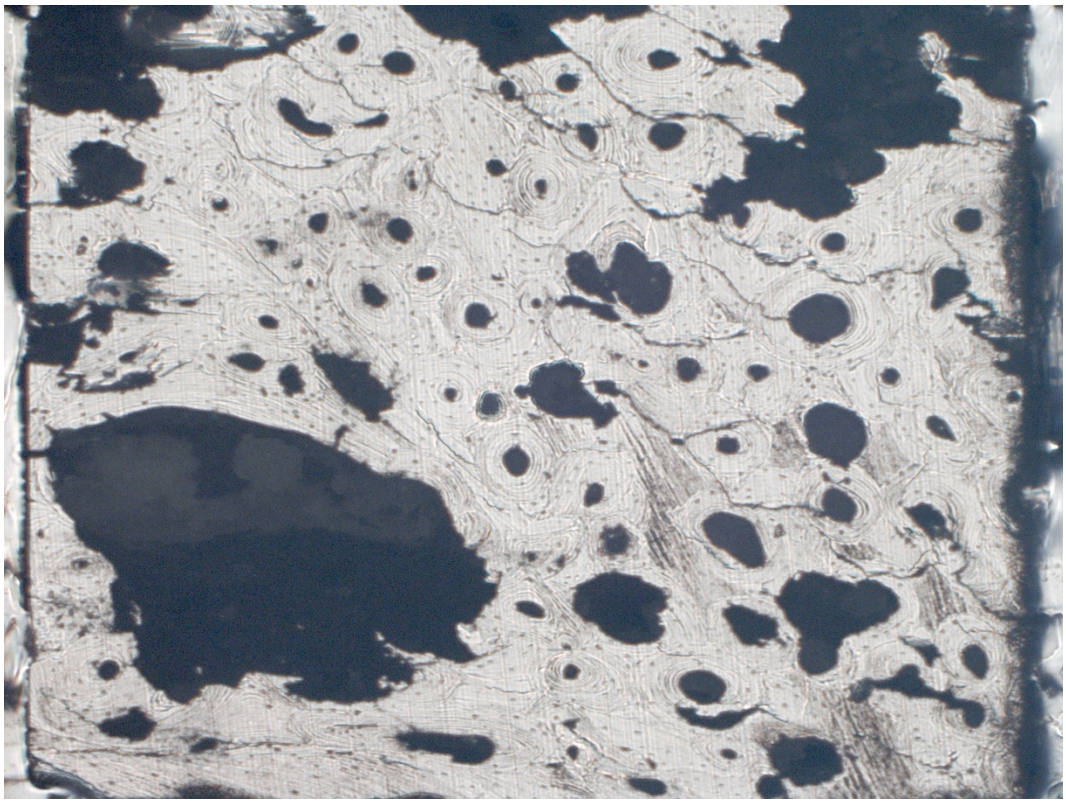

S2E:

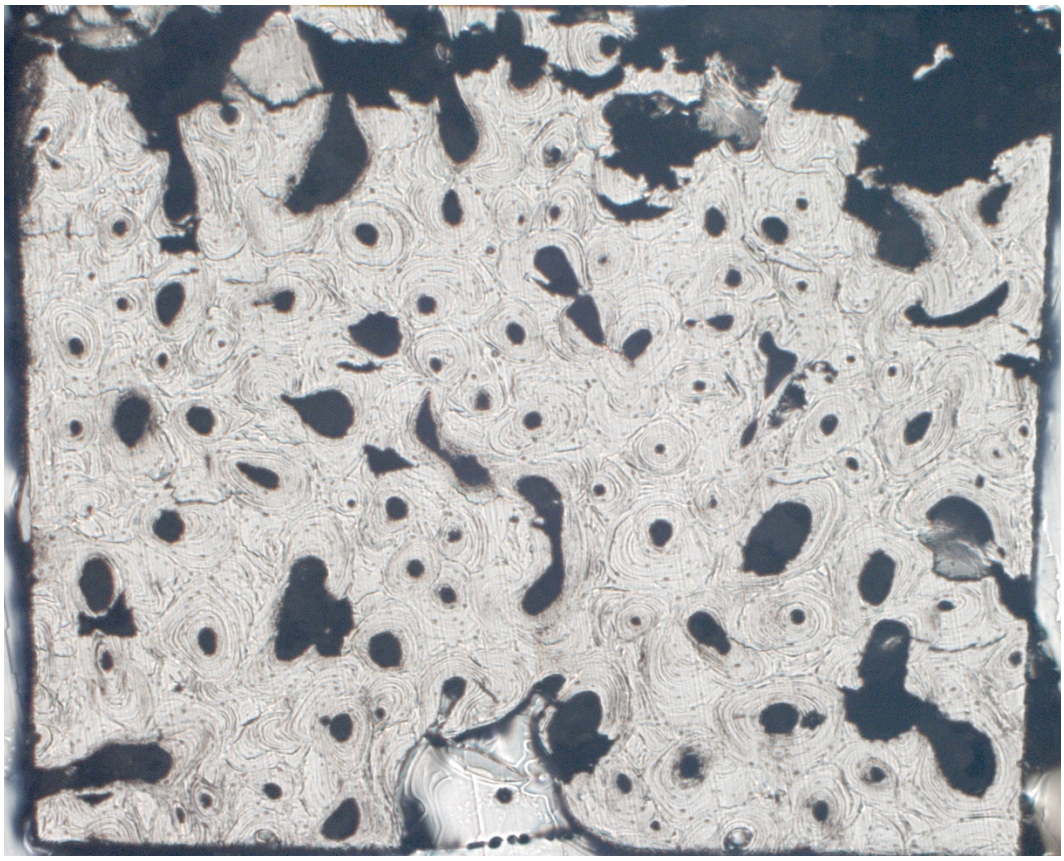

S3A:

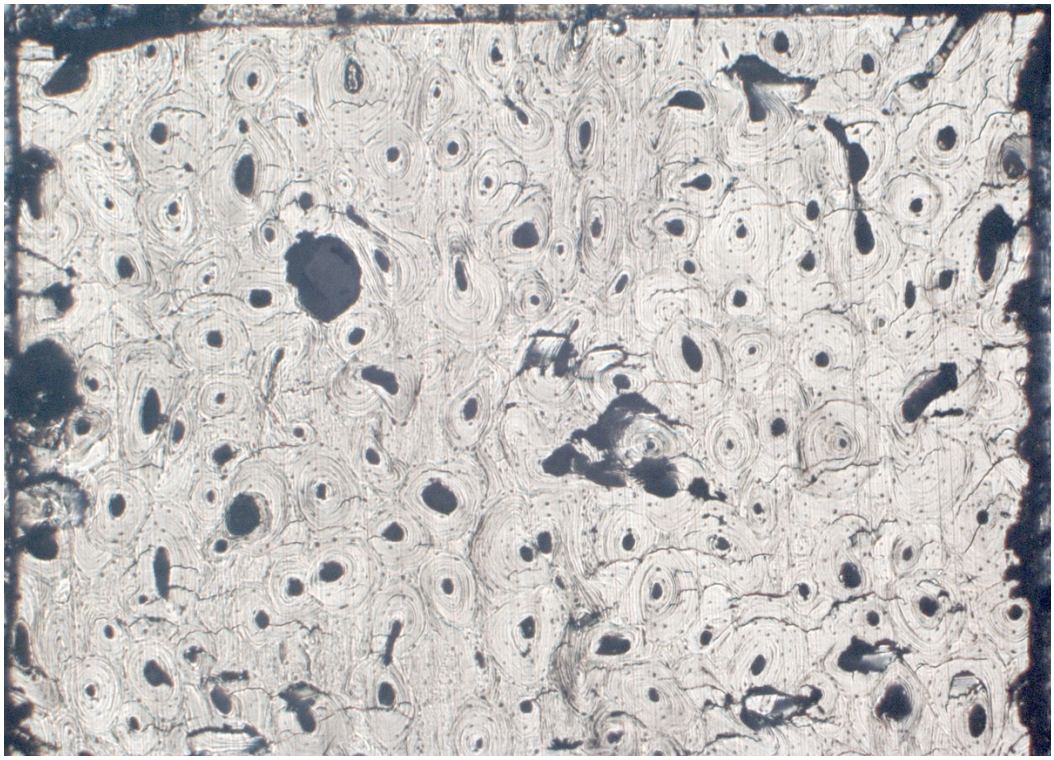

S3B:

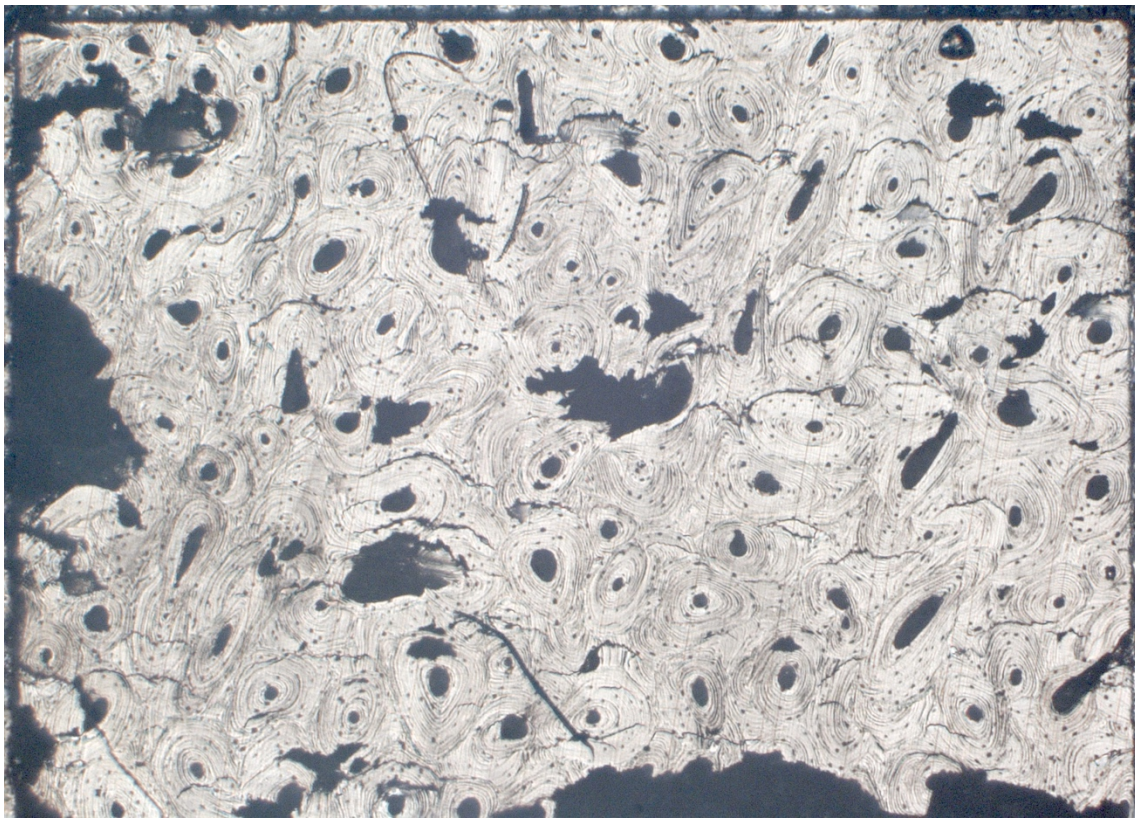

S3C:

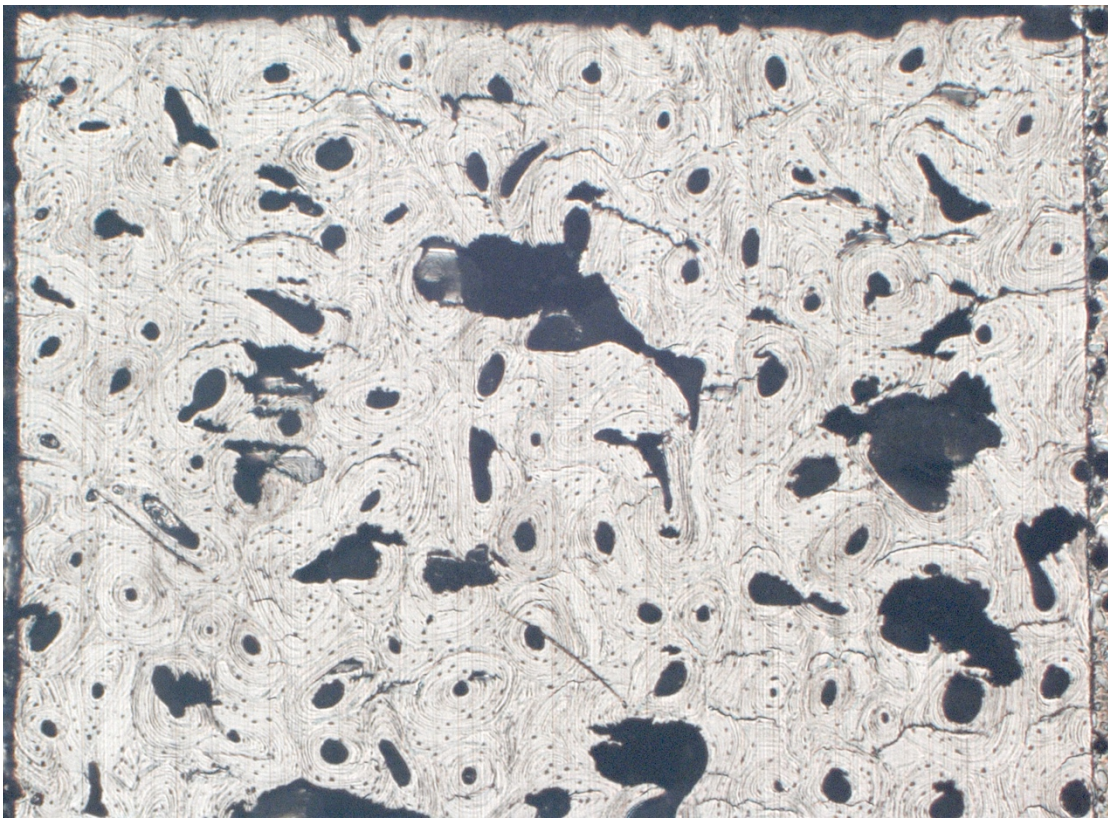

S3D:

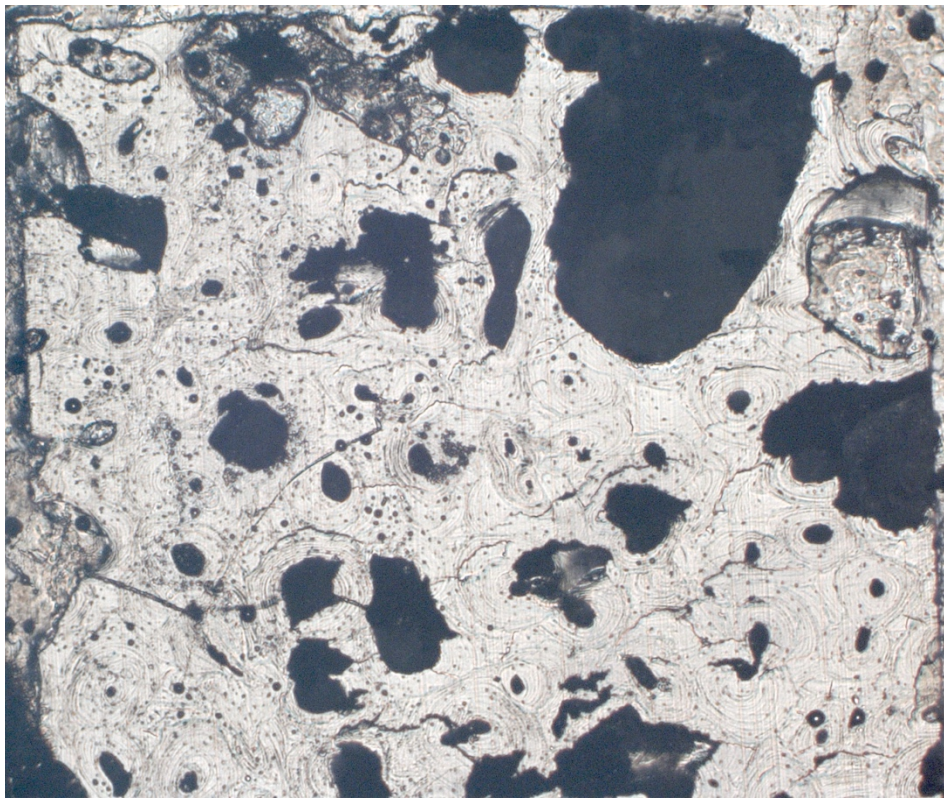

S3E:

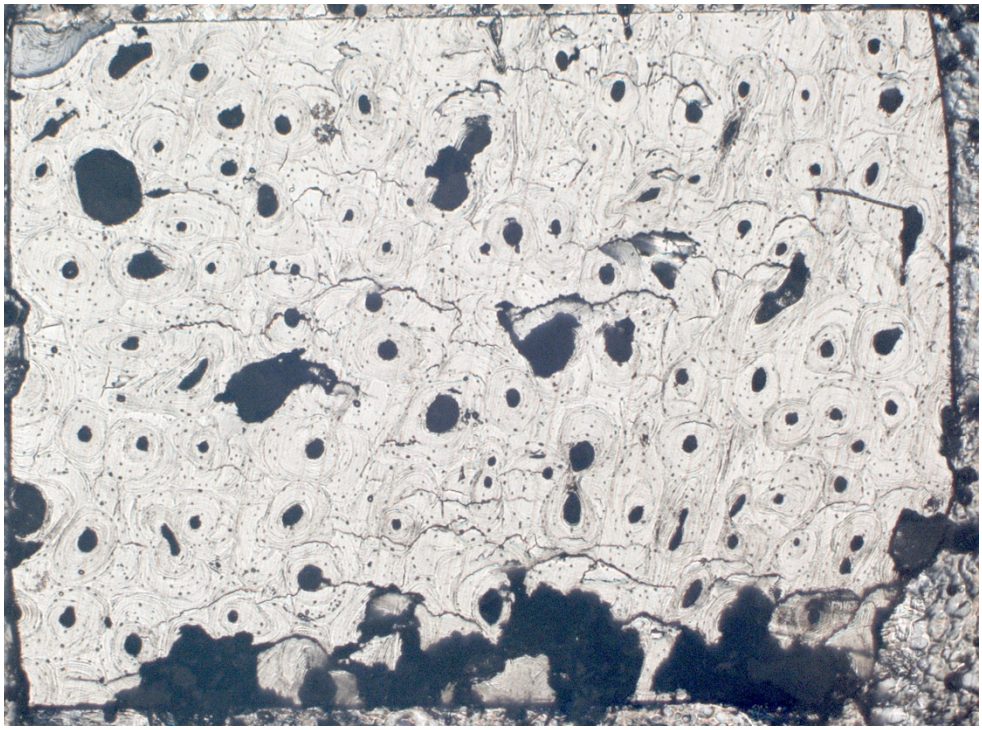

Annex ii: SHG Microscope Images

N1A:

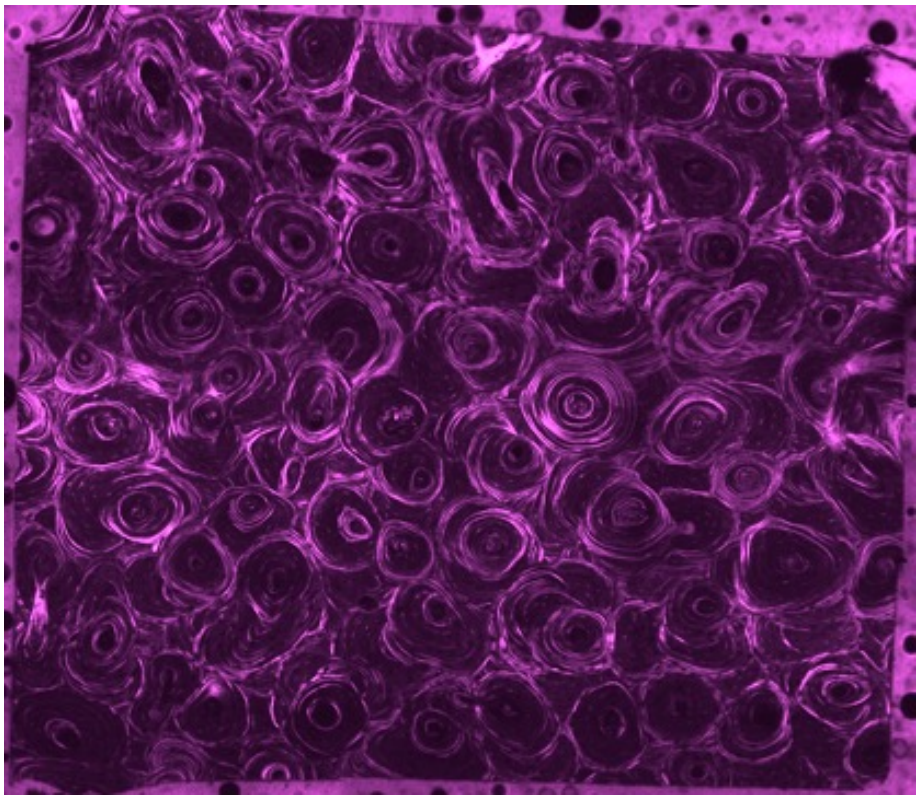

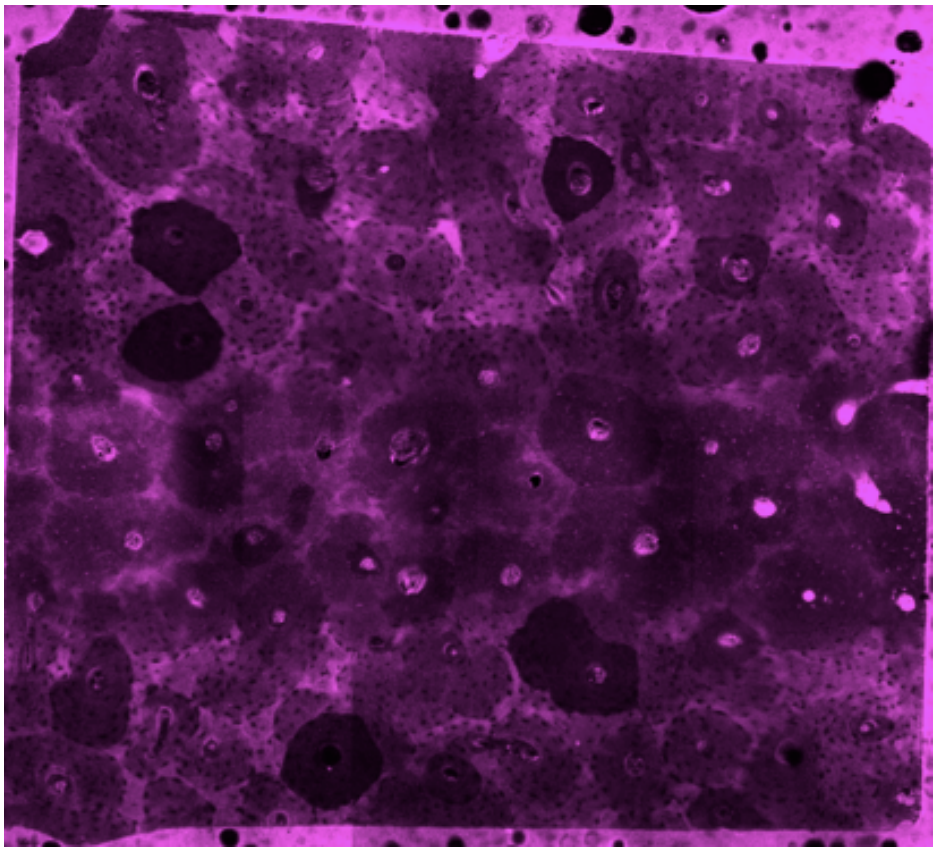

N1C:

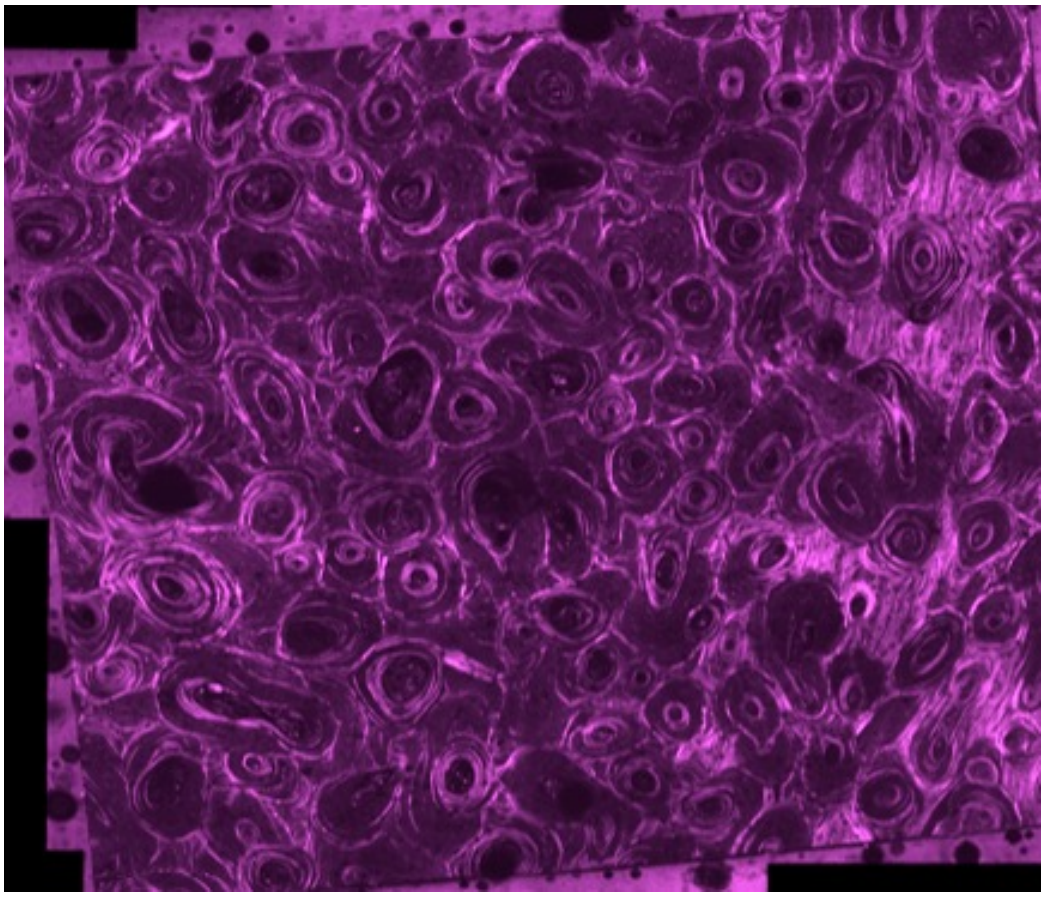

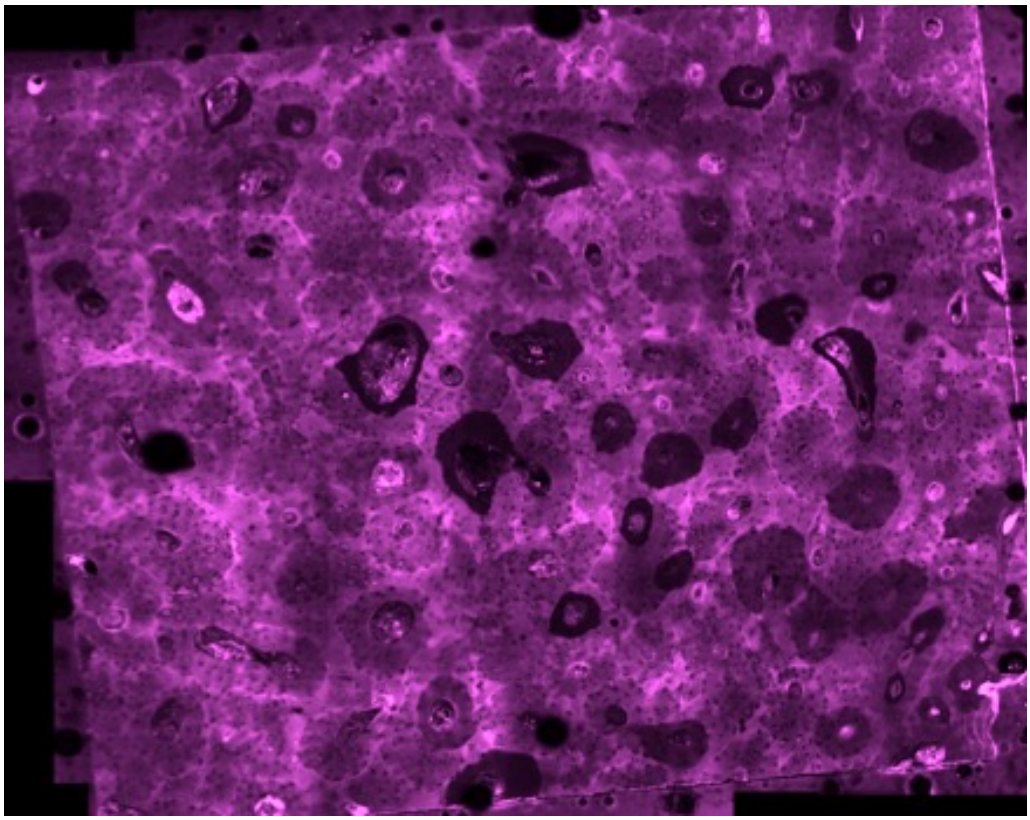

N1D:

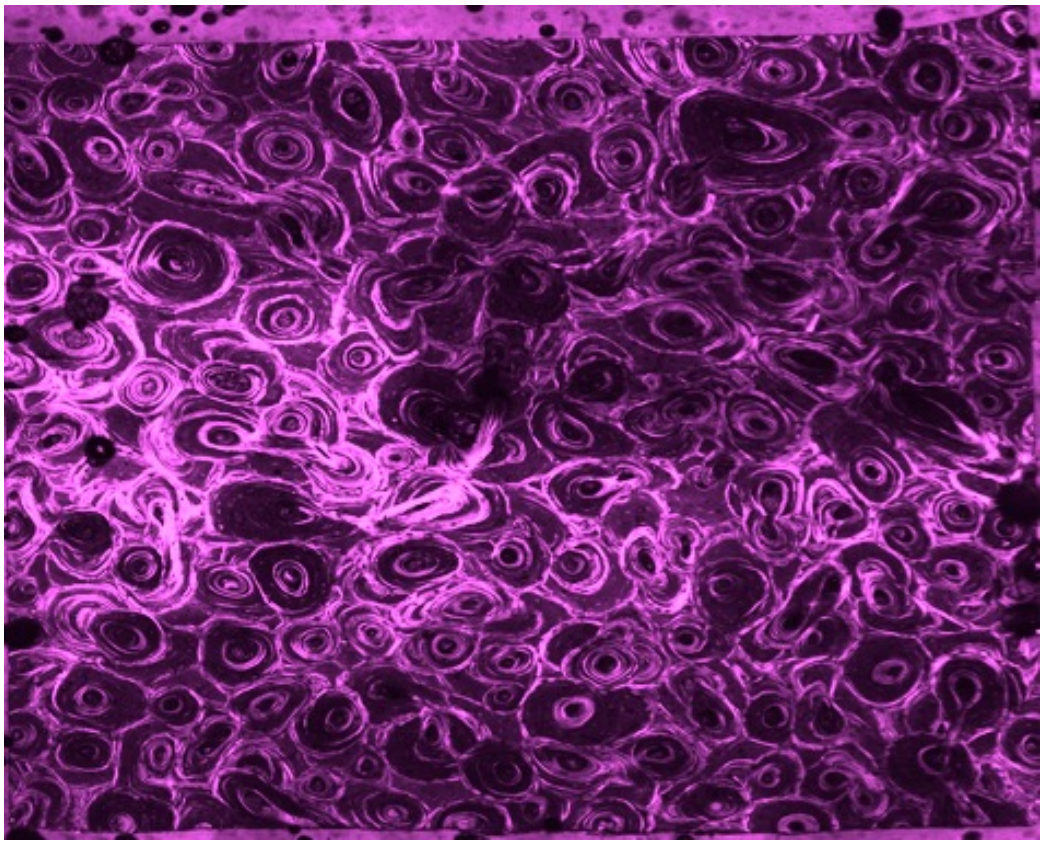

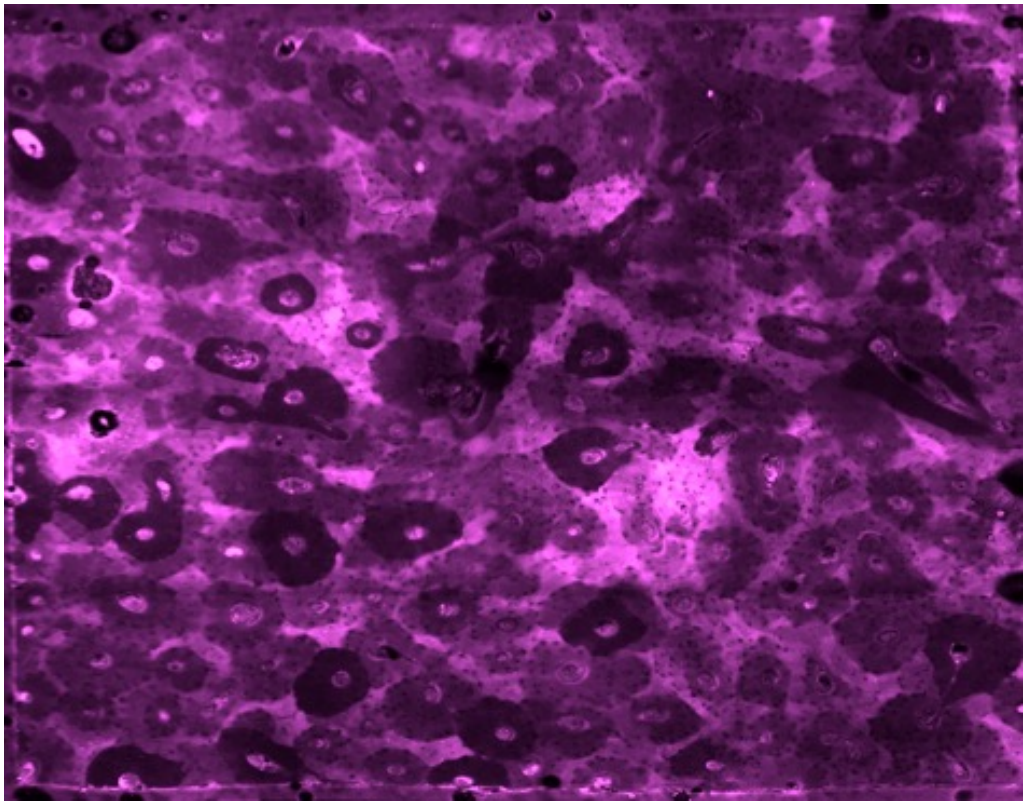

N1E:

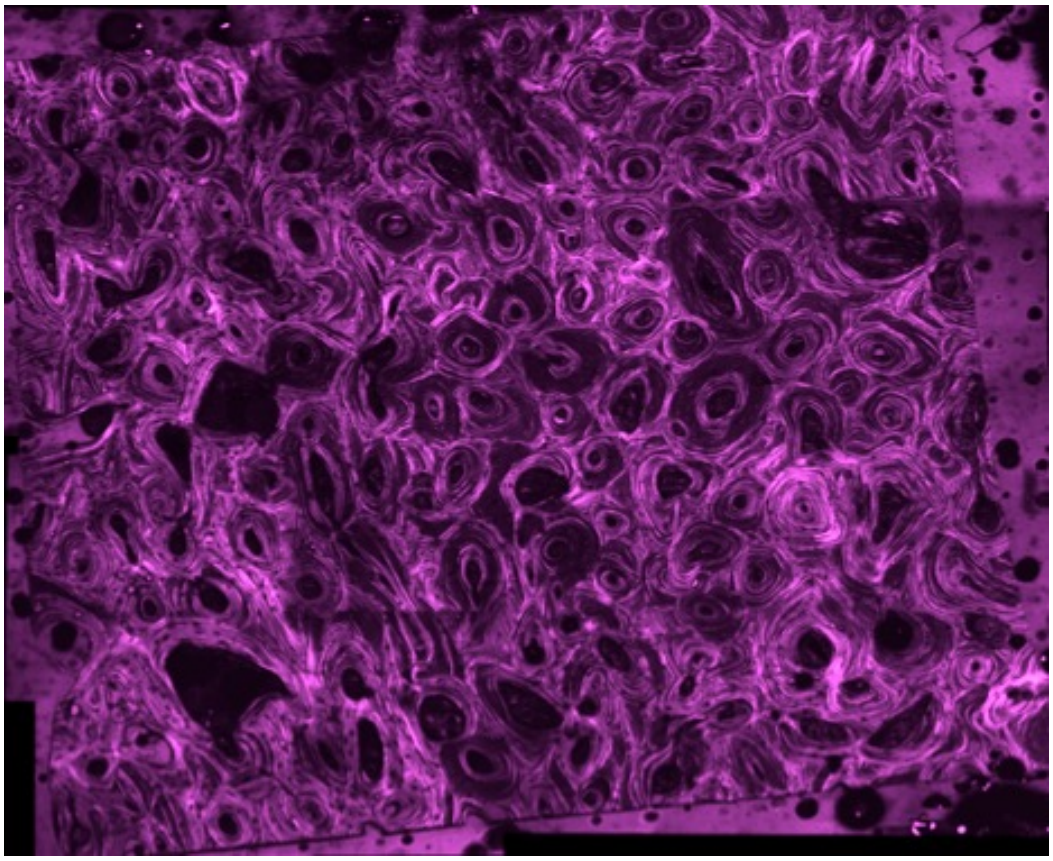

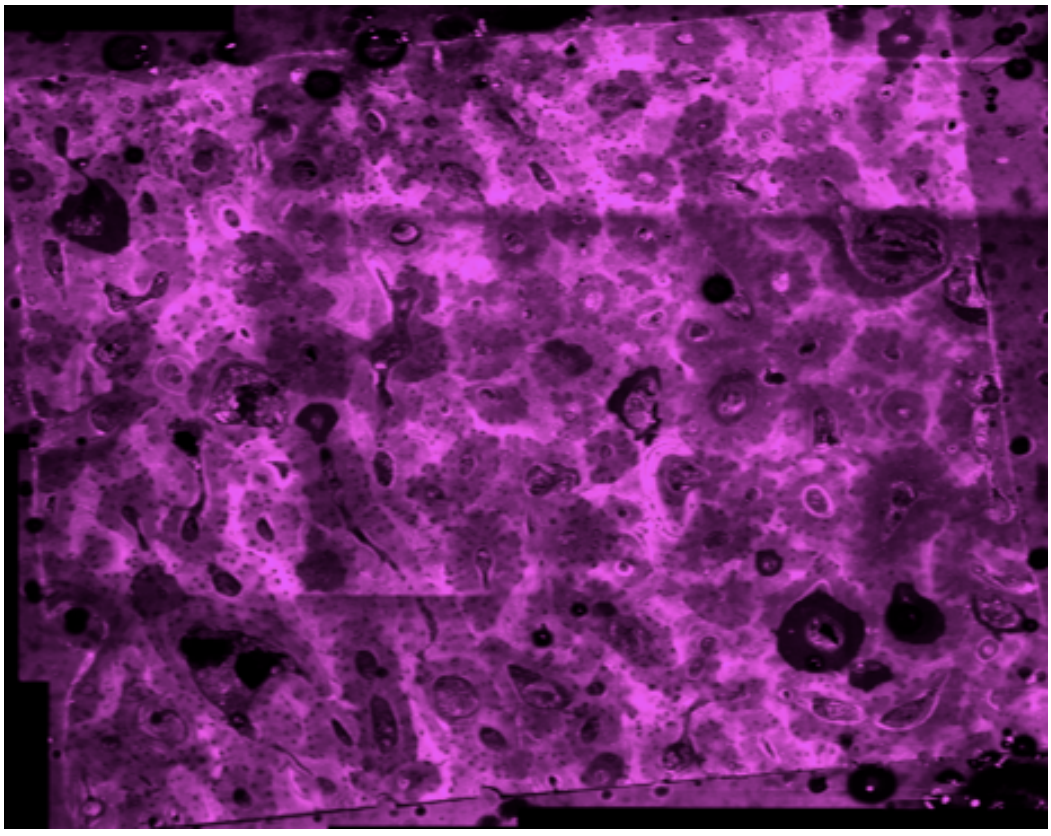

N2A:

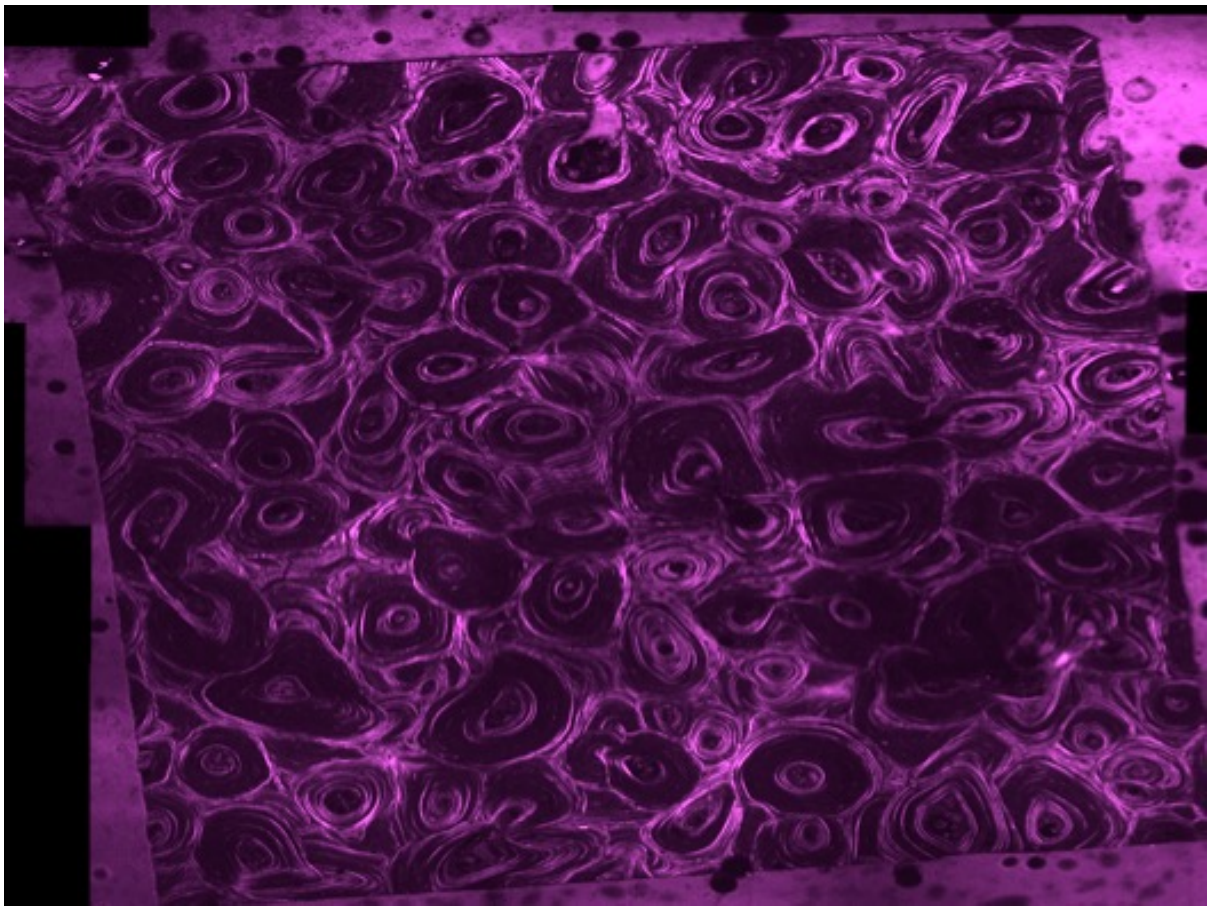

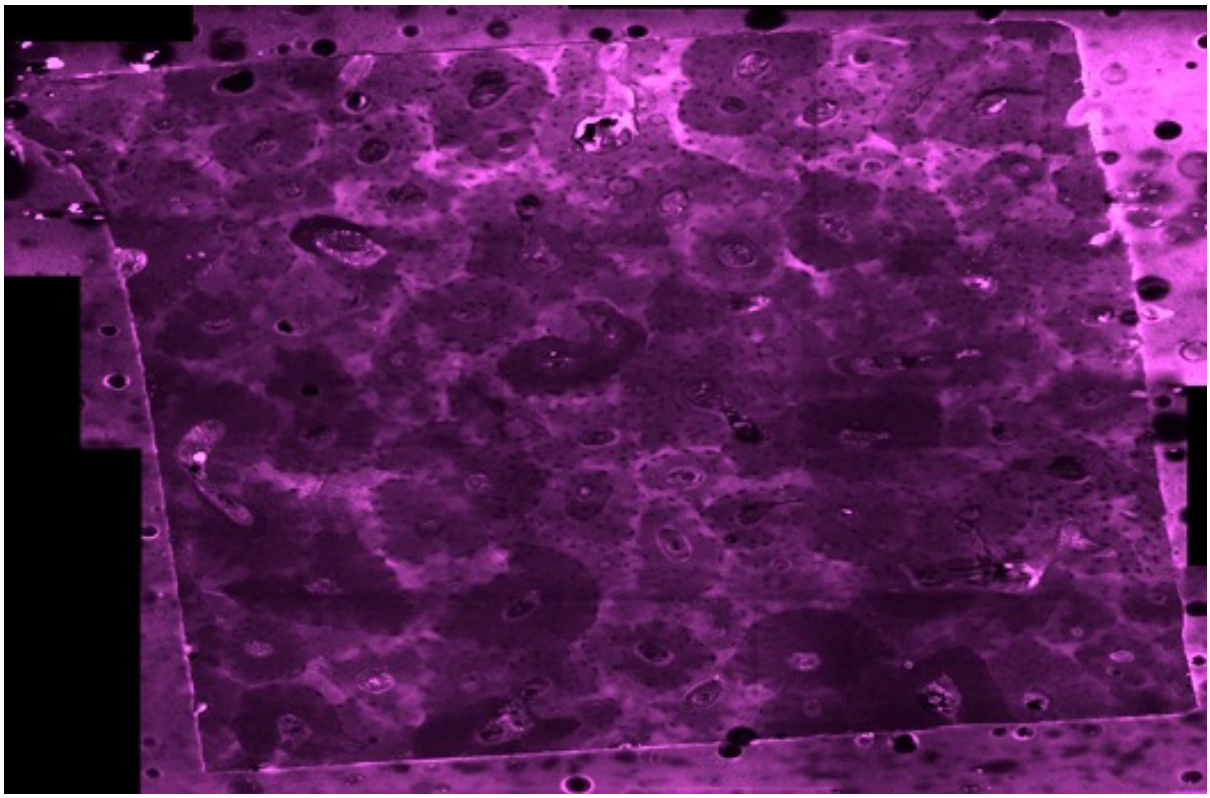

N2B:

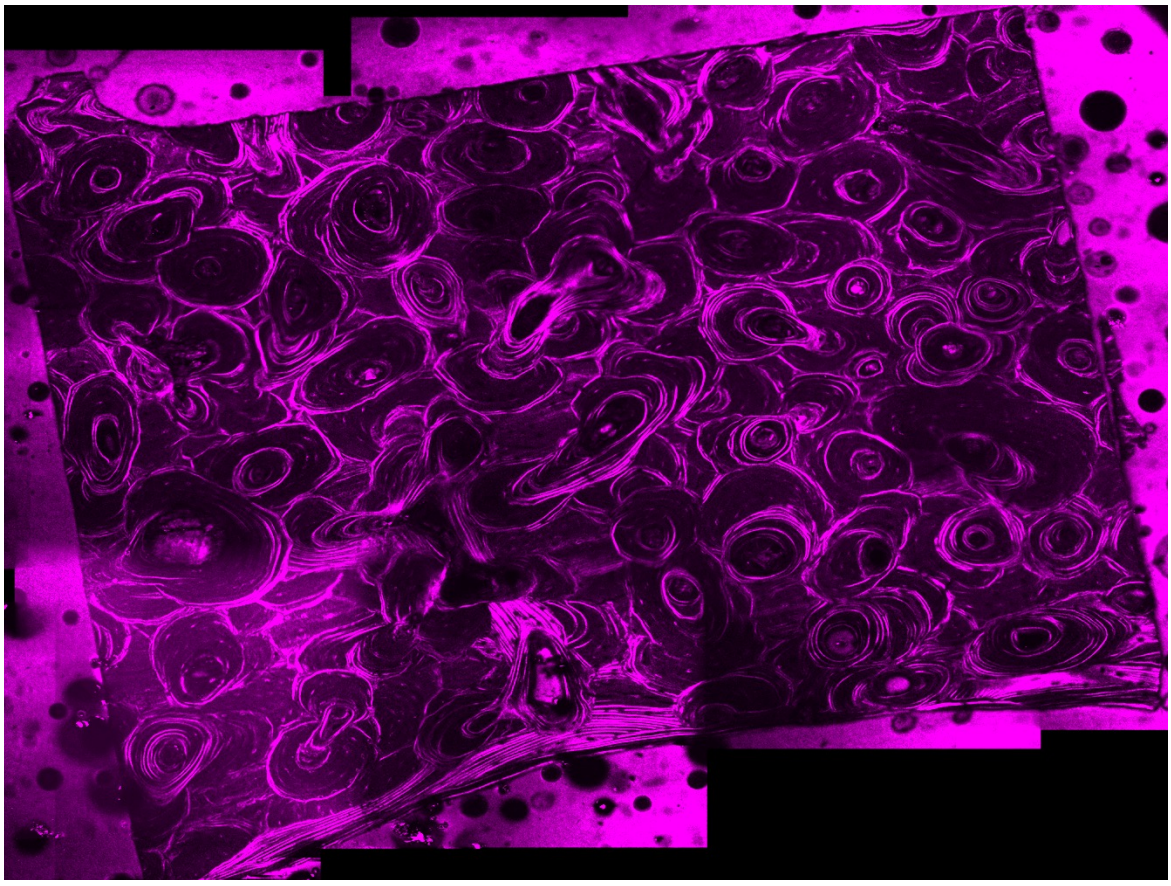

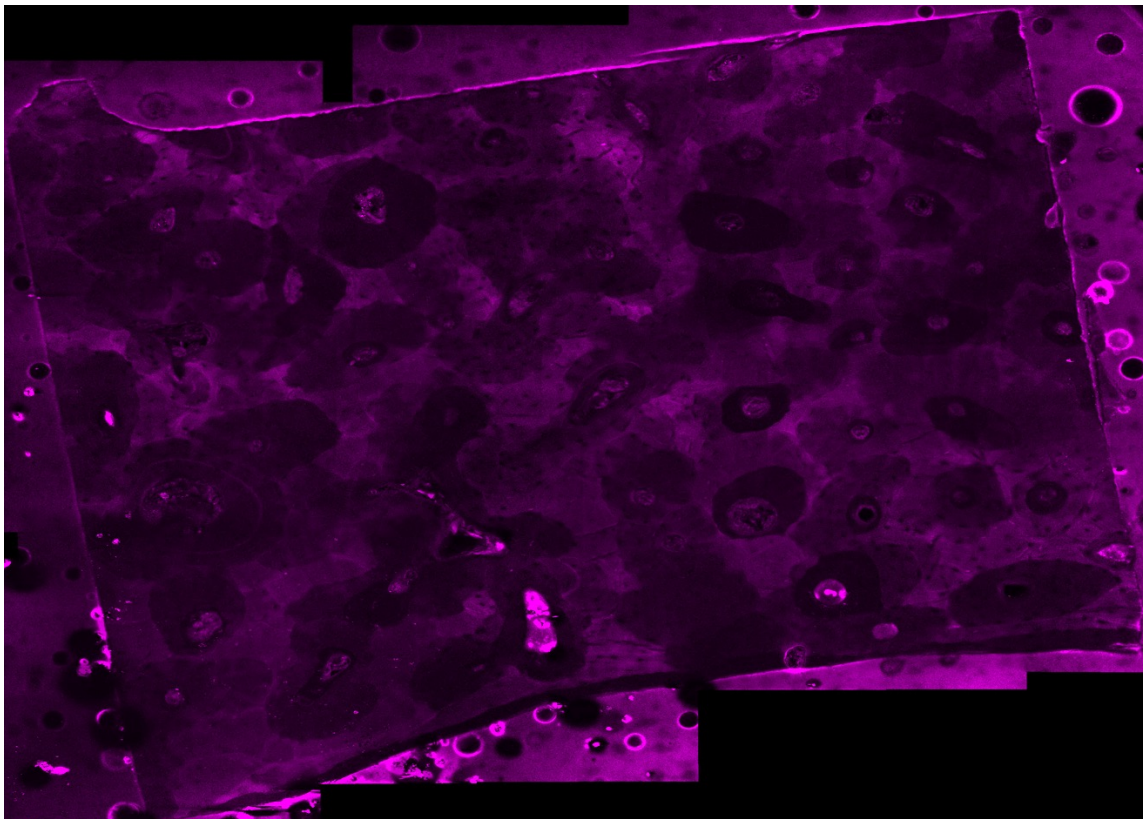

N2C:

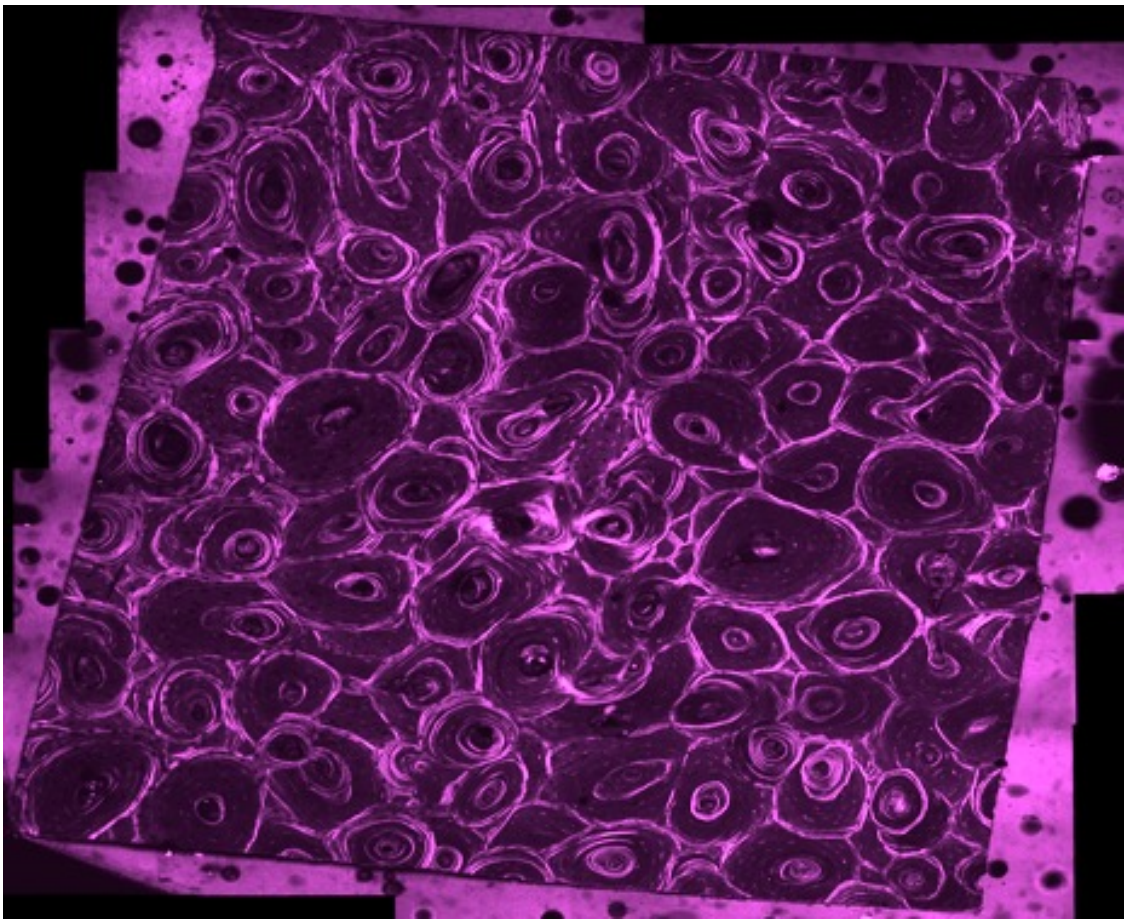

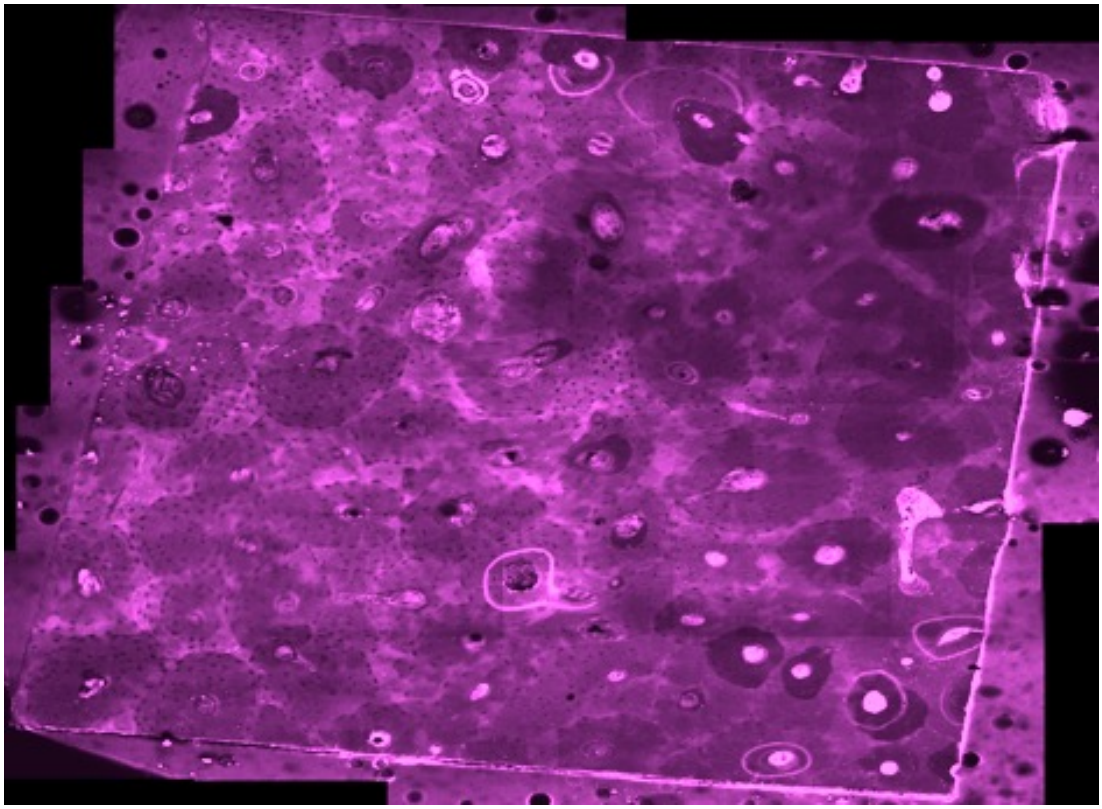

N2D:

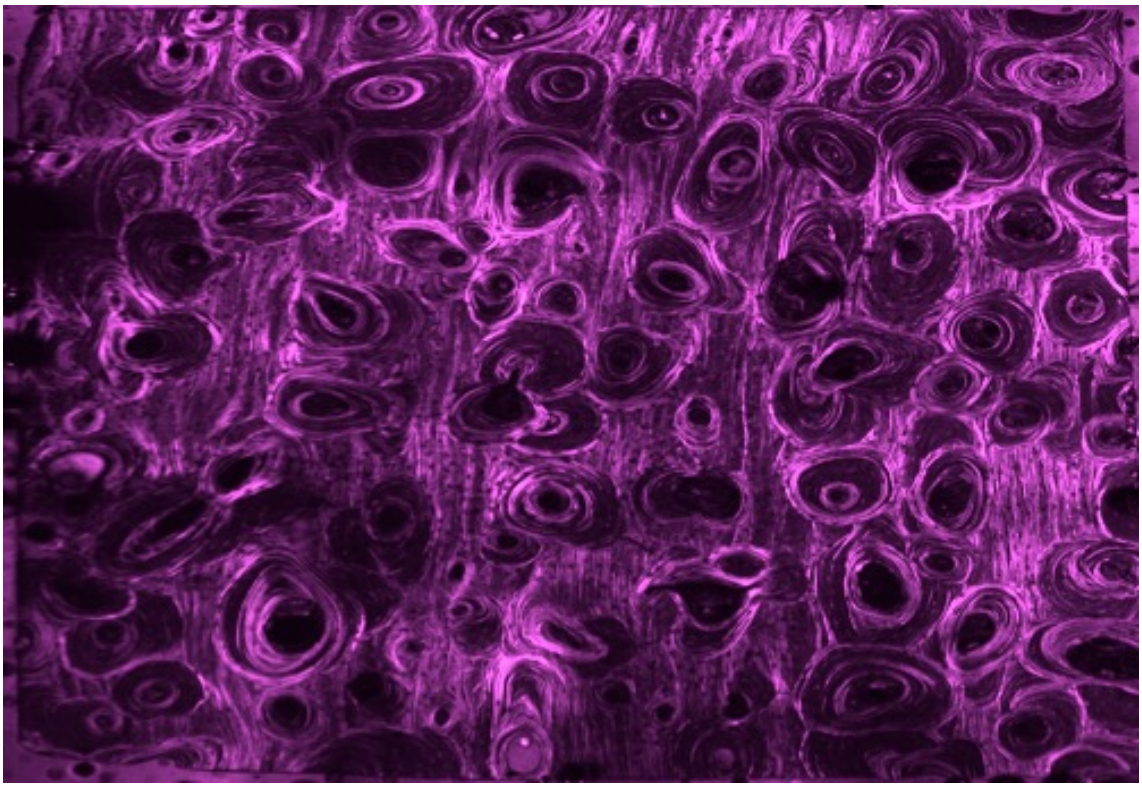

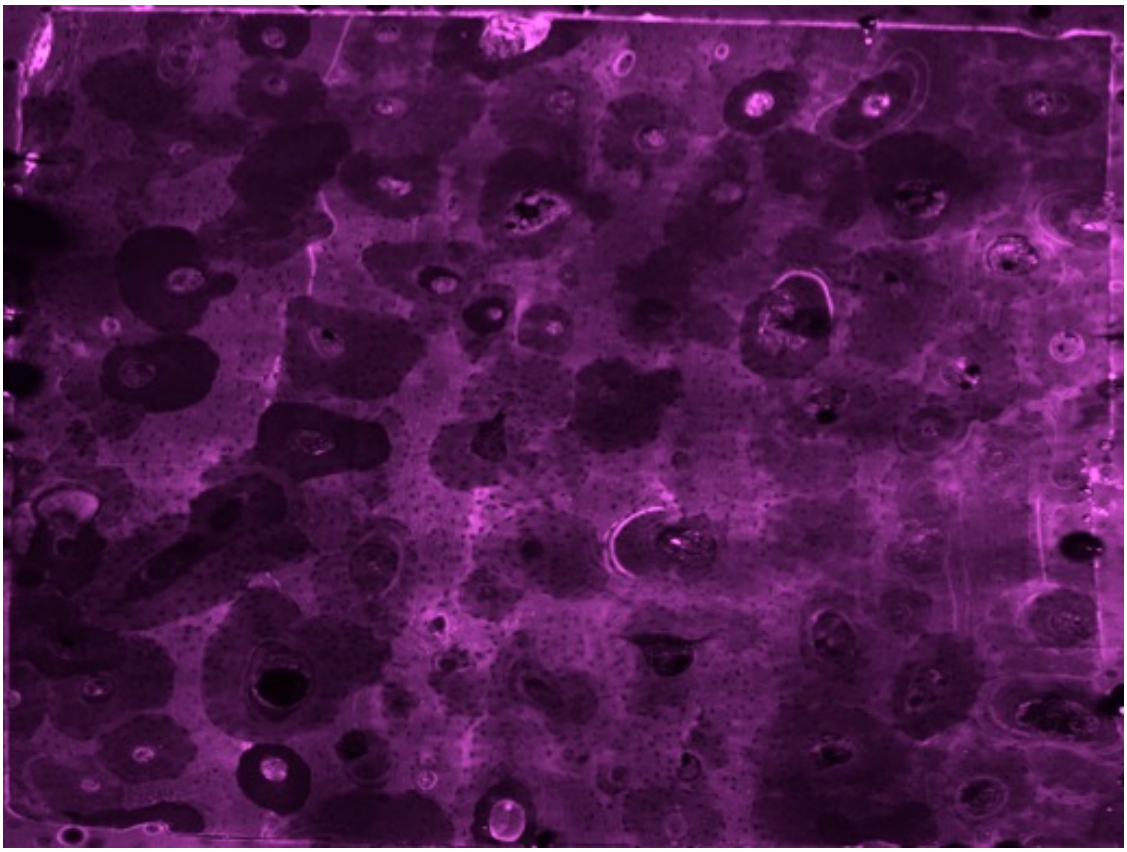

N2E:

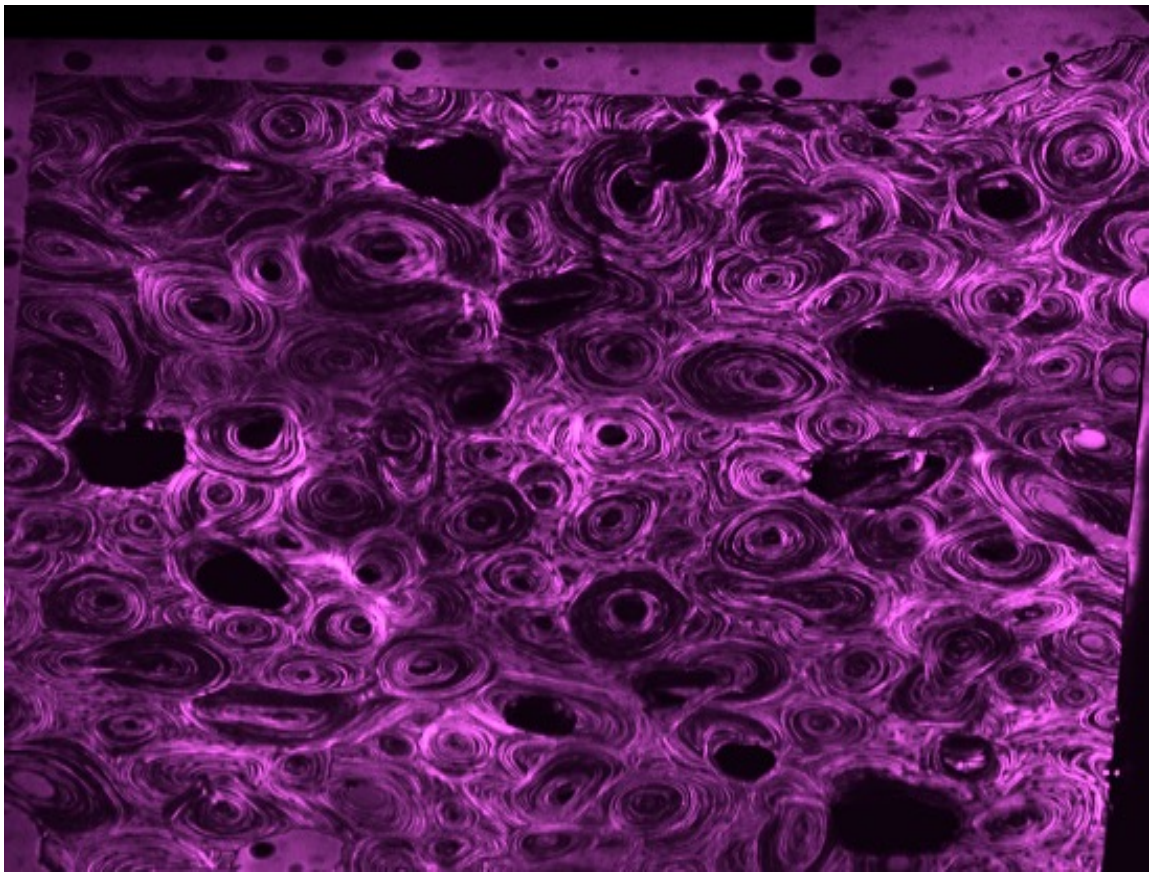

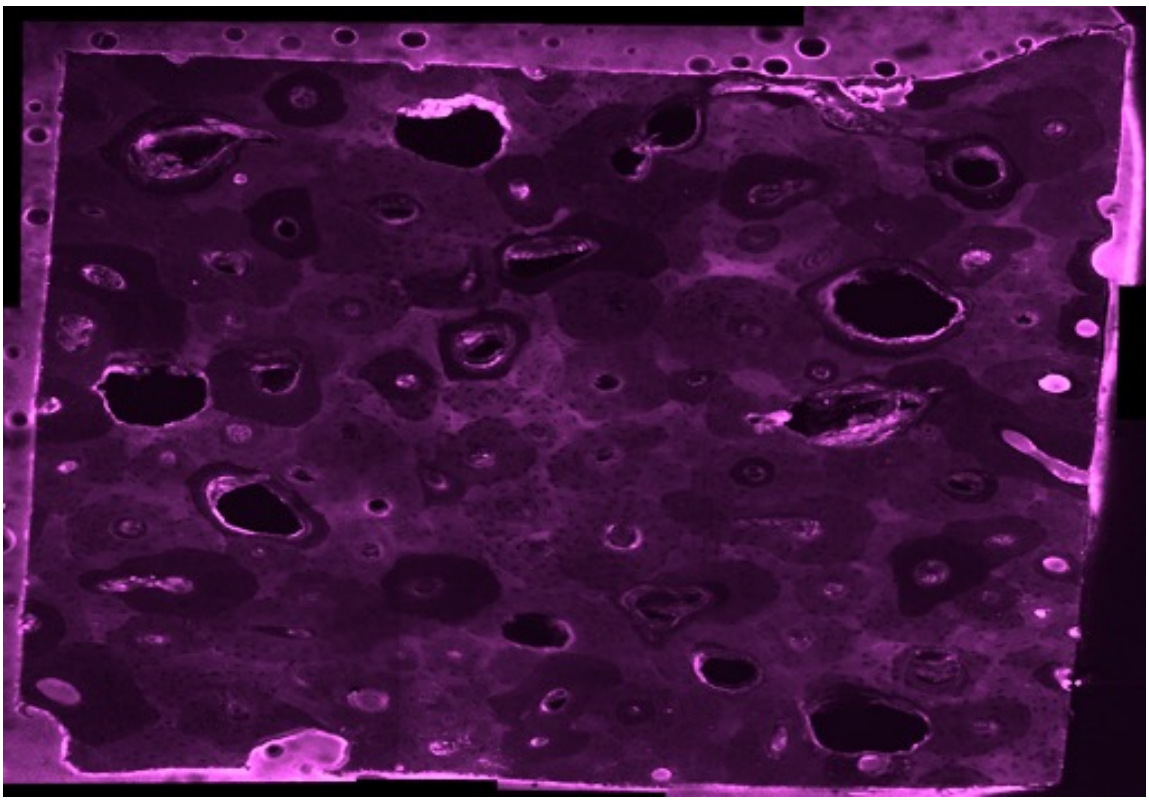

N3A:

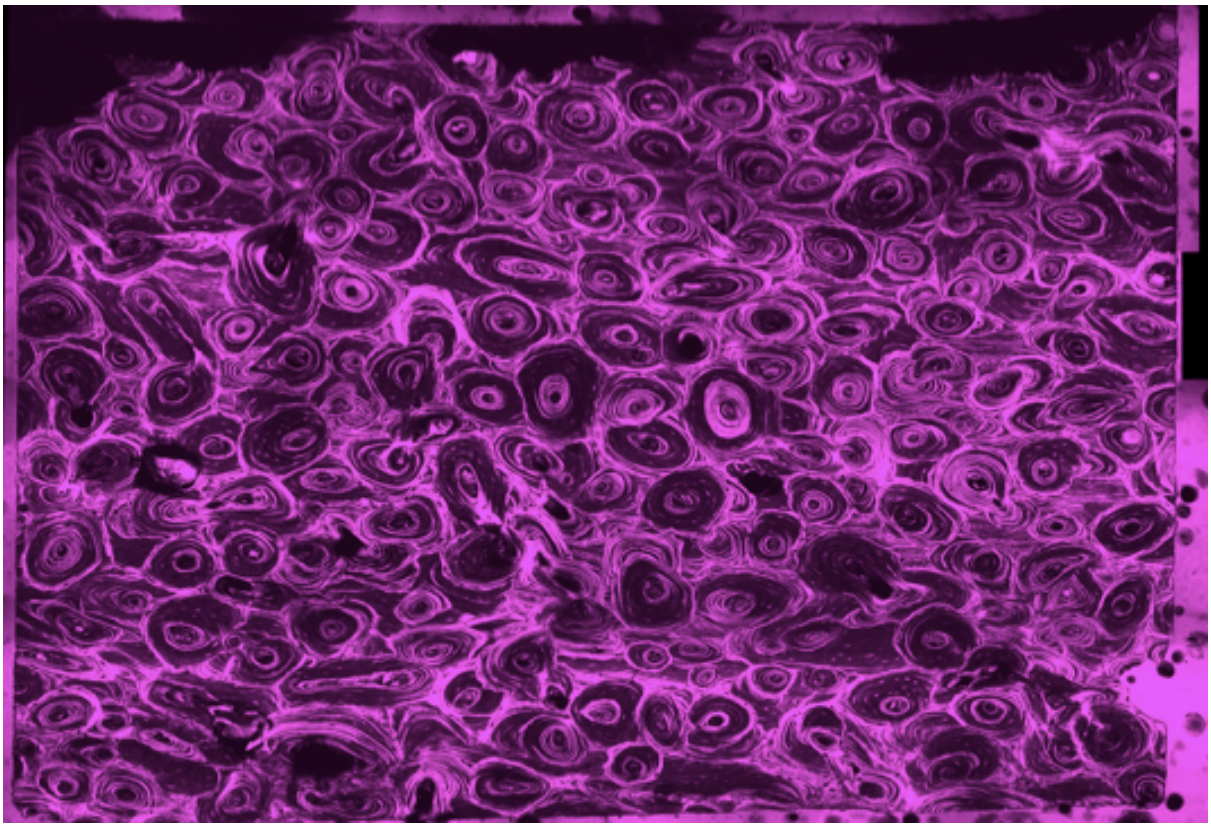

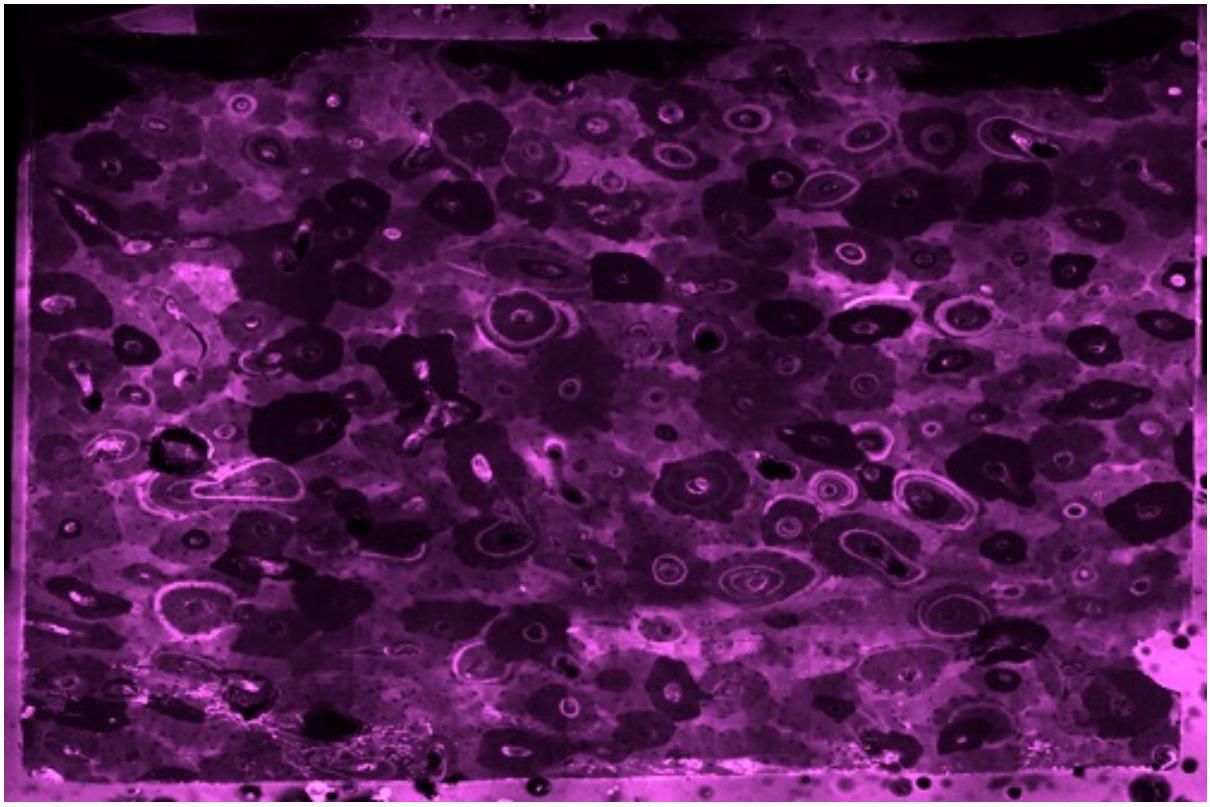

N3B:

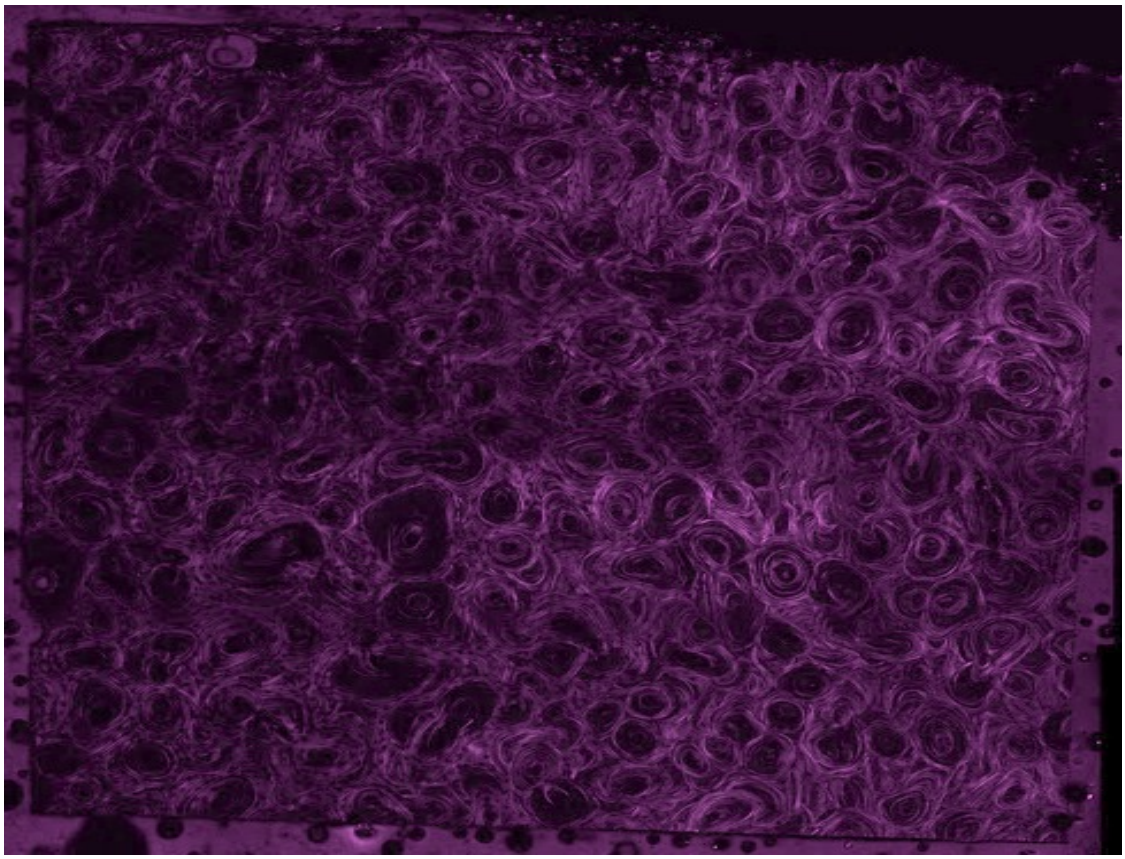

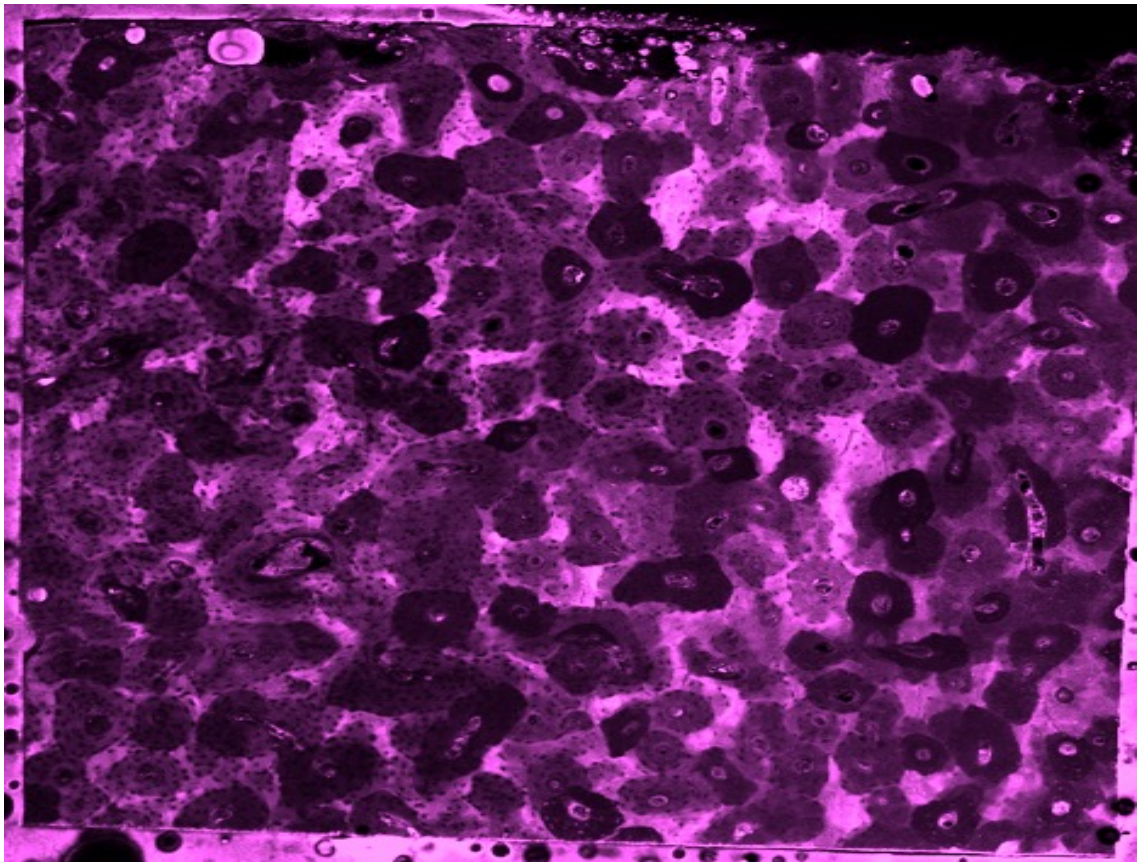

N3C:

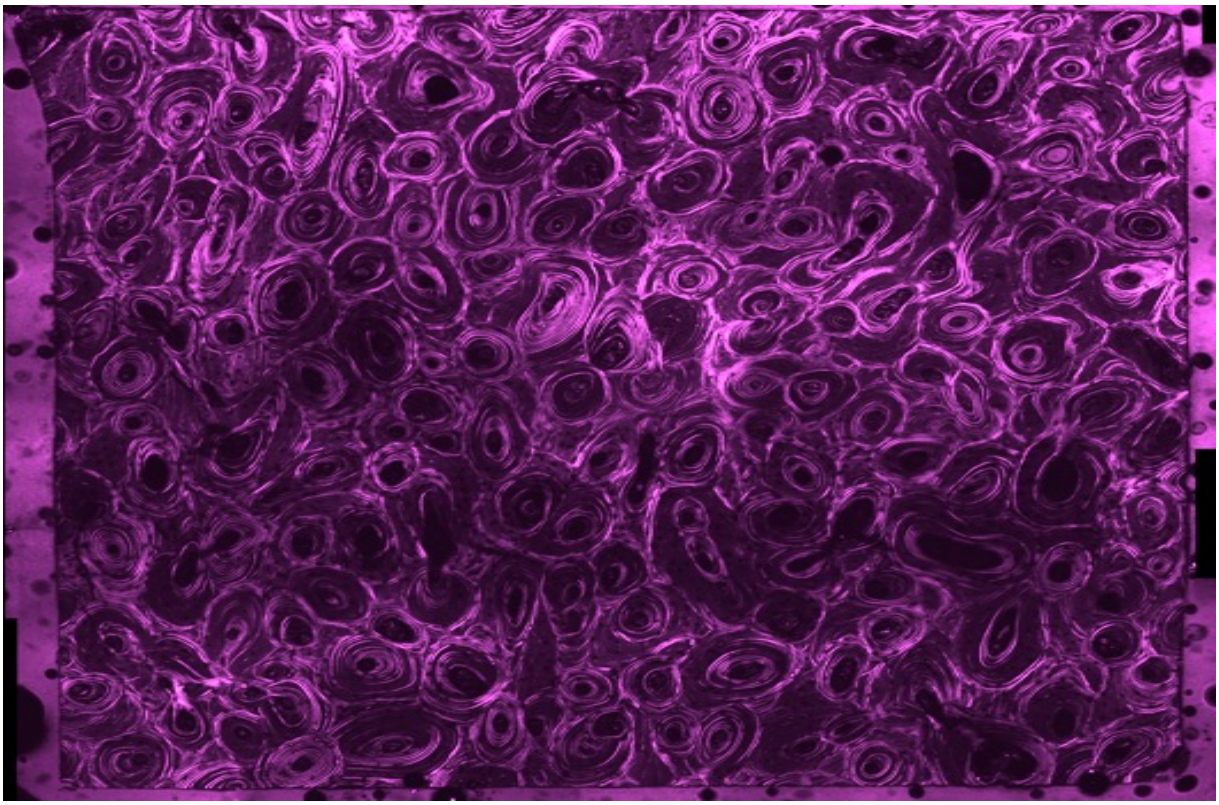

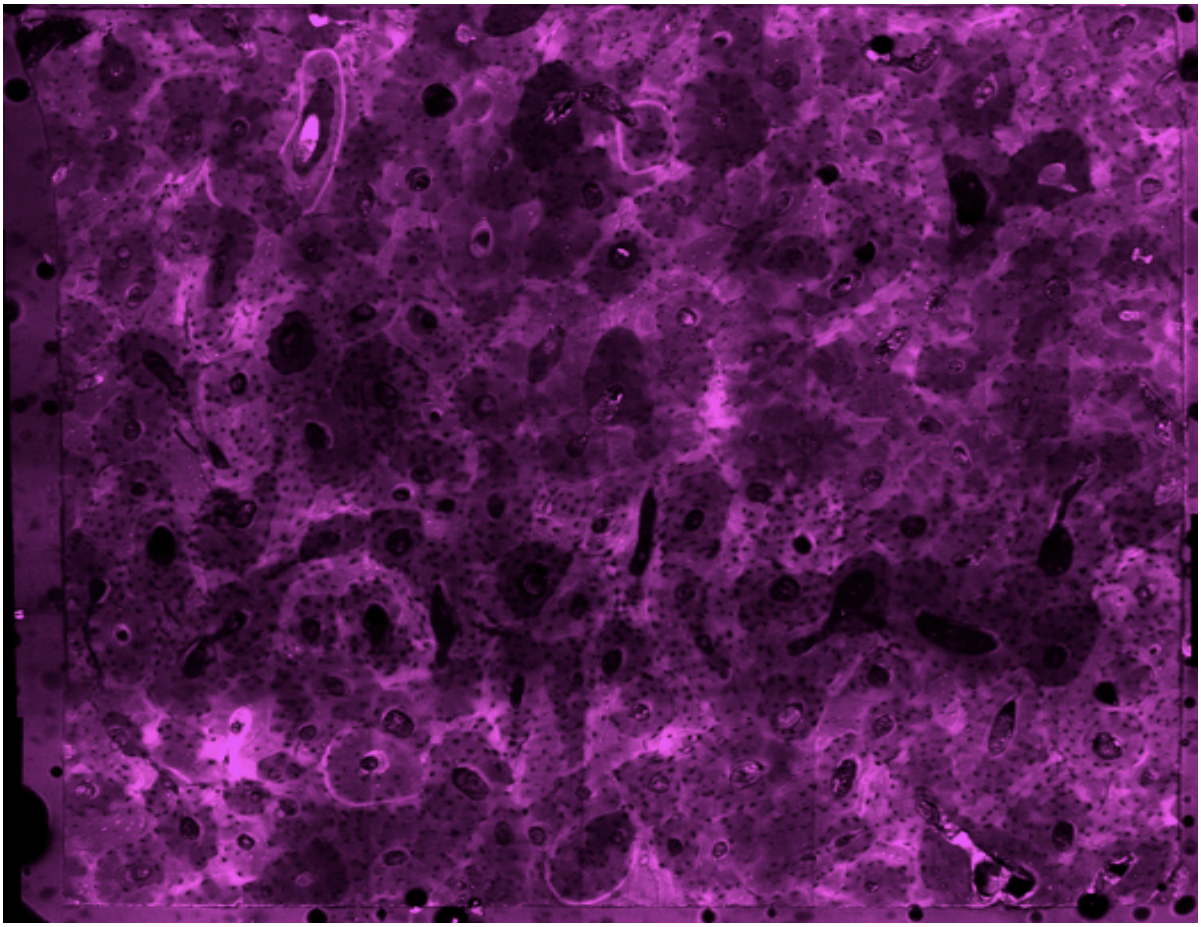

N3D:

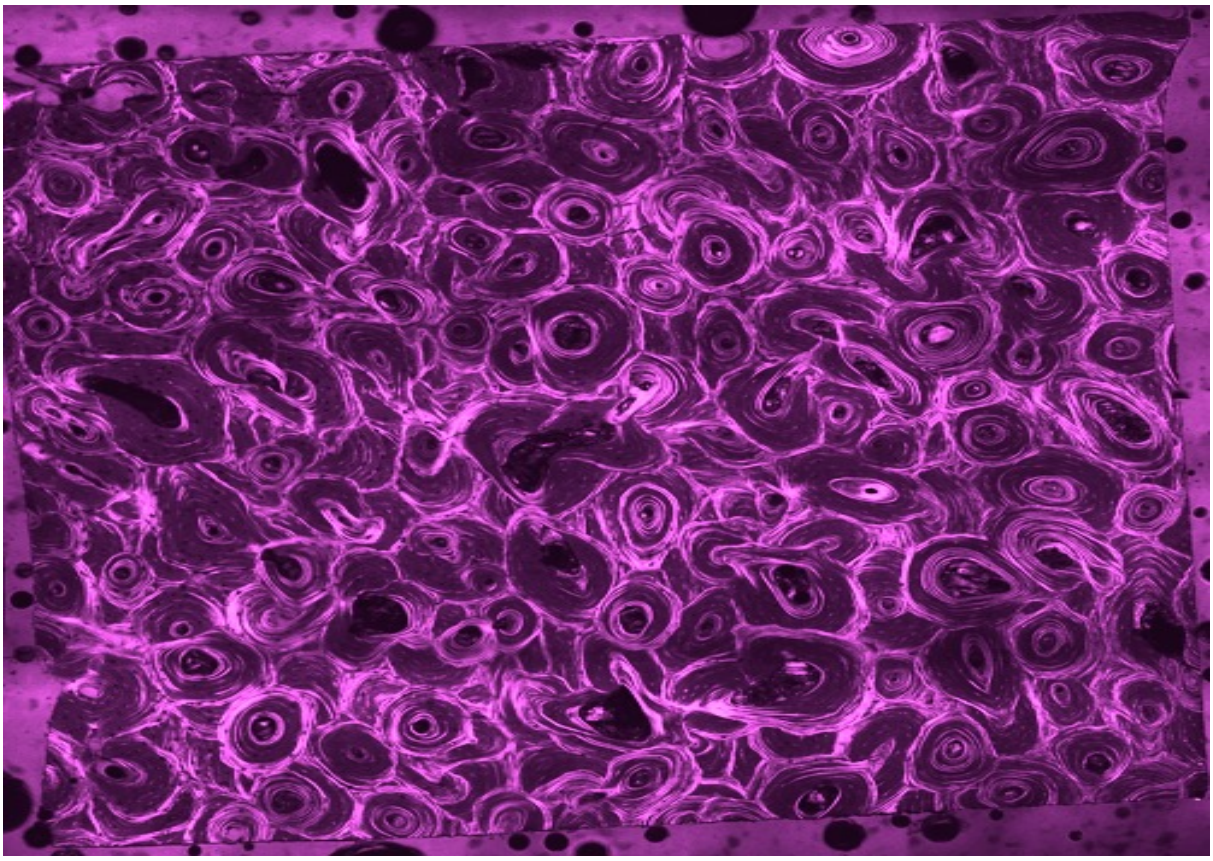

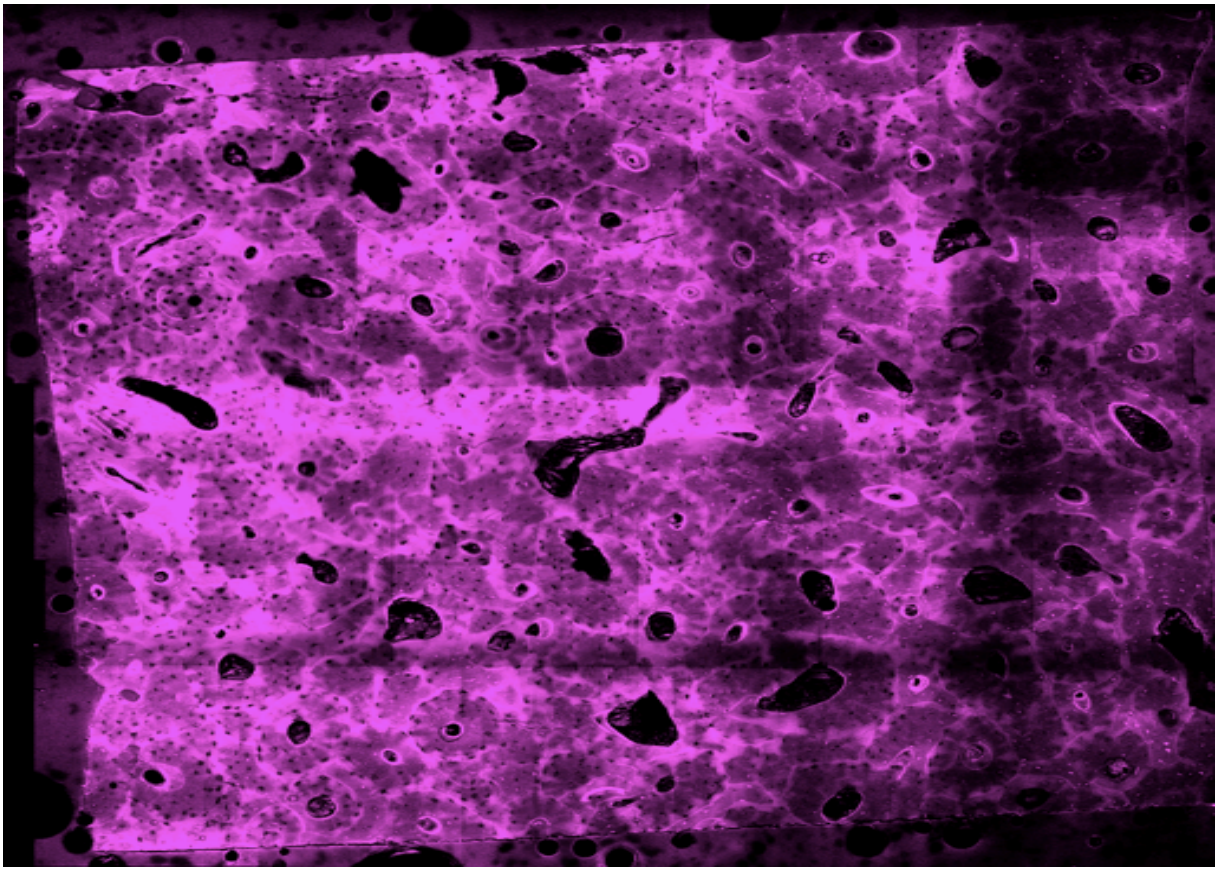

N3E:

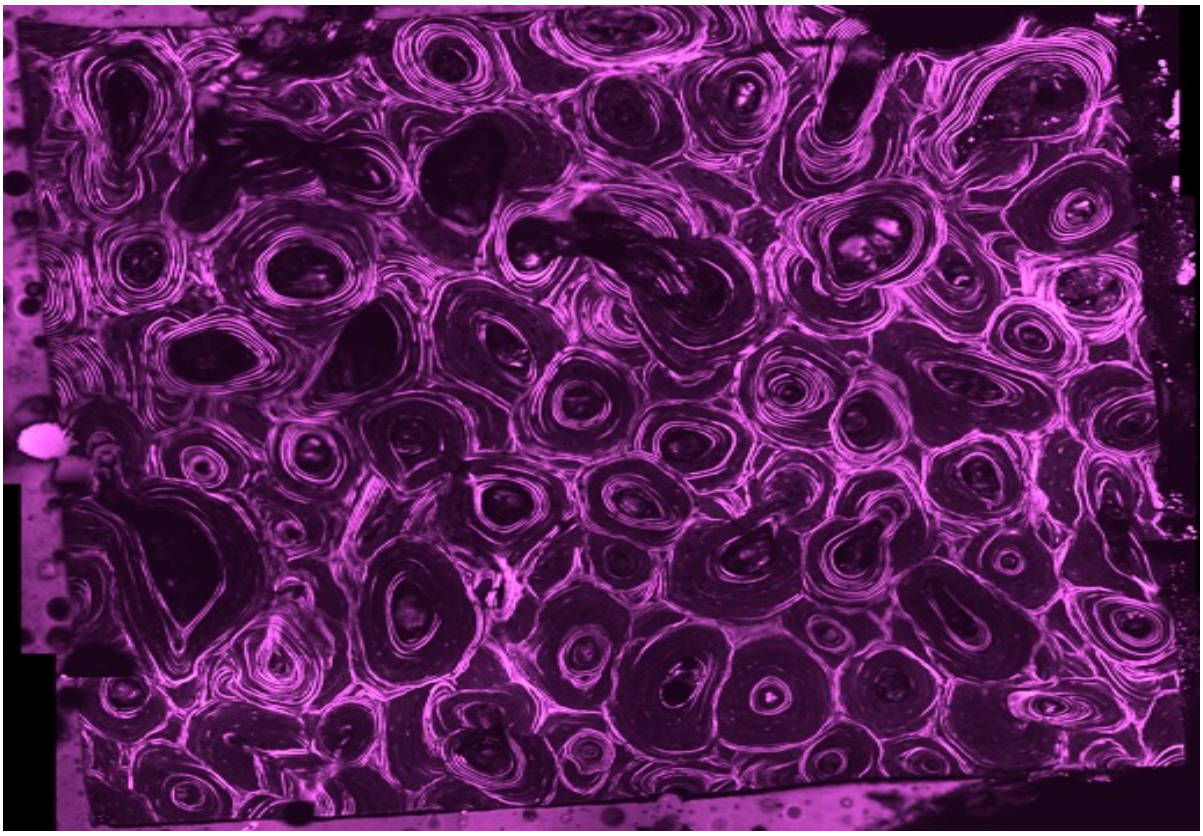

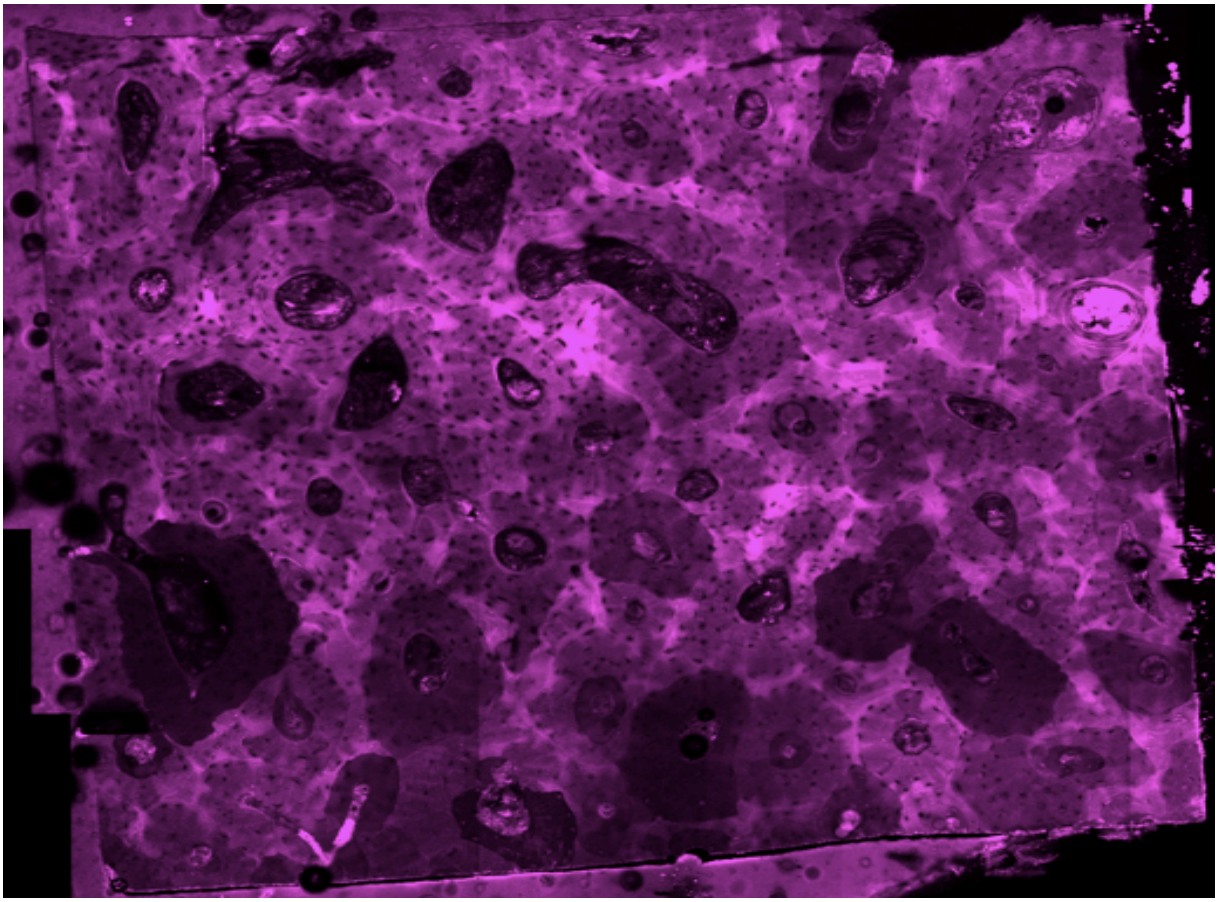

S1A:

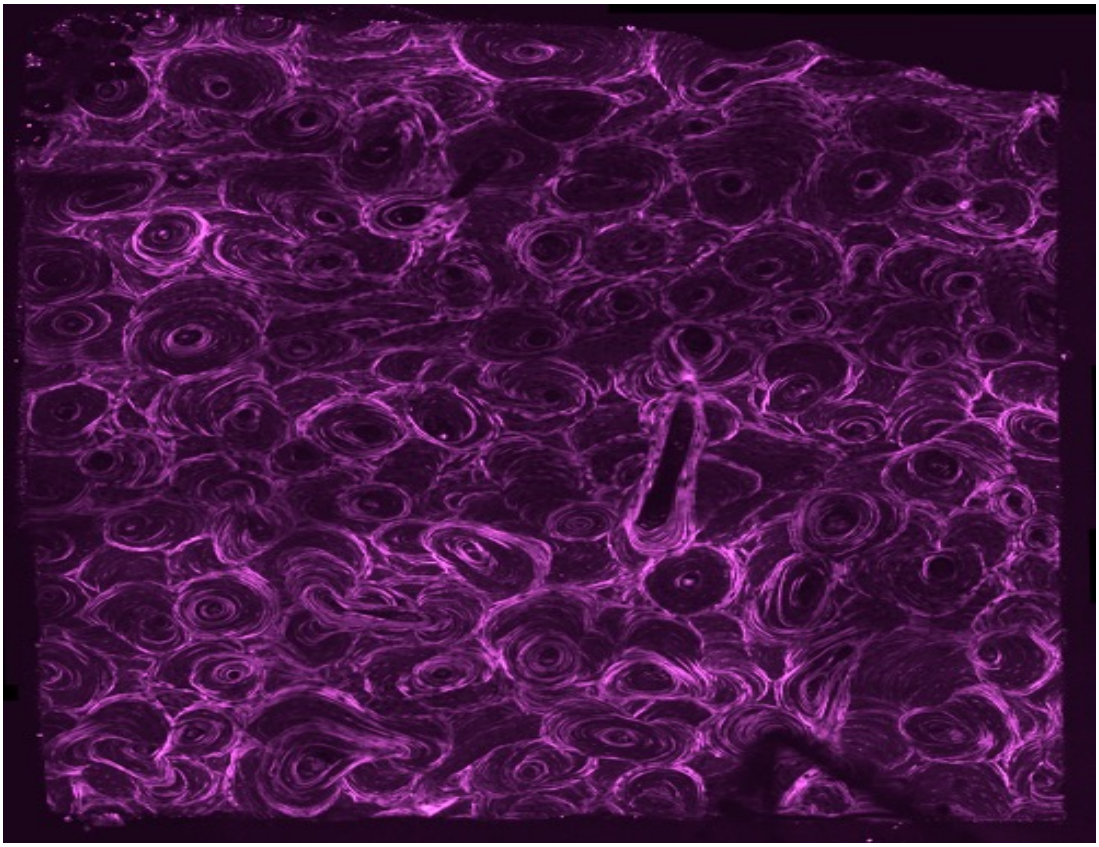

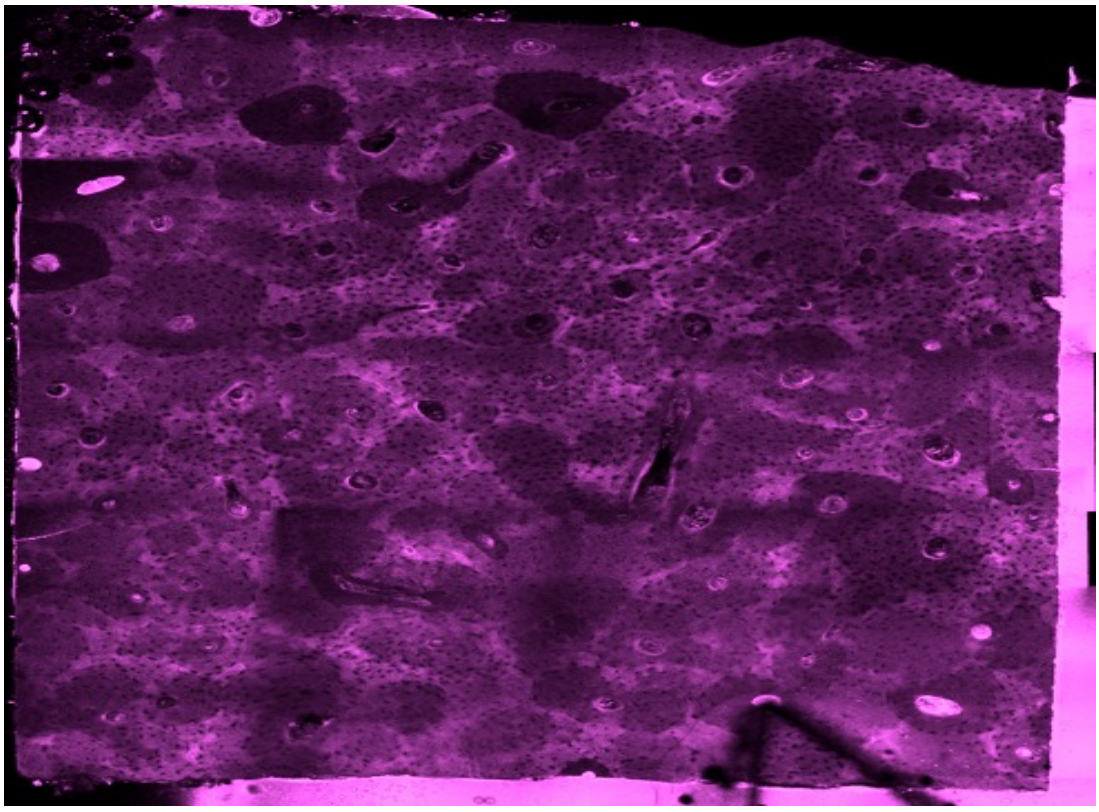

S1B:

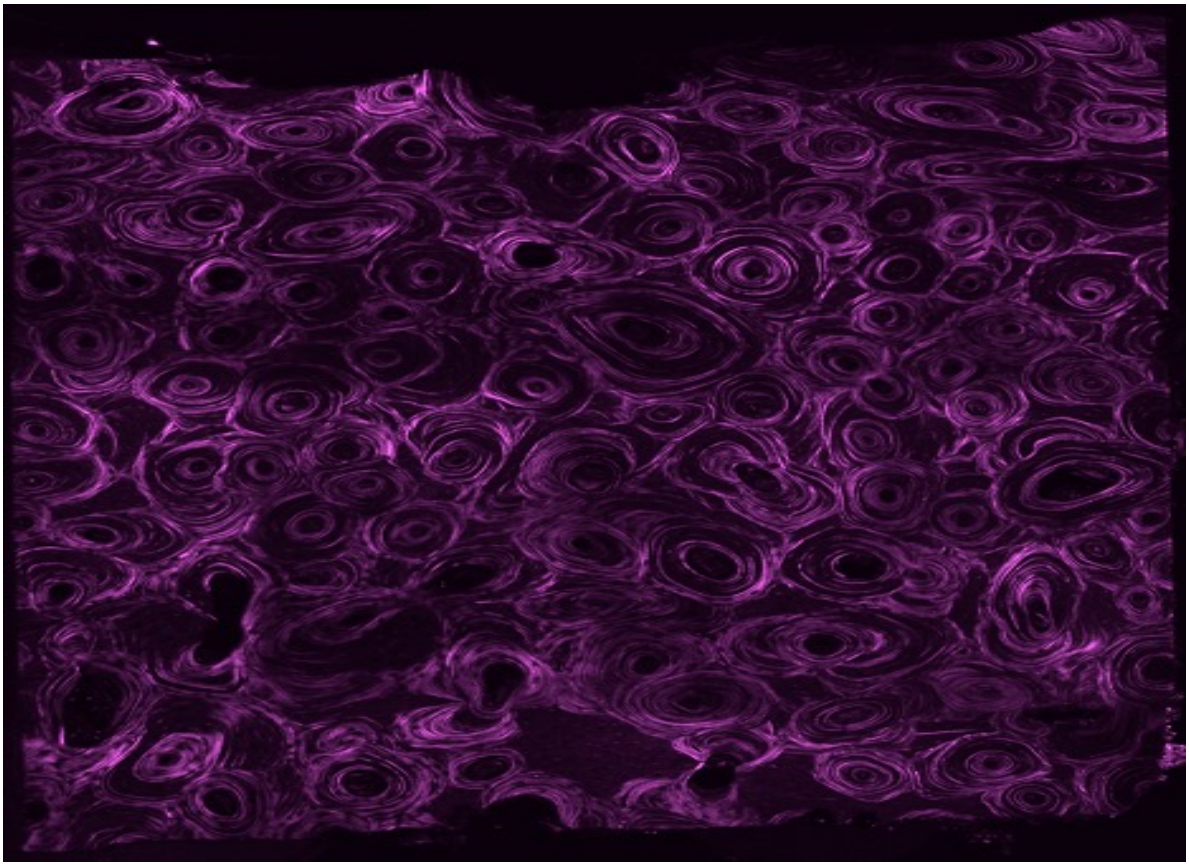

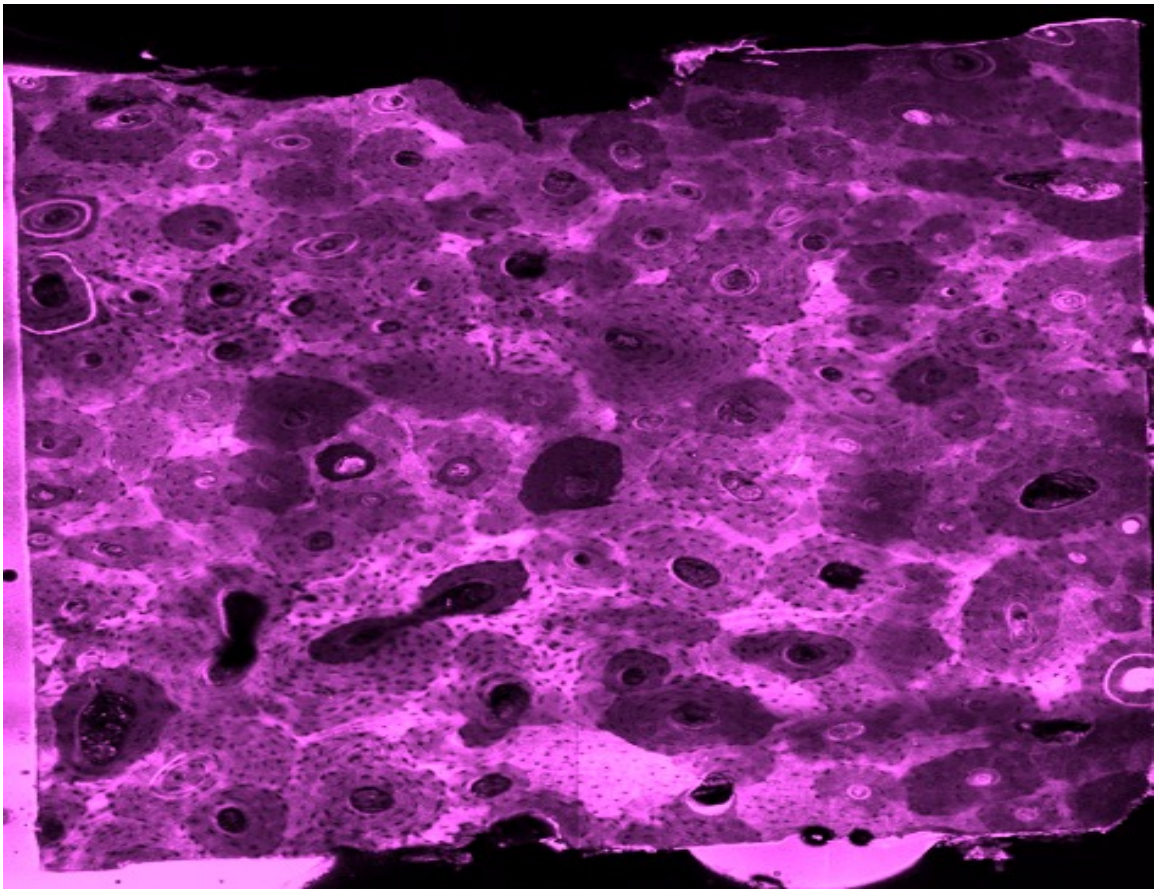

S1C:

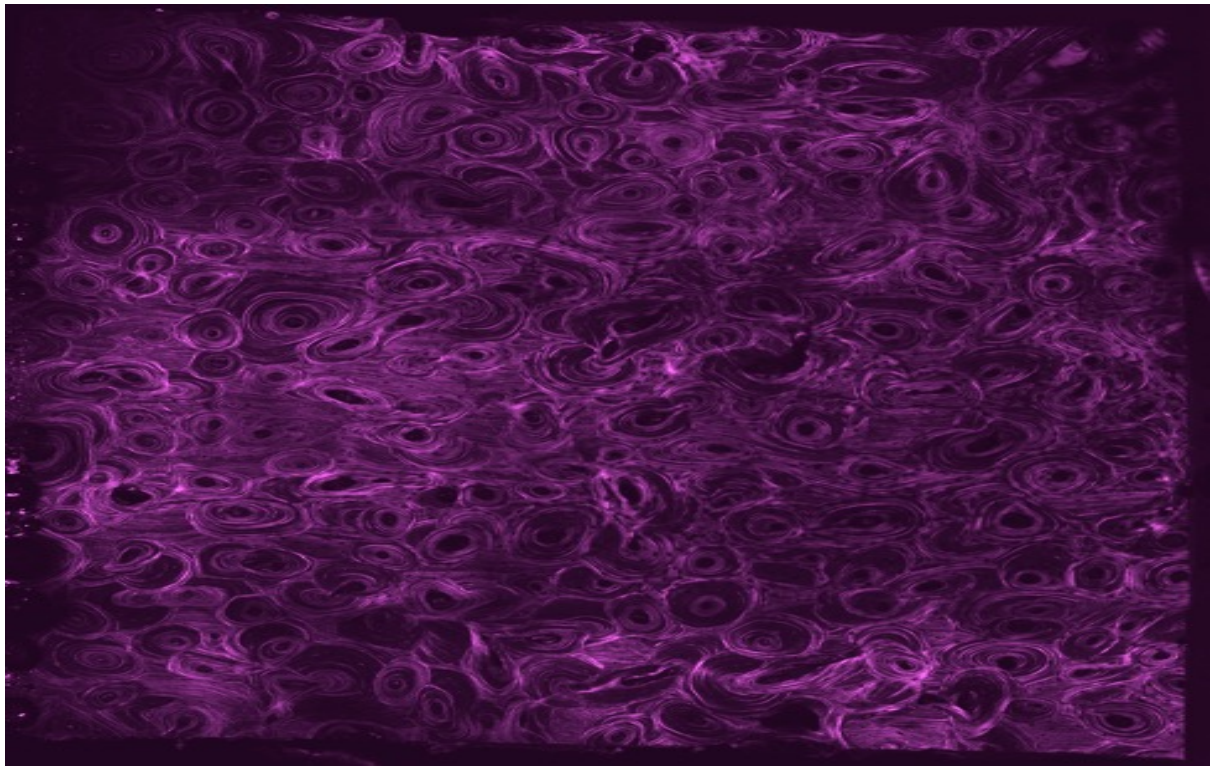

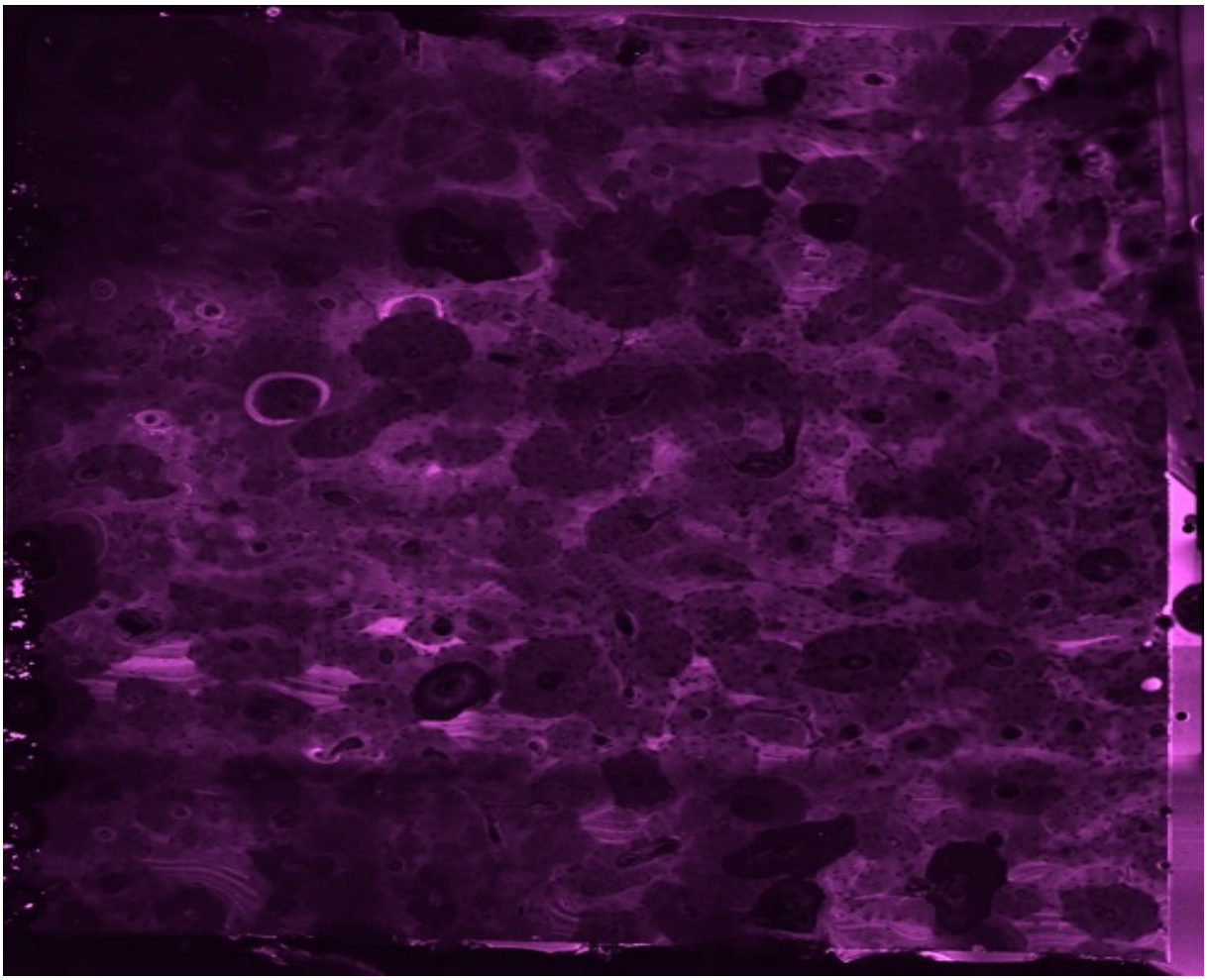

S1D:

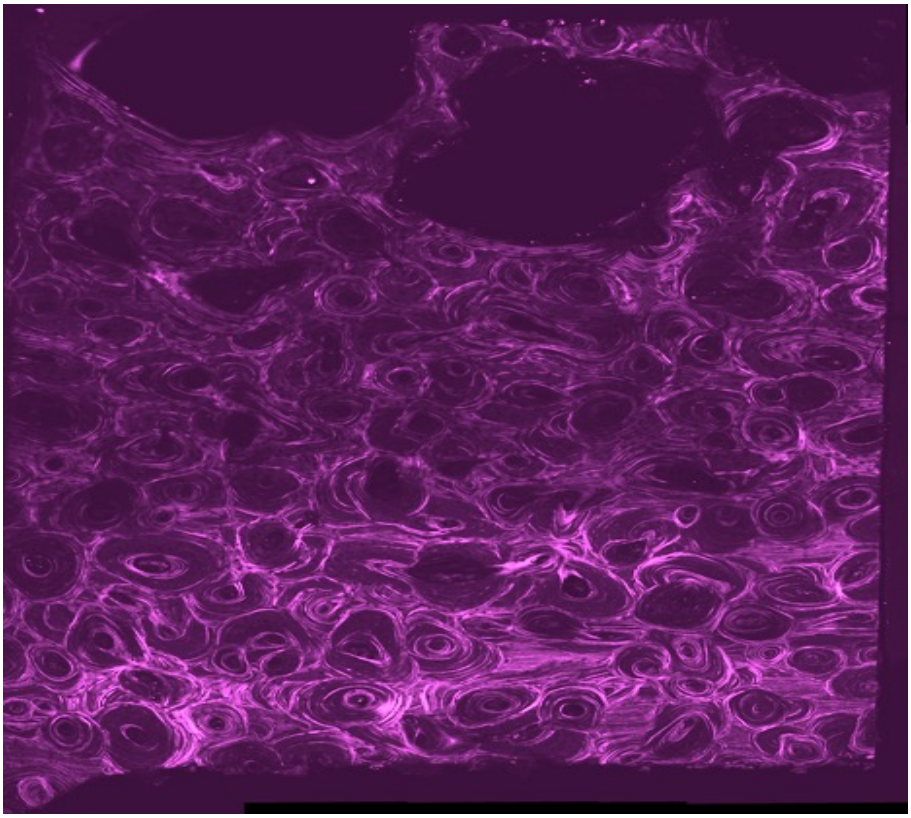

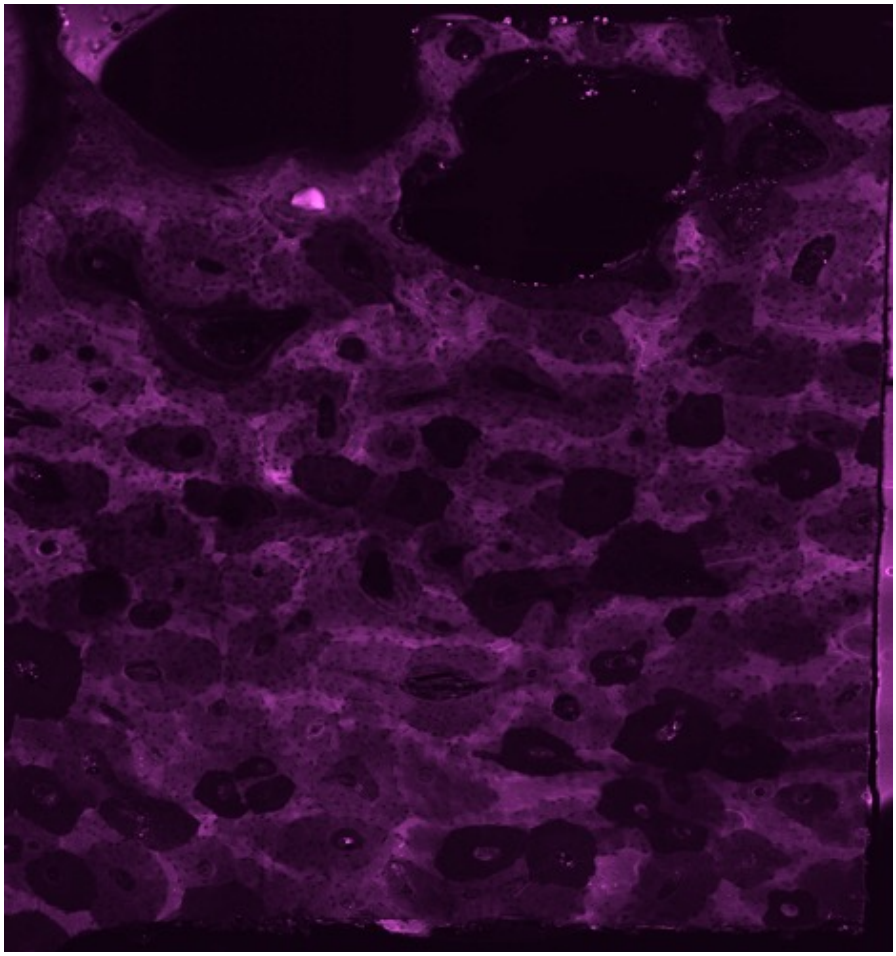

S1E:

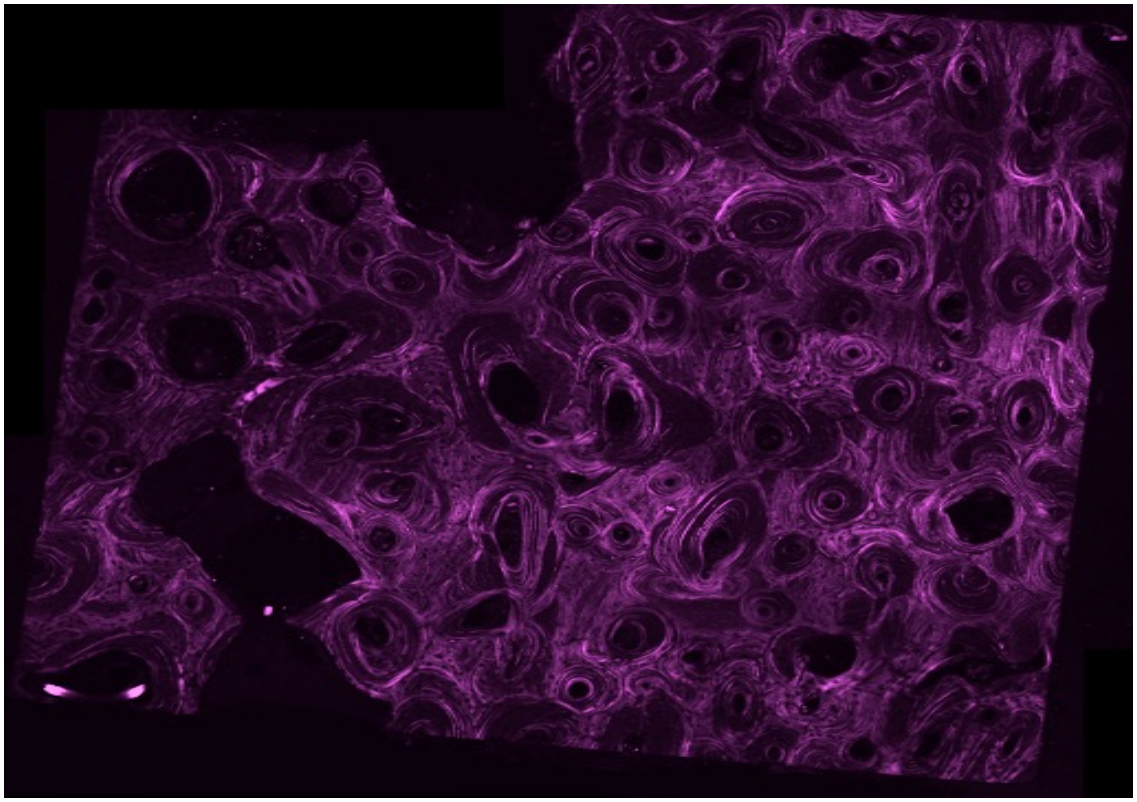

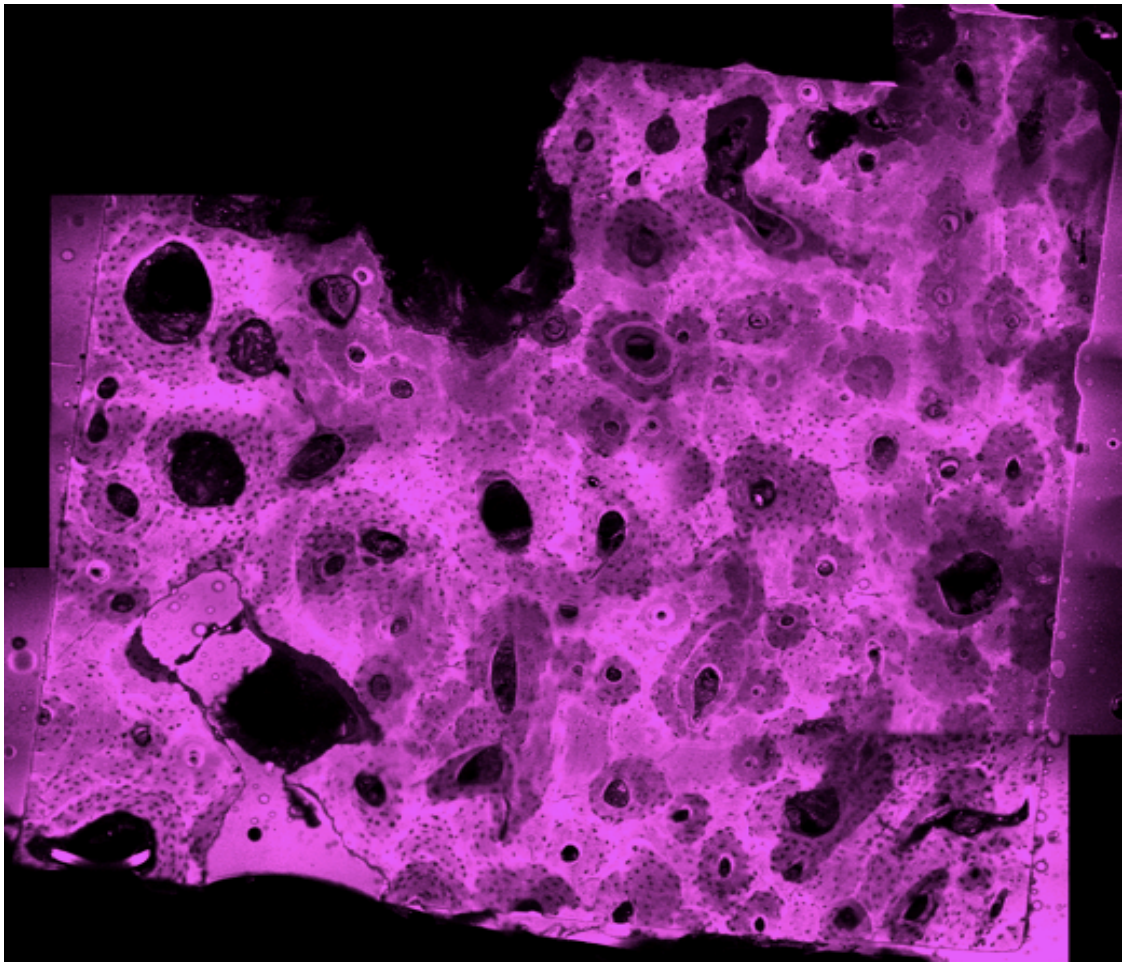

S2A:

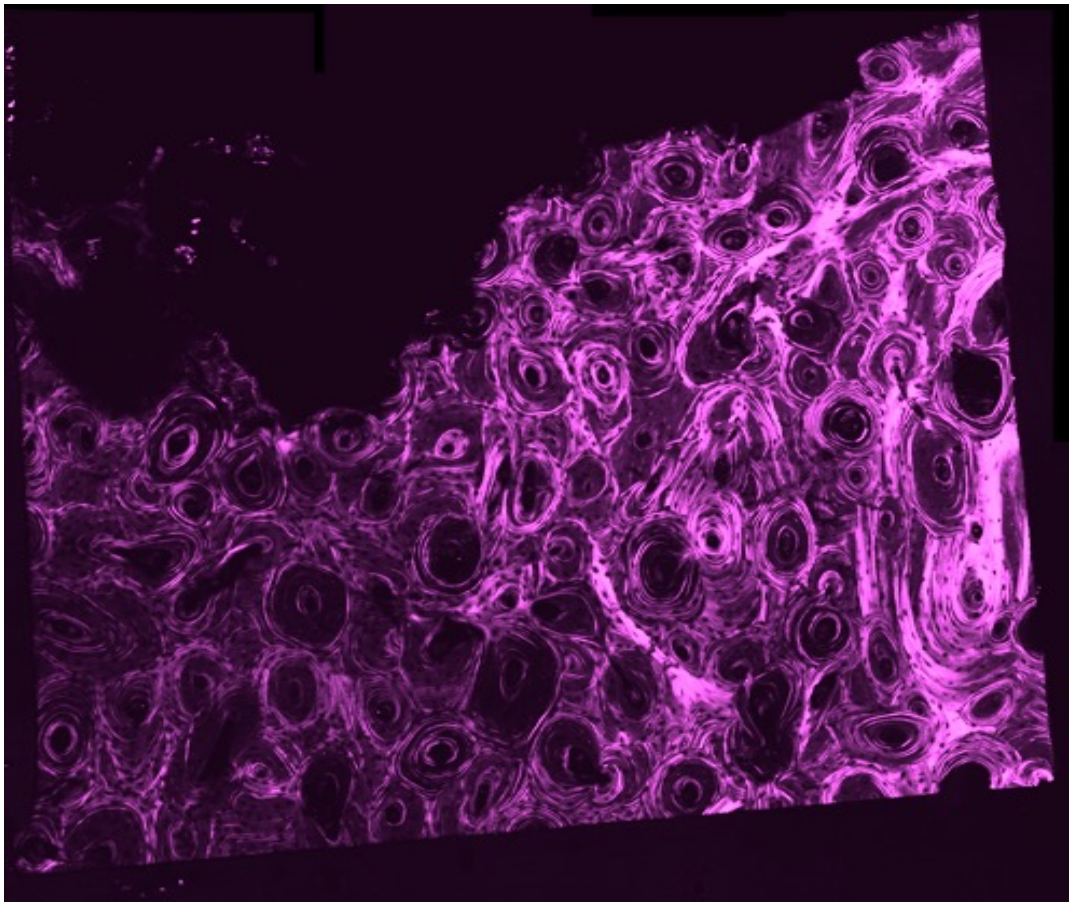

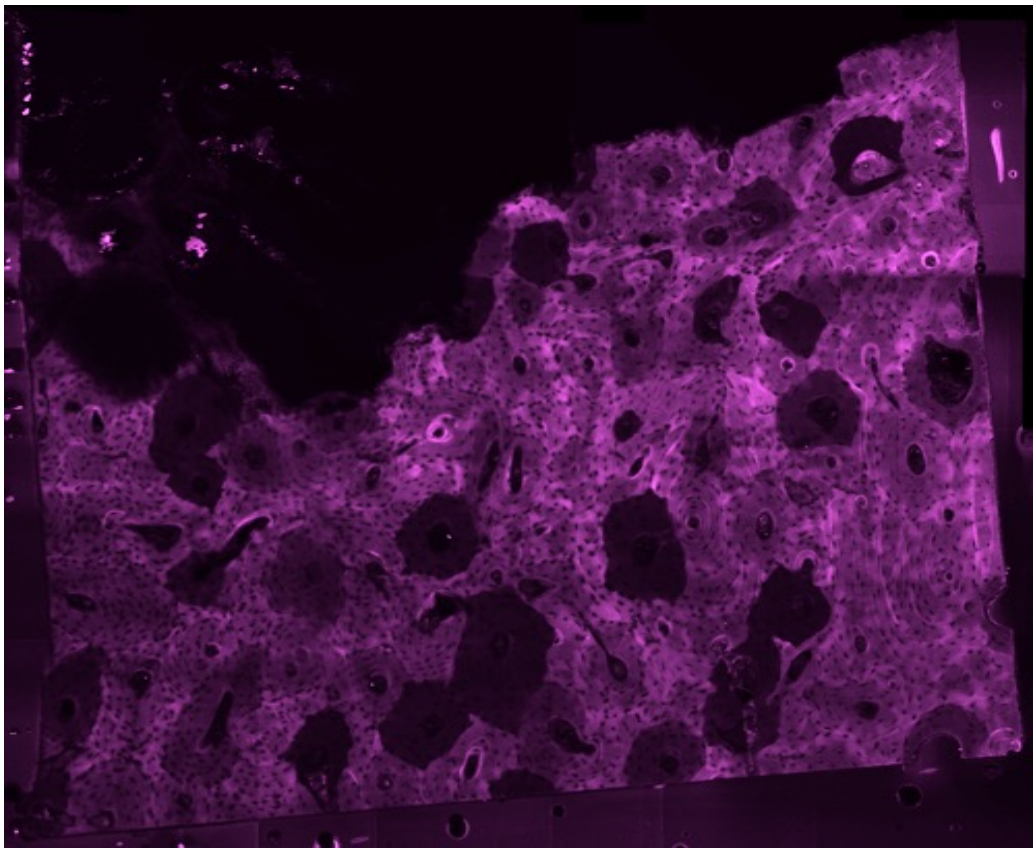

S2B:

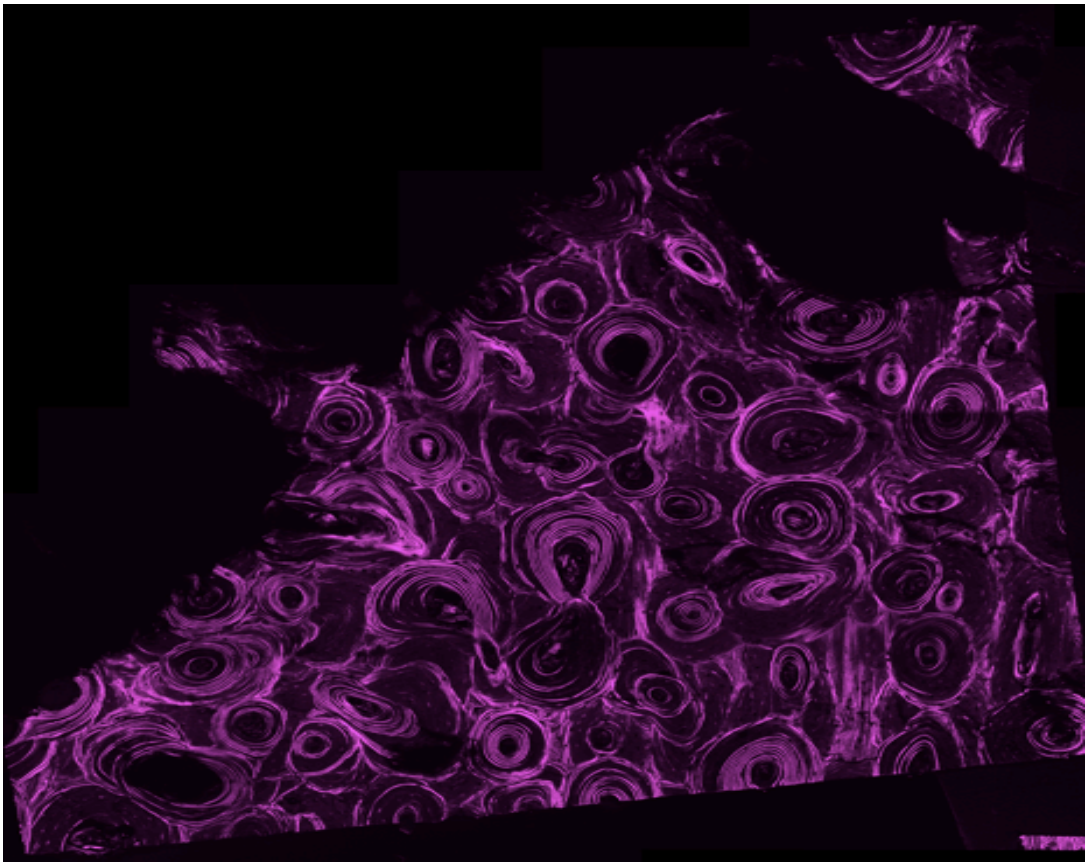

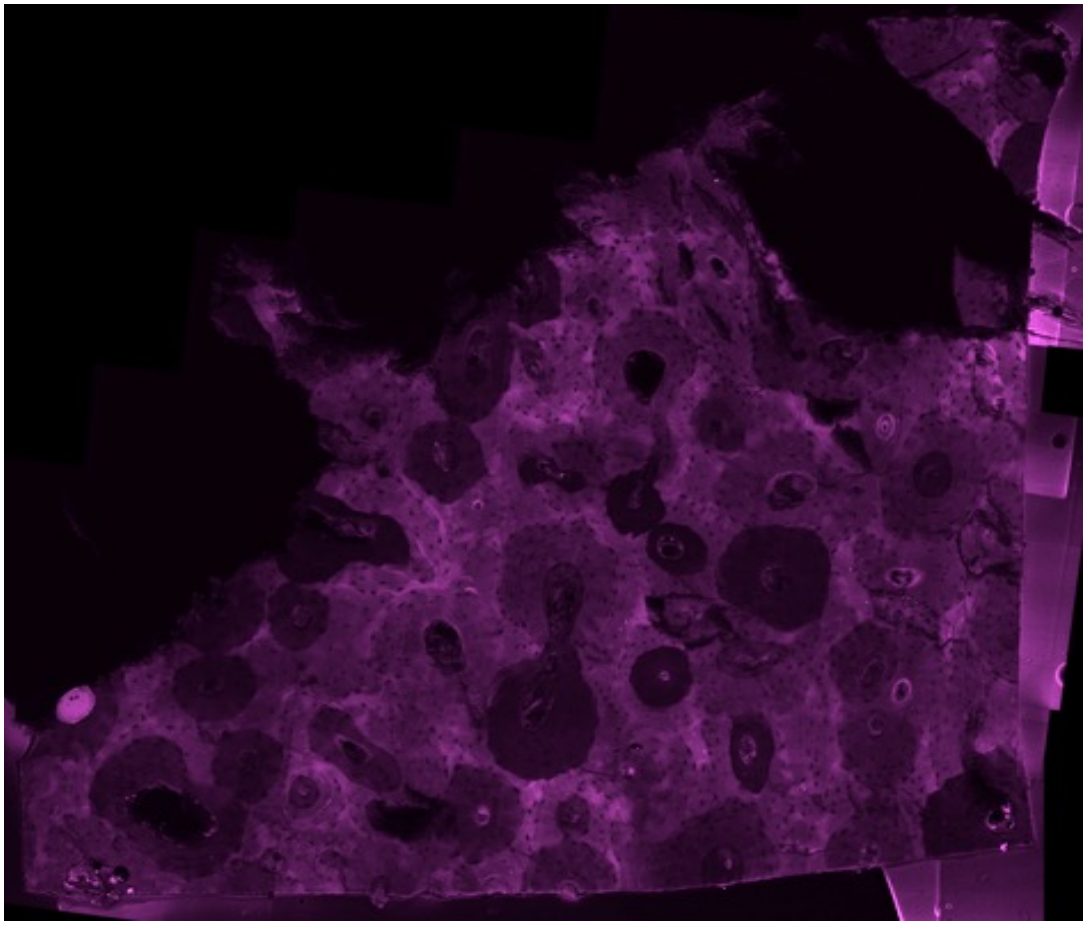

S2C:

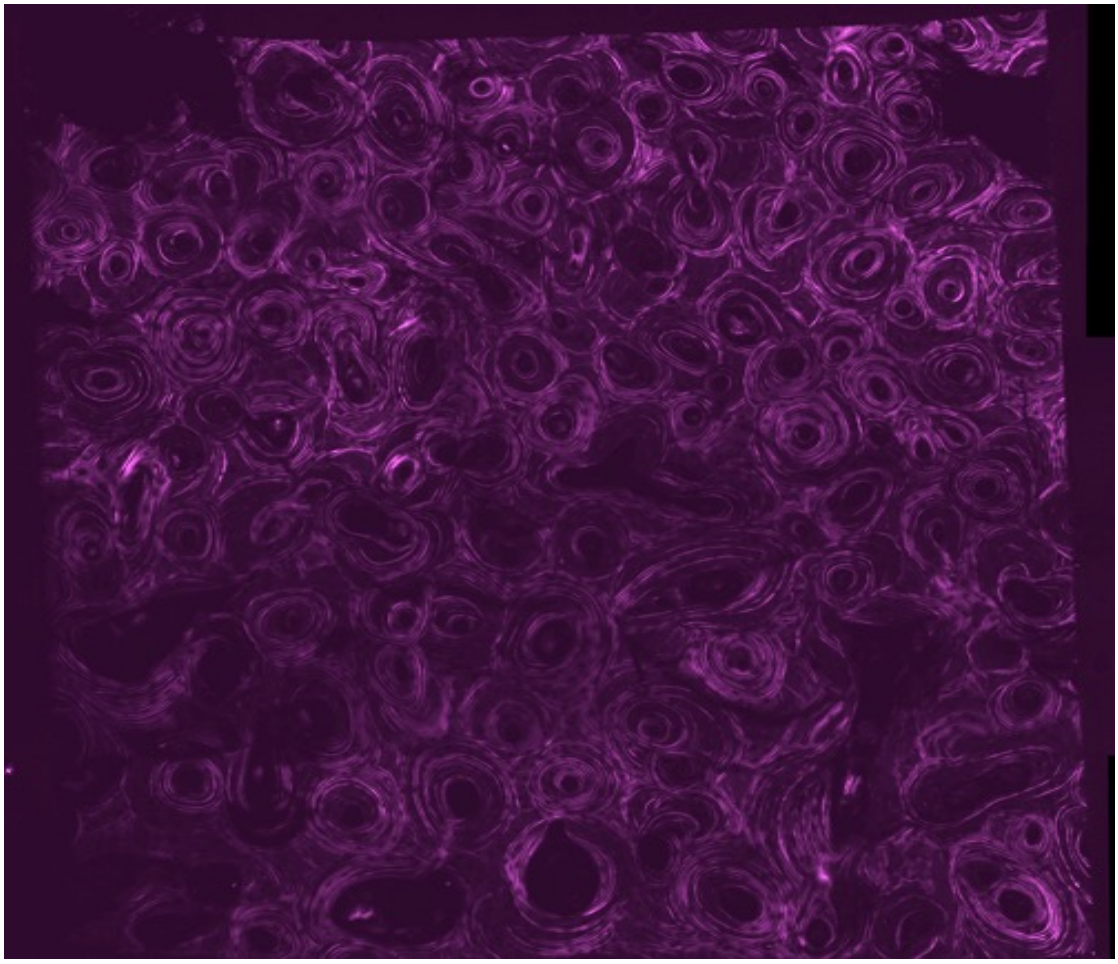

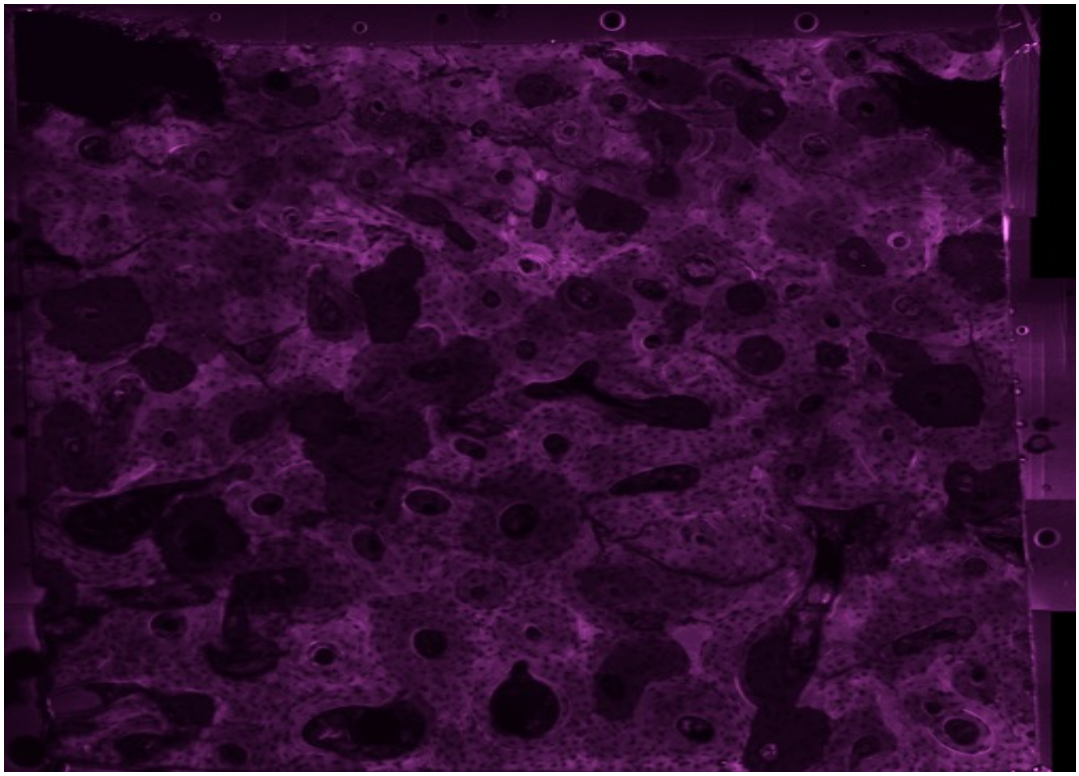

S2D:

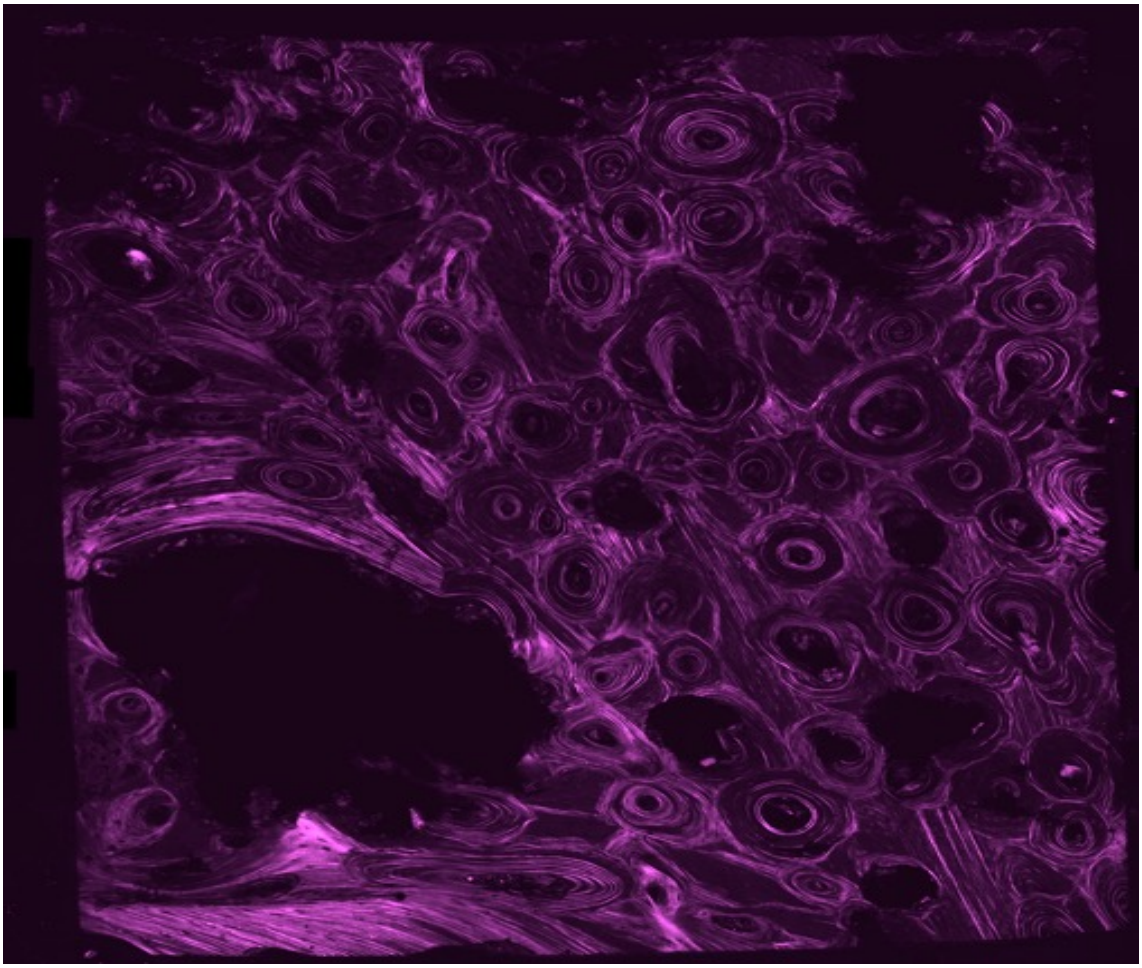

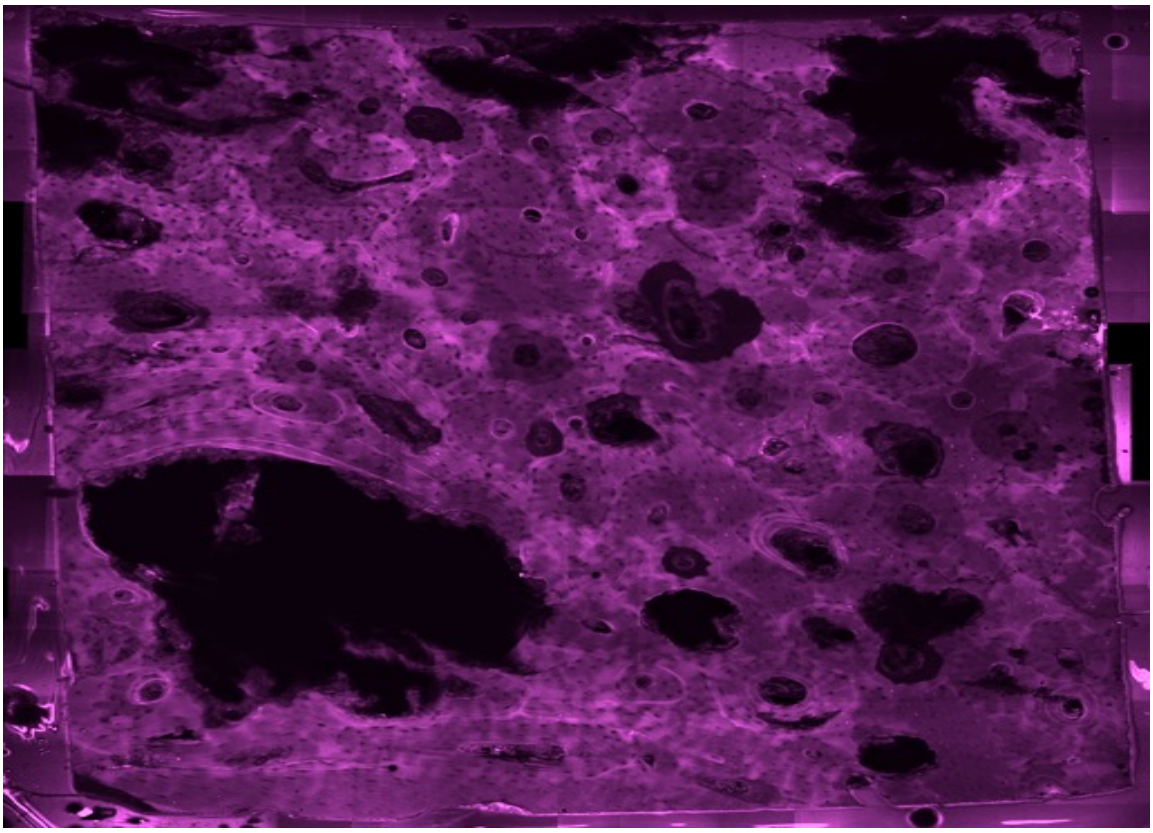

S2E:

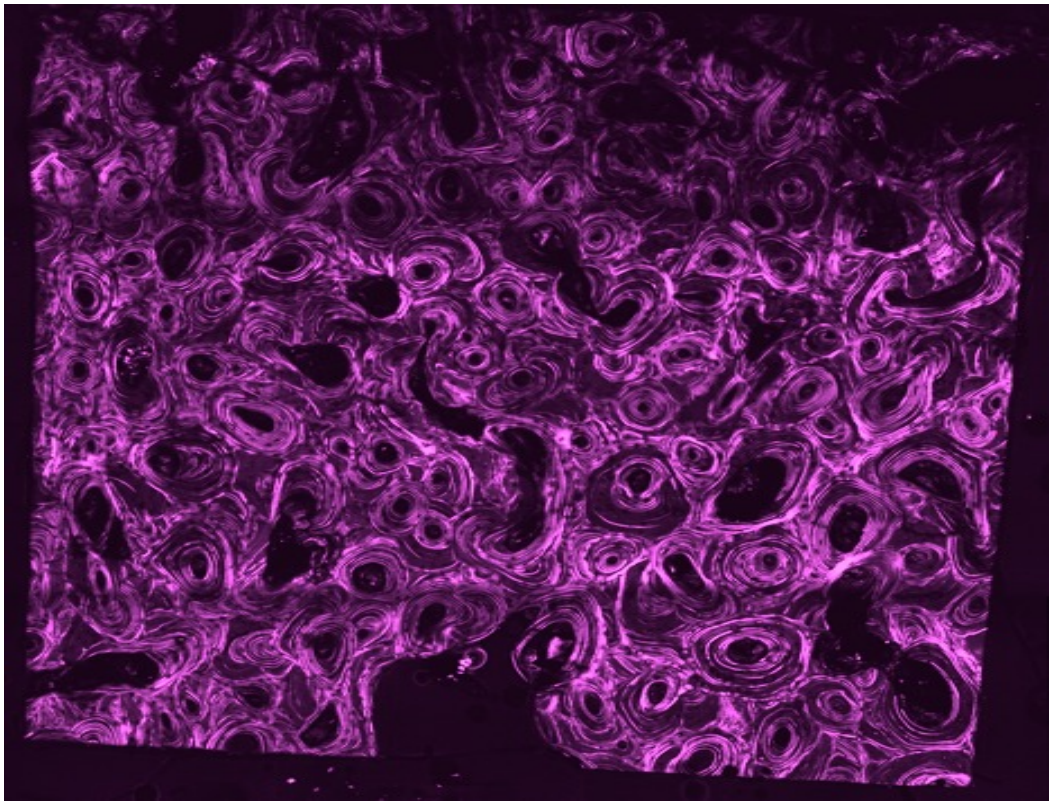

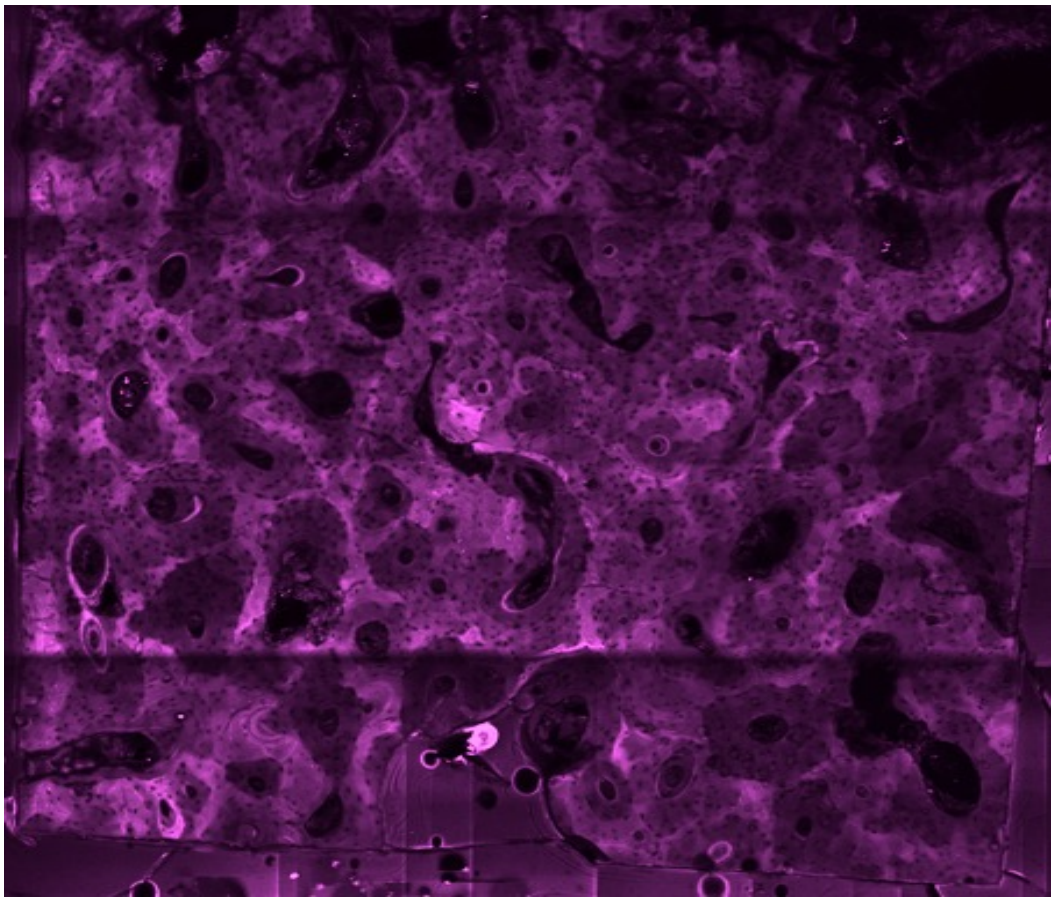

Annex iii: Sample Preparation Protocol

Bone Sectioning:

The sectioning of the bone samples was done following these steps:

1. The water bath of the saw was filled with distilled water just above the bottom of the blade to reduce friction heat (cooling).
2. The bone sample was mounted on the clamp, by fixing the screws of the clamp using Allen wrench.
3. The clamp was screwed on the lever arm of the saw.
4. The length of the cut (in this case was about 3-4 mm) was determined, by rotating the scale knob four full rotations to get 4 mm or more if needed.
5. Cutting was started by turning the saw on at speed 4
6. All samples were cut roughly in equal dimensions.

Bone Surface Polishing:

This step clarifies how to use the Micromiller to polish the bone specimens after they have been glued on the glass slides. Time required: 2-3 Hours.

Note: The milling takes about 1 hour, if you have the specimens equally in height. However, he time might increase if you have specimens which vary in height.

1. Wear proper protection equipment; lab coat and gloves
2. Turn the Micromilling (Leica Sp2600) on
3. Click Stand By
4. Place the stage on its track in the device
5. Place the bone glass slide on the stage
6. Connect the stage with the compressor (to make sure the glass slide is fixed on the stage)
7. Critical Point: Find out the highest point on the bone surface, set mode: Manual, then move the stage forward and backword, up and down till the highest point of the glass approximates the diamond knife, it is very important to find the highest point, otherwise if the diamond knife starts cutting from a lower point, it might get broken. Moving the diamond head above the surface will give an indication if the highest point is close or not. If you are sure of the starting position, then

8. Set the Front and Rear position to tell the device where the cutting interval starts and ends. Move the stage to the front position then clicking on FRONT, then click the opposing arrows (⇓⇑) and then move it to the rear position, click REAR and click the opposing arrows (⇓⇑) again (it should stop blinking)
9. Click on Run Mode to change the Mode to: Auto
10. Turn on the attached biological vacuum, Mode: Manual
11. Ready? Click Run Enable and Run Stop at the same time, then click on the Vacuum button
12. Observe the progress of milling, the stage should be moving between the Front and Rear position
13. Check if the surface is shiny: stop by clicking on Run Enable and Run Stop at the same time, turn off the compressor, carefully remove the glass slide of the stage
14. Observe the glass slide under the microscope, if the osteons can be clearly seen and if the surface is even then the specimen is ready if not, then mount it back on the milling stage and another few microns are needed to be removed.

Annex iv: Measurement on Bone Surface via AFM

Measuring with the AFM was done following these steps:

1. The AFM was calibrated before each measurement; the cantilever chip was mounted on the glass block and then on the cantilever head.
2. Laser alignment: the laser was aligned at the centre of the photodetector, using the knobs on the cantilever head 1 to 5. Knob 1 and 2 are used to find the laser spot and positioning it on the tip, then knob 3 is used to adjust the mirror to achieve a maximum reflection of the laser signal, then using knob 4 and 5, the laser dot is brought to the centre of the detector, Figure 7.1.

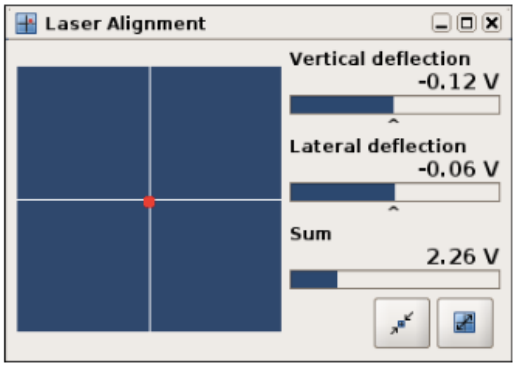

Figure 7. 1: Four quadrant detector. Source (JPK.com)

3. Sensitivity (as explained in section 3.2.3), converting the cantilever deflection unit from volts into nanometres. Here, the cantilever sensitivity is measured on a hard substrate (Mica) in air. The cantilever is pressed into the Mica substrate, and the indentation is assumed to be equal to zero. From the inverse of the slope of the unloading curve, it is possible to obtain how many nanometres the cantilever has deflected corresponding to one voltage unit. A force map was obtained in contact mode with relative set point 0.4 V, z-length 0.5 µm, extend speed 1µm/s, delay mode: constant force, and with 8x8 indentation curves.

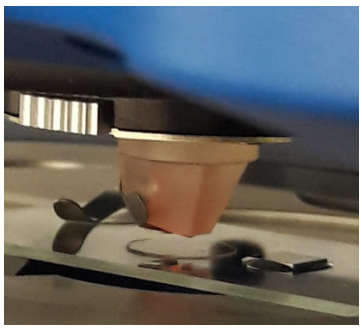

Figure 7. 2: Cantilever head with the glass block, and Mica substrate.

After approaching the surface, force maps were recorded, then using JPK Data Processing software, batch processes applied a linear fit to transform the deflection curve from volts into nanometres. Through selected operations (Linear Fit and Vertical Deflection Calibration) a mean value of the curve's slope is calculated *i.e* for NSC 80, the mean deflection value was 48.88 V/µm. Consequently, the slope's inverse (µm/V) is calculated as 20.46 nm/V, which is equal to the sensitivity factor. This value is then used in the *Calibration Manager* and subsequently the setpoint is transformed from volts to nanometres.

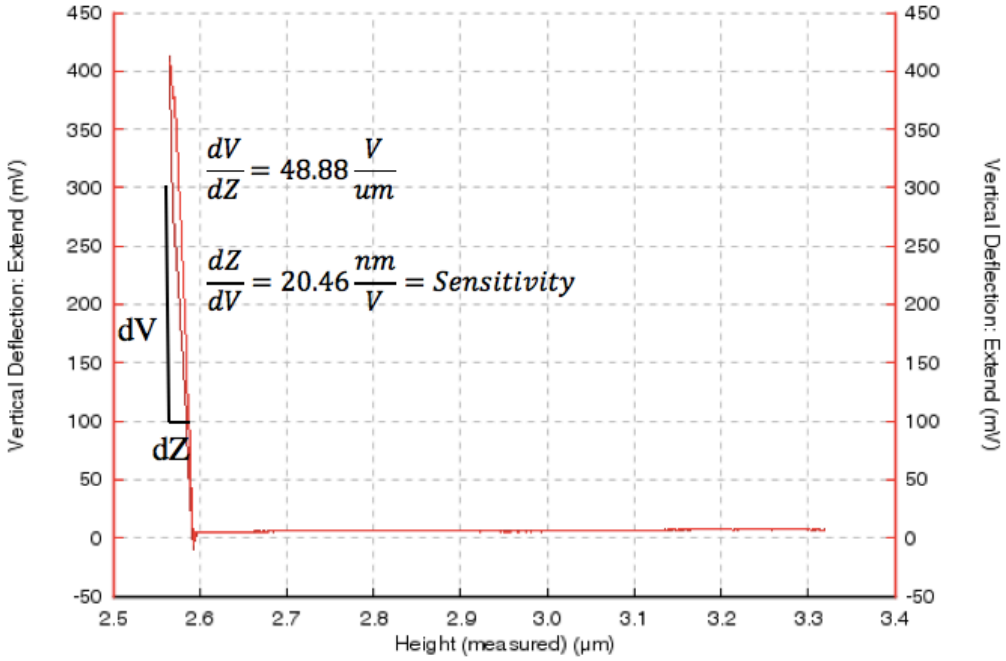

Figure 7. 3: Force map for sensitivity measure on Mica

4. Cantilever stiffness determination (k_c), using the thermal tuning, the tip oscillates in air at some 100s µm away from the substrate, and a plot of the oscillation magnitude vs.

frequency of the oscillation is generated, a peak of the oscillation, like a Gaussian curve, is found around 280 KHz (depends on the cantilever type). A Fit Range is selected and the vertical spring constant is calculated (see section 3.2.2), *i.e.* 25.32 N/m, using a correction factor, the value is corrected to 20.96 N/m.

5. Via Hooke's law, the force (setpoint, nN) is calculated by multiplying the cantilever deflections (D_c) and the cantilever spring constant (k_c).
6. After finalizing these important calibration steps, the mica slide was exchanged with the bone glass slide. Here, the top view optics are needed.
7. As these experiments are conducted in hydrated conditions (PBS), the sensitivity changes slightly between air and fluid, thus, it is necessary to repeat the sensitivity measure in fluid. By pressing the cantilever onto on the tiny glass piece glued next to bone samples.

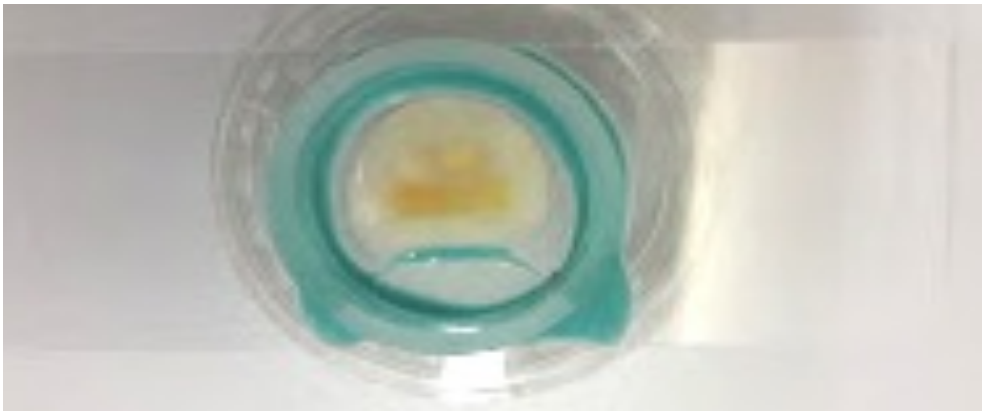

Figure 7. 4: Bone specimen within the fluid cell

Further, a little silicon is applied surrounding the epoxy on the glass slide; otherwise, the epoxy surrounding the bone samples will detach from the glass slide when HBSS in applied.

8. Using the top view optics and focusing on the bone specimens through the cantilever head.
9. PBS (pH 7.4), at room temperature, was added in the fluid cell. The laser must be re-aligned and the AFM should be left to equilibrate thermal drift for 30-60 minutes.
10. Before measuring the sensitivity on glass in fluid, the vertical deflection on the laser detector should be stable without drift. Only then, the cantilever should be approached to the surface to record a force map.
11. Using the JPK Data Processing software, batch processing is applied to find sensitivity in fluid, three operations (Vertical Deflection Calibration, Baseline Offset and Slope

Measure) are selected. (i) in Vertical Deflection Calibration operation, the indentation curve is given in N, by clicking on ignore spring constant, the deflection is now in nm, (ii) in the Baseline Offset operation, a linear fit is selected (Offset+Tilt), this operation subtract the baseline deflection value at zero force, then (iii) in the Slope Measure operation, the slope range is selected to find the contact-point offset (choose the segment to be: retract, x-channel: head-height and y-channel: vertical deflection), then, by applying these settings to all pixels, the slope is transformed into nm/nm, the accepted mean value is 1±0.1. If this is the case, then the mean sensitivity in nm/Volts for these curves need to be calculated, this calculated sensitivity in fluid should be used in the *Calibration Manager*.

12. After having the calibration steps completed, measurements on bone were possible. Some parameters were adjusted on the feedback loop, a force of 150 nN was applied, the QI^{TM} images dimensions were 25 μm x 25 μm with 128 x128 pixels and 256 x 256 resolution. In most of the experiments, the force applied was 150 nN. However, for some experiments, the force was in the range of 100 - 170 nN. Two channels were recorded; namely the vertical deflection and the height data. In total a sum of 126 QI^{TM} images were generated from 22 samples under ambient conditions.

Annex v: Bone Specimens List

#	Specimen ID	Age	Sex	Slide No.	Specimen No.
1	**0170910354R**	**25**	**M**	N1	A
2	**2383854L**	**53**	**F**	N1	B
3	**0781204098L**	**60**	**F**	N1	C
4	**6200L**	**74**	**M**	N1	D
5	**6138R**	**89**	**M**	N1	E
6	**290903379L**	**32**	**F**	N2	A
7	**0031205143L**	**54**	**F**	N2	B
8	**0941207926L**	**63**	**F**	N2	C
9	**6562R**	**81**	**F**	N2	D
10	**6456L**	**94**	**F**	N2	E
11	**0231204243R**	**47**	**F**	N3	A
12	**0271205510R**	**58**	**F**	N3	B
13	**6129R**	**69**	**F**	N3	C
14	**6568L**	**85**	**F**	N3	D
15	**6434R**	**101**	**F**	N3	E
16	**008130079L**	**23**	**F**	S1	A
17	**0171006928L**	**42**	**F**	S1	B
18	**02374848L**	**57**	**M**	S1	C
19	**6440R**	**70**	**F**	S1	D
20	**6108R**	**82**	**M**	S1	E
21	**0211006981R**	**29**	**F**	S2	A
22	**2781152L**	**51**	**F**	S2	B
23	**03376332L**	**59**	**M**	S2	C
24	**6198L**	**80**	**F**	S2	D
25	**6457R**	**87**	**F**	S2	E
26	**0641206338L**	**35**	**F**	S3	A
27	**0441208247R**	**54**	**F**	S3	B
28	**0431302068R**	**62**	**F**	S3	C
29	**6576R**	**80**	**M**	S3	D
30	**6199R**	**98**	**M**	S3	E

Annex vi: Statistical Summary of the Indentation Modulus

Age	Area	Mean	Median	Variance	Std. Deviation
25	Interlamella	.1030	.0557	.028	.166
	Lamella	.2347	.1218	.090	.300
29	Interlamella	.1042	.0521	.073	.271
	Lamella	.4780	.1994	1.155	1.075
32	Interlamella	.5559	.3068	.546	.739
	Lamella	1.1778	.7184	2.068	1.438
51	Interlamella	.1260	.0430	.405	.637
	Lamella	.8090	.2456	9.374	3.062
53	Interlamella	.0536	.0350	.008	.089
	Lamella	.1380	.0768	.060	.245
60	Interlamella	.1712	.1005	.079	.281
	Lamella	.3692	.2195	.265	.515
74	Interlamella	.1939	.1052	.183	.428
	Lamella	.3788	.1953	.310	.556
80	Interlamella	.6962	.1944	7.306	2.703
	Lamella	2.3153	.5915	32.975	5.742
87	Interlamella	.5793	.2224	5.243	2.290
	Lamella	1.6180	.4849	15.445	3.930
89	Interlamella	.1709	.0970	.083	.288
	Lamella	.3714	.2027	.3017	.5492

Annex vii: Statistical Summary of Collagen Fibrils Orientation

Age	Area	Mean	Median	Variance	Std. Deviation
25	Interlamella	52.10	53.59	213.44	14.61
	Lamella	76.21	76.17	15.89	3.99
29	Interlamella	44.25	49.11	298.53	17.28
	Lamella	68.24	68.58	29.01	5.39
32	Interlamella	53.30	53.88	137.84	11.74
	Lamella	67.10	67.79	25.75	5.07
51	Interlamella	33.00	32.91	346.80	18.62
	Lamella	69.84	71.12	24.85	4.98
53	Interlamella	56.13	59.39	173.44	13.17
	Lamella	72.76	74.21	29.84	5.46
60	Interlamella	54.96	55.73	132.33	11.50
	Lamella	69.60	70.65	30.67	5.54
74	Interlamella	24.88	25.16	478.28	21.87
	Lamella	58.76	59.53	82.29	9.07
80	Interlamella	47.76	49.80	114.79	10.71
	Lamella	67.86	68.41	13.62	3.69
87	Interlamella	47.76	51.89	221.35	14.88
	Lamella	65.97	66.27	23.73	4.87
89	Interlamella	44.90	49.94	406.01	20.15
	Lamella	71.07	72.02	26.40	5.14